MARIANNE AANVIK ENGVOLL

REACTIVITY OF ANODE RAW MATERIALS AND ANODES FOR PRODUCTION OF ALUMINIUM

Thesis submitted in partial fulfillment of the requirements
for the degree ***Doktor Ingeniør***

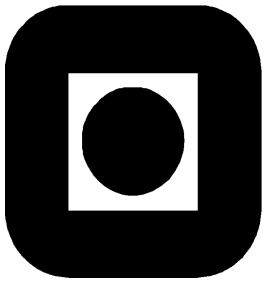

INSTITUTT FOR KJEMI

NORGES TEKNISK
NATURVITENSKAPELIGE UNIVERSITET
NTNU

IUK-thesis: 106 – DESEMBER 2001

URN:NBN:no-2325

URN:NBN:no-2325

Preface

This thesis summarizes 3 years of work at the Department of Inorganic Chemistry, Institute of Chemistry, at the Norwegian university of science and technology (NTNU).

My sincere gratitude is given to my supervisors Professor Harald A. Øye and Professor II Morten Sørlie for introducing me to the exiting field of carbon chemistry and for their guidance and support throughout this work. I would also thank the Norwegian aluminium industry and the Norwegian Research Council (NFR) for financial support through the PROSMAT program. A special thank is given to Elkem Aluminium ANS for providing extra financial resources and for giving me the opportunity to stay at and do the majority of my work at Elkem Aluminium Research's laboratories in Kristiansand.

I am further grateful to Stein Rørvik at Sintef Applied Chemistry, Thor Rostøhl and Øyvind Larsen at Elkem Aluminium Research and Andrzej Piotrowski at Penn State University for assistance on parts of the experimental work. Furthermore, I want to thank the whole staff at Elkem Research, Elkem Aluminium Research, Sintef Applied Chemistry and dept. of Inorganic Chemistry, NTNU for help and interest during the years of my work.

Professor Semih Eser and dr. Maria Klimkiewicz are thanked for giving me the opportunity to visit the Energy Institute at Penn State University. Although the ESEM didn't work, I enjoyed my stay and learned a lot about carbon science and electron microscopy work.

Finally, I want to thank my family and friends for their support. A special thanks is given to my husband Krister for his patience, encouragement and excellent dinners…

Kristiansand, December 2001

Marianne Aa. Engvoll

URN:NBN:no-2325

Abstract

In the Hall-Héroult process for primary production of aluminium, a considerable amount of anode carbon is lost through unwanted gasification in air and CO_2. The carbon gasification reactions are catalyzed by a number of inorganic impurities normally present in the anodes. Some of these impurities follow the anode raw materials while others are introduced during the anode manufacturing process.

The aim of this work is to obtain a fundamental knowledge of how the bath compounds: AlF_3, Al_2O_3, NaF, Na_3AlF_6 and CaF_2, which may be introduced in various amounts to prebaked anodes through the addition of recycled anode butts, influence the air and CO_2 reactivity of anode carbon. In order to avoid the disturbing and possibly masking effect of other impurities normally present in industrial anode materials, this work uses cokes made by carbonization of high purity carbon precursors (tar oil/petroleum pitch) in a laboratory scale coke reactor. Known amounts of fluoride salts or the corresponding metal acetylacetonates are added to the liquid precursor prior to carbonization. “High”-sulfur cokes are prepared by also adding 4.5 weight percent dibenzothiophene to the precursor (corresponds to an addition of 1 wt% elemental sulfur). The calcined coke samples are characterized in terms of reactivity towards air and CO_2 gasification, size and shape of optical texture units and degree of turbostratic order. Scanning electron microscopy and surface area measurements are used to study the surface textural changes resulting from the catalyzed gasification.

The extent of gasification inside industrial prebaked and Søderberg anodes is investigated by characterizing anode core samples in terms of air permeabilities, contamination profiles and reactivities towards air and CO_2 gasification. The characteristics are related to findings from electron microscopy examinations.

COKES DOPED WITH SODIUM ACETYLACETONATE, SODIUM FLUORIDE AND CRYOLITE

Sodium acetylacetonate decomposes completely to sodium carbonate during carbonization and calcination of the coke samples. At the initial stages of gasification, the sodium carbonate particles decompose to a sodium oxide phase, which catalyzes the air and CO_2 gasification reactions strongly.

Sodium fluoride and cryolite also act as strong gasification catalysts. Due to formation of higher amounts of inhibiting fluorine gases (COF_2, $AlOF_2$), the cryolite doped cokes are less reactive than the corresponding sodium fluoride cokes. The difference between the two coke series is especially pronounced during air gasification.

The air reactivity of the sodium-doped cokes is markedly reduced when 4.5 weight percent dibenzothiophene is added to the coke precursors prior to carbonization. During carbonization, the sulfur is stabilized in large aromatic molecules and it is only liberated when the carbon matrix is gasified. The free sulfur adsorbs on the active sites of the sodium particles and lowers their catalytic activity. The Na-S adsorption complexes are thermally unstable at the CO_2 gasification temperature (960 °C) and the CO_2 gasification rates are therefore not affected by the dibenzothiophene additions.

The additions of various amounts of sodium acetylacetonate, sodium fluoride or cryolite (< 0.7 wt%) do not affect the optical texture and turbostratic structure development processes during carbonization and calcination of the coke samples.

COKES DOPED WITH CALCIUM ACETYLACETONATE AND CALCIUM FLUORIDE

Both calcium oxide (from decomposition of calcium acetylacetonate) and calcium fluoride act as very strong catalysts towards the carbon-CO_2 gasification reaction. Presumably because of the low reaction temperature (525 °C), the air gasification rate is only slightly enhanced by the calcium additions.

Due to sulfur poisoning of the catalytically active calcium oxide particles, the CO_2 reactivities of the calcium acetylacetonate doped cokes are markedly reduced when 4.5 weight percent dibenzothiophene is added to the coke precursors prior to carbonization. Because of the low reactivity of the calcium acetylacetonate doped cokes towards air gasification, the amount of sulfur released from the coke matrix is too low to provide a measurable air reactivity reduction.

Sulfur is unable to adsorb on and deactivate the catalytic sites of calcium fluoride.

Neither the optical texture nor the turbostratic coke structure is affected by the additions of various amounts of calcium acetylacetonate and calcium fluoride (< 0.5 wt%).

COKES DOPED WITH ALUMINIUM ACETYLACETONATE AND ALUMINIUM FLUORIDE

When heated to temperatures above 110 °C, aluminium acetylacetonate decomposes completely to aluminium oxide. During carbonization of the tar oil, the small aluminium oxide particles adhere to the surface of the mesophase spheres and prevent them from coalesce on contact. Addition of 1 – 2 wt% aluminium acetylacetonate has the largest textural effects and gives very fine-grained mosaic textures. At higher dopant loadings, the aluminium oxide particles form agglomerates and their influence on the texture development becomes smaller. Since the concentration of active carbon sites is affected by the fineness of the coke texture, the measured coke reactivities are influenced by both the coke texture and the concentration and dispersion of the catalytically active aluminium oxide.

Aluminium fluoride reduces the gasification rates if added to cokes with fine optical textures. The air and CO_2 reactivities go through a minimum at an aluminium content of approximately 0.4 wt%, which corresponds to an addition of about 1.7 wt% AlF_3 to the precursor prior to carbonization. At higher AlF_3 additions the reactivities increase again. The observed reactivity behavior probably results from a competition between deactivation of active carbon sites by adsorption of gaseous fluorine compounds ($AlOF_2$, COF_2) and the weak catalytic effect of the condensed aluminium species present (AlF_3 and Al_2O_3). At low aluminium fluoride additions, the fluoride deactivation dominates, but at higher additions, the catalytic activity of aluminium oxide and aluminium fluoride takes over. Due to a low concentration of active sites, the addition of aluminium fluoride has only a minor reducing effect on the reactivity of cokes with coarse-grained textures.

The reactivities of neither the aluminium acetylacetonate nor the aluminium fluoride doped cokes are influenced by the concurrent addition of 4.5 wt% dibenzothiophene.

GENERAL REMARKS ON RELATIVE CATALYTIC STRENGHTS

Based on relative catalytic strengths, the contamination species studied may be ordered as follows (strongest catalyst set as 100):

"Low"-sulfur cokes:

CO_2 gasification:

CaF_2	=	CaO	>>	NaF	>	Na_3AlF_6	>	Na_2O	>>	Al_2O_3
100		100		26		21		15		3

Air gasification:

NaF	=	Na_2O	>>	Na_3AlF_6	>>	CaF_2	>	Al_2O_3	>	Na_2O
100		100		57		29		24		19

"High"-sulfur cokes:

CO_2 gasification:

CaF_2	>>	CaO	>>	NaF	>	Na_3AlF_6	>	Na_2O	>>	Al_2O_3
100		50		25		21		15		3

Air gasification:

Na_2O	>>	CaF_2	=	Al_2O_3	>	NaF	>	Na_3AlF_6	=	CaO
100		19		19		16		13		13

Aluminium fluoride inhibits the gasification reactions.

There are no cocatalytic effects between calcium and sodium *i.e.* the catalytic activity of calcium is not affected by the concurrent presence of sodium and *vice versa*.

GAS REACTIVITY OF INDUSTRIAL ANODES

The carbon dioxide produced at the anode working surface, percolates through the open porosity of the anodes and reacts with accessible carbon in the lower parts. Airburn is mainly of concern at the exposed parts of prebaked anodes (anode tops and the sides near the tapping positions) and under the gas skirts of the Søderberg anodes. From air permeability measurements and electron microscopy examinations, internal CO_2 gasification is found to occur in the lower 3 – 5 cm of prebaked anodes. Depending on the anode top surface temperature, air gasification may occur as deep as 4 cm below the anode top surface. In Søderberg anodes the extent of internal CO_2 gasification strongly depends on the gas permeability of the anode. In high-permeability Søderberg anodes, CO_2 gasification may occur as far as 60 cm above the working surface. Higher up, the temperature is normally too low for gasification. In some particular low-permeability Søderberg anodes (permeability resembling "bad" prebaked anodes), internal CO_2 gasification is limited to the lower 15 – 20 cm of the anodes.

In both prebaked and Søderberg anodes, the more reactive binder coke is selectively gasified. Since much of the binder phase in the lower parts of the high-permeability Søderberg anodes

is consumed, substantial dusting is expected from the working surface of these anodes. In the prebaked anodes, the binder phase is mostly structurally intact.

Catalytically active sodium and calcium impurities are mainly introduced to prebaked anodes via the addition of butts. Pot-room dust is an important contamination source in Søderberg anodes. Additionally, the lower parts of especially the high-permeability Søderberg anodes are contaminated by gaseous sodium and aluminium bath species that penetrates into the anode open porosity and condense within the anodes.

Contents

1 Introduction

1.1 The Hall-Héroult process

1.1.1 Fundamentals

In the Hall-Héroult process aluminium is produced by electrolysis of aluminium oxide (Al_2O_3) dissolved in an electrolyte (bath) mainly consisting of cryolite. The electrolysis is carried out in large cells where the liquid metal serves as a cathode. The anodes, which are made of petroleum coke and carbonized coal tar pitch, is continually consumed during the electrolysis.

Oxygen from the aluminium oxide is discharged electrolytically onto the anode as an intermediate product. However, the oxygen reacts immediately with the carbon anodes under the formation of gaseous carbon dioxide (CO_2). Aluminium is formed at the bath/metal interface and the overall chemical reaction can be written as:

$$2\ Al_2O_3\ (diss.) + 3\ C\ (s) = 4\ Al\ (l) + 3\ CO_2\ (g) \qquad E^0_{1250K} = -\ 1.18V \quad \textbf{Eq. 1.1}$$

Since the decomposition voltage of alumina (without carbon) is - 2.21 V, the depolarization of carbon reduces the reaction voltage by - 1.03 V.

In addition to cryolite, the bath in a modern alumina reduction cell may typically contain 6 – 13 wt% excess AlF_3, 4 – 6 wt% CaF_2, 2 – 4 wt% Al_2O_3 [1]. In some cases small amounts of LiF (2 – 4 wt%) and/or MgF_2 are also added. The bath temperature during cell operation is normally in the range 940 °C to 970 °C.

The theoretical amount of energy required to produce one kg of aluminium is 6.4 kWh. This includes the energy required to heat the reactants from room temperature to the cell operation temperature. However, the typical industrial average energy consumption values are close to 14.5 kWh/kg Al [1]. The increased energy requirement is due to ohmic heat loss in the electrolyte, anode and cathode lining together with a cell current efficiency, which due to back reaction between Al (l) and CO_2 (g) at the anode, always is less than 100 %. The required energy are supplied both in the form of electrical energy and as thermal energy in form of carbon.

1.1.2 Carbon anodes

Two different anode designs are currently in use, prebaked anodes and Søderberg anodes. Prebaked anodes are made from a mixture of 50 – 65 % petroleum coke, 14 – 17 % coal tar pitch binder and 15 – 30 % recycled anode butts. They are formed into blocks and baked in separate anode baking furnaces to temperatures of about 1100 °C. Since the anode carbon is one of the reactants in the electrolysis reaction, the prebaked anodes have to be replaced at regular intervals, usually after 22 – 26 days, when they have reacted down to one third or one fourth of their original size. The remaining anode butts are cleaned and crushed, and used as

a raw material in the production of new anodes. Figure 1.1 shows a sketch of an electrolysis cell with prebaked anodes.

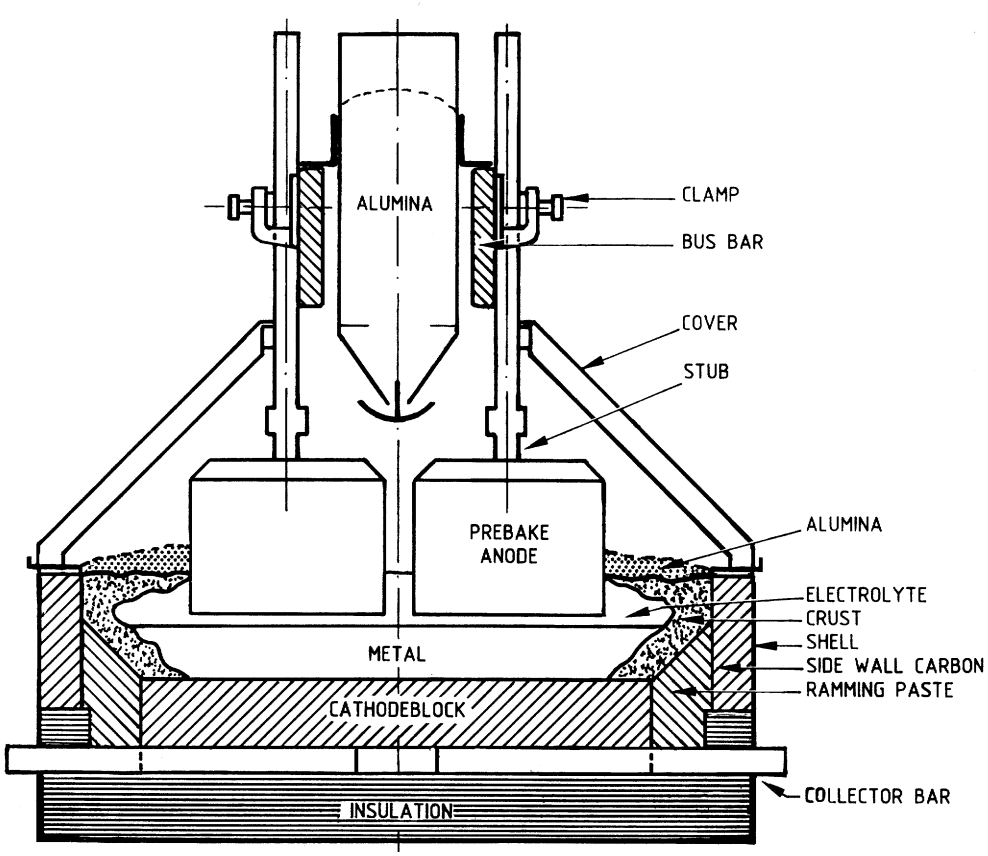

Figure 1.1 Electrolysis cell with prebaked anodes. *Taken from Grjotheim and Kvande* [1]

Søderberg anodes are continuos and self-baking, which in principle is advantageous. Anode paste briquettes, made of petroleum coke and coal tar pitch (~ 25 weight percent), are added to the top of the anode. As the anode is consumed at the working surface, the paste moves slowly downwards through the steel casing, and bakes as it reaches the hotter zone of the anode. The maximum baking temperature is between 950 and 980 °C. A sketch of a typical Søderberg electrolysis cell is given in Figure 1.2.

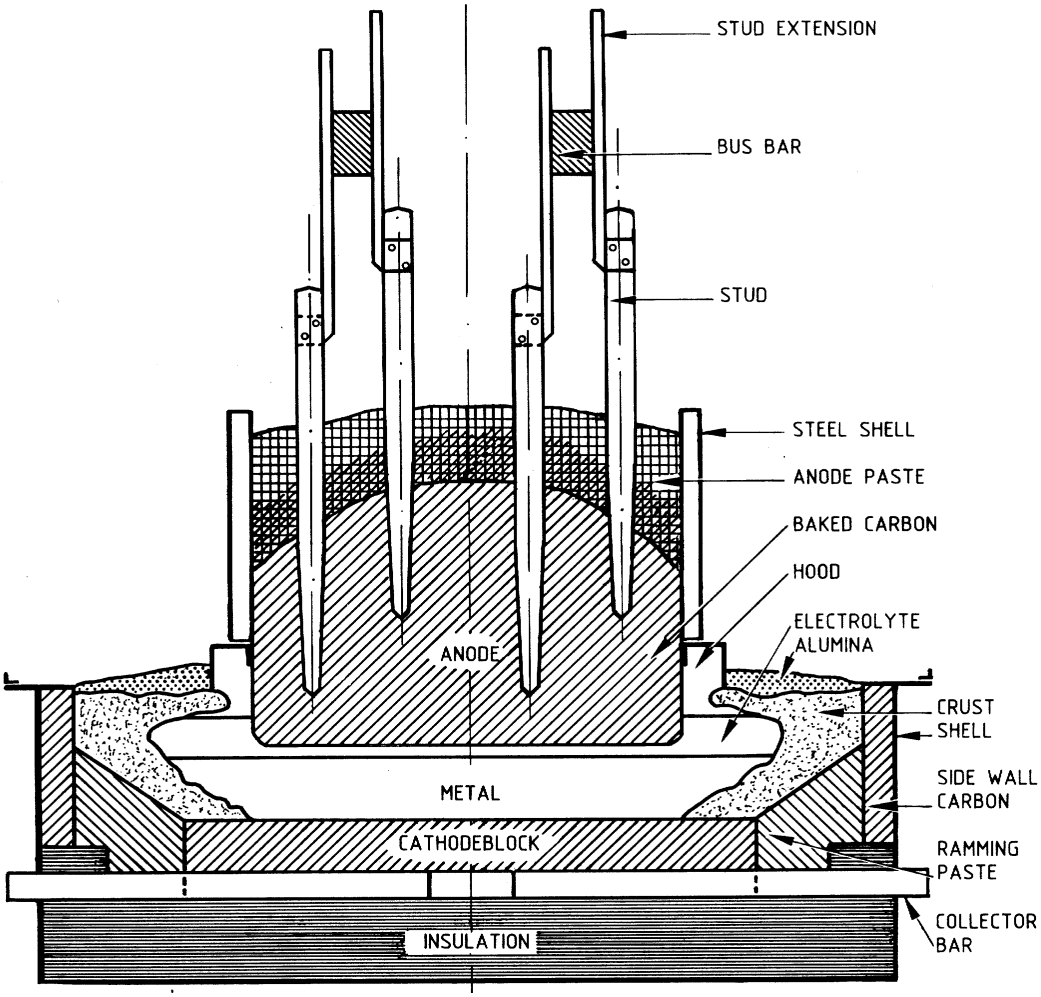

Figure 1.2 Electrolysis cell with Søderberg anode. *Taken from Grjotheim and Kvande* [1]

The prebaked technology has the advantage that it gives a better and more consistent anode quality and hence significantly reduces the anode consumption compared to the Søderberg technology. However, the carbon consumption is still higher than the theoretical value of 0.334 kg C/kg aluminium produced. Figure 1.3 gives an overview of the total anode consumption in a prebaked anode cell.

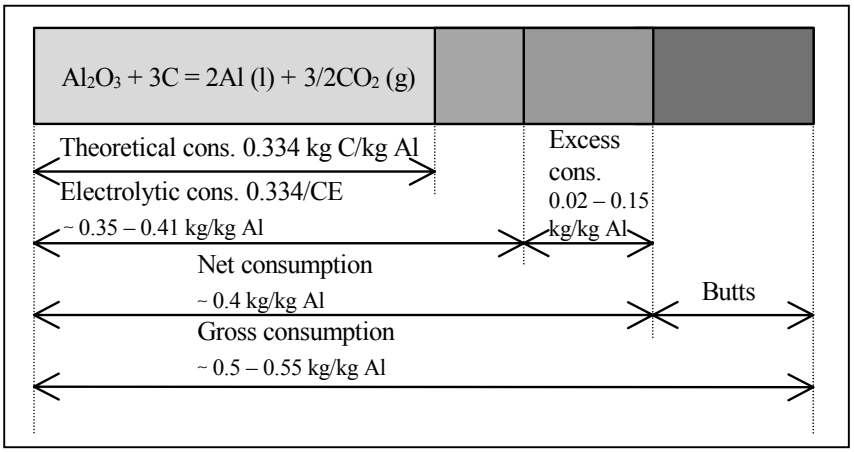

Figure 1.3 Anode consumption in an electrolysis cell with prebaked anodes

According to the main electrochemical cell reaction (reaction 1.1), the minimum *theoretical carbon consumption* is 0.334 kg C/kg Al produced. However, since the cell current efficiency is always less than 100 %, the real *electrolytic consumption* is higher, normally between 0.35 and 0.41 kg/kg Al produced.

The *excess consumption* is caused by reactions between the anode carbon and CO_2 and air as well as dusting. The term "dusting" describes the phenomena where coke aggregate is dislodged from the anode as a result of selective oxidation of the more reactive binder matrix. The excess carbon consumption is normally between 0.02 and 0.15 kg/kg Al produced, depending on the anode quality and technology. The air gasification reaction contributes significantly. Estimates vary between 8 and 30 % of the total carbon consumption where a value of about 10 % is commonly quoted for prebaked anodes. Rough estimates suggest that the carbon consumption due to CO_2 gasification varies in the range of 2 – 10 % [2]. The net carbon consumption may be close to 0.4 kg C/kg Al produced for modern prebaked anode cells. The gross consumption, which also includes the mass of the butts, may amount to 0.5 – 0.55 kg/kg Al produced.

The carbon-CO_2 gasification reaction rate becomes significant at temperatures above 800 °C. In Hall-Héroult cells the anodes are in contact with CO_2 at sufficiently high temperatures at all submerged surfaces and in the lower part of the open pore system of the baked anodes. The amount of CO_2 that may enter the anode bodies is determined by the gas permeability of the baked anodes and the hydrostatic pressure (anode submersion depth). A part of the anode above the electrolyte, particularly between the bath level and the top crust (the lower flange of the anode casing in Søderberg cells), will also be at a temperature where the carboxyl reaction may play a part.

A prebaked anode will be in contact with air at exposed anode surfaces above the bath level. Air has access to the vertical anode sides directly above the electrolyte only if it leaks in through the top crust cover. If not properly covered by crushed bath and/or alumina, the hot anode tops are exposed to air at atmospheric pressures. In a Søderberg anode the magnitude of air exposure to the anode sides depends on air leaks through the top crust and gas manifolds and the magnitude of negative pressure in the gas channels. The temperature of the

anode sides directly above the bath level is, however, well within a diffusion controlled regime; *i.e.* the reaction rate depends on how fast O_2 can be transported to the reaction zone. Air has also free access to the Søderberg anode top, but the temperature there is too low for gasification.

1.2 Aim of the present work

Although the electrochemical consumption of anode carbon is a valuable energy source, the carbon anodes represent a major cost in the primary production of aluminium. Hence, a lot of research has been done to reduce the excess carbon consumption caused by gasification by oxidation in air and CO_2 as well as dusting. Apart from improving the anode and cell design and operation, it is also a requisite to have a proper understanding of the oxidation mechanisms.

The reactivity of carbon materials is mainly influenced by the following factors:

Surface area accessible for reacting gas

Structure

Presence of gasification catalysts or inhibitors

Carbon anodes are normally contaminated by a number of inorganic impurities. Some follow the anode raw materials while others are introduced through the anode manufacturing process. The aim of this work is to obtain a fundamental knowledge of how the bath components; cryolite, aluminium fluoride, aluminium oxide, sodium fluoride and calcium fluoride, which may be introduced to prebaked anodes via the addition of butts (recycled anodes remnants), influence the air and CO_2-reactivity of the carbon anodes. Previously, several studies have been carried out in order to clarify the effect of these contamination species on the anode reactivity [3-13], but many of the results reported are rather nonconclusive. Most of the previous studies have been performed on commercial anode raw materials, which normally contain considerable amounts of other metal impurities (*e.g.* vanadium, nickel, iron, zinc and lead) that are known to catalyze the gasification reactions. To avoid the masking and maybe disturbing effect of these uncontrollable impurities, this work uses cokes with defined contamination profiles, produced by carbonization of high purity coke precursors in a special pressurized laboratory scale coke reactor. The calcined coke samples are characterized in terms of air and CO_2 reactivity, optical coke texture and turbostratic structure. The surface of the oxidized samples is examined by use of a scanning electron microscope.

In order to investigate to what extent carbon gasification occurs inside industrial anodes during electrolysis, prebaked anode butts and core samples from Søderberg anodes are characterized in terms of air permeabilities, contamination profiles and reactivities towards air and CO_2 gasification. The properties are related to findings from electron microscopy examinations.

Most of the work presented in this thesis has also been published earlier [14-19].

2 Background

2.1 Theory

2.1.1 Mesophase development, carbonization and graphitization

Anisotropic carbons are exclusively formed during pyrolysis and carbonization of parent materials that pass through a fluid phase during heat treatment. Common examples of parent materials are coal-tar pitch, petroleum pitch, solvent-refined coals, polyvinyl chloride and aromatic compounds.

Both coal-tar pitch (derived from coal-tar) and petroleum pitch (residue from heat treatment of petroleum fractions), are complex mixtures of numerous organic compounds, predominately different polycyclic hydrocarbons with 3 or more aromatic rings (PAH). Coal-tar pitches have a very wide molecular weight distribution. In addition to PAHs, they contain alkylated PAH, partially hydrogenated PAH, hetero-substituted PAH *e.g.* amino and hydroxy derivatives, carbonyl derivatives of PAH, polycyclic heteroatomic compounds and oligomeric/polymeric systems. The composition of petroleum pitches varies to a significant degree depending on the feedstock used for its production and the process applied. However a common characteristic of petroleum pitches is that their aromaticity is lower than that of coal-tar pitches. Accordingly petroleum pitches have a higher content of alkyl-substituted and partially hydrogenated PAH [20].

The study of chemical transformations occurring during pitch pyrolysis is very difficult because of the complexity and heterogeneity of the materials. Different kinds of chemical reactions are occurring and their relative contribution is dependent on the concentration and reactivity of the different pitch components. Upon high temperature heat treatment (HTT) at about 400 – 500 °C, petroleum and coal-tar pitches form cokes in relatively high yields. A rather complex thermal chemistry occurs during the heat treatment, but the dominant chemical reaction is dehydrogenative polymerization of aromatic compounds. This type of reaction has been termed “aromatic growth” and the mechanism is schematically depicted in Figure 2.1.

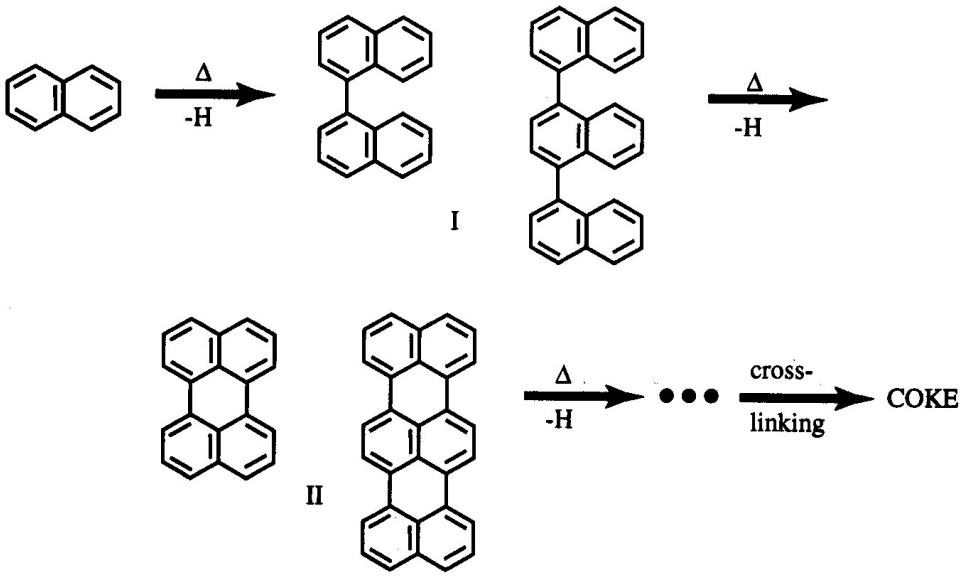

Figure 2.1 Mechanism of aromatic growth. *Taken from Zander* [21]

In the first step monomeric PAHs and structurally related heteroaromatic systems form biaryls and oligo-aryls of type I. In the next step the bi- and oligo-aryls undergo intramolecular dehydrocyclization reactions to form pericondenzed aromatic systems of type II. This sequence occurs repetitively and by crosslinking in the later stages of the liquid phase carbonization, a solid green coke is formed.

Although dehydrogenative polymerization and subsequent dehydrocyclization are the main reactions occurring during HTT of pitches, other types of reactions have also been observed. Hydrogen transfer to stabilize polycyclic aromatic molecules and subsequent splitting of C-C single bonds initially formed leads to the formation of fragmentation products, mainly methyl derivatives of aromatics which are smaller in size than the starting hydrocarbons [21].

Studies of the pyrolysis of pure compounds indicate that radical polymerization is the main reaction of the systems. However, the continuos increase in temperature produces modifications of the system, which tries to get to its maximum thermodynamic stability by cracking, isomerization and molecular rearrangements.

There exist several proposals of how the anisotropic carbon originates from the isotropic pitch melts. Brooks and Taylor [22] initially advanced the proposal that during heat treatment, a carbonaceous *mesophase* grows within the pitch. This phase is more viscous than the parent pitch and has an anisotropic texture, but is yet able to flow. Brooks and Taylor's proposal was that this new phase was a *nematic liquid crystal* which is distinguished from other forms of liquid crystal systems in that the lamellar constituent molecules of pitch precursors are stacked approximately parallel to each other, other types of order being absent.

When aromatic growth during liquid phase thermolysis of a pitch has led to a sufficiency high concentration of sufficiency large aromatic systems (molecular weights > approx. 600 amu), mesophase formation occurs if some critical parameters as *e.g.* viscosity, heating rate and others are met. The mesophase is strongly anisotropic and takes a spherical form in order to minimize its surface energy. As shown in Figure 2.2, the lamellas are oriented against the poles of the sphere and cross the sphere-surface in right angels.

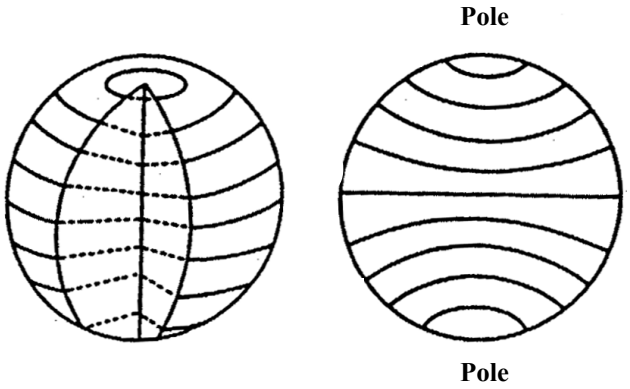

Figure 2.2 Carbon mesophase

At further heating or increasing residence time, more and more mesophase is formed from the isotropic pitch. The size of the mesophase spheres increases and they start to coalesce into bigger and bigger anisotropic areas. The transition from a flowing/plastic pitch to a rigid semi-coke (green coke) occurs in a narrow temperature interval around 500 °C. Still a significant amount of hydrogen is present, but most will be gone when the temperature reaches 800 °C.

The composition of the precursor is a key factor on the process of mesophase formation. The amount and type of compounds will control the reactivity of the pitch, which again will determine the rate of polymerization, the temperature dependence and the viscosity development of the system. The optical coke texture is controlled by the development of mesophase during the carbonization process. The texture is defined by size, shape and orientation of the different crystalline structures, as determined by optical microscopy of polished sections of the material. The size of the optical texture components is a measure of the coalescence behavior of the developing mesophase, the viscosity development in the pitch, the heteroatom content and the size and type of particles present in the pitch. Highly reactive systems give cokes with small optical texture units (domains). Pitches with a high content of PAH of high molecular weight will produce cokes with large domains, corresponding to low viscosity systems which favors mesophase formation and development [23].

The thermally stable, hexagonal graphite structure (see Figure 2.3) involves stacks of layers of condensed benzene rings (graphene layers). The carbon-carbon distances within a layer

(strong σ-bonds) are shorter than between the layers (weak van der Waals bonds), giving graphite an anisotropic character.

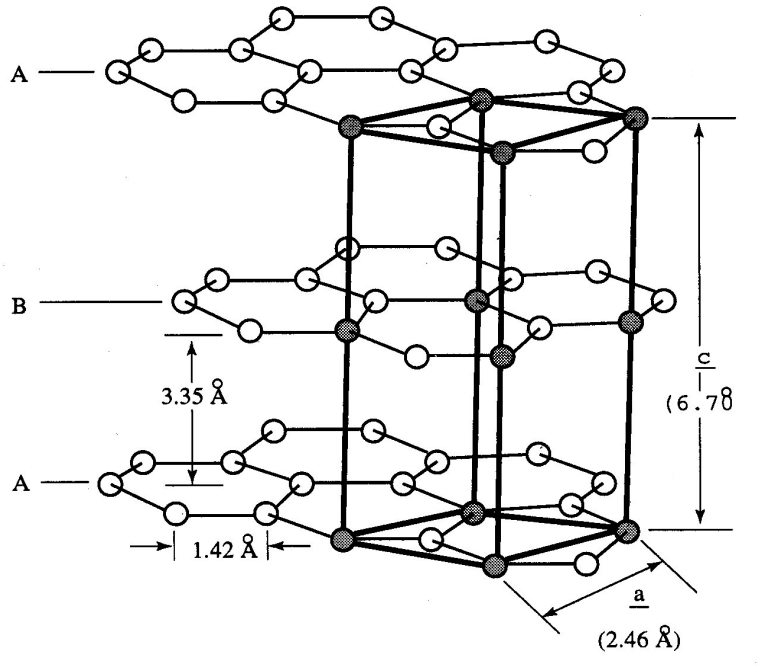

Figure 2.3 Hexagonal graphite structure. *Taken from Redmount and Heintz* [24]

In 1942, Biscoe and Warren introduced the concept of turbostratic order of graphitic materials as: *"consisting of turbostratic groups, each group consisting of a number of graphite layers stacked together roughly parallel and equidistant, but with each layer having a completely random orientation about the layer normal"* [25]. At the green coke stage (HTT: 500 – 550 °C), the coherent domains are small, less than 0.1 nm in diameter, consisting of a stack of 2 or 3 aromatic graphene layers which are orientated roughly parallel. Structural features such as carbon porosity, density and graphitizability are fixed in an irreversible manner [26].

In the columnar stage, extending in the range from 800 to 1500 °C, only the number of graphene layers in the stack increases (up to about 10 layers). Neighboring layers tend to be parallel within bent columns and recover the "discotic" structure the carbon underwent during the liquid mesophase stage. The layer diameter is almost constant in this temperature interval [26].

Above 1500 °C lateral coalescence of the layers begins, edge to edge from one column to the neighbors, entrapping many of the defects within the graphene layers. The real layer diameter increases considerably at this stage. As the coalescence proceeds, the number of layers stacked in coherence also increases. At a threshold, which occurs at about 2000 °C,

the activation energy is sufficiency high for the internal lattice defects to be removed. The lattice distortions relax and the layers become straight [26]. The process of graphitization is shown schematically in Figure 2.4.

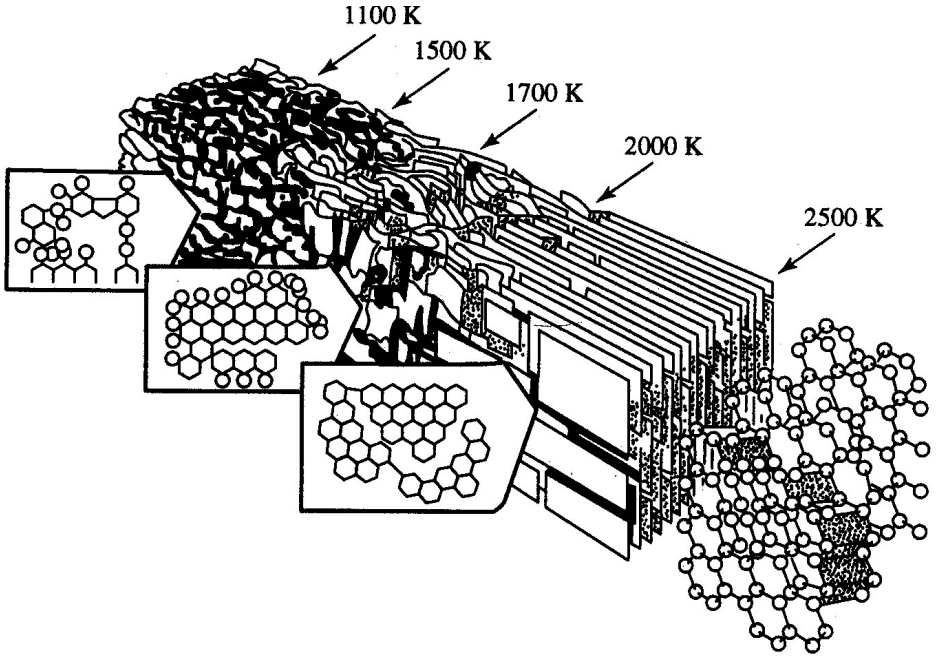

Figure 2.4 Development of crystalline alignment during graphitization. *Taken from Marsh* [27]

2.1.2 Carbon-gas reactions

2.1.2.1 General

Gasification of carbon materials has been the subject of extensive studies, both from a fundamental and a more applied point of view. Carbon gasification reactions form the basis of several important industrial processes. A major part of the world's energy requirements are met by the combustion of coals in electrical power stations. Cokes are gasified as anodes for aluminium production, metallurgical cokes are gasified in the blast furnace and special carbon composites are constructed to withstand oxidation. Reactions with oxygen, steam and carbon dioxide result in carbons being selectively and continuously removed:

$C + O_2 \Leftrightarrow CO_2$ or **Eq. 2.1**

$2\,C + O_2 \Leftrightarrow 2\,CO$ **Eq. 2.2**

$C + H_2O \Leftrightarrow CO + H_2$ **Eq. 2.3**

$C + CO_2 \Leftrightarrow 2\,CO$ **Eq. 2.4**

The characteristics of the reactions are summarized in Table 2-1.

Table 2-1 Thermodynamical and kinetic characteristics of carbon gasification reactions

Reaction	**$\Delta H^0_{800°C}$** *kJ/mol*	**Rel. rate** (800 °C, 1 atm)	**E_A** *kJ/mol*
$C + O_2 = CO_2$	- 395	- [1]	- [1]
$2\,C + O_2 = 2CO$	- 225	100 000	230-270
$C + H_2O = CO + H_2$	136	3	270-310
$C + CO_2 = 2CO$	169	1	333-375

[1] CO dominating reaction product at temperatures above 750 °C

It has proven difficult to obtain a complete understanding of the carbon gasification reactions. Different carbons exhibit different reactivities to oxidizing gases. Marsh [27] has summarized the factors which affect the gas reactivity of carbon materials:

- Concentration of active sites. Carbons do not gasify evenly. Selective gasification occurs at particular sites while other sites remain unaffected. Such active or favored sites are mainly located at the prismatic edges of the carbon layers and at defects such as vacancies or dislocations in the basal plane. The number of structural defects decreases with increasing heat treatment temperature.

- Total surface area accessible for the oxidizing gas and number of active sites per unit surface area.

- Presence of catalyzing or inhibiting impurities.

- Oxygen heteroatoms, especially if carbonylic or heterocyclic, promote reactivity via electron exchange. Chemisorbed hydrogen is said to enhance reactivity by providing sites of preferential oxidation with subsequent production of highly reactive “nascent” carbon sites. The availability of p-electrons at heterocyclic sites (e.g. nitrogen and sulfur) does also favor ring structure attack.

The carbon gasification reactions are sensitive to mass-transfer effects. The gasification rate may be controlled by one of the following steps [27]:

1. Mass transfer (by diffusion) of gaseous reactant(s) from the bulk gas phase to the carbon surface.

2. Adsorption of reactant(s) on the carbon surface.

3. Chemical rearrangements (reactions) on the surface, mobility and formation of adsorbed product(s).

4. Desorption of product(s).

5. Mass transport (by diffusion) of the gaseous reaction product(s) away from the carbon surface.

The rate-determining step is dependent on both process parameters and carbon properties. The reaction temperature, the pressure and the particle size are the most important process parameters, while the porosity, the active site concentration and the presence of catalytic impurities are important carbon properties.

The process' activation energy E, may be visualized by plotting the logarithmic reaction rate as a function of the reciprocal temperature (idealized Arrhenius plots). As it is shown in Figure 2.5 the temperature scale can be divided into three temperature zones corresponding to different rate determining steps. In each zone, the curve-slope (d log(rate)/d (1/T)), is equivalent to the activation energy of the rate-determining process. At low temperatures (zone 1) the rate of the chemical reaction is low and the gasification rate is chemically controlled over the entire accessible carbon surface. The reactant gas concentration is uniform throughout the bulk carbon sample and is equal to the bulk gas phase concentration (C_g). In this zone, the measured activation energy is equal to the true chemical activation energy ($E_{obs} = E_A$). At intermediate temperatures (zone 2), the gasification rate is partly controlled by pore diffusion. The gaseous reactant concentration is zero at some point in the pore system and the apparent activation energy is lower than in zone 1 ($E_{obs} = 0.5 \cdot (E_A + E_D)$, E_D = activation energy of diffusion). At high temperatures (zone 3) the chemical reaction rate is very high and the bulk diffusion from the bulk gas phase to the carbon surface is rate limiting. A gas concentration gradient is build up at the surface and the apparent activation energy is equal to the activation energy of diffusion (E_D).

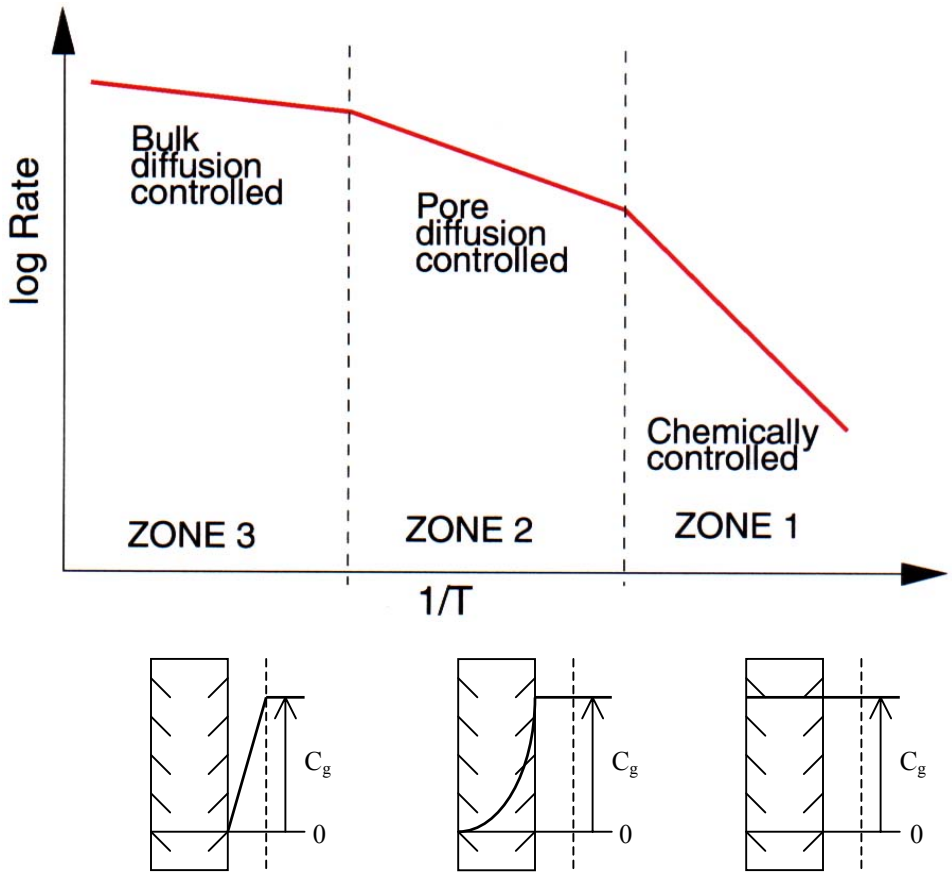

Figure 2.5 Gasification reaction rate and reactant gas concentration of a porous carbon as a function of temperature. *C_g: bulk gas concentration*

It must be emphasized that Figure 2.5 shows an ideal situation. In practice transition regions with deviations from the ideal Arrhenius behavior are often observed between the zones. Also the "high" and "low" temperatures in the above context are relative concepts, as a high temperature for one gasification reaction may be a low temperature for another.

2.1.2.2 Carbon-CO_2 reaction

Carbon reacts with CO_2 under formation of carbon monoxide (Boudouard reaction):

$$C\,(s) + CO_2\,(g) \quad \Leftrightarrow \quad 2\,CO\,(g) \qquad \textbf{Eq. 2.5}$$

The reaction free energy is negative for all temperatures above 700 °C. Figure 2.6 shows how the equilibrium gas composition changes with temperature (1 atm. total pressure).

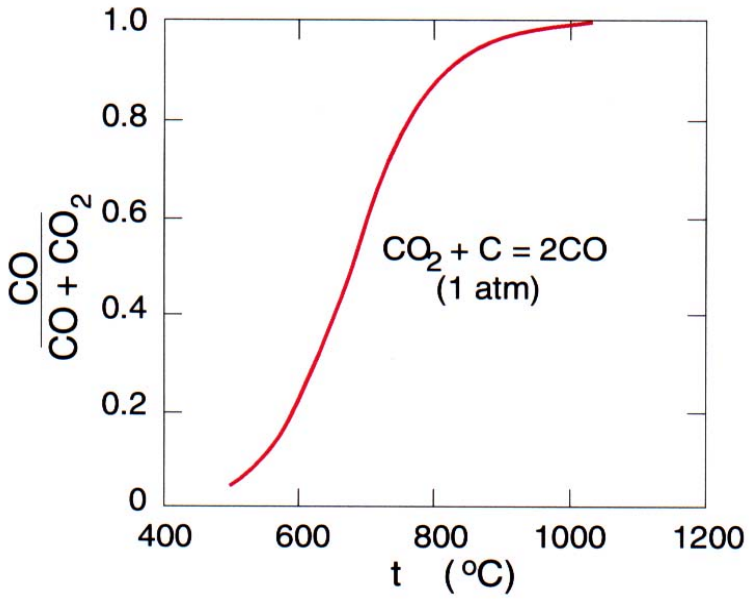

Figure 2.6 C-CO_2 reaction equilibrium, fraction CO in gas phase as a function of temperature

The carbon monoxide produced acts as a gasification inhibitor. Two main reaction mechanisms are put forward. The difference between the two mechanisms lies in the explanation for the retardation of the reaction by carbon monoxide. Gadsby *et al.* [28] proposed that the inhibition by CO is due to chemisorption at the free active carbon sites (C_f):

$$C_f + CO_2\,(g) \Rightarrow C(O) + CO\,(g) \qquad \textbf{Eq. 2.6}$$

$$C(O) \Rightarrow CO\,(g) + nC_f \qquad \textbf{Eq. 2.7}$$

$$C_f + CO\,(g) \Rightarrow C(CO) \qquad \textbf{Eq. 2.8}$$

This model is analogous to the Langmuir-Hinshelwood kinetic models, extensively used in heterogeneous catalysis. Ergun [29] and Walker *et al.* [30] assumed that the uncatalyzed reaction with CO_2 proceeds via a two-step oxidation-reduction cycle:

$$C_f + CO_2\,(g) \Rightarrow C(O) + CO\,(g) \qquad \textbf{Eq. 2.9}$$

$$C(O) \Rightarrow CO\,(g) + C_f \qquad \textbf{Eq. 2.10}$$

In the first reaction "free" carbon sites (C_f) are oxidized by CO_2 to carbon-oxygen complexes C(O). These decompose in a rate determining second step to CO (g). The authors explained

the inhibiting effect of CO by a lowering of the steady-state concentration of C(O) complexes by the reverse of the first reaction (Eq. 2.9). This mechanism is now generally favored.

In aluminium electrolysis cells, CO_2 gasification becomes important at temperatures near the pot operating temperature. However, during electrolysis the anode reaction seems to block the anode working surface, preventing the Boudouard reaction from occurring. Above a certain current density, the surface is occupied by C-O complexes formed by discharge of oxygen atoms (anode reaction) and there are no free sites left where the Boudouard reaction can occur [31]. However, the CO_2 formed at the anode surface percolates the open pore system and gasify accessible carbon within the anode body. The gasification reaction can also take place at the vertical anode sides, above the bath level. However, the reaction rate is very temperature dependent, and it is fastest near the electrolyte, where the temperature is highest.

The kinetic data on the carboxy reaction reported in the literature is very discordant. The reaction rate depends on the structure of the carbon being oxidized and is slowest for structurally well-ordered carbons (graphite, pyrolytic carbons). Generally, the reaction rate is considered slow compared to the rate of the reaction between carbon and oxygen.

2.1.2.3 Carbon-O_2 reaction

Carbon reacts with oxygen under the formation of carbon dioxide and carbon monoxide:

$$C\,(s) + O_2\,(g) \quad \Leftrightarrow \quad CO_2\,(g) \qquad \textbf{Eq. 2.11}$$

$$2\,C\,(s) + O_2\,(g) \quad \Leftrightarrow \quad 2\,CO\,(g) \qquad \textbf{Eq. 2.12}$$

Both reactions are strongly exothermic and CO_2 is the favored product at temperatures below about 700 °C. However, the pCO/pCO_2 ratio increases strongly with increasing temperature and above 800 °C, CO is dominating (see Figure 2.6). The oxygen gasification reaction is significant from temperatures around 300 – 400 °C, but the rate is still moderate at 400 °C. At temperatures of 430 – 530 °C, normal anode cokes may ignite and the gasification rate becomes mass-flow controlled.

Despite extensive investigations, the mechanism of the carbon-oxygen reaction is not understood in detail. The reasons for this are that the reaction is highly exothermic and extremely sensitive to the limitations imposed by energy and mass transfer processes. Based on the knowledge of the important role of surface oxygen complexes, Marsh [27] suggests the following reaction stages to explain the formation of carbon monoxide and carbon dioxide:

C_f	+	O_2 (g)	⇒	$C(O_2)$	or	$C(O_2)_m$		**Eq. 2.13**
		$C(O_2)_m$	⇒	C(O)	+	$C(O)_m$	and/or	
			⇒	$C(O)_m$	+	$C(O)_m$	and/or	**Eq. 2.14**
			⇒	C(O)	+	C(O)		**Eq. 2.15**
		C(O)	⇒	CO (g)				**Eq. 2.16**
		$C(O)_m$	⇒	CO (g)				**Eq. 2.17**
$C(O)_m$	+	$C(O)_m$	⇒	C_f	+	CO_2 (g)		**Eq. 2.18**
$C(O)_m$	+	C(O)	⇒	C_f	+	CO_2 (g)		**Eq. 2.19**
CO (g)	+	C(O)	⇒	C_f	+	CO_2 (g)		**Eq. 2.20**
CO (g)	+	$C(O)_m$	⇒	C_f	+	CO_2 (g)		**Eq. 2.21**
O_2 (g)	+	2 C(O)	⇒	2 CO_2 (g)				**Eq. 2.22**

where C_f is a free active carbon site, $C(O_2)$/C(O) describes a localized, chemisorbed oxygen molecule/atom and $C(O_2)_m$/$C(O)_m$ a mobile chemisorbed oxygen molecule/atom.

The carbon-O_2 reaction has a large negative free energy at all temperatures of interest in the aluminium electrolysis. However, because of limited air access, it is mainly of concern at the exposed parts of the prebaked anodes (top and tapping positions) and under the gas skirts of the Søderberg anodes. The top surface temperature of newly set prebaked anodes is normally within the range where the reaction is chemically controlled. Below the gas-skirts of the Søderberg anode, the temperature is so high that the mass-transport *i.e.* the rate of air leaking is rate determining.

2.1.3 Catalysis of carbon gasification reactions

2.1.3.1 General

A number of compounds have been shown to exhibit catalytic activity towards the carbon-gas reactions, the most active being the transition metals, the alkali metals and the alkaline earth metals. In a literature review, Houston and Øye [2] classify Si, Fe, V, Ni, Na, S, Ca, Pb, Cu, Cr, Ti and Al as catalysts to the carbon-O_2 reaction. All the elements, except Si, Zn, Cr and Ti are also found to catalyze the carbon-CO_2 reaction. The role of sulfur appears uncertain (inactive/inhibitor), while aluminium fluoride, boron and phosphor are reported to act as inhibitors towards both the C-O_2 and the C-CO_2 reactions.

It is important to note that a catalyst or inhibitor only affects the gasification rates in the temperature range where the reaction is chemically controlled. In principle, there are many possibilities to explain the catalysis in carbon gasification. For instance, the catalysis of the carbon-CO_2 reaction can be explained as follows:

1. The CO_2 dissociation reaction is accelerated, *e.g.* by a redox cycle, or the equilibrium is shifted to the right due to the involvement of catalytic species in the reaction stoichiometry.

2. The surface reaction is accelerated by increasing the concentration of chemisorbed oxygen (C(O)) or free active carbon sites (C_f) by increasing the intrinsic rate constant.

3. The decomposition of the C(O) surface complexes is accelerated.

Other possibilities are:

4. The catalysts may generate highly reactive carbon atoms by disrupting the carbon structure.

5. The catalysts may create active carbon atoms by effectively dissolving carbon into a surface catalysts phase.

6. The catalysts may create active carbon atoms by perturbing the electronic structure of the carbon; this could include formation of intercalation compounds or indirect multi-center carbon-oxygen-catalysts bonds.

7. The catalysts may participate in a chemical step either by transferring atoms, electrons or both between reagents and carbon.

According to Marsh [27], the efficacy of an inorganic catalyst within a carbon material is a complex function of many variables including: (1) the metal concerned, (2) its chemical state, (3) the size of the catalyst particles and their dispersion throughout the carbon and (4) the relative amount of catalyst.

Normally catalysts increase the reaction rate by changing the reaction route to one with a lower activation energy for the rate determining step. However, in the case of carbon gasification, it is generally accepted that most catalysts enlarge the number of active sites at the carbon surface, without fundamentally changing the kinetic network [32]. In agreement with this, the slopes of the Arrhenius plots do not differ much between catalyzed and non-catalyzed gasification.

2.1.3.2 Topographical effects of catalyzed carbon-gas reactions

There have been many investigations of the topographical effects of catalyzed carbon gasification reactions, most performed on graphite single crystals [33-36]. A unique and most intriguing phenomenon associated with the catalyzed carbon-gas reactions is the motion of the catalyst particles. Three major catalyst actions have been observed:

1. **Pitting:** Catalyst particles located at vacancies within a graphite basal plane form hexagonal pits perpendicular to the plane. The pits can continue to increase in depth due to further penetration of the catalyst. They can also expand due to edge recession of the hole. The larger the pits become, the more circular they appear. An illustration is given in Figure 2.7.

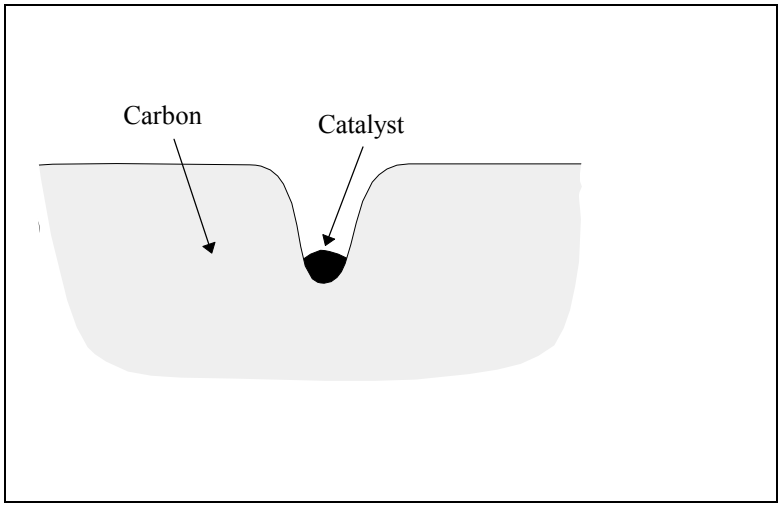

Figure 2.7 Pitting perpendicular to the carbon basal plane. *Seen from the side*

2. **Channeling:** Catalyst particles at edges or steps in the graphite lattice act specifically on the edges and channel into the graphite layers. Channeling occurs when the interaction between the catalyst and the carbon is moderate. The particles carve monolayer channels oriented parallel to the basal planes. The particles and thus also the channels may change direction. The channels might propagate at high speeds, contributing significant to the overall gasification rates. An illustration is given in Figure 2.8.

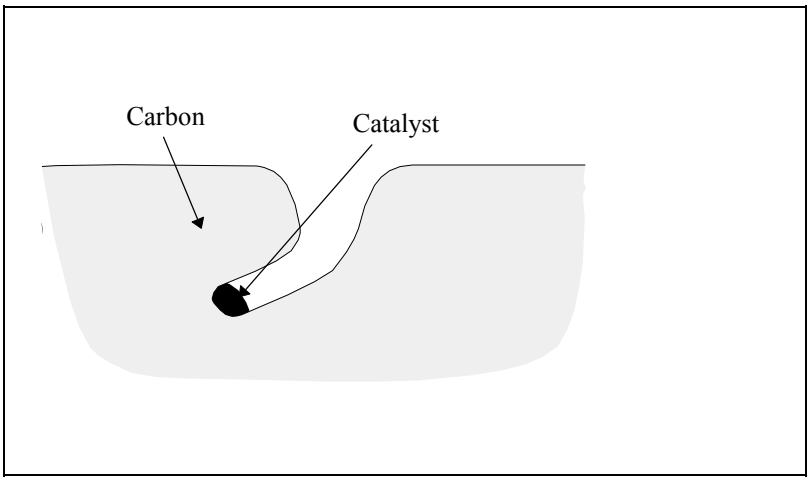

Figure 2.8 Channeling parallel to the basal plane. *Seen from above*

3. **Edge recession:** The catalysts show a strong interaction with the carbon substrate and spread out as a thin film over the edges of the graphene layers. During the catalytic attack, the graphene layers is consumed from the edge. Edge recession is an action similar to channeling; it can involve both multilayer and monolayer edge. The phenomenon is illustrated in Figure 2.9.

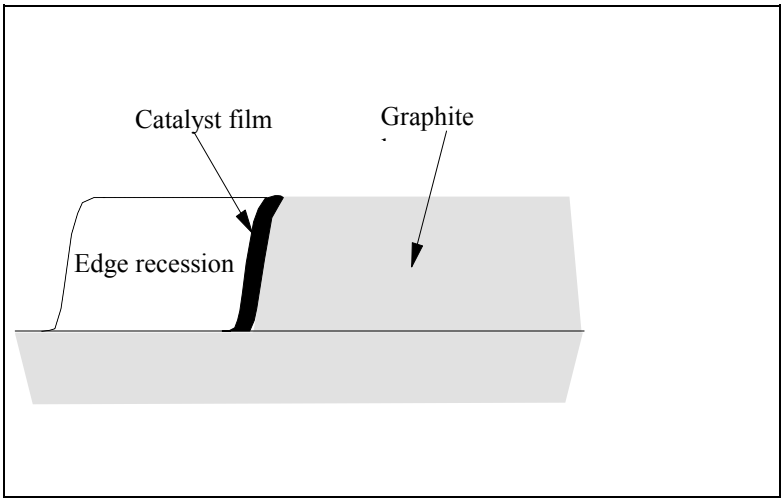

Figure 2.9 Edge recession caused by catalyst film. *Seen from the side*

2.1.3.3 Inhibition of the carbon-gas reactions

There are at least five possible ways of reducing the reactivity of carbon materials [27]. Two are directly connected to the structure of the carbon material:

1. Reduction of the reactive surface area.

2. Improvement of the crystalline order of the carbon material and thereby reduce the number of active sites for gasification.

The three other methods are:

3. Removal of catalytically active impurities.

4. Introduction of atoms/compounds which reduce the rate of the carbon-gas reactions.

5. Formation of a diffusion barrier on the carbon surface.

Only possibility number 4 is a true chemical inhibition of the gasification reactions. This inhibition is understood as a blocking of possible active site at the carbon surface.

There are only a few known inhibitors to the carbon-gas reactions. The most common are compounds containing phosphorus and halogens, and to some extent boric acid and its derivatives. The mode of action of the inhibitors has been widely investigated. In some cases,

the inhibitor reduces the effect of intrinsic catalysts, *e.g.* deactivating them by forming stable compounds (e.g. phosphates), but the principal effect is adsorption of stable compounds at the active sites in the carbon structure [27].

2.2 Mechanisms of catalyzed carbon gasification, literature overview

During the last 3 – 4 decades, the interest in catalytic gasification of carbon materials has expanded rapidly. An enormous amount of work describing mechanisms of catalysis and catalytic activities of a variety of species may hence be found. The aim of this chapter is to summarize and collate some of the available information dealing with the catalytic activity of different sodium, calcium and aluminium compounds.

Two main theories have been advanced to account for the effects of catalysis on carbon gasification reactions; the oxygen-transfer mechanism and the electron-transfer mechanism. The oxygen-transfer mechanism involves extraction of oxygen from the reactant gas by the catalyst which then supplies it in an active form to the carbon. The principal embodiment of such a process is a redox mechanism in which the catalyst is alternately oxidized by the gaseous reactant and reduced by the carbon.

In the electron transfer mechanism the electron configuration of the catalyst is considered. Many of the known gasification catalysts either have unfilled electron shells and can accept electrons from the carbon matrix or have labile electrons that can be donated. The electron transfer leads to a rearrangement of the π-electrons in the carbon. This weakens the carbon-carbon bonds at the edges of the carbon lattice, allowing bond formation with an adsorbed oxygen atom which then requires less energy to be removed as a CO molecule.

Today, the oxygen-transfer mechanism is most widely accepted [27, 37]. The catalysts are known to have a localized behavior *i.e.* the catalyzed reactions do only occur at the point of contact between the catalyst and the carbon matrix as explained by the oxygen-transfer mechanism. The activation energy of the carbon gasification reactions is independent of the catalyst concentration. This it not expected by the electron-transfer mechanism. Because of the leading role of the oxygen-transfer mechanism, this chapter concentrates on the mechanisms that are based on this theory.

All thermodynamical data used in this chapter are taken from Barin [38].

2.2.1 Catalytic effect of sodium

The alkali metals are known to catalyze the carbon gasification reactions strongly. Although many attempts have been made to explain the behavior of alkali metal salts in catalyzing the oxidation of carbon by oxygen and carbon dioxide, no single theory has been found capable of interpreting all the observed results [39].

One of the most quoted mechanisms for the sodium carbonate catalyzed CO_2 gasification reaction was initially proposed by Fox and White [40]:

$$Na_2CO_3 + 2\,C \Leftrightarrow 2\,Na + 3\,CO\,(g) \quad \Delta G^0_{950°C} = 139.3\ kJ/mol \quad \textbf{Eq. 2.23}$$

$$2\,Na + CO_2\,(g) \Leftrightarrow Na_2O + CO\,(g) \quad \Delta G^0_{950°C} = -74.5\ kJ/mol \quad \textbf{Eq. 2.24}$$

$$Na_2O + CO_2\,(g) \Leftrightarrow Na_2CO_3 \quad \Delta G^0_{960°C} = -151.1\ kJ/mol \quad \textbf{Eq. 2.25}$$

where reaction 2.23 is assumed to be rate determining. The free energy change of this step is highly positive at the usual CO_2 gasification temperatures (900 – 1000 °C). However, McKee [41] has claimed that the sodium vapor pressure easily can reach values approaching 10^{-3} atm (depending on the ambient pressure of CO). It has been proposed that the overall gasification rate depends on the salt-carbon interfacial contact area, which will be rapidly enlarged when the sodium carbonate melts (T_m = 854 °C) and spreads on the carbon surface [42].

In an attempt to unravel the mechanism of the catalyzed O_2 gasification process, McKee and Chatterji [39] studied the effect of alkali-metal carbonates and oxides on the oxidation of graphite by means of simultaneous TGA-DTA and hot-stage microscopy. The reaction between graphite and carbonate in an inert gas (He) was only detectable by weight loss at temperatures in excess of 700 °C. In presence of O_2 the catalyzed exothermic oxidation of graphite was measurable at a temperature 150 °C below the normal oxidation temperature of pure graphite (~ 650 °C), and at a temperature close to the melting point of sodium peroxide, Na_2O_2 (460 °C). The catalyzed oxidation was accompanied by movement of liquid-like particles on the graphite basal-plane (channeling). Three stages were believed to be involved in the Na_2CO_3 catalyzed O_2 gasification of carbon:

$$Na_2CO_3 + C + O_2\,(g) \Leftrightarrow Na_2O + 2\,CO_2\,(g) \quad \Delta G^0_{500°C} = -189.2\ kJ/mol \quad \textbf{Eq. 2.26}$$

$$Na_2O + \tfrac{1}{2}\,O_2\,(g) \Leftrightarrow Na_2O_2 \quad \Delta G^0_{500°C} = -32.8\ kJ/mol \quad \textbf{Eq. 2.27}$$

$$Na_2O_2 + C \Leftrightarrow Na_2O + CO\,(g) \quad \Delta G^0_{500°C} = -147.2\ kJ/mol \quad \textbf{Eq. 2.28}$$

where oxygen first reacts with sodium carbonate in intimate contact with carbon (Eq. 2.26).

One problem with this type of redox mechanisms is that the reactions between sodium carbonate and the carbon are thermodynamically unfavourable at the normal gasification temperatures. The free energy change of reaction 2.23 is highly positive while the energy change of reaction 2.26 is negative only because reaction 2.29 provides a substantial thermodynamic driving force to the otherwise non-productive dissociation process.

$$C + O_2\,(g) \Leftrightarrow CO_2\,(g) \quad \Delta G^0_{500°C} = -395.5\ kJ/mol \quad \textbf{Eq. 2.29}$$

The thermal dissociation of sodium carbonate:

$$Na_2CO_3 \Leftrightarrow \quad Na_2O + CO_2\,(g) \quad \Delta G^0_{500°C} = 206.4\ kJ/mol \quad \textbf{Eq. 2.30}$$
$$\Delta G^0_{950°C} = 151.1\ kJ/mol$$

occurs to only a very small extent in the vicinity of 500 °C and only to the extent of 1 % at temperatures near the carbonate melting point [41]. However, in an open system the removal of the products could displace the equilibrias to favor the conversion of the carbonates. According to Wood and Sancier [37], there are several experimental evidences for the reduction of alkali metal carbonates when heated in an oxidizing atmosphere in the presence of carbon.

It is generally agreed that the presence of sodium only increases the steady state concentration of oxygen on the carbon surface (k_0, the pre-exponential factor in the Arrhenius equation increases) and leaves the activation energy, E_A, unaffected [43-45]. Based on this, Kapteijn *et al.* [46] argued that a mechanism involving a direct reaction between the catalyst and carbon is unlikely. Several workers have proposed that the alkali carbonates decompose into CO or CO_2 and a stable surface salt complex [43, 45, 47-50]. From high-resolution solid-state NMR experiments, Mims *et al.* [49] found that the alkali catalyst produced by the interaction between the carbonate and the carbon substrate becomes dispersed and stabilized by the formation of surface anionic complexes, such as an alkali metal phenolate group (see Figure 2.10) at temperatures well below the gasification level. The mechanism by which the catalyst forms the phenolate group was not described.

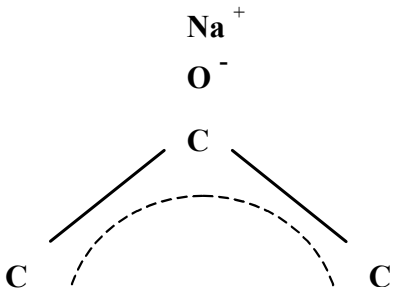

Figure 2.10 Sodium surface phenolate group

The precise interaction of the phenolate groups with the gaseous oxidants and their role in the breakdown of the carbon structure to form CO/CO_2 has not been addressed in detail. Mims and Pabst [51] cite the observed stability and steady-state population of these groups at the gasification temperatures to indicate that the reactions involve a further reversible oxidation of the surface salt followed by a rate-determining decomposition step. Freriks *et al.* [48] suggested that the metal phenolate group weakens the adjacent carbon-carbon bonds, making them susceptible to attack by an oxidant. Chen and Yang [36] used a TEM technique to measure the rates of monolayer edge-recession (uncatalyzed or catalyzed by C-O-M groups) and rates of monolayer channeling (catalyzed by small oxide particles, size < 750 Å) on the basal plane of graphite reacted with H_2O. Calculations of the turnover frequencies (rate/catalyst unit) revealed that the particles had higher activities than the C-O-M groups. Semi empirical molecular orbital calculations revealed that the carbon atom bridging two C-O-K groups (on a zigzag face) gains a large negative charge and is hence a favourable site for binding an O atom (see Figure 2.11 and Table 2-2). The O atoms are supplied by dissociation of CO_2, O_2 and H_2O. A possible reason for the alkali particles being more active than the C-O-M groups is that the particles can dissociate CO_2, O_2 and H_2O at higher rates, by providing either more active sites or higher activities [36]. From gasification and temperature programmed desorption (TPD) measurements Meijer *et al.* [45] concluded that the catalytic active alkali clusters are anchored to the carbon surface via the phenolate groups and are capable of chemisorbing one CO_2 molecule per three to five alkali metal atoms.

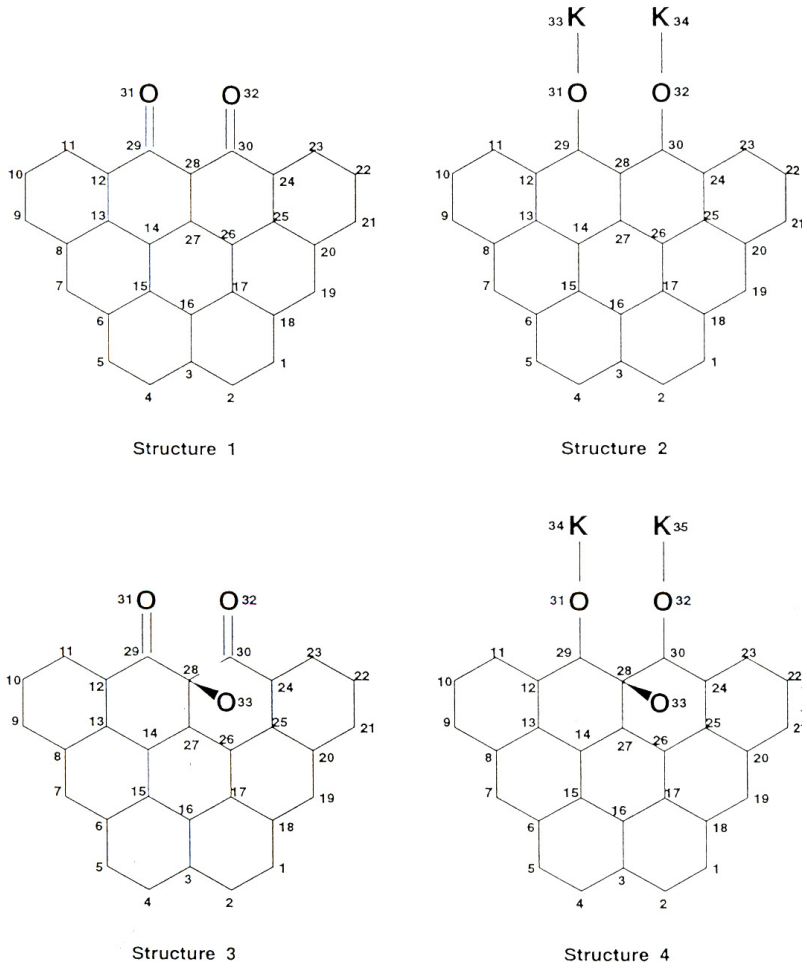

Figure 2.11 Model substrates with zigzag face on graphite for CNDO molecular orbital calculation. *Taken from Chen and Yang* [36]

Table 2-2 Net Charge (electrons) of carbon atoms in substrates with zigzag edge (see Figure 2.11). *Cited from Chen and Yang* [36]

Number	Structure 1	Structure 2	Number	Structure 1	Structure 2
12	0.1579	-0.1548	25	0.2401	-0.0626
13	0.2401	-0.0626	26	0.1359	-0.1605
14	0.1359	-0.1605	27	0.3211	-0.1867
24	0.1579	-0.1548	28	-0.0128	**-0.4863**

Most likely the dissociation of CO_2 on the surface of the sodium particles may be described by [35]:

$$CO_2\,(g) + * \quad \Leftrightarrow \quad CO + O* \qquad \textbf{Eq. 2.31}$$

where * denotes an active site on the sodium catalyst surface. The adsorbed oxygen (O*) diffuses rapidly across the particle and reacts with an free active carbon site (C_f):

$$O* + C_f \quad \Leftrightarrow \quad C(O) + * \qquad \textbf{Eq. 2.32}$$

The carbon-oxygen complexes C(O), decompose in the rate determining second step to CO (g):

$$C(O) \quad \Leftrightarrow \quad CO\,(g) \qquad \textbf{Eq. 2.33}$$

If the catalytically active particles or clusters are anchored to the active carbon sites though C-O-Na phenolate groups the liberation of CO may be expressed in a more exact manner [35]:

$$\text{— C — C — O — Na} + O* \quad \Rightarrow \quad \text{— C(O) — C— O — Na}$$

$$\Rightarrow \quad CO + \text{ — C — O — Na} \qquad \textbf{Eq. 2.34}$$

From similar considerations, the sodium catalyzed O_2 gasification reaction may be described by the following equations:

$$O_2\,(g) + 2\,* \quad \Leftrightarrow \quad 2\,O* \qquad \textbf{Eq. 2.35}$$

$$O* + C_f \quad \Leftrightarrow \quad C(O) + * \qquad \textbf{Eq. 2.36}$$

$$2\,C(O) \quad \Leftrightarrow \quad CO_2\,(g) + C_f \quad \text{or:} \qquad \textbf{Eq. 2.37}$$

$$CO\,(g) + C(O) \quad \Leftrightarrow \quad CO_2\,(g) + C_f \quad \text{or:} \qquad \textbf{Eq. 2.38}$$

$$C(O) \quad \Leftrightarrow \quad CO\,(g) \qquad \textbf{Eq. 2.39}$$

The actual composition of the catalytically active sodium particles is not known. Probably they are nonstoichiometric oxides (Na_xO_y) through which an oxygen ion can be transported [52-54]. Most likely, the composition varies within the particles, being more reduced towards the catalyst-carbon interface (Na_xO_{y-}) and permanently oxidized towards the gas-catalyst interface (Na_xO_{y+}). During gasification, the particle composition may be determined by a dynamic balance between a reduction process at the carbon-catalyst interface and an oxidation process at the surface in contact with the gaseous reactant.

In general, the alkali carbonates are often found to be more active than other salts such as sulfates or halides. Lang [55] investigated the anion effect in alkali catalyzed steam

gasification of coal chars. Different alkali metal salts were applied to the coal by aqueous impregnation and the gasification rates were measured in a small fluidized-bed gasifier. Generally, the catalytic activity of the alkali metal salts increased with the size of the cation, from lithium to cesium, but the associated anion influenced the activity more than the cation. It was proposed that some anions could compete with the carbon material for the alkali cations and thus inhibit the formation of an alkali-carbon complex. It was found that the alkali salts of weak acids were good gasification catalysts, while those of strong acids were poor. The catalytic activity of the alkali metal salts was believed to be determined by the outcome of the competition illustrated in Figure 2.12.

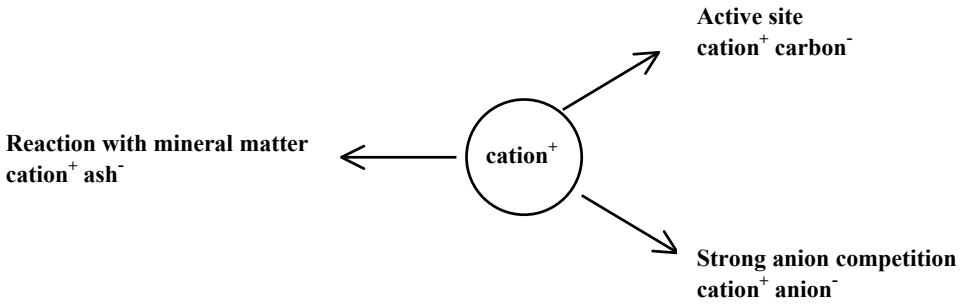

Figure 2.12 Competition for alkali cation. *Cited from Lang* [55]

Lang [55] proposed that weak-acid salts might react with carbon to form surface complexes that act as active sites. When mineral matters are present, the cation might react with them to form catalytically inactive compounds and thus limit the number of gasification sites (ionic association between the alkali cation and the anionic carbon). It was thought that the carbon behaves like a weak-acid anion and in the presence of relatively strong-acid anions such as sulfate and chloride, the cation^{+} carbon^{-} association is unfavored. Unless the competing anion is changed or removed from the system, poor catalytic activity results. The reactivity measurements confirmed that the salts of weak acids or those which decompose to salts of weak acid generally were most catalytic active. The sodium and potassium salts of strong halogen acids were poor catalysts. The activities of the phosphates, borates and silicates were low, probably due to the tendency of these materials to form polymeric glassy compounds, which may coat the carbon surface and act as a diffusion barrier towards the gas phase. A comparison of the catalytic activity of the different sodium salts is shown in Figure 2.13.

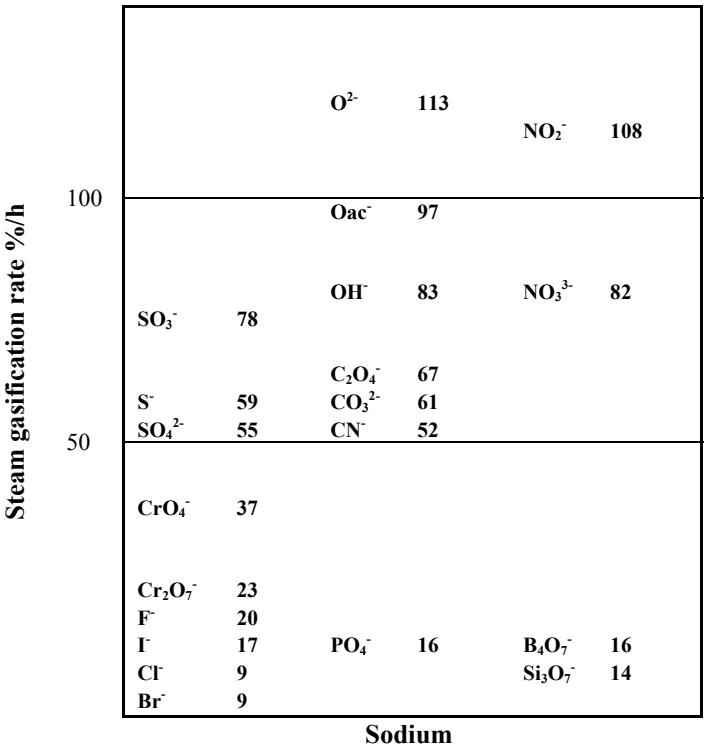

Figure 2.13 Comparison of gasification rates of Illinois coal char catalyzed with sodium compounds containing a variety of anions. *Catalyst loading equivalent to 15 wt% Na_2CO_3 on coal. Cited from Lang* [55]

2.2.2 Catalytic effect of calcium

Since calcium is regarded as one of the best catalysts for the coal gasification process, much work has been performed in order to understand the mechanisms of the catalyzed reactions, possible active calcium intermediates and other phenomena involved in the catalyst behavior.

Essentially, two different mechanisms have been proposed to explain the catalysis of the carbon-CO_2 reaction by alkaline earths. Based on the results from thermogravimetric experiments and thermodynamical considerations, McKee [41, 56] proposed the following carbonate-oxide cycle:

$$CaCO_3 + C \Leftrightarrow CaO + 2\,CO\,(g) \quad \Delta G^0_{950°C} = -51.5\ kJ/mol \quad \textbf{Eq. 2.40}$$

$$CaO + CO_2\,(g) \Leftrightarrow CaCO_3 \quad \Delta G^0_{950°C} = 8.3\ kJ/mol \quad \textbf{Eq. 2.41}$$

However, as for the alkali metals, it is generally agreed that the alkaline earths catalyze the carbon-CO_2 gasification reaction by increasing the number of active sites, not by lowering

the reactions' activation energy [35, 57, 58]. This point led Kapteijn *et al.* [46] to consider that the active catalyst species is the oxide and that the carbon gasification involves an oxygen transfer via the formation of a peroxide:

$$CaO + CO_2\,(g) \Leftrightarrow CaO{\cdot}O + CO\,(g) \qquad \textbf{Eq. 2.42}$$

$$CaO{\cdot}O + C \Leftrightarrow CaO + C(O) \qquad \textbf{Eq. 2.43}$$

$$C(O) \Leftrightarrow CO\,(g) \qquad \textbf{Eq. 2.44}$$

Based on results from temperature programmed reaction (TPR) experiments with labeled compounds, Chang *et al.* [57] supported the carbonate-oxide mechanism proposed by McKee (Eq. 2.40-2.41) for barium, but not for calcium. By secondary ion mass spectroscopy, CaO was identified as an active species and it was thus suggested that $CaCO_3$ decomposed directly to CaO and CO_2. The CaO was oxidized in the presence of CO_2, but no evidence was obtained to prove that CaO_2 was the oxidized form. On basis of the TPR results, the following mechanism was proposed:

$$C\text{-}CaO + CO_2\,(g) \Leftrightarrow C\text{-}CaO_2 + CO\,(g) \qquad \textbf{Eq. 2.45}$$

$$a\,[C\text{-}CaO_2 + C \Rightarrow C\text{-}CaO + CO\,(g)] \qquad \textbf{Eq. 2.46}$$

$$(1\text{-}a)\,[C\text{-}CaO_2 + CO\,(g) \Leftrightarrow C\text{-}CaO + CO_2\,(g)] \qquad \textbf{Eq. 2.47}$$

Note that CaO_2 only is written as a possible form of oxidized CaO.

Recently, from an extensive study of carbon gasification catalyzed by calcium, a carbonate-oxide cycle was deduced in which the carbon-calcium contact is the key factor [59]. Several workers have reported that the CO_2 reactivity increases linearly with the calcium loading up to a saturation level after which the reactivity decreases again [59-61]. This phenomenon is normally attributed to a loss in the calcium dispersion. The catalytic activity of calcium towards the carbon-CO_2 reaction is directly related to the carbon-calcium contact. At high calcium loadings, sintering might occur. This is accompanied with a decrease in the reactivity which is associated with the drop in the surface area of the calcium catalyst and therefore with a decrease in the calcium-carbon contact [60].

Cazorla-Amorós *et al.* [60] used temperature programmed desorption (TPD) to study the catalytic activity of calcium and its deactivation in the carbon-CO_2 gasification reaction. On basis of the TPD spectra, a novel model for CO_2 adsorption on CaO particles and its subsequent redistribution was proposed. According to this model, the CaO surface may be divided into three zones of different stability:

Zone A: The interface of contact with carbon.
Zone B: The perimeter of zone A.
Zone C: The external surface of CaO without any contact with carbon.

Zone A and B are responsible for the observed catalytic activity of CaO. Zone C is responsible for the inactive CaO. Using this three-zone CaO model, the CO_2-adsorption was interpreted as follows [60]:

- When CO_2 interacts with CaO at low temperatures, there is a CaO surface coverage which is mainly restricted to a monolayer. Zone B and C are occupied by CO_2

- During temperature rise, a CO_2 redistribution through the CaO particles takes place. CO_2 diffuses from zone B to zone A and from zone C to zone B, leaving a part of zone C unoccupied. It is assumed that CO_2 is more stable in zone A and B than in zone C because of the stabilizing interaction of CO_3^{2-} ion with the carbon. Thus a $*CO_2$ species is formed (* active catalyst site) with participation of the catalyst:

$$* + CO_2 \Rightarrow \quad *CO_2 \qquad \textbf{Eq. 2.48}$$

- When the temperature is further increased, species at the interface (zone A) have sufficient energy to dissociate CO_2 to give CO through Eq. 2.49-2.50. Thus the gasification reaction is completed.

$$*CO_2 + C_f \Rightarrow C(O) + CO\ (g) \qquad \textbf{Eq. 2.49}$$

$$C(O) \Rightarrow CO\ (g) \qquad \textbf{Eq. 2.50}$$

At high temperatures, some bulk $CaCO_3$ was formed at the interface with carbon (zone A). The calcium carbonate formed was believed to dissociate as follows [62, 63]:

$$CaCO_3\text{-}C \Leftrightarrow CaO\text{-}C(O) + CO\ (g) \qquad \textbf{Eq. 2.51}$$

$$CaO\text{-}C(O) \Rightarrow CaO\text{-}C + CO\ (g) \qquad \textbf{Eq. 2.52}$$

According to this mechanism, the catalyst particles act as a medium for the transport of CO_2 to the carbon-catalyst interface where it dissociates when the temperature is adequate.

As seen from Eq. 2.40 and 2.41, $CaCO_3$ is not stable at the normal CO_2 gasification temperatures (900 – 1000 °C). The carbonate may either dissociate thermally or react with carbon under the formation of CaO. It may be expected that the catalytically active CaO particles is anchored to the carbon surface through Ca-surface phenolate groups similar to those observed in the alkali metal-carbon systems (see chapter 2.2.1). Based on the above proposals, the CO_2 gasification mechanism may be summarized as: (1) decomposition of calcium carbonate to an oxide phase (2) adsorption and dissociation of CO_2 at active sites on the catalyst particles, (3) diffusion of chemisorbed oxygen atoms to carbon surface, (4) reaction between chemisorbed oxygen and active carbon sites (formation of C(O) complexes) and (5) desorption of CO (see Eq. 2.31-2.33). As for sodium catalyzed gasification, the actual composition of the catalytically active calcium oxide phase is not known.

Although far less investigated, calcium is also regarded as a catalyst towards the O_2 gasification reaction [8, 64-67]. However, in comparison with other oxides of the alkali and alkaline earth metals, the catalytic activity of CaO in the carbon-O_2 reaction does not appear to be outstanding [39, 56].

By isothermal thermogravimetric analysis, Radovic *et al.* [66] studied the CaO-catalyzed air gasification of lignite chars (reaction temperatures: 525 – 725 °C). The catalyst dispersion within the char was found to be crucial for the char reactivity. At high heat treatment temperatures (1000 °C), the CaO crystallite growth (measured by X-ray diffraction line broadening) was very rapid and a loss in char reactivity was observed. The following oxygen-transfer mechanism was proposed:

$$C_e + CaO + O_2\,(g) \Rightarrow CaO_2 + C_e\text{-}O\,(ads) \qquad \textbf{Eq. 2.53}$$

$$C_b + CaO + O_2\,(g) \Rightarrow CaO_2 + C_b\text{-}O\,(ads) \qquad \textbf{Eq. 2.54}$$

$$2\,C_e + O_2\,(g) \Rightarrow 2\,C_e\text{-}O\,(ads) \qquad \textbf{Eq. 2.55}$$

$$C_b\text{-}O\,(ads) \Rightarrow C_e\text{-}O\,(ads) \qquad \textbf{Eq. 2.56}$$

$$C_e\text{-}O\,(ads) \Rightarrow CO\,(g) \qquad \textbf{Eq. 2.57}$$

$$2\,C_e\text{-}O\,(ads) \Rightarrow CO_2\,(g) + C_e \qquad \textbf{Eq. 2.58}$$

$$CaO_2 + C_b \Rightarrow CaO + C_b\text{-}O\,(ads) \qquad \textbf{Eq. 2.59}$$

$$CaO_2 + C_e \Rightarrow CaO + C_e\text{-}O\,(ads) \qquad \textbf{Eq. 2.60}$$

where C_e denotes an active carbon site located at the edge of the carbon "crystallite" and C_b a basal (inactive) carbon atom at the carbon-catalyst interface. The proposed mechanism, which basically is equal to that proposed for the sodium catalyzed O_2 gasification reaction (see Eq. 2.35-2.39), reflects the experimental findings that both catalyst and carbon active sites influence the overall reactivity. It also provides independent, parallel paths for the catalyzed and uncatalyzed reactions. Reactions 2.53-2.55 represent the catalyst oxidation and the dissociative chemisorption of O_2 either on a catalyst or on an active carbon site. CaO has been found to act as an excellent O_2 dissociation catalyst [68] and dissosiative chemisorption of oxygen was expected to occur both on the catalyst and carbon active sites. Oxygen spills over from the catalyst-carbon interface and diffuses to an active carbon site where gasification takes place.

2.2.3 Catalytic effect of aluminium

Only a few reports are available on the effect of aluminium compounds on the gas reactivity and consumption of carbon materials. Since no proposals for the mechanism of the aluminium catalyzed carbon gasification are found, this section is used to give an overview of some of the experimental results reported.

In 1964 Rakszawski and Parker [3] did a fundamental study of the effect of the group IIIA-VIA elements and their oxides on the oxidation of spectroscopically pure graphite powder in air at 700 and 800 °C. They found that aluminium was a weak oxidation catalyst when added as a metal, but a better catalyst when added as an oxide. At 700 °C, the addition of 0.1 mol% aluminium metal enhanced the air gasification rate from 0.0719 g/h·g (pure graphite) to 0.118 g/h·g. The reaction rate was increased to 0.181 g/h·g when 0.1 mol% Al_2O_3 was added.

Based on the electron transfer mechanism, the weak catalytic activities of aluminium metal and aluminium oxide were explained by the relatively high electron affinity of aluminium (-5.98 eV).

Müftüoglu and Øye [9] studied the reactivity and electrolytic consumption of carbon anode samples containing various amounts of aluminium oxide (0 – 5 wt%). The measured CO_2 reactivities [mg/cm^2·h] (measured at 948 °C) were not affected by the Al_2O_3 additions. The air reactivities on the other hand (measured at 530 °C) decreased linearly with the increasing Al_2O_3 contents. The different behavior in air and CO_2 was explained by the different reaction temperatures rather than the change in oxidizing gas (CO_2 gasification temperature within diffusion controlled regime).

In order to obtain a better understanding of the many factors affecting the anode consumption during aluminium electrolysis, Rhedey [5] used a laboratory electrolytic cell for determination of the anode consumption under various conditions, simulating those of industrial reduction cells. Several additives were tested both in the laboratory cell and in plant-scale tests. Addition of 3 – 5 % aluminium chips to a Søderberg paste gave 2 – 3 % reduction in the total consumption (electrolytic consumption, oxidation and dusting) of the test anodes, expressed on an aluminium-free basis. The air oxidation rate was also found to decrease with the addition of aluminium metal. On the other hand, the test-electrode consumption increased when Al_2O_3 of various particle sizes, was added. Later Rhedey also studied the effect of aluminium fluoride on the air reactivity (525 °C) of laboratory scale Søderberg test anodes [8]. Compared to the non-doped electrodes, the air reactivity [g/cm^2·h] (measured at 525 °C) was reduced by about 80 percent when 3 – 5 wt% AlF_3 was added.

In the light of the work done by Rhedey, Braunswarth *et al.* [69] investigated the effect of aluminium fluoride additions to Søderberg pastes (laboratory and plant tests). In the laboratory, they prepared Søderberg paste containing up to 3.4 wt% AlF_3 of different particle sizes. The rate of air oxidation of the baked laboratory electrodes (measured at 525 °C with a linear air velocity of 22 cm/s) was reduced by 60 to 70 % nearly independent of the aluminium fluoride particle size.

Yanko *et al.* [6] and Lazarev *et al.* [7] investigated the effect of adding 1 wt% AlF_3 to an industrial anode mass. Compared to a control specimen without any additions, the AlF_3-doped anode mass showed a lower CO_2 gasification rate (22.3 *vs.* 30.9 mg/cm^2·h [6]) and a lower carbon dusting loss.

Sørlie, Kuang and Thonstad [12, 13] studied the effect of aluminium fluoride additions on the air and CO_2 reactivity of anode carbon. The CO_2 reactivity (measured at 960 °C) was lowered by about 30 % when moderate amounts of AlF_3 were added to the anodes (< 1.5 wt% in green anodes), but increased again at higher additions. The air reactivity (525 °C) was permanently reduced to about half of its initial value when the aluminium fluoride content exceeded 0.6 wt%. The dusting index (relative amount of loose carbon particles accumulated on the anode surface) dropped to near zero for AlF_3-contents above 2 wt%.

3 Experimental procedures

3.1 Preparation of coke samples

3.1.1 Laboratory coker

A sketch of the laboratory coker, which was used to make cokes with controlled contamination profiles by carbonization of pure carbon precursors, is given in Figure 3.1.

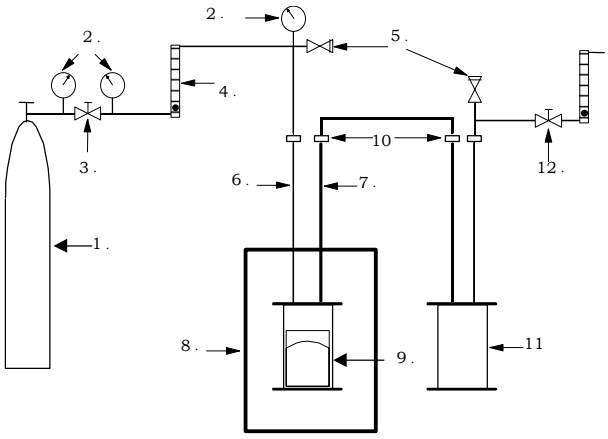

1. Argon cylinder
2. Manometer
3. Pressure reduction valve
4. Flowmeter
5. Relief valve, max. bearing pressure 18 bar
6. Stainless steel tube, Ø 8 mm
8. Furnace
9. Pressurized reactor chamber, stainless steel
10. Quick joints
11. Cold trap, pressure stabilizing chamber
12. Flow control valve
13. Flowmeter

Figure 3.1 Sketch of the laboratory coker. *Not in scale. Taken from Eidet* [70]

The reaction chamber is pressurized in order to avoid foaming and to insure a high coke yield. A gas cylinder equipped with a pressure reduction valve, provides the desired pressure and purge gas flow. Relief valves are placed both upstream and downstream from the coke reactor to avoid pressure buildup if the tubes are blocked by solid depositions. The furnace has three heating elements adjusted to give a minimum temperature gradient in the furnace (maximum ± 0.07 °C/cm). The furnace temperature is controlled with aid of a thermocouple (Ni10Cr/Ni5Al), mounted on the top lid of the reactor chamber, and a PID-controller. The

gas flow out from the system is adjusted by a needle valve. A more detailed sketch of the reactor chamber is given in Figure 3.2.

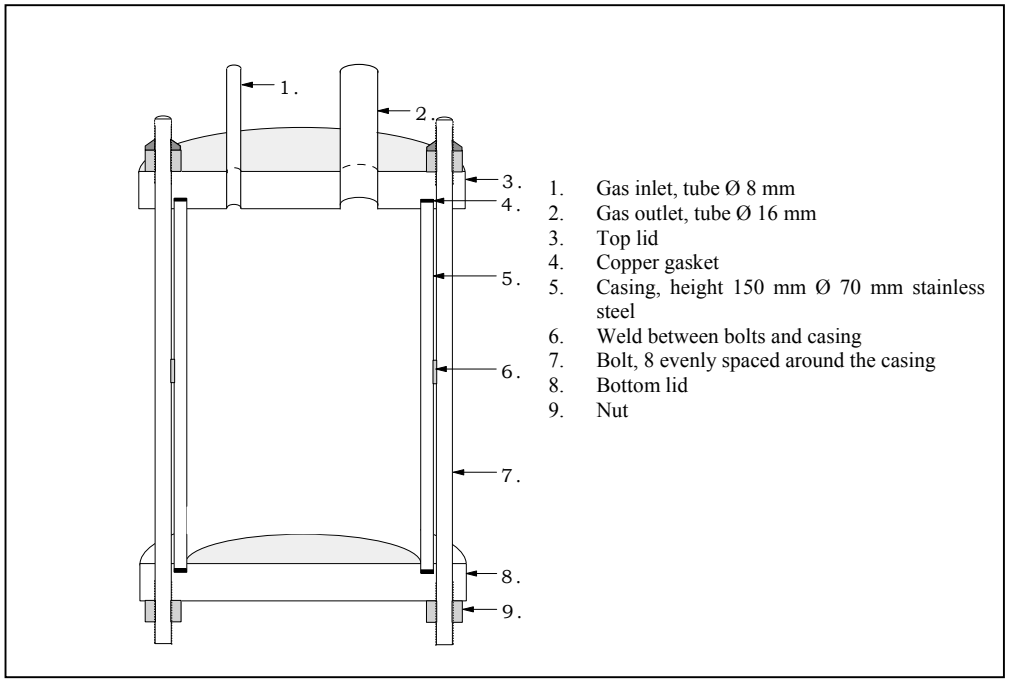

Figure 3.2 Cross-section of reactor chamber. *Not in scale. Taken from Eidet* [70]

Aluminium soft-drink cans are used as crucibles inside the reactor chamber. The crucibles facilitate an easy removal of the finished green cokes.

3.1.2 Chemicals

The chemicals used are listed in Table 3-1

Table 3-1 Chemicals used for preparation of doped coke samples

Chemical	Producer	Quality
Heavy tar oil	Koppers, Denmark	CBFS-fraction, ash-cont. < 5 ppm, 0.30 % S
Petroleum pitch	Koppers, Denmark	Softn. point (Mettler) 120.3 °C, ash-cont. < 22 ppm, 0.54 % S
Aluminium acetylacetonate ($Al(C_2H_7O_2)_3$)	Merck	Pro Analysis
Sodium acetylacetonate [1] ($Na(C_2H_7O_2)$)	Alfa Products	Purity > 98.8 %
Calcium acetylacetonate [1] ($Ca(C_2H_7O_2)_2$)	Alfa Products	Purity > 98.8 %
Dibenzothiophene ($C_{12}H_8S$)	Merck	For synthesis Purity > 98 %
Aluminium oxide (Al_2O_3)	Merck	γ-alumina, anhydrous Purity > 99.9 %
Aluminium fluoride (AlF_3)	Merck	Pro analysis, purified by 2x sublimation
Sodium fluoride (NaF)	Merck	Pro analysis, purified by recrystallization
Cryolite (Na_3AlF_6)	-	Natural hand-picked Greenland cryolite, dried
Calcium fluoride (CaF_2)	1) Acros Organics 2) Merck	1) Pro analysis, anhydrous 2) Suprapur ® 99.95 %

[1] Labeled as Na/Ca 2,4-pentanedionate

The tar oil (main components: fluoranthene (16.2 %), pyrene (14.5 %), phenanthrene (5.6 %) and chrysene (5.5 %)) was used as a precursor for the cokes doped with the metal acetylacetonates while the petroleum pitch was used as a precursor for the cokes doped with the inorganic salts.

3.1.3 Cokes doped with metal acetylacetonates

Approximately 280 gram tar oil was added to the aluminium crucible (soft drink can). Known amounts of acetylacetonate powder (aluminium acetylacetonate, sodium acetylacetonate or calcium acetylacetonate) were added and dissolved in the oil by stirring. The amount added (m_{added}) was calculated from the equation:

$$m_{added} = m_{precursor} \cdot \frac{M_{W,acetylacetonate}}{M_{W,impurity}} \cdot C_Y \cdot c_{wanted} \cdot 10^{-6} \qquad \text{Eq. 3.1}$$

where $m_{precursor}$ is the amount of tar oil [gram], $M_{W,\ acetylacetonate}$ is the molar molecule weight of the metal acetylacetonate, $M_{W,\ impurity}$ is the atomic mass of the impurity element (Al, Na, Ca), C_Y is the expected coke yield (82 %) and c_{wanted} is the predefined impurity level (ppm). Series of "high"-sulfur cokes were prepared by a concurrent addition of 4.5 weight percent dibenzothiophene (corresponds to an addition of 1 wt% elemental sulfur).

The doped precursors were carbonized in the coke reactor at 525 °C for 4 hours (heating rate 3 °C/h). A pressure of 15 bar and an inert gas (argon) flow rate of about 100 Nml/h was maintained in the reactor chamber.

After carbonization, the green cokes were crushed to a grain size less than 10 mm (jaw-crusher) and calcined in a closed graphite crucible to a maximum temperature of 1010 °C for 2 hours (heating rate 67 °C/h). To prevent oxidation, the graphite crucible was embedded in crushed petroleum coke and placed inside a stainless steel box with lid.

Table 3-2 shows the impurity profile of the reference coke (refcoke-oil), which was made by carbonization of the pure tar oil.

Table 3-2 Impurity profile of tar oil and reference coke (refcoke-oil)

	Ash	S	Na	Mg	Al	Si	Ca	V	Fe	Ni	Zn	Pb
	wt%		*ppm*									
tar oil [1]	<0.0005	0.30										
refcoke-oil	0.007	0.26	2	26	6	4	2	< 3	8	4	2	< 3

[1] Ash-content too low for trace element analyses

Computer tomography (CT) was used to get a picture of the density distribution within the green coke samples (before removal of aluminium crucible). The samples were scanned in horizontal sections of 2 mm height every 4 mm. A water sample was used as calibration. As seen from the CT-micrographs given in Figure 3.3, the green reference coke has a quite narrow and uniform density distribution. The average density is about 1.1 g/cm^3. As determined by Hg-porosimetry (method described in section 3.2.3), the total porosity of the calcined coke grains (grain size –2 + 1 mm) is between 10 – 15 %. Figure 3.4 shows that neither the total porosity nor the pore size distribution varies significantly from one sample to another.

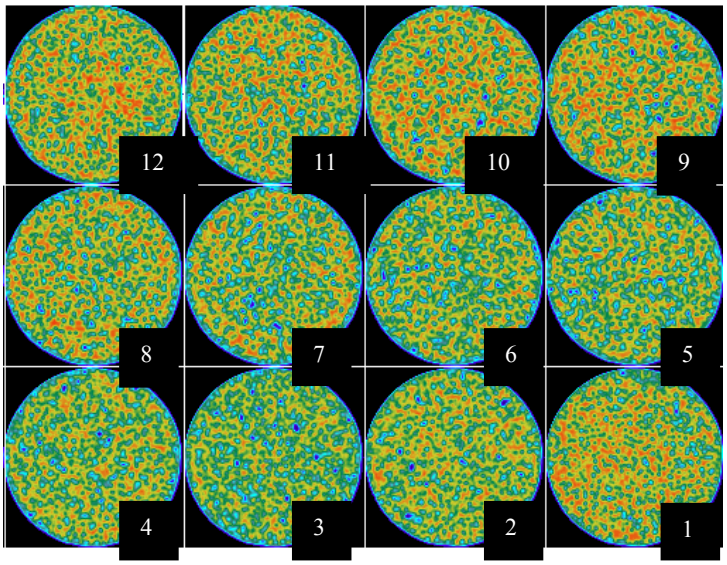

A) Density distribution within coke slices. Slice 1: top of green coke sample, slice 12: bottom

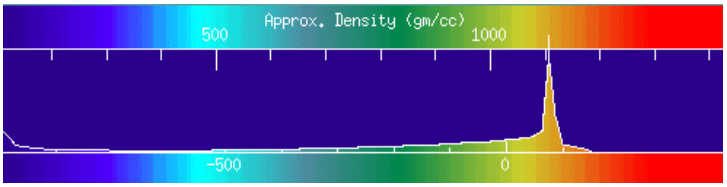

B) Overall density distribution whole coke sample (all slices)

Figure 3.3 CT-density distribution of reference coke (green) made by carbonization of the tar oil. Average density: 1.1 g/cm^3. *Blue color: low density, red color: high density. CT-numbers can be converted as 0 being approximately 1 g/cm^3 and every 100 CT number changes it by 0.1 g/cm^3*

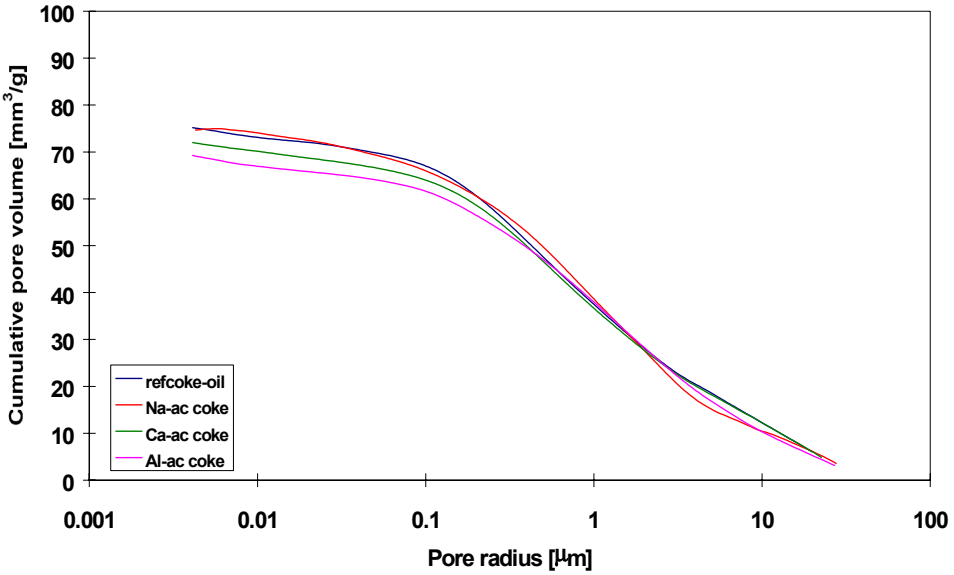

Figure 3.4 Porosity and pore size distribution, cokes made by carbonization of the tar oil. *Total porosity: 10 – 15 %. Analyzed by Hg-porosimetry (grain size – 2 + 1 mm). refcoke-oil: reference coke; Na-ac coke: coke doped with Na-acetylacetonate (0.4 wt%); Ca-ac coke: coke doped with Ca-acetylacetonate (0.4 wt%); Al-ac coke: coke doped with Al-acetylacetonate (1.2 wt%)*

3.1.4 Cokes doped with inorganic salts

The cokes doped with the inorganic compounds (AlF_3, Al_2O_3, NaF, Na_3AlF_6 or CaF_2) were prepared by a slightly different procedure.

Weighed amounts of inorganic salt (amount calculated from Eq. 3.1) were mixed with about 15 gram solid pitch using a swing mill (tungsten carbide). The finely milled salt/pitch mixture (grain size < 63 µm) was mixed with about 230 gram molten pitch (200 °C) by stirring. The mixture were cooled to room temperature and carbonized in the coke reactor in the same manner as described in chapter 3.1.3. However, due to the gas evolution, the inorganic additives floated up during the first stages of the carbonization process. As a result the dopant concentration of the top 2 centimeters of the green coke sample was about 10 times higher than in the bottom 2 centimeters. In order to avoid such a big concentration difference within a single sample, the green cokes were cut into 4 slices as shown in Figure 3.5. The dome at the top was very porous and hence thrown away. Slice 1, 2, 3 and 4, which were treated as four separate samples, were calcined at 1010 °C for 2 hours (closed graphite crucible).

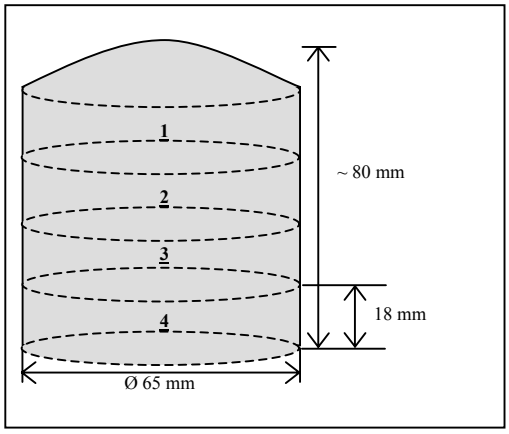

Figure 3.5 Slicing of green coke samples doped with inorganic salts

A two-times ("2x") carbonization procedure was used to prepare a series of fine-textured AlF_3-doped cokes. The initial green coke sample was milled in the swing mill and the coke powder (grain size < 63 µm) was mixed with small amounts of liquid petroleum pitch (preheated to 200 °C) into a non-fluid paste. This paste was carbonized once more in the coke reactor. The procedure ensured a homogeneous distribution of aluminium fluoride within the finished coke samples and there was hence no need to slice the green cokes into different sub-samples. Instead the whole sample was crushed (grain size < 10 mm) and calcined in the same way as the acetylacetonate-doped cokes.

Table 3-3 shows the impurity profile of the petroleum pitch and the single carbonized and 2x carbonized reference cokes (refcoke-pitch (1x/2x)). The contamination profile of a relatively pure commercial available anode coke is also given.

Table 3-3 Impurity content of petroleum pitch (petr. pitch), single and two times carbonized reference cokes (refcoke-pitch (xx)) and low-ash commercial anode coke

	Ash	S	Na	Mg	Al	Si	Ca	V	Fe	Ni	Zn	Pb
	wt%		*ppm*									
petr. pitch	0.002	0.54	6	< 1	2	3	< 1	< 1	2	< 1	< 1	< 1
refcoke-pitch (1x)	0.014	0.44	19	15	8	17	5	< 5	7	2	1	< 1
refcoke-pitch (2x)	0.037	0.44	18	25	24	14	6	< 2	63	1	2	< 1
anode coke	0.053	1.09	21	2	42	59	11	60	112	25	2	< 5

The CT micrographs given in Figure 3.6 show the density distribution of the green single carbonized reference coke (before removal of Al can). The average density is about 0.65 g/cm^3. As seen from the micrographs, the upper 4 – 8 millimeters of the coke sample (dome, see Figure 3.5) has a far lower density than the rest of the sample.

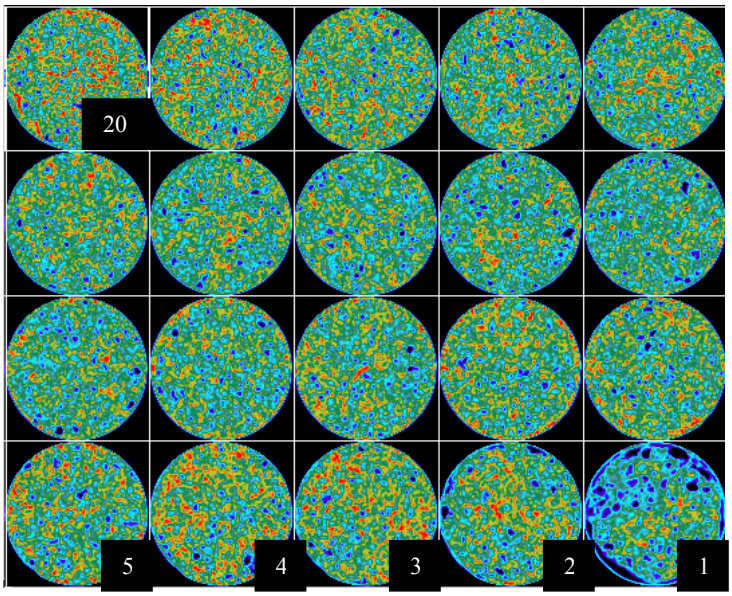

A) Density distribution within coke slices. Slice 1: top of green coke sample, slice 20: bottom

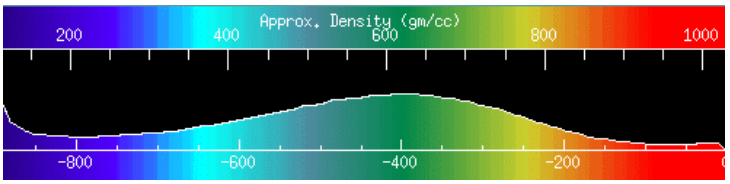

B) Overall density distribution whole coke sample (all slices)

Figure 3.6 CT-density distribution, refcoke-pitch (1x). Average density 0.65 g/cm^3. *Blue color: low density, red color: high density. CT-numbers can be converted as 0 being approximately 1 g/cm^3 and every 100 CT number changes it by 0.1 g/cm^3*

Figure 3.7 shows the total porosity and pore size distribution of some of the coke samples (grain size: –2 + 1 mm) made from the petroleum pitch. The total porosity varies between 10 and 20 percent and is slightly lower for the two-times carbonized cokes than for the single carbonized cokes.

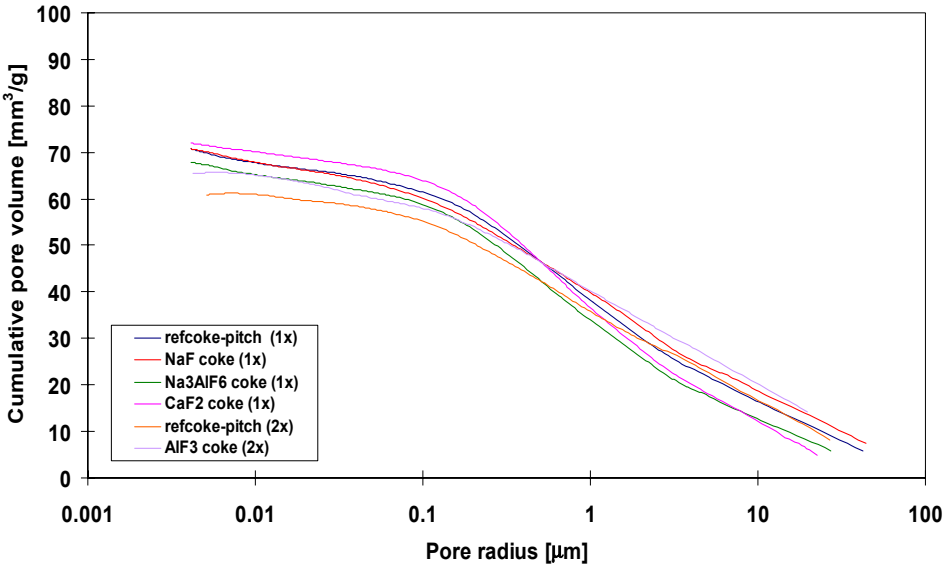

Figure 3.7 Porosity and pore size distribution, cokes made by carbonization of petroleum pitch. Total porosity: 10 – 20 %. *Analyzed by Hg-porosimetry (grain size – 2 + 1 mm). refcoke-pitch (xx): reference cokes, single and 2x carbonized; AlF3 coke (1x/2x): cokes doped with aluminium fluoride (1.7 wt%); NaF coke: coke doped with sodium fluoride (0.2 wt%); Na3AlF6 coke: coke doped with cryolite (0.3 wt%); CaF2 coke: coke doped with calcium fluoride (0.2 wt%)*

3.2 Characterization

3.2.1 Reactivity measurements

The air and CO_2 reactivities of the calcined coke samples were determined using a standard thermobalance type equipment manufactured by Hydro Aluminium. The apparatus consists of five fused silica tube furnaces (gold coated), which can be run in parallel. A sketch of a furnace is given in Figure 3.8. About 8 gram of coke aggregate (grain size – 2 + 1 mm) is placed in a standard size platinum wire mesh basket (Ø 20 mm, height 50 mm) which is mounted on a sample holder inside the furnace. The sample holder is connected to a balance. To insure a satisfactory temperature regulation, the thermocouple controlling the furnace temperature is mounted into the coke aggregate.

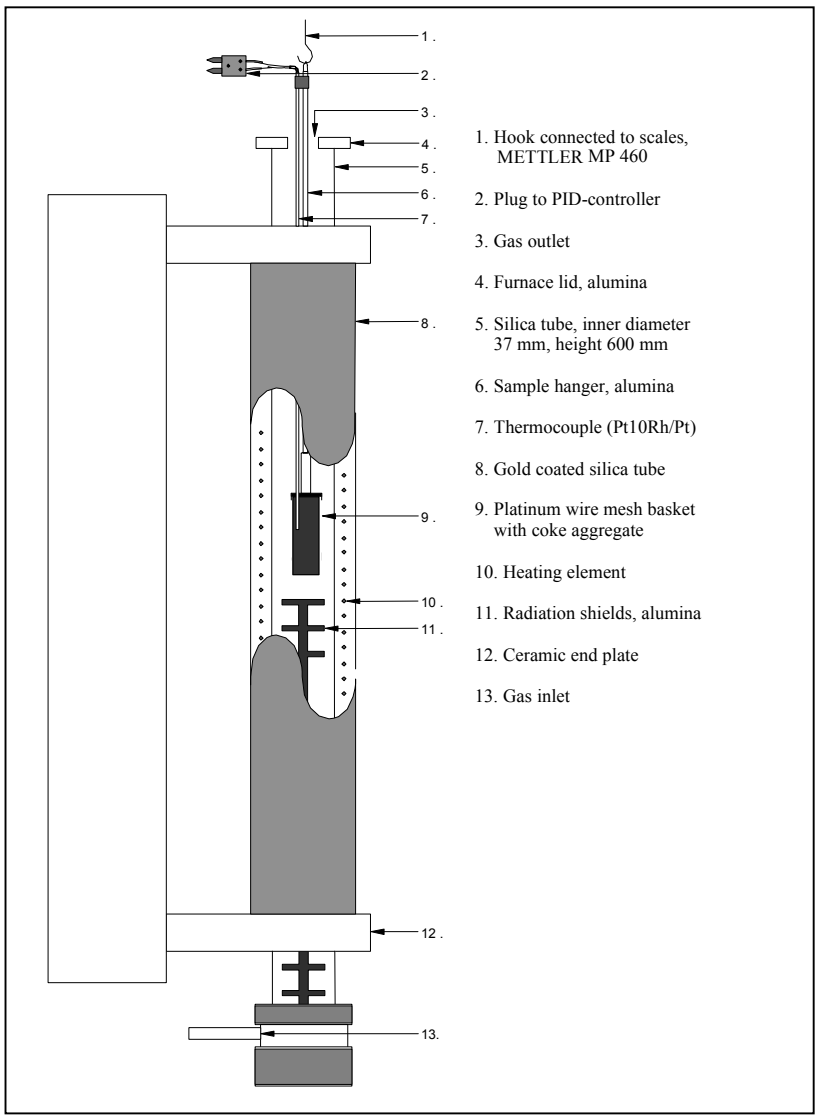

Figure 3.8 Reactivity apparatus furnace with sample holder and coke sample assembled. *Not in scale. Taken from Eidet* [70]

The coke samples were heated to the reaction temperature (heating time 65 minutes) in a flow of N_2 (~ 1.6 Nl/min). At the pre-set reaction temperature, the gas flow was switched to air (~ 3.6 Nl/min) or CO_2 (~ 1.8 Nl/min). For the CO_2 reactivity tests, the reaction temperature was 960 °C or 990 °C. Depending on the coke reactivity, the air reactivity tests were performed at 475, 525 or 550 °C. Both the samples temperature and weight loss was continuously recorded during the reaction period. After 190 minutes the gas was switched to N_2 and the samples were cooled to room temperature. The reactivity R_g, based on the sample mass, was calculated as:

$$R_g = \frac{r}{m_0} \qquad [\text{mg/g·h}] \qquad \textbf{Eq. 3.2}$$

where m_0 is the initial sample mass and r is the weight loss rate calculated by linear regression of the weight loss *vs.* reaction time data. For the CO_2 reactivity measurements, r was calculated from the data recorded during the last 30 minutes of the reaction period. For the air reactivity tests, the data recorded between 95 and 125 minutes after reaction start was used to calculate the weight loss rate.

3.2.2 Texture and structure analyses

The optical coke texture was characterized by use of a metallurgical inverted reflecting light microscope (Leica MeF3A) with polarizing modules. The microscope is equipped with an electronic video camera, whose images are digitized and stored by a computer. An image analysis program (NIH Image version 1.62 mod.) automatically extracts gradient lines between the optical domains in the coke grains (grain size: –1 + 0.5 mm), and calculates a *Mosaic Index* and a *Fiber Index*. The Mosaic Index is a measure of total gradient lines that has been thinned to one pixel width. The Fiber Index is calculated from the line density in four perpendicular directions. The Mosaic Index is thus a measure of the fineness of the coke texture while the Fiber Index is a measure of the coke's anisotropy. A total of 144 grains are analyzed and the final mosaic and fiber indexes are calculated as the average of all the analyzed grains. A more detailed description of the procedure and the equipment is given by Rørvik *et al.* [71].

The crystalline coke structure was characterized by powder X-ray diffraction (XRD) analysis (PHILIPS D5000) and expressed in terms of the average coherent stacking height (L_c) and the spacing between the graphene layers (d_{002}). Coke powder with grain size less than 63 µm was used for the analyses. L_c were calculated from the half-width of the 002-diffraction peak using the Scherrer equation:

$$L_c = \frac{K\lambda}{\beta \cos\theta} \qquad \textbf{Eq. 3.3}$$

where λ is the radiation wavelength (154.18 pm for $CuK_{\alpha 1+2}$), β the width at half peak-height, θ the Bragg angle of the line and K the Scherrer parameter (0.89 for L_c). d_{002} was calculated from the 2θ–value of the peak maximum using Bragg's law:

$$2d \sin\theta = n\lambda \qquad \textbf{Eq. 3.4}$$

3.2.3 Other analyses

A scanning electron microscope, SEM (PHILIPS 515/Hitatchi SN-3000) was used for examinations of the coke surfaces after oxidation in the reactivity apparatus. The elemental composition of the particles found at the coke surfaces were semi-quantitatively determined using the energy dispersive X-ray analysis system, EDX (EDAX PV9900/Oxford Inca) connected to the SEM.

The concentration of trace elements in the calcined coke samples was determined by use of atomic absorption spectroscopy (GBC Avanta). Before analysis, the coke samples were burned in air at 710 °C for 15 hours. A mixture of the remaining ash and $LiBO_2$ was melted and dissolved in diluted HNO_3.

A LECO CS-444 Carbon/Sulphur analyzer was used for analyses of the bulk sulfur contents. The fluorine concentrations were determined using ion selective electrodes (Sintalyzer).

N_2-adsorption at 77K (Micromeritics Flowsorb II 2300) was used to determine the specific surface area of the coke aggregates after reaction with air and CO_2. The surface area was calculated from the simplified BET-equation (1-point method, assumes C ~ 100):

$$v_m \approx \frac{v_a(p_0 - p)}{p_0} \qquad \textbf{Eq. 3.5}$$

where v_a is the volume of adsorbed N_2, v_m the volume of one N_2-monolayer, p the N_2-pressure and p_0 the saturation pressure. The measurements were performed with a gas mixture consisting of 30 % N_2 and 70 % He (p/p_o ~ 0.15).

A scanning mercury porosimeter (Carlo Erba 2000) was used to determine the total porosity and the pore size distributions of the unoxidized coke aggregates (grain size: –2 + 1 mm). Two units were used for determination of the pore volume and size distribution. The first unit is a filling apparatus and a low pressure porosimeter measuring pores with a radius from approximately 80 to 6.8 μm (pressure range 0.095 – 1.1 bar). The second unit measures pores with radius as low as 0.0037 μm (pressure range from atmospheric pressure to 2000 bar). Calculation of pore radius is based on the assumption of cylindrical pores and the Washburn equation:

$$r = -\frac{2\gamma\cos\alpha}{p} \qquad \textbf{Eq. 3.6}$$

where r is the pore radius (Å), γ is the mercury surface tension (480 dyn/cm^2), α is the contact angle between mercury and carbon (140 °) and p the applied mercury pressure (bar).

The coke ignition temperature in oxygen was determined using a multiphase carbon/hydrogen/moisture analyzer from LECO. The instrument is set up with a nondispersive IR-detector for CO_2 detection at the ppm level. The coke samples (~ 0.3 gram, grain size – 2 + 1 mm) was heated in a flow of oxygen (UHP, 750 cm^3/min) at a heating rate

of 19.5 °C/min. The amount of CO_2 formed was continuously recorded as a function of the sample temperature.

The air permeability of the industrial anodes was measured using an AP-50 permeability instrument from R&D Carbon, Switzerland. The air permeability is calculated from the time it takes for a certain volume of air to pass through a cylindrical sample with diameter 50 mm and a given height (20 – 60 mm). The permeability is expressed in Nanoperms (1 nPm = 1 Darcy/9.87)

4 Effect of sodium compounds on coke reactivity

4.1 Cokes doped with sodium acetylacetonate

In order to investigate the activity of sodium oxide as a catalyst towards the air and CO_2 gasification reactions, cokes doped with various amounts of sodium acetylacetonate were prepared from the tar oil by the method described in chapter 3.1.3. "High"-sulfur cokes was prepared by a concurrent addition of 4.5 weight percent dibenzothiophene (corresponds to 1 weight percent elemental sulfur). Table 4-1 gives an overview of the coke samples produced.

Table 4-1 Cokes doped with sodium acetylacetonate.
Na-ac = sodium acetylacetonate, DBT = dibenzothiophene

Sample	Additions	Analyzed dopant content calcined cokes	
		Na *ppm*	S *wt%*
refNaac	-	2	0.26
30Naac	0.02 wt% Na-ac	30	
40Naac	0.04 wt% Na-ac	40	
200Naac	0.11 wt% Na-ac	200	0.28
400Naac	0.22 wt% Na-ac	400	0.29
800Naac	0.44 wt% Na-ac	800	
900Naac	0.55 wt% Na-ac	900	0.28
975Naac	0.58 wt% Na-ac	975	
1305Naac	0.67 wt% Na-ac	1305	
refSNaac	0 wt% Na-ac + 4.5 wt% DBT	1	0.74
S210Naac	0.11 wt% Na-ac + 4.5 wt% DBT	210	0.81
S370Naac	0.23 wt% Na-ac + 4.5 wt% DBT	370	0.93
S775Naac	0.42 wt% Na-ac + 4.5 wt% DBT	775	
S1340Naac	0.44 wt% Na-ac + 4.5 wt% DBT	1340	0.84
S1530Naac	0.55 wt% Na-ac + 4.5 wt% DBT	1530	0.94

As seen from the X-ray diffractogram given in Figure 4.1, sodium acetylacetonate decomposes completely to sodium carbonate during carbonization and calcination of the coke samples.

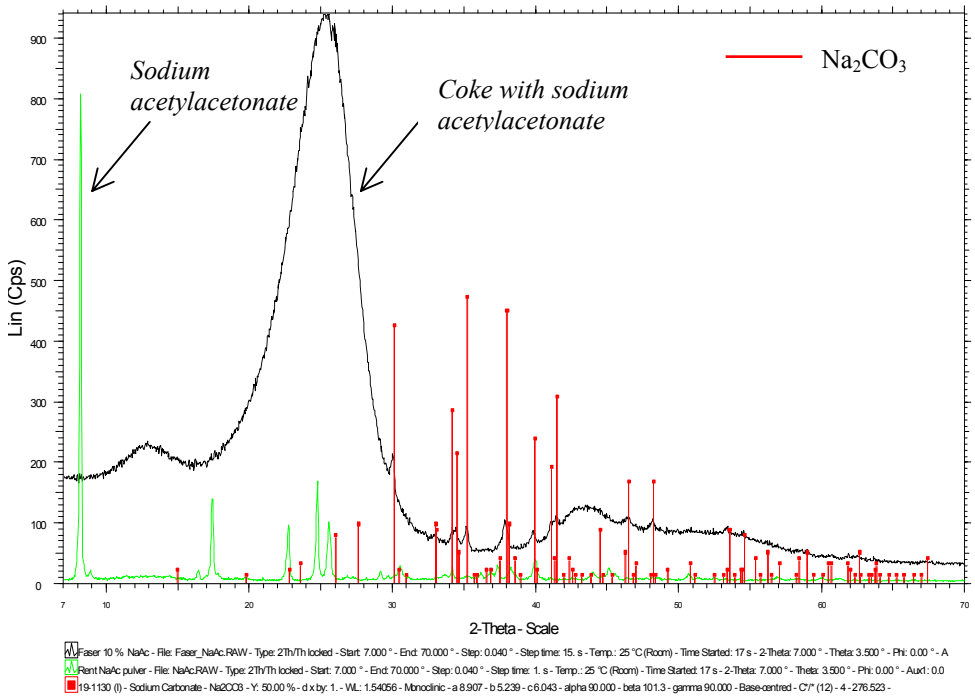

Figure 4.1 X-ray diffractogram, coke doped with sodium acetylacetonate. *Diffractogram from analysis of sodium acetylacetonate powder is included. Broad peak at $2\theta \sim 25°$ is identified as the graphite 002 diffraction peak*

The SEM-micrograph given in Figure 4.2 shows the distribution of sodium carbonate particles at the coke surface.

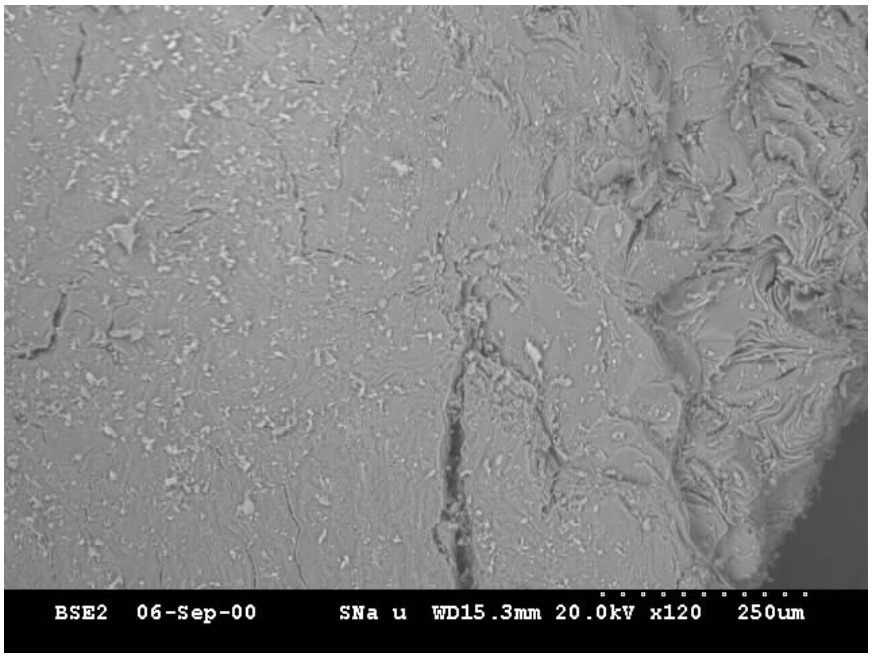

Figure 4.2 Sodium carbonate particles (light gray) on surface of coke doped with sodium acetylacetonate. *SEM-micrograph, backscatter detector.*

4.1.1 Air and CO_2 reactivity

Figure 4.3 and Figure 4.4 show the measured air and the CO_2 reactivities of the sodium acetylacetonate doped coke samples. The reactivities are shown as a function of the analyzed bulk sodium contents. Due to the high catalytic activity of sodium, the air reactivity was measured at 475 °C instead of at the "standard" reaction temperature of 525 °C.

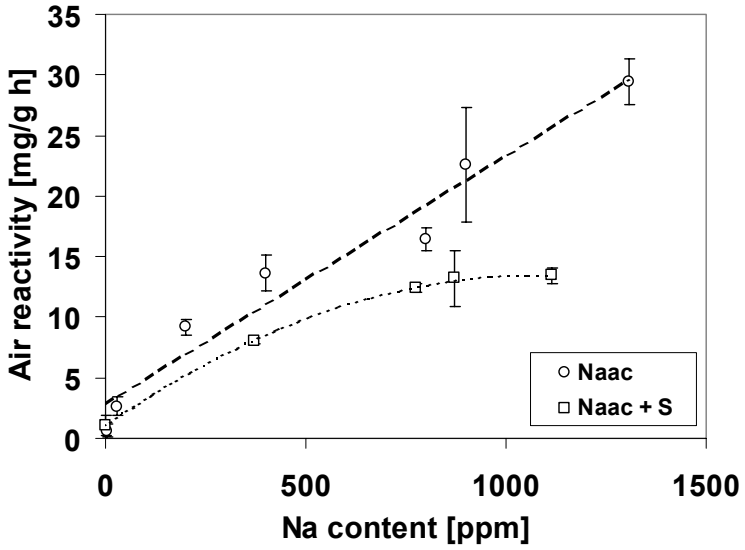

Figure 4.3 Air reactivity (475 °C) of sodium acetylacetonate doped cokes *vs.* analyzed sodium content. *Average values of five parallel measurements. Standard deviations represented by error bars*

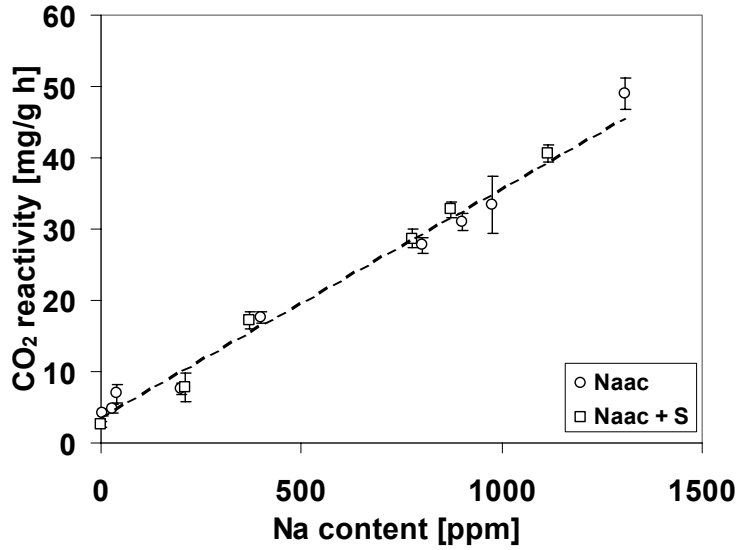

Figure 4.4 CO_2 reactivity (960 °C) of sodium acetylacetonate doped cokes *vs.* analyzed sodium content. *Average values of five parallel measurements. Standard deviations represented by error bars*

Both the air and CO_2 reactivities increase strongly with increasing sodium concentrations. The air reactivities of the "high"-sulfur cokes are considerably lower than the reactivities of the corresponding "low"-sulfur cokes. The difference increases with increasing reactivity. The CO_2-reactivities are not affected by the dibenzothiophene additions. Energy dispersive X-ray analyses (EDX) reveal that the elemental composition of the particles at the surface of the oxidized coke grains corresponds to that of Na_2O (analyzed Na:O ratio ~ 2:1). The sodium oxide particles at the surface of the unoxidized "high"-sulfur cokes contain a little more sulfur than the particles at the surface of the unoxidized "low"-sulfur cokes (~ 8 at% *vs.* ~ 5 at%). After the air-reactivity tests, the sulfur content of the particles at the surface of the "high"-sulfur cokes is increased to 10 – 15 at% while it after the CO_2 reactivity tests is reduced to the same level as for the "low"-sulfur cokes (~ 5 at%).

Figure 4.5 shows a SEM-micrograph of a sodium acetylacetonate doped coke grain which has been oxidized in air for 190 minutes. Due to edge-recession, the layers within the coke lamellas have become visible. The topographical changes are probably caused by the catalytic activity of the small sodium oxide particles (Ø < 0.25 μm) now located at the edges of the layers. Presumably, these particles have been highly mobile at the reaction temperature. The larger particles (Ø > 2 μm) seem inactive and appear to have poor contact with the carbon surface.

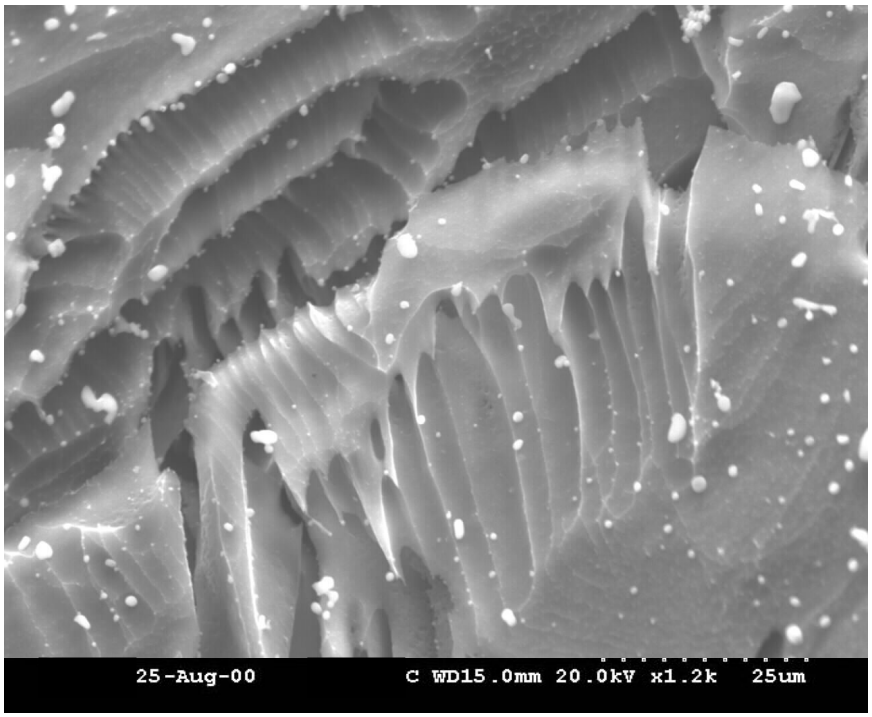

Figure 4.5 Surface of Na-acetylacetonate doped coke grain after oxidation in air for 190 minutes (475 °C), edge-recession. *Catalytically active sodium oxide particles on edges of coke lamellas*

During oxidation in CO_2, a lot of pits (Ø 0.5 – 5 µm) are formed in the coke surface. As seen from the SEM-micrograph given in Figure 4.6, small droplet-like sodium oxide particles are spread out over the entire coke surface. The particles are also found in the bottom of the shallowest pits.

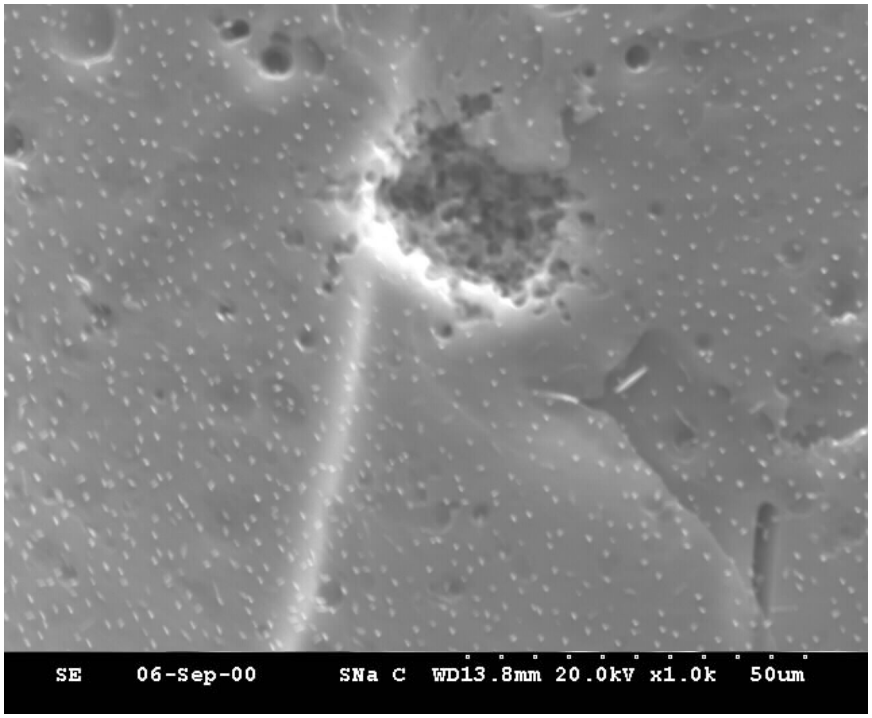

Figure 4.6 Surface of Na-acetylacetonate doped coke grain after oxidation in CO_2 for 190 minutes (960 °C), pitting. *Sodium oxide particles uniformly distributed on coke surface.*

SEM-micrographs showing the surface of a coke grain which has been oxidized in air (1.8 torr) at 600 °C for 7 hours (vacuum chamber of an controlled atmosphere scanning electron microscope (ESEM) used as oxidation chamber), are given in Figure 4.7 and Figure 4.8.

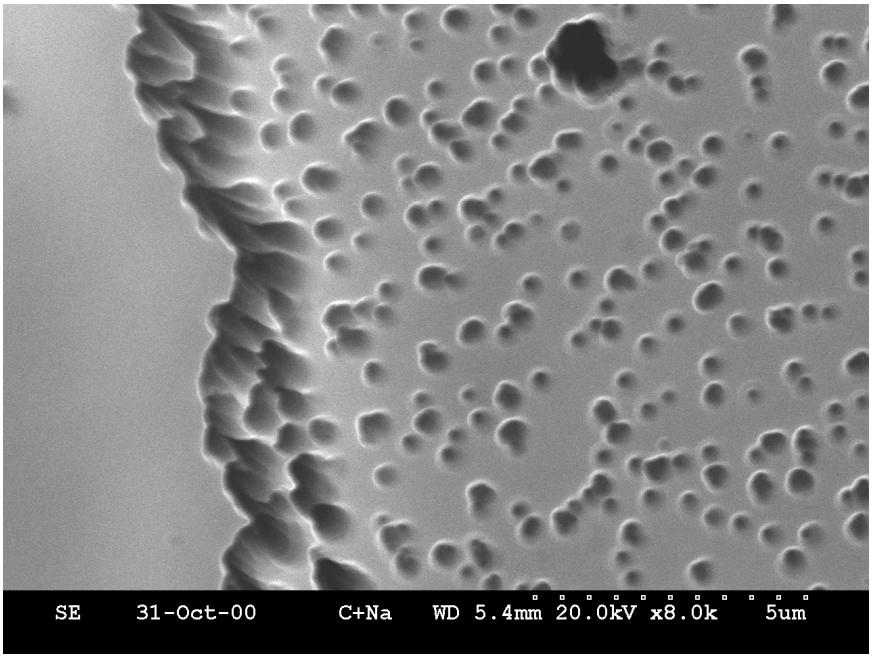

Figure 4.7 Surface of coke grain oxidized in air (1.8 torr) at 600 °C for 7 hours, formation of hexagonal pits

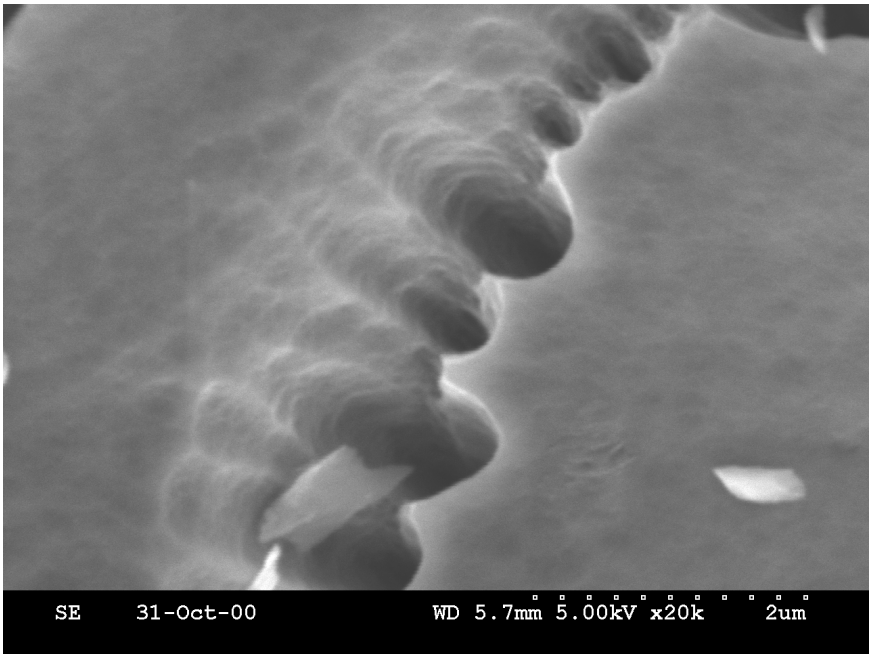

Figure 4.8 Pits formed perpendicular to the graphene layers. *Graphene layer edges are visible at left side of pits*

Due to the low air pressure, the gasification conditions in the ESEM were far less severe than in the reactivity apparatus. It is hence possible to observe that sodium induced pit-formation also occurs during air gasification. As seen from Figure 4.7, the smallest pits have a diffuse hexagonal shape, indicating that they are formed by the catalytic activity of a catalyst located in vacancies in the graphene layer. However, because of edge-recession, the pits become more and more circular as they grow. The micrograph in Figure 4.8 shows that the pits are oriented perpendicular to the graphene layers.

As seen from Figure 4.7, pitting is only taking place in some limited areas. Most likely, the phenomenon is related to the orientation of the graphene layers within the coke lamellas. In the oxidized areas, the graphene layers are probably oriented parallel to the outer coke surface while they in the unoxidized areas are angled more edge-on the outer coke surface. The lack of topographical features in the edge-on areas indicates that channeling (parallel to the graphene layers) is not an important mode of catalytic action of sodium oxide. Due to a high concentration of active sites, the grain boundaries are heavily oxidized.

4.1.2 Optical texture and turbostratic structure

Micrographs showing the optical texture of some of the sodium acetylacetonate doped cokes are given in Figure 4.9.

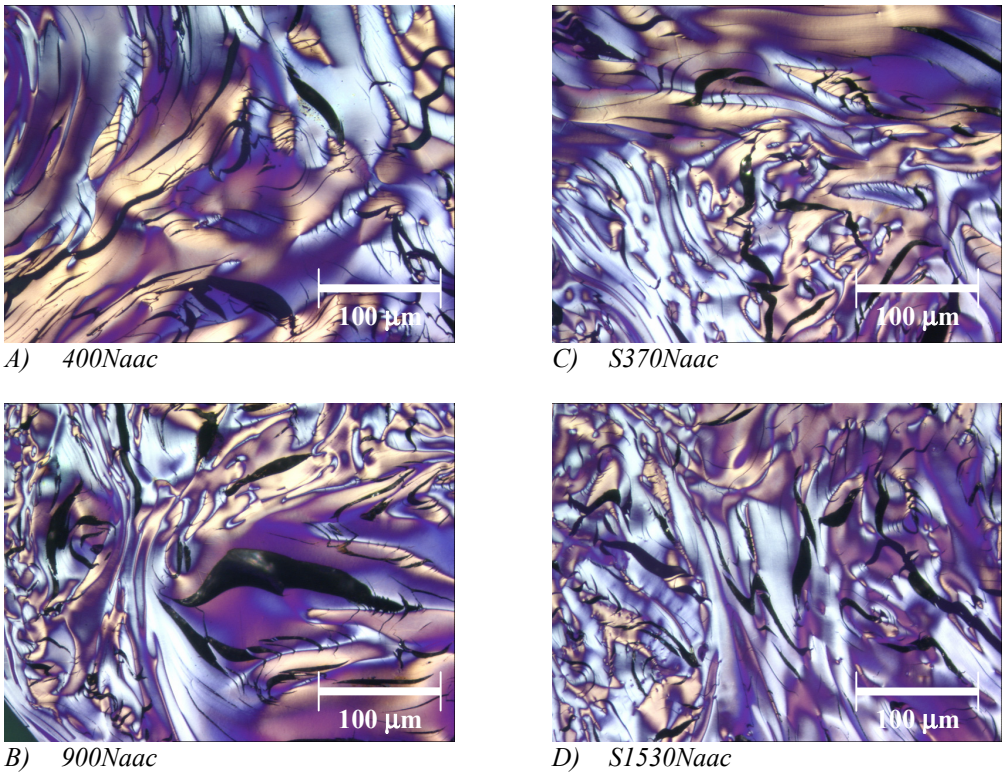

A) 400Naac *C) S370Naac*

B) 900Naac *D) S1530Naac*

Figure 4.9 Optical texture of cokes doped with sodium acetylacetonate

The textures are relatively fibrous with large optical domains. Qualitatively, it appears to be no significant differences among the coke samples. By use of an optical light microscope and an automatic image analysis program, the optical coke texture may be quantified in terms of a Mosaic Index and a Fiber Index. The Mosaic Index is a measure of the coarseness of the coke texture, while the Fiber Index is a measure of the anisotropy (method and definitions are described in chapter 3.2.2). A fine-grained texture is described by a high Mosaic Index. A high Fiber Index is given to a fibrous texture. For each sample, a total of 144 grains is analyzed. The final mosaic and fiber index is calculated as the average of all the analyzed grains.

The mosaic and fiber indexes of the sodium acetylacetonate doped cokes are given in Figure 4.10 and Figure 4.11. As seen from the charts, the indexes of the sodium acetylacetonate doped samples are comparable to the indexes of the pure reference cokes. There are some minor variations within each coke series, but since the cokes are very inhomogeneous (high standard deviations among analyzed grains), the variations are not statistically significant.

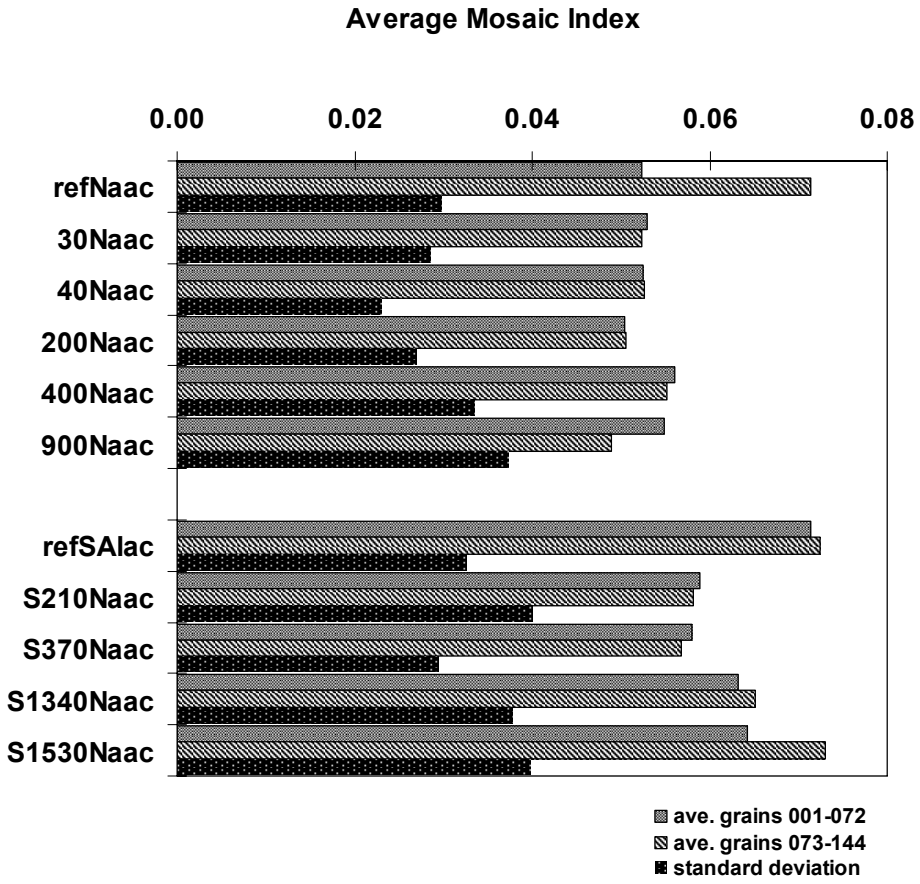

Figure 4.10 Mosaic Index, cokes doped with sodium acetylacetonate. *Average of two halves of analyzed grains with standard deviation*

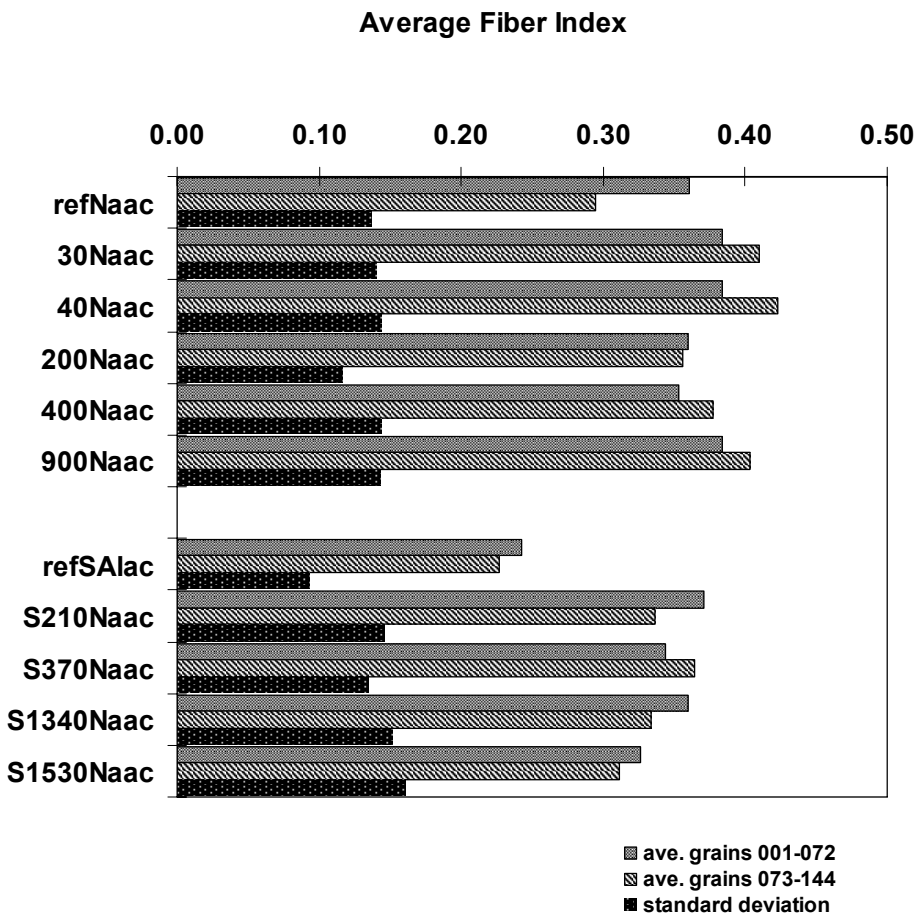

Figure 4.11 Fiber Index, cokes doped with sodium acetylacetonate. *Average of two halves of analyzed grains with standard deviation*

The "high"-sulfur cokes seem to have a slightly finer and less anisotropic texture than the "low"-sulfur cokes. In order to control whether the differences are statistically significant, variance analyses were performed. The values calculated for the mosaic indexes are presented in Table 4.2.

Table 4-2 Analysis of variances, mosaic indexes

Source of variations	Sum of squares	Degrees of freedom	Mean square
Between coke series	$S_T = 0.00048$	1	$s^2_T = 0.00048$
Within coke series	$S_R = 0.00022$	11	$s^2_R = 0.00002$
Total about grand average	0.00070	12	$s^2_T/s^2_R = 24.59$

From a statistical table [72], it was found that the upper 0.1, 1 and 5 % significance points of the F-distribution with 1 and 11 degrees of freedom are 19.69, 9.65 and 4.89 respectively. The calculated s^2_T/s^2_R-values (variance between series/variance within series) is higher than these numbers, and it is hence believed that a real difference exist. However, the texture differences are small and it is assumed that they have no significant influence on the measured coke reactivities.

Figure 4.12 shows the graphite 002 diffraction peak of some of the sodium acetylacetonate doped coke samples. The calculated L_c and d_{002}-values are presented in Figure 4.13.

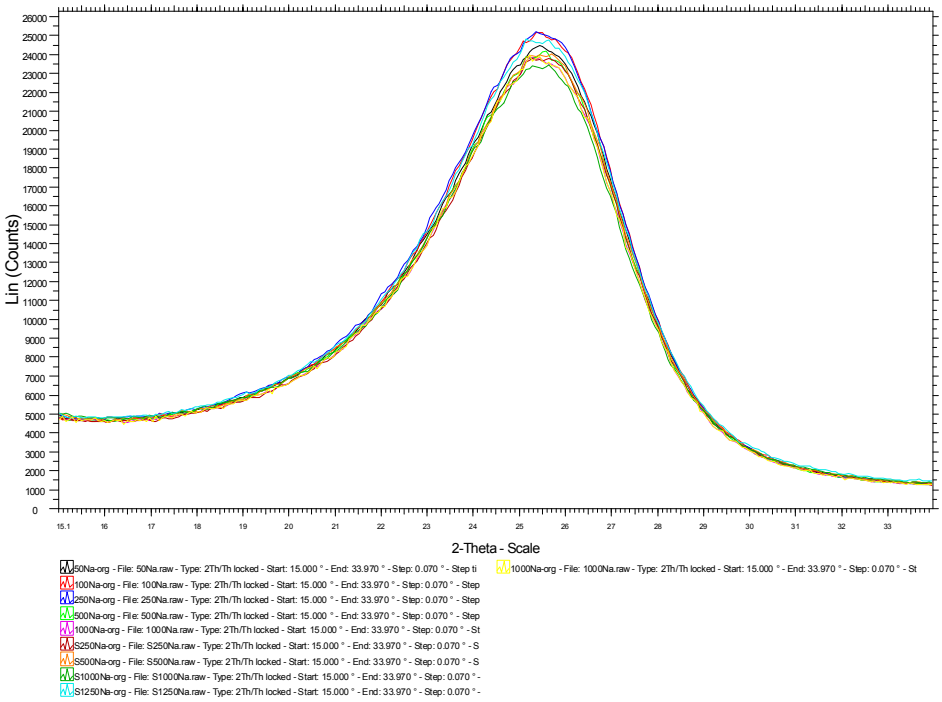

Figure 4.12 Graphite 002 diffraction peak, cokes doped with sodium acetylacetonate

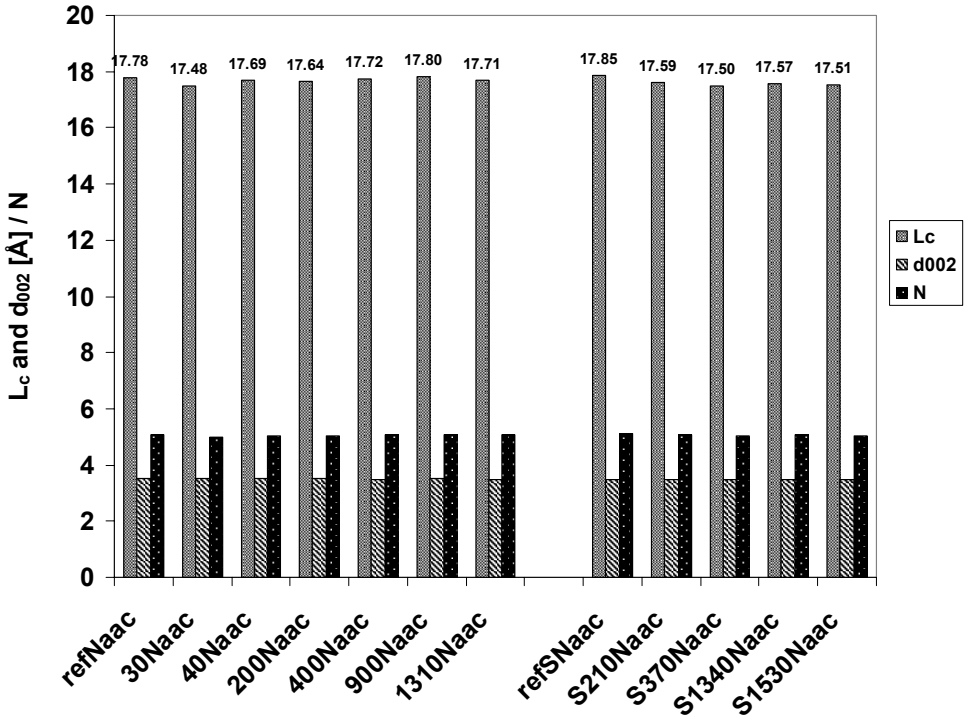

Figure 4.13 Coherent stacking height (L_c), distance between graphene layers (d_{002}) and average number of graphene layers in a coherent domain (N). *Variance between two parallel measurements: L_c: < 0.0016, d_{002}: < 0.000016*

Due to the low maximum heat treatment temperature and soaking time (1010 °C/2h), the degree of graphitization is low. The variance among the different samples is in the same order of magnitude as the variance between two parallel measurements and it thus is concluded that the graphitization process is not influenced by the sodium acetylacetonate additions.

4.2 Cokes doped with sodium fluoride and cryolite

Cokes doped with various amounts of sodium fluoride (NaF) and cryolite (Na_3AlF_6) were prepared from the petroleum pitch by the method described in chapter 3.1.4. Table 4-3 shows the contamination profiles of some of the calcined coke samples. The numbers in the sample labeling are referring to the slice number (see Figure 3.5) and the amount of elemental sodium (ppm) added to the pitch prior to carbonization. An "S" recognizes the "high"-sulfur cokes.

Table 4-3 Cokes doped with sodium fluoride (NaF) and cryolite (Na_3AlF_6).
DBT = dibenzothiophene

Sample	Additions	Analyzed dopant content calcined cokes			
		Na	Al	F	S
		ppm			*wt%*
800NaF.1	0.22 wt% NaF	2500	30	660	
800NaF.2		620	30	55	0.41
800NaF.3		260	20	25	0.39
800NaF.4		180	20	30	
S800NaF.1	0.17 wt% NaF + 5.6 wt% DBT	2080	40	700	
S800NaF.2		410	20	50	1.10
S800NaF.3		270	20	20	
S8000NaF.4		20	40	30	0.90
800Na3AlF6.1	0.31 wt% Na_3AlF_6	1490	580	1500	
800Na3AlF6.2		540	265	400	0.46
800Na3AlF6.3		370	190	200	0.46
800Na3AlF6.4		265	160	80	
S800Na3AlF6.1	0.32 wt% Na_3AlF_6 + 5.4 wt% DBT	1900	830	1200	0.87
S800Na3AlF6.2		460	200	200	0.83
S800Na3AlF6.3		130	60	40	
S800Na3AlF6.4		80	60	30	0.92

As seen from the X-ray diffractograms given in Figure 4.14 and Figure 4.15, both Na_3AlF_6 and NaF persist as the main crystalline phases within the calcined coke matrixes. However, compared to the analyzed sodium content, the bulk chemical analyses reveal a fluorine deficiency of about 60 percent for the cryolite doped cokes. The sodium fluoride doped cokes have a fluorine deficiency of about 80 percent.

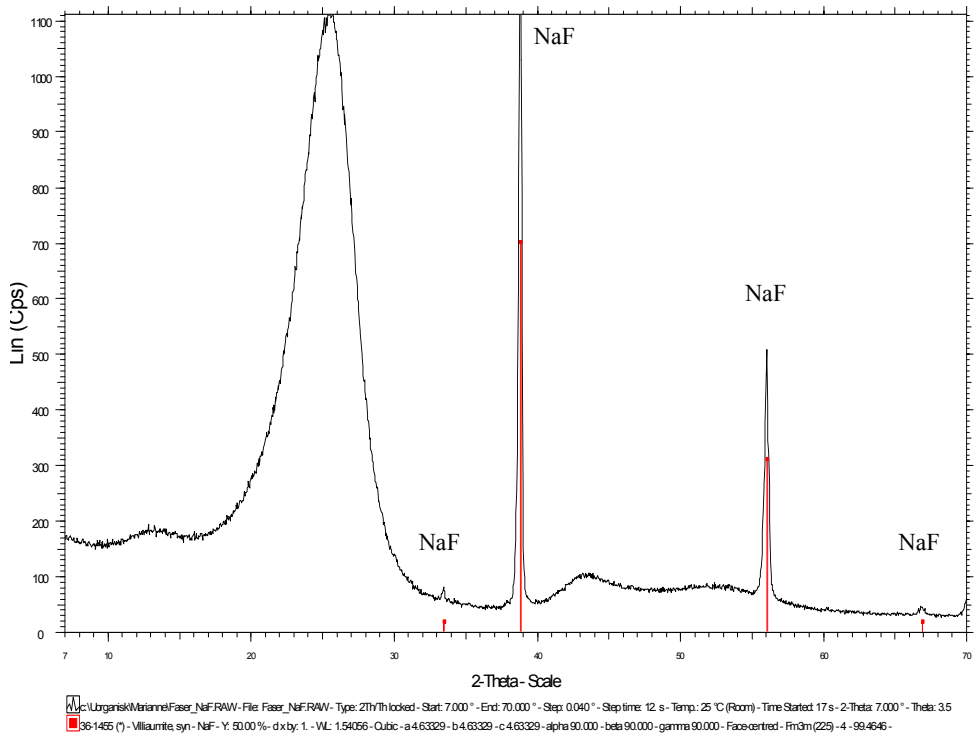

Figure 4.14 X-ray diffractogram, coke doped with sodium fluoride. *Broad peak at 2θ ~ 25° is identified as the graphite 002 diffraction peak*

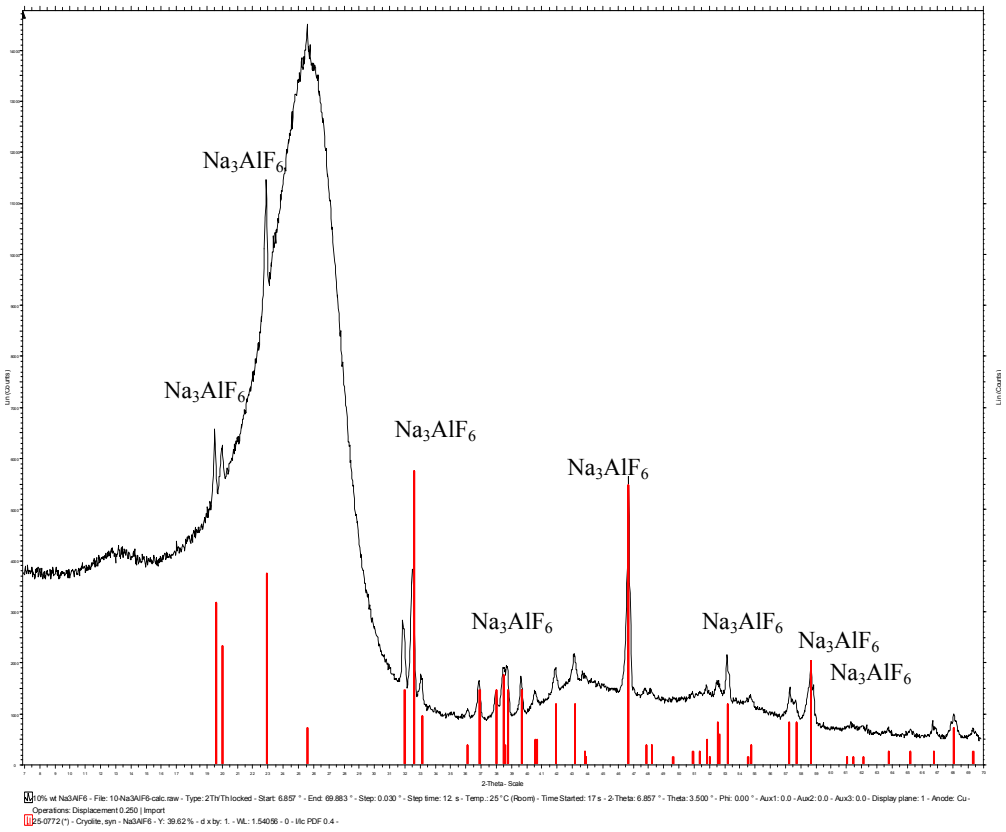

Figure 4.15 X-ray diffractogram, coke doped with cryolite. *Broad peak at 2θ ~ 25° is identified as the graphite 002 diffraction peak*

4.2.1 Air and CO_2 reactivity

Figure 4.16 and Figure 4.17 show the measured air and CO_2 reactivities of the sodium fluoride doped cokes. The reactivities are plotted as a function of the analyzed sodium contents. Sodium fluoride acts as a strong gasification catalyst and both the air and the CO_2 reactivity increase strongly with increasing sodium concentrations. As for the sodium acetylacetonate doped cokes, the addition of 4.5 weight percent dibenzothiophene (1 wt% sulfur), lowers the air reactivity of the sodium fluoride doped cokes while the CO_2 reactivity is nearly unaffected.

The sodium fluoride particles at the surface of the unoxidized coke grains contain considerable amounts of oxygen (30 – 50 at%, analyzed by EDX). The particles at the surface of the "high"-sulfur cokes contain a little more sulfur than the particles at the surface of the "low"-sulfur cokes (~ 6 at% *vs.* ~ 4 at%). After the air-reactivity tests, the sulfur content of the particles at the surface of the "high"-sulfur cokes is increased to about 10 – 12 at%, while it after the CO_2 reactivity tests is reduced to the same level as for the "low"-sulfur cokes (~ 4 at%).

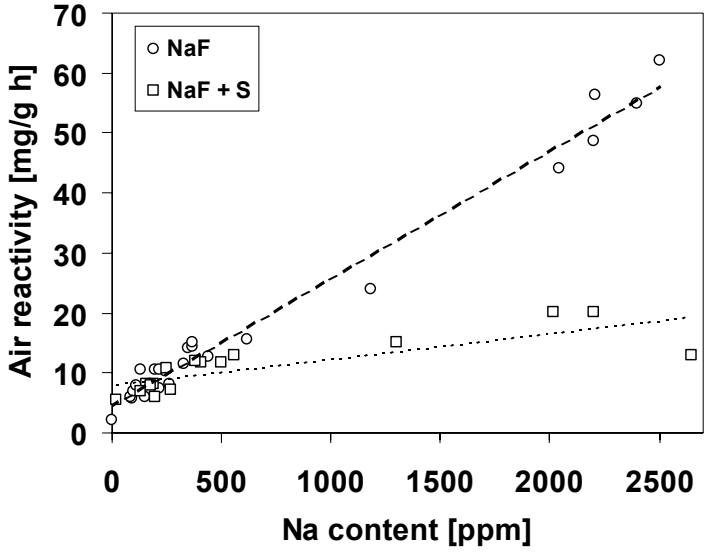

Figure 4.16 Air reactivity (475 °C) of sodium fluoride doped cokes *vs.* analyzed sodium content. *Average values of two parallel measurements. Standard deviations < 1.5 mg/g·h*

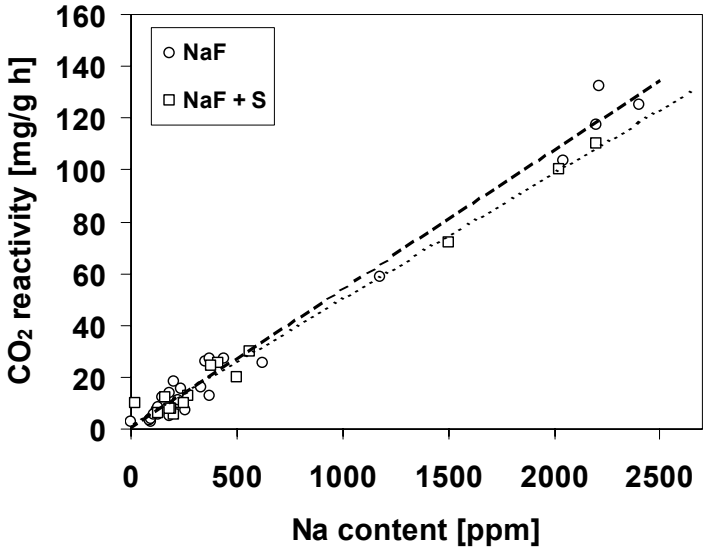

Figure 4.17 CO_2 reactivity (960 °C) of sodium fluoride doped cokes *vs.* analyzed sodium content. *Average values of two parallel measurements. Standard deviations < 1.3 mg/g·h*

The measured air and CO_2 reactivities of the cryolite-doped cokes are given in Figure 4.18 and Figure 4.19. As for the sodium fluoride doped cokes, both the air and CO_2 reactivity increase strongly with increasing sodium concentrations. The air reactivity is reduced when dibenzothiophene is added. The sulfur additions have no significant influence on the CO_2 reactivity.

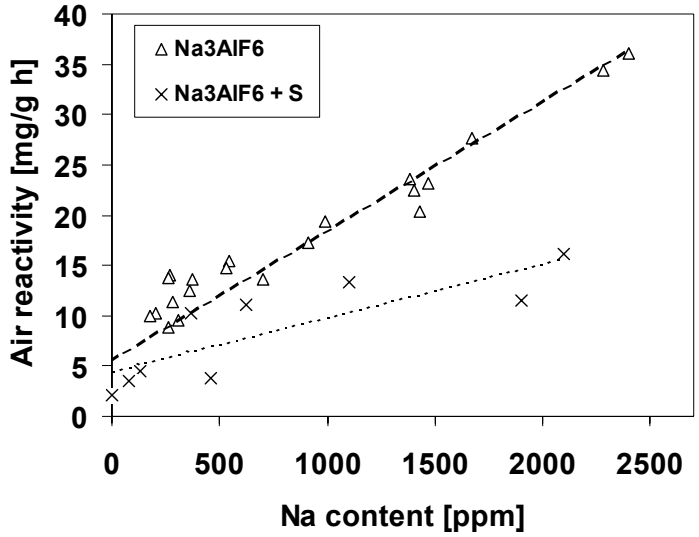

Figure 4.18 Air reactivity (475 °C) of cryolite doped cokes *vs.* analyzed sodium content.
Average values of two parallel measurements. Standard deviations < 1.5 mg/g·h

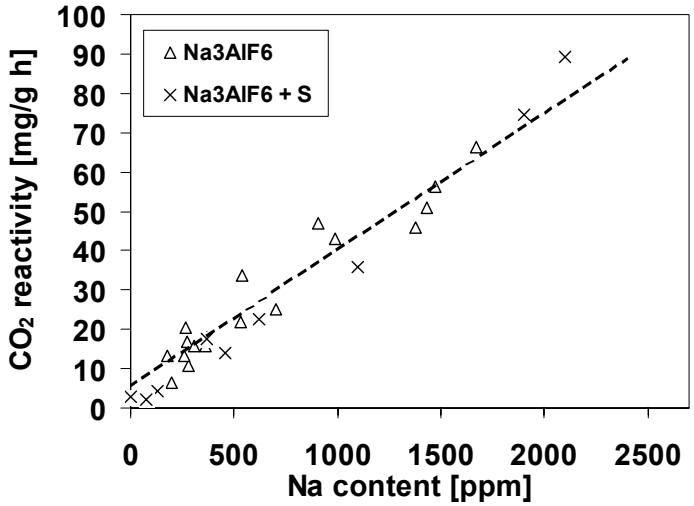

Figure 4.19 CO_2 reactivity (960 °C) of cryolite doped cokes *vs.* analyzed sodium content.
Average values of two parallel measurements. Standard deviations < 1.2 mg/g·h

Figure 4.20 and Figure 4.21 compares the reactivities of the "low"-sulfur sodium fluoride and cryolite doped cokes.

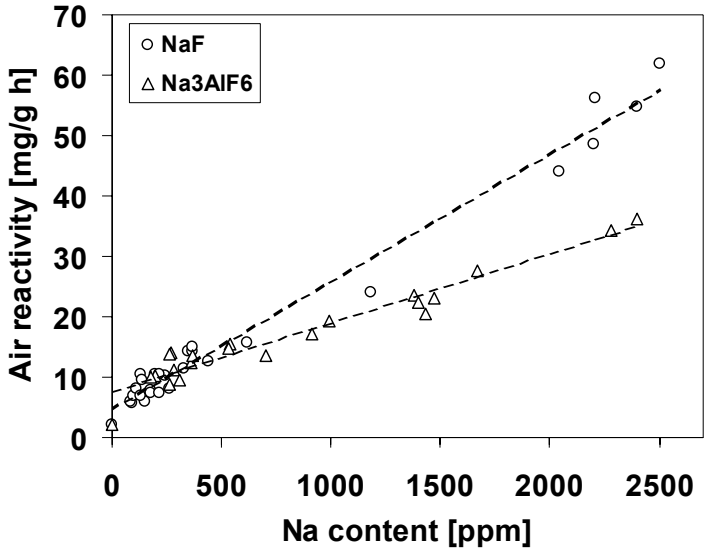

Figure 4.20 Air reactivities (475 °C) of cokes doped with sodium fluoride and cryolite, "low"-sulfur cokes

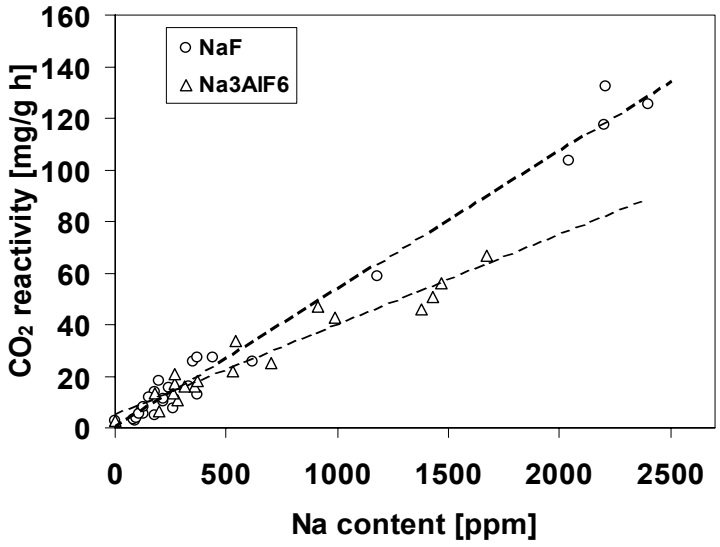

Figure 4.21 CO_2 reactivities (960 °C) of cokes doped with sodium fluoride and cryolite, "low"-sulfur cokes

At low sodium concentrations (< 500 ppm) it is, with the experimental setup used, not possible to detect any reactivity difference between the cokes doped with sodium fluoride and those doped with cryolite. However, at higher concentrations, the cryolite doped cokes are less reactive than the sodium fluoride doped cokes. The difference is especially marked for the air reactivity and is in accordance with the results reported by Rhedey [5] who found that cryolite was a weaker catalyst towards the carbon-air reaction than sodium fluoride. Possible reasons are discussed in chapter 4.3.2.

The SEM-micrograph given in Figure 4.22 shows that the sodium fluoride catalyzed CO_2-gasification reaction causes extensive pitting and channeling. Due to the high concentration of active sites, the pits are aligned along the edges of the coke lamellas. No sodium-containing particles remain at the outer coke surface. Figure 4.23 shows a SEM-micrograph of an air-oxidized coke grain. The surface textural changes are different to those observed for the CO_2 oxidized samples. Instead of pitting, channeling and edge recession appear to be predominating.

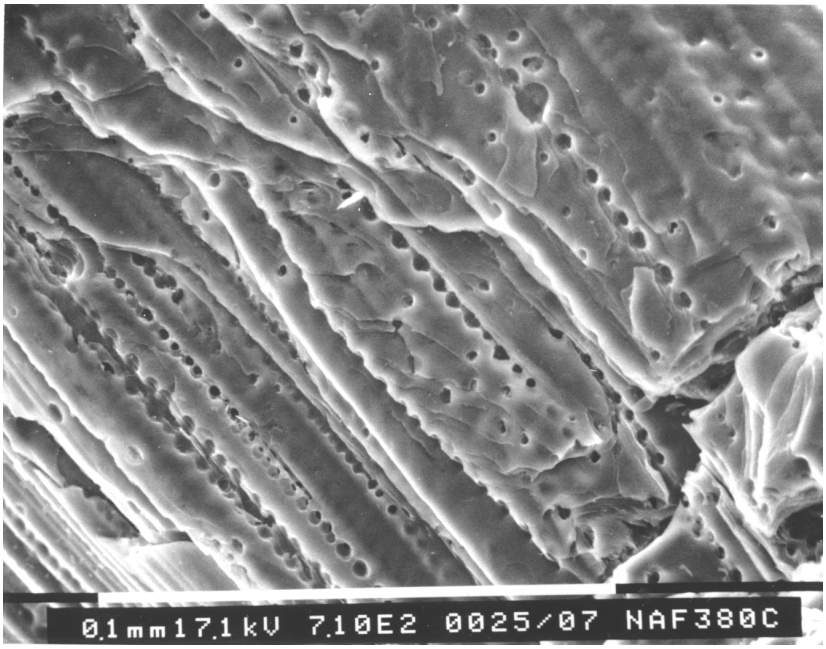

Figure 4.22 Surface of sodium fluoride doped coke grain after oxidation in CO_2 for 380 minutes (960 °C), pits formed perpendicular to graphene layers. *No sodium particles remain on coke surface*

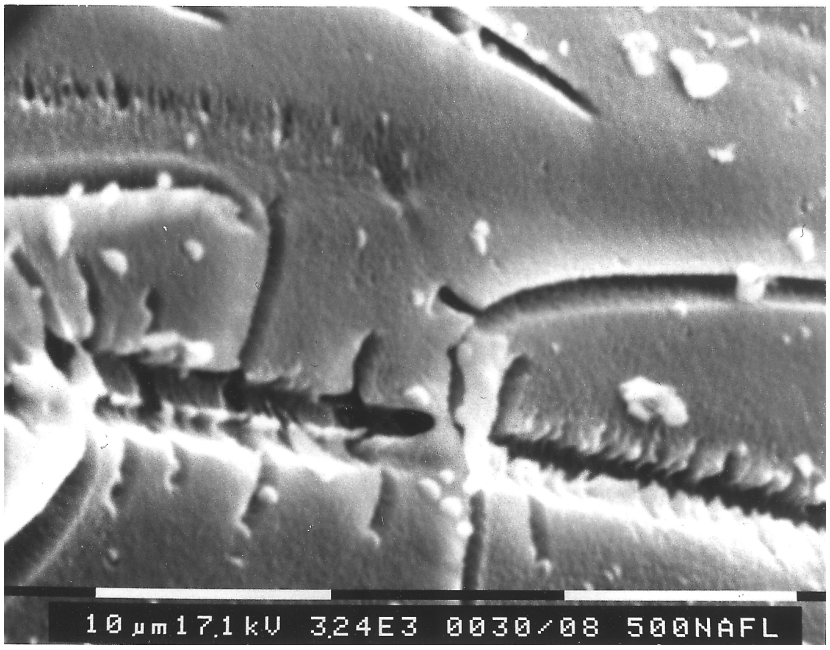

Figure 4.23 Surface of sodium fluoride doped coke grain after oxidation in air for 190 minutes (475 °C), channeling and edge recession. *Catalytically active sodium fluoride particles observed in bottom of channels*

The cryolite catalyzed gasification reactions cause topographical changes similar to those observed for the cokes doped with sodium acetylacetonate and sodium fluoride. The SEM-micrograph given in Figure 4.24 shows examples of both pitting and edge recession. A cryolite particle which is “eating” its way through the carbon lamellas is seen in the enlarged section inserted.

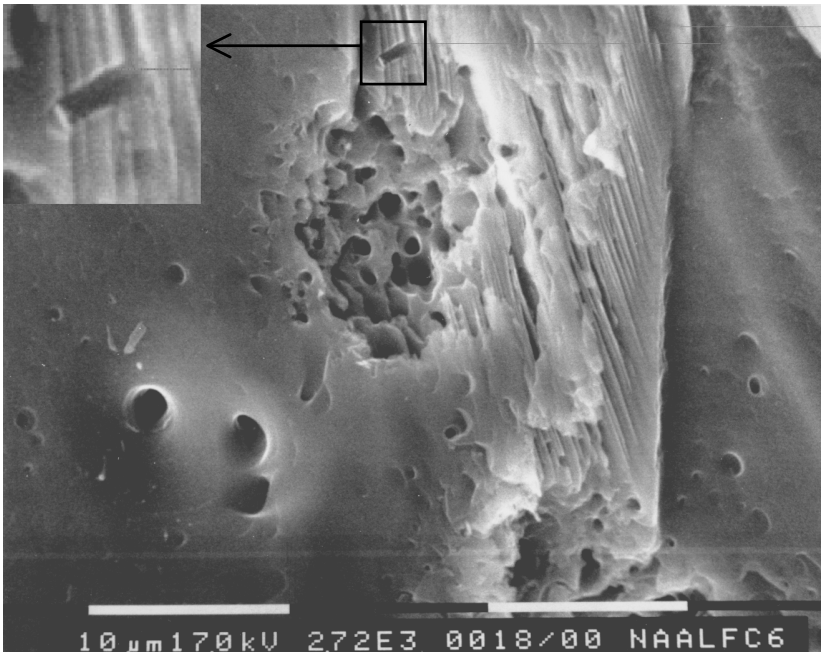

Figure 4.24 Surface of cryolite doped coke grain after oxidation in CO_2 for 190 minutes (960 °C), pit formation. *Enlarged section shows cryolite particle eating its way through the coke lamellas*

4.2.2 Optical texture and turbostratic structure

Figure 4.25 and Figure 4.26 show the calculated mosaic and fiber indexes of some of the sodium fluoride and cryolite doped coke samples.

Because of the considerably higher dopant concentrations, the top-samples (slice 1) have a slightly finer texture than the other samples. However, the variations are small and are believed to not have any influence on the measured coke reactivities.

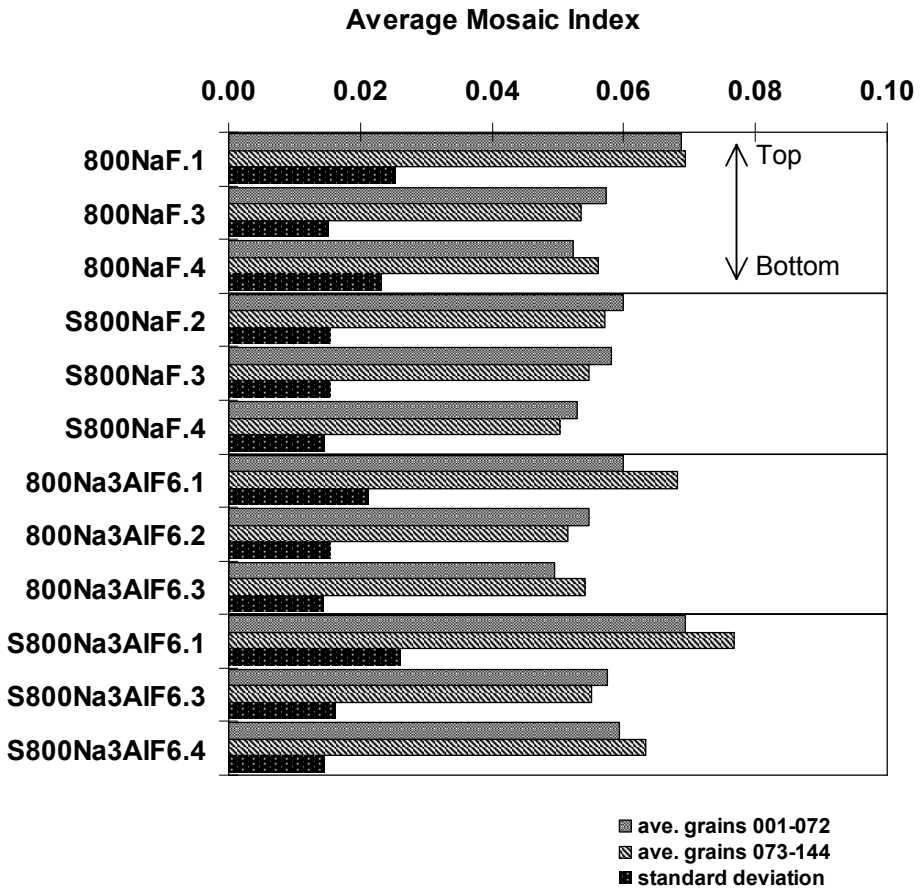

Figure 4.25 Mosaic Index, cokes doped with sodium fluoride or cryolite. *Average of two halves of analyzed grains with standard deviation*

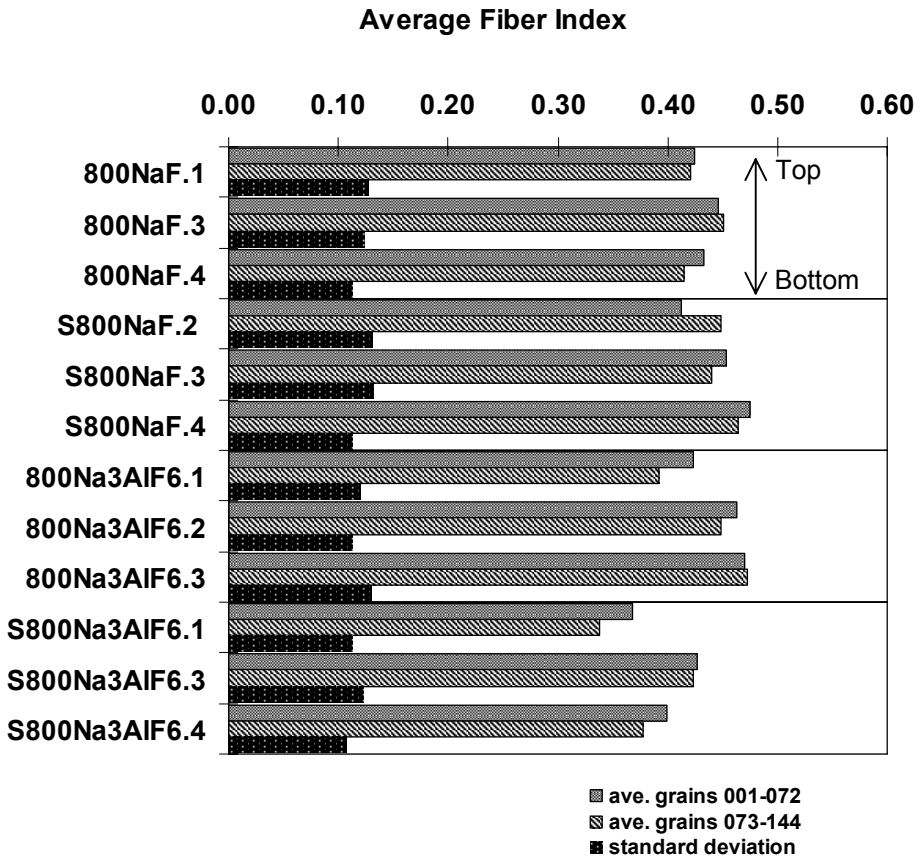

Figure 4.26 Fiber Index, cokes doped with sodium fluoride or cryolite. *Average of two halves of analyzed grains with standard deviation*

The measured L_c, d_{002} and N-values are presented in Figure 4.27. The variance among the different samples is slightly larger than the variance between two parallel measurements and the differences observed are thus believed to be true. However, there is no correlation between the structure parameters and the dopant concentrations ($R^2 < 0.3$).

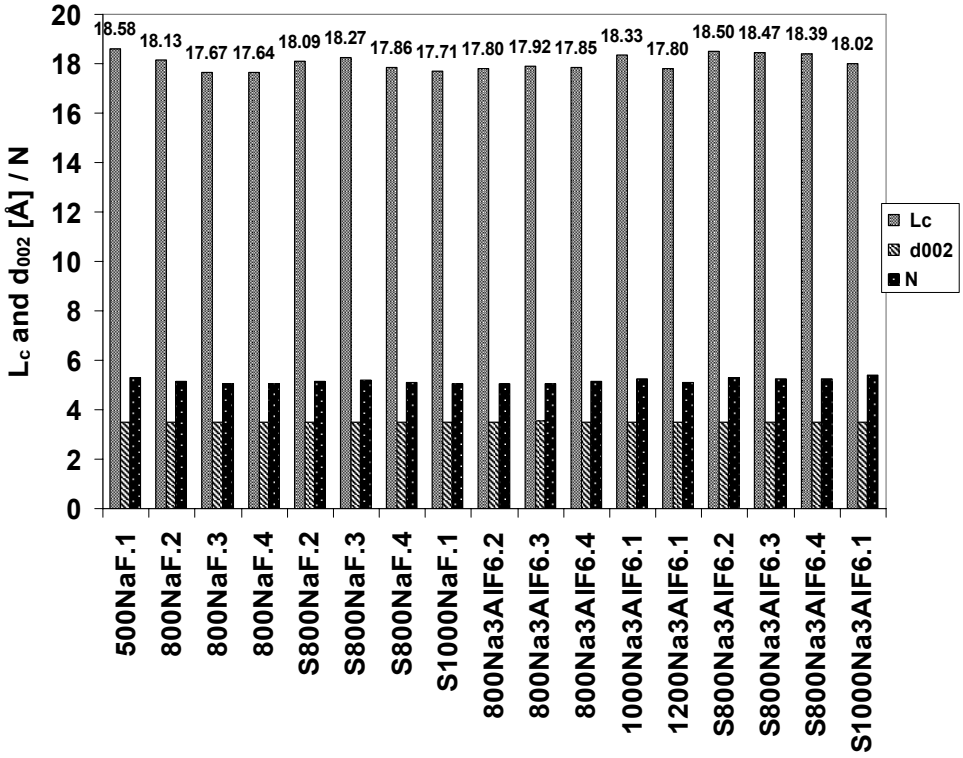

Figure 4.27 Coherent stacking height (L_c), distance between graphene layers (d_{002}) and average number of graphene layers in a coherent domain (N). *Variance between two parallel measurements: L_c: < 0.0015, d_{002}: < 0.000018*

4.3 Mechanistic considerations

4.3.1 Catalytic activity of sodium oxide

The X-ray diffraction analyses reveals that sodium acetylacetonate decomposes completely to sodium carbonate during preparation of the coke samples (see Figure 4.1). However, as observed from the EDX analyses, the sodium carbonate particles at the surface of the coke grains are not stable during the reactivity measurements. Only sodium oxide containing particles are found at the surface of the oxidized coke grains (see chapter 4.1.1).

As was shown in chapter 2.2.1, several mechanisms have been proposed to account for the catalytic activity of sodium and sodium compounds. However, evidences are quite compelling for the existence of catalytically active nonstoichiometric sodium oxide particles/clusters, which may be anchored to the carbon surface via C-O-Na phenolate groups (see Figure 2.10). The catalytically active sodium oxide particles provide sites for adsorption and dissociation of CO_2 and O_2 and thereby act as a medium to increase the concentration of adsorbed oxygen at the carbon surface.

The gasification mechanisms may be summarized as done in Figure 4.28 and Figure 4.29.

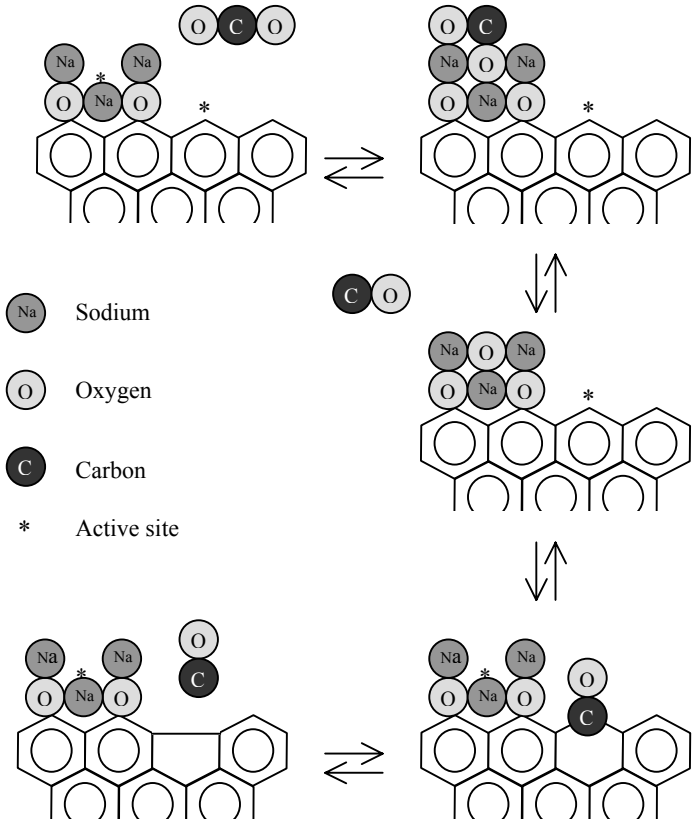

Figure 4.28 Mechanism of sodium oxide catalyzed CO_2 gasification. *Figure based on figure presented by Moulijn and Kapteijn* [32]

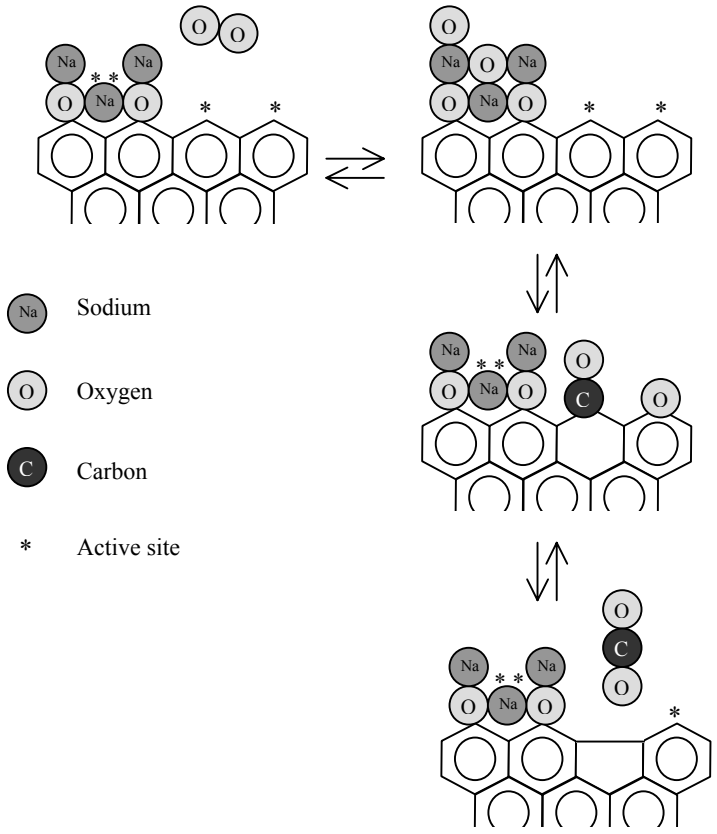

Figure 4.29 Mechanism of sodium oxide catalyzed O_2 gasification. *Figure based on figure presented by Moulijn and Kapteijn* [32]

From a thermodynamic viewpoint, sodium carbonate is expected to be stable at the gasification conditions:

$$Na_2CO_3 \Leftrightarrow Na_2O + CO_2 \qquad \Delta G^0_{960°C} = 150.2 \text{ kJ/mol} \qquad \textbf{Eq. 4.1}$$
$$\Delta G^0_{475°C} = 209.7 \text{ kJ/mol}$$

$$Na_2CO_3 + C \Leftrightarrow Na_2O + 2\,CO \qquad \Delta G^0_{960°C} = 105.3 \text{ kJ/mol} \qquad \textbf{Eq. 4.2}$$
$$\Delta G^0_{475°C} = 249.6 \text{ kJ/mol}$$

However, although thermodynamically unfavorable, decomposition of alkali carbonates in presence of carbon has also been observed by others [47, 53, 73]. It is assumed that the sodium oxide particles are stabilized in the presence of carbon through the surface phenolate groups. Hence it depends on the contact of the carbonate phase with the carbon and on the gas phase composition whether sodium carbonate is transformed into catalytically active sodium oxide or not.

4.3.2 Catalytic activity of sodium fluoride and cryolite

In principle, the catalytic activity of sodium fluoride and cryolite may be explained by two different mechanisms:

1. Oxygen adsorbs directly to the active sites at the surface of the NaF and Na_3AlF_6 particles and is redistributed to the active carbon sites via a "spill-over" mechanisms (see Eq. 2.31-2.33 and 2.35-2.39). The catalytic activity is determined by the ability of the fluoride salts to adsorb and redistribute the oxygen atoms. Possible anion effects may also play a part (see section 2.2.1).

2. During the initial stages of gasification, NaF and Na_3AlF_6 are activated via a transformation to an intermediate species (*e.g.* Na_2CO_3 or Na_2O) which decomposes to the catalytically active compound. The kinetics of activation and hence also the catalytic activity are controlled by the catalyst precursor anion *i.e.* the ease with which the intermediate species is formed.

Hüttinger and Minges [54, 74] applied the second mechanisms to account for the catalytic activity of various potassium salts (hydroxide, carbonate, nitrate, sulfate, chloride) towards water vapor gasification. Based on thermodynamical considerations and gas analyses, KOH was proposed to be the key component of all the activation processes, from which the catalytically active species, a non-stoichiometric potassium oxide was formed.

From the previous discussion, sodium carbonate or sodium oxide seems to be the most plausible intermediate species of the sodium catalyzed gasification reactions. However, as seen from the free energy change of the reactions given below, neither sodium fluoride nor cryolite is likely to go through a bulk chemical transformation at the gasification conditions (only reactions with most stable reaction products are shown). Thus, alternative 1 appears to be most plausible.

$2\ NaF + 2\ CO_2\ (g) \quad \Leftrightarrow \quad Na_2CO_3 + COF_2\ (g)$ **Eq. 4.3**

$\Delta G^0_{960°C} = 320.6$ kJ/mol

$4\ NaF + O_2\ (g) \quad \Leftrightarrow \quad 2\ Na_2O + 2\ F_2\ (g)$ **Eq. 4.4**

$\Delta G^0_{475°C} = 1358.8$ kJ/mol

$2\ Na_3AlF_6 + 9\ CO_2\ (g) \quad \Leftrightarrow \quad 3\ Na_2CO_3 + Al_2O_3 + 6\ COF_2\ (g)$ **Eq. 4.5**

$\Delta G^0_{960°C} = 1743.3$ kJ/mol

$2\ Na_3AlF_6 + 3\ O_2\ (g) \quad \Leftrightarrow \quad 3\ Na_2O + Al_2O_3 + 6\ F_2\ (g)$ **Eq. 4.6**

$\Delta G^0_{475°C} = 3400.9$ kJ/mol

As shown in chapter 4.2.1, the cokes doped with cryolite are less reactive than the corresponding cokes doped with sodium fluoride. The difference is most pronounced for the air reactivities, and it increases with increasing dopant additions. It is likely to assume that sodium fluoride and cryolite have the same ability to dissociate CO_2 and O_2, and to redistribute the adsorbed oxygen atoms to the active sites at the carbon surface. The key to understand the reactivity differences is hence expected to be related to the thermal stability of the two dopant species. At elevated temperatures, catalytically active sodium may be lost through evaporation. At the same time possible inhibiting fluoride gases may be formed. Gaseous halogen compounds are by several authors reported to inhibit the carbon gasification reactions by adsorbing to and thereby deactivate the active carbon sites [75-78]. The exact nature of the inhibiting carbon-halogen adsorption products is not reported. However, gaseous species containing polar oxygen groups such as ―OH or ―CO are presumed to be most effective since they provide sites for attachment to the carbon atoms [78].

As described in chapter 3.1.3, the coke samples were calcined to 1010 °C in a closed graphite crucible. By using the HSC Chemistry © thermodynamic computer package [79], the equilibrium conditions during calcination are calculated. Figure 4.30 shows how the calculated activities of the most stable solid and gaseous species in the two systems vary as a function of the temperature. The activities at 1010 °C (maximum calcination temperature) are given in Table 4-4.

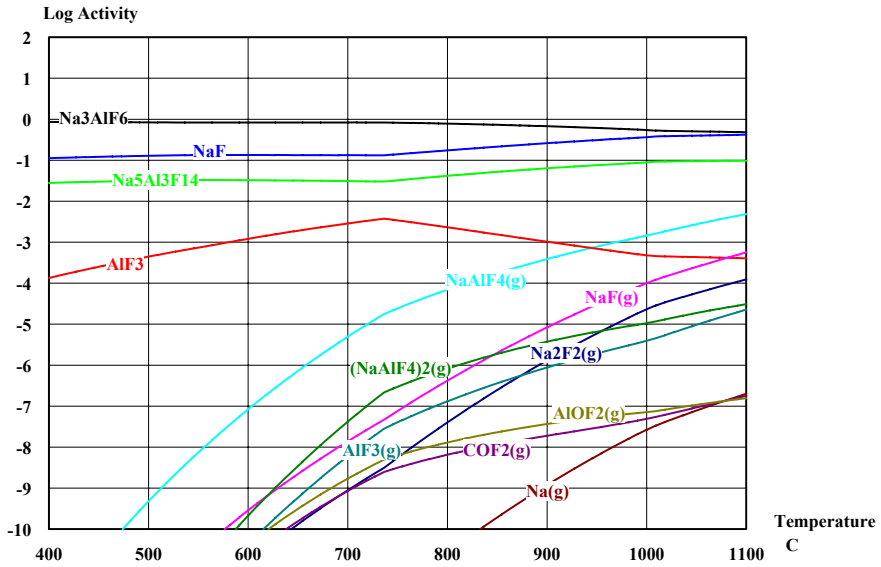

A) Coke doped with cryolite

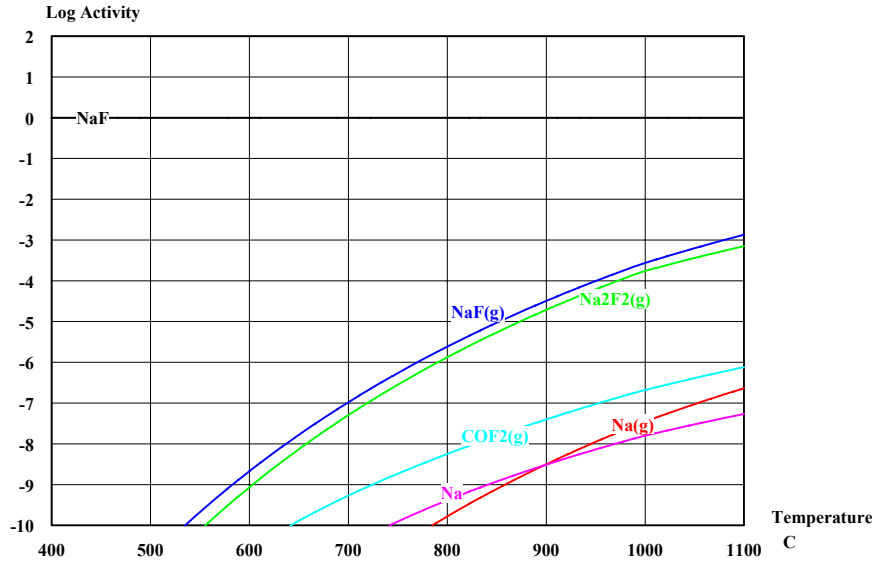

B) Coke doped with sodium fluoride

Figure 4.30 Calculated activities (logarithmic) *vs.* temperature, calcination of cokes doped with cryolite and sodium fluoride. *Calculated by use of HSC Chemistry* © [79]. *Initial conditions: T = 25 °C, p_{O2} = 0.2 atm, p_{N2} = 0.8 atm, $c_{Na3AlF6}/c_{NaF}$ = 0.25 wt%, excess carbon. Activities of C, O_2, CO and CO_2 are not shown, CO dominates at temperatures above 700 °C*

Table 4-4 Calculated activities of most stable solid and gaseous species at maximum calcination temperature (1010 °C), cokes doped with cryolite and sodium fluoride.
Calculated by use of HSC Chemistry © [79]. Initial conditions: T = 25 °C, p_{O2} = 0.2 atm, p_{N2} = 0.8 atm, c_{NaF} = 0.25 wt%, excess carbon. Activities of C, O_2, CO and CO_2 are not given.

Cokes with Na_3AlF_6		Cokes with NaF	
Species	**Log Activity** *1010 °C*	**Species**	**Log Activity** *1010 °C*
Na_3AlF_6 (s)	-0.3		
NaF (s)	-0.4	NaF (s)	0
$Na_5Al_3F_{14}$ (s)	-1.0	Na (s)	-7.6
AlF_3 (s)	-3.4		
$NaAlF_4$ (g)	-2.7		
NaF (g)	-3.8	NaF (g)	-3.3
Na_2F_2 (g)	-4.4	Na_2F_2 (g)	-3.5
$(NaAlF_4)_2$ (g)	-4.8		
AlF_3 (g)	-5.2		
COF_2 (g)	-7.1	COF_2 (g)	-6.5
$AlOF_2$ (g)	-7.2		
Na (g)	-7.3	Na (g)	-7.2
Sum gas phase activities	-2.6	Sum gas phase activities	-3.1
Sum activities gaseous Na species	-2.6	Sum activities gaseous Na species	-3.1
Sum activities gaseous F species with polar oxygen groups ($AlOF_2$, COF_2)	-6.8	Sum activities gaseous F species with polar oxygen groups (COF_2)	-6.5

Above approximately 700 °C, solid Na_3AlF_6 appears to decompose gradually into $Na_5Al_3F_{14}$, NaF and AlF_3:

$$3\ Na_3AlF_6 \Leftrightarrow Na_5Al_3F_{14} + 4\ NaF \qquad \textbf{Eq. 4.7}$$

$\Delta G^0_{1010\,°C} = 46.3$ kJ/mol

$$Na_3AlF_6 \Leftrightarrow 3\ NaF + AlF_3 \qquad \textbf{Eq. 4.8}$$

$\Delta G^0_{1010\,°C} = 106.2$ kJ/mol

Sodium fluoride on the other hand, is stable throughout the whole temperature range.

$NaAlF_4$, NaF and Na_2F_2 (dimer) appear to be the most important gaseous species in the cryolite-carbon system, while NaF and Na_2F_2 dominate in the sodium fluoride system. About equal amounts of possible inhibiting fluorine species (COF_2 and $AlOF_2$) are formed. However, due to higher volatility, the cryolite doped cokes are expected to suffer from a higher sodium evaporation loss than the sodium fluoride doped cokes.

The gasification systems invariably represent non-equilibrium states, which should be specified through open system, multiphase, multicomponent thermodynamics. However, as

argued by McKee and Chatterji [39], traditional closed system thermodynamics may be useful to get an overview of the stability of the catalysts species at the gasification conditions. It might be assumed that local equilibrium is achieved in a microscopic sense in the immediate vicinity of the catalyst particles. Although the lack of detailed knowledge of the local environment around a reaction site on the coke surface precludes quantitative thermodynamic calculations, useful qualitative information could be obtained.

Table 4-5 gives the equilibrium activities of the most stable solid and gaseous species in the C-Na_3AlF_6 and C-NaF gasification systems. The calculations were performed at the actual gasification temperatures (475 °C/960 °C) in excess of carbon and oxidizing reactant gas (O_2/CO_2).

Table 4-5 Equilibrium compositions in vicinity of cryolite and sodium fluoride particles on coke surface during air and CO_2 gasification. *Activities calculated at actual gasification temperature in excess of carbon and O_2/CO_2 (HSC Chemistry © [79]) $c_{Na3AlF6}$ / c_{NaF} = 0.25 wt%. Activities of C, O_2, CO and CO_2 are not given*

Cokes with Na_3AlF_6			**Cokes with NaF**		
Species	**Log Activity**		**Species**	**Log Activity**	
	CO_2 gas. *960 °C*	Air gas. *475 °C*		CO_2 gas. *960 °C*	Air gas. *475 °C*
Na_3AlF_6 (s)	-0.3	-0.07			
NaF (s)	-0.4	-0.9	NaF (s)	0	0
$Na_5Al_3F_{14}$ (s)	-3.4	-1.5			
AlF_3 (s)	-4.5	-3.5			
$NaAlF_4$ (g)	-4.0	-10.0			
NaF (g)	-4.1		NaF (g)	-3.9	(-11.4)
Na_2F_2 (g)	-4.4		Na_2F_2 (g)	-4.1	(-12.0)
$AlOF_2$ (g)	-6.7	-8.9			
COF_2 (g)	-6.9	-9.2	COF_2 (g)	-8.0	(-13.7)
AlF_3 (g)	-7.0				
$(NaAlF_4)_2$ (g)	-7.1				
Na (g)	-8.3		Na (g)	-7.7	
Sum gas phase activities	-3.7	-8.7	Sum gas phase activities	-3.7	(-11.3)
Sum activities gaseous Na species	-3.7	-10	Sum activities gaseous Na species	-3.7	(-11.3)
Sum activities gaseous F species with polar oxygen groups ($AlOF_2$, COF_2)	-6.5	-8.7	Sum activities gaseous F species with polar oxygen groups (COF_2)	-8.0	(-13.7)

At the CO_2 gasification conditions, the two dopant species show a comparable volatility. The two systems are excepted to suffer from about the same sodium evaporation loss, but the cryolite containing cokes seem to have the highest potential for formation of inhibiting fluorine gases (COF_2 and $AlOF_2$). At the air gasification conditions, the situation is more pronounced. Although the activities are very low, cryolite appears to be considerably more volatile than sodium fluoride. The thermodynamic calculations are confirmed by chemical

analyses which reveal that the sodium fluoride and cryolite doped cokes lose about equal amounts of sodium during the CO_2 reactivity measurements (~ 15 – 20 %). During the air reactivity tests, no sodium evaporates from the sodium fluoride doped cokes whereas the cryolite doped cokes lose about 10 % sodium and 30 % aluminium.

5 Effect of calcium compounds on coke reactivity

5.1 Cokes doped with calcium acetylacetonate

Cokes doped with various amounts of calcium acetylacetonate were prepared from the tar oil by the method described in chapter 3.1.3. An overview of the coke samples is given in Table 5-1.

Table 5-1 Cokes doped with calcium acetylacetonate.
Ca-ac = calcium acetylacetonate, DBT = dibenzothiophene

Sample	Additions	Analyzed dopant content calcined cokes	
		Ca *ppm*	S *wt%*
refCaac	-	2	0.26
180Caac	0.05 wt% Ca-ac	180	0.27
200Caac	0.07 wt% Ca-ac	200	
240Caac	0.11 wt% Ca-ac	240	
400Caac	0.17 wt% Ca-ac	400	
570Caac	0.34 wt% Ca-ac	570	0.30
600Caac	0.25 wt% Ca-ac	600	0.30
650Caac	0.37 wt% Ca-ac	650	
875Caac	0.43 wt% Ca-ac	875	0.31
refSCaac	0 wt% Ca-ac + 4.5 wt% DBT	1	0.74
S160Caac	0.07 wt% Ca-ac + 4.5 wt% DBT	160	0.83
S335Caac	0.14 wt% Ca-ac + 4.5 wt% DBT	335	0.85
S635Caac	0.23 wt% Ca-ac + 4.5 wt% DBT	635	0.87
S900Caac	0.38 wt% Ca-ac + 4.5 wt% DBT	900	0.90

As seen from the X-ray diffractogram given in Figure 5.1, calcium acetylacetonate decomposes completely to calcium oxide and calcium carbonate during the carbonization and calcination processes.

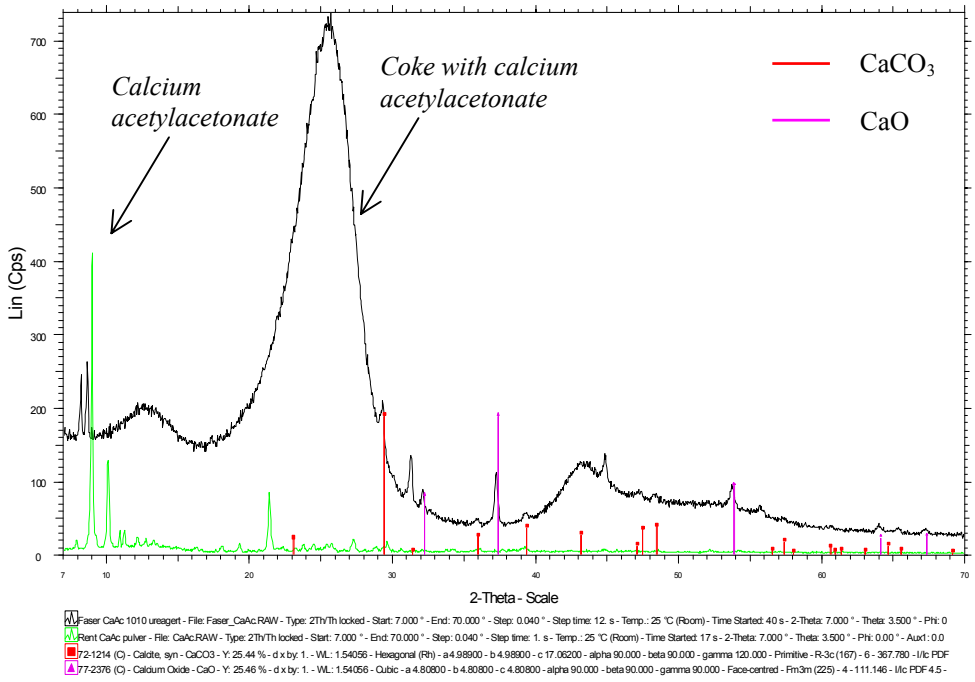

Figure 5.1 X-ray diffractogram, coke doped with calcium acetylacetonate. *Diffractogram from analysis of sodium acetylacetonate powder is included. Broad peak at $2\theta \sim 25°$ is identified as the graphite 002 diffraction peak*

The SEM-micrograph given in Figure 5.2 below shows the distribution of calcium containing particles on the surface of a calcined coke grain.

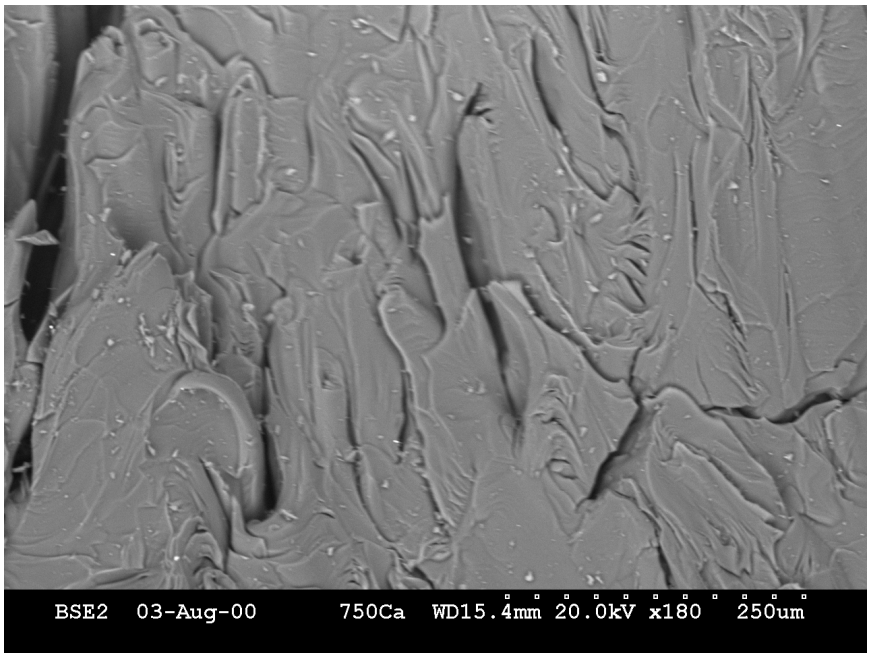

Figure 5.2 Calcium oxide and calcium containing particles (light gray) on surface of coke doped with calcium acetylacetonate. *SEM-micrograph, backscatter detector*

5.1.1 Air and CO_2 reactivity

Figure 5.3 and Figure 5.4 show the measured air and CO_2 reactivities of the calcium acetylacetonate doped cokes. The reactivities are given as a function of the analyzed bulk calcium contents.

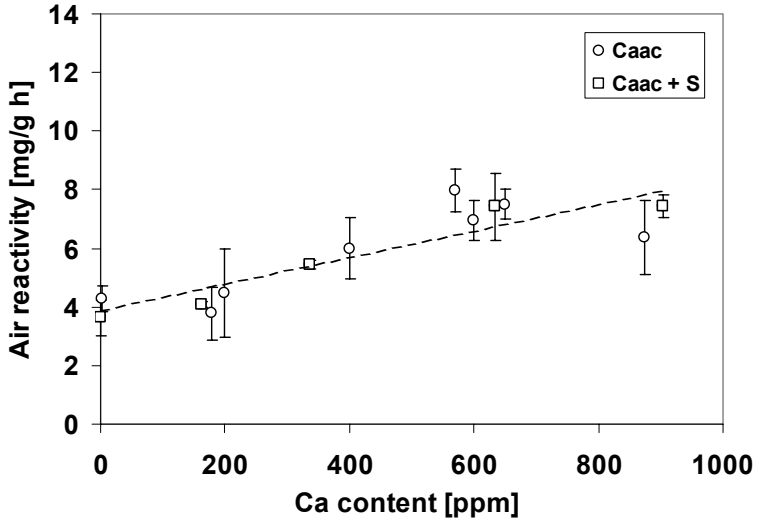

Figure 5.3 Air reactivity (525 °C) of calcium acetylacetonate doped cokes *vs*. analyzed calcium content. *Average values of five parallel measurements. Standard deviations represented by error bars.*

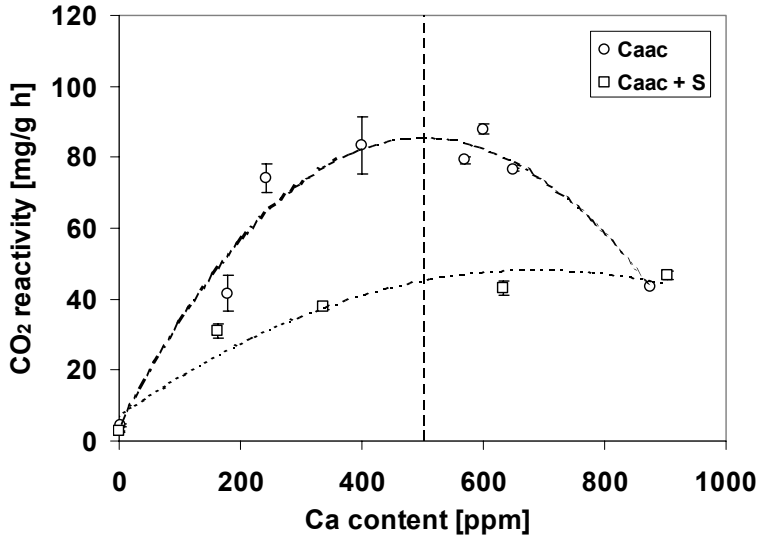

Figure 5.4 CO_2 reactivity (960 °C) of calcium acetylacetonate doped cokes *vs*. analyzed calcium content. *Average values of five parallel measurements. Standard deviations represented by error bars.*

The CO_2 reactivity increases strongly with the increasing calcium concentration while the air reactivity is barely affected. The CO_2 reactivity is markedly reduced when 4.5 wt% dibenzothiophene is added to the tar oil prior to carbonization. The air gasification rates are not affected by the dibenzothiophene additions. As analyzed by EDX, there is no enrichment of sulfur in the calcium containing particles at the surface of the unoxidized "high"-sulfur cokes compared to the particles at the surface of the "low"-sulfur cokes (sulfur content ~ 5 at%). However, after the CO_2 reactivity tests, the sulfur content of the particles at the surface of the "high"-sulfur cokes is considerably enhanced (sulfur content ~ 15 – 20 at%).

The CO_2 reactivity seems to reach some kind of saturation at about 500 ppm Ca. This phenomenon is also observed by other workers [59-61, 66] and is attributed to a decrease of the calcium dispersion. Cazorla-Amorós *et al.* [60] reported that the catalytic activity of calcium towards the carbon-CO_2 reaction is directly related to the calcium-carbon contact. However, at high calcium loadings, sintering (grain coarsening) of the catalyst particles might occur. This is accompanied by a decrease in the reactivity which is associated with the drop in the surface area of the calcium catalyst and therefore with a decrease in the calcium-carbon contact area [60].

The SEM micrograph given in Figure 5.5 shows the surface of an CO_2-oxidized "high"-sulfur coke grain. Due to the catalytic activity of the calcium oxide particles, large circular pits have been formed in the carbon basal plane.

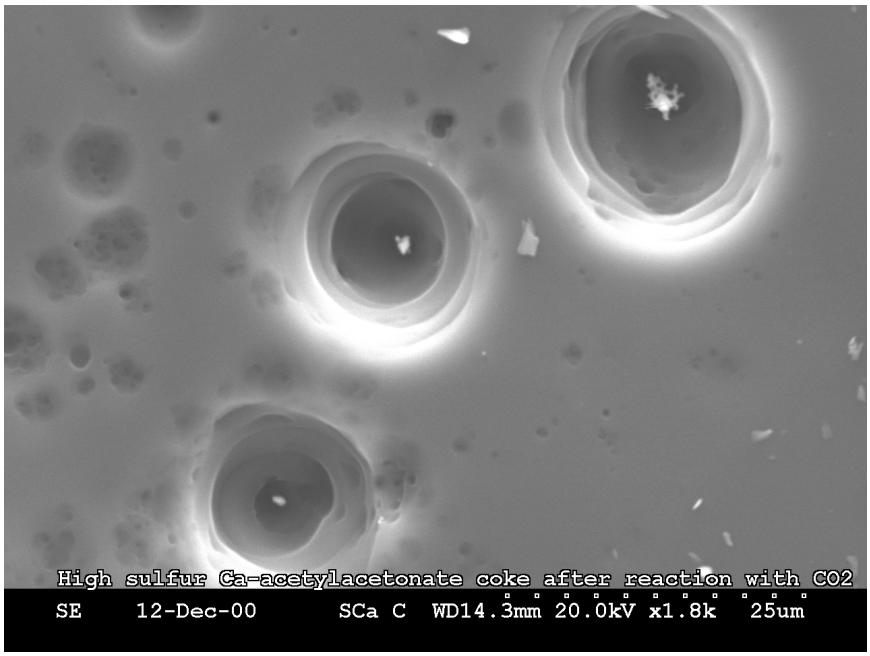

Figure 5.5 Surface of Ca-acetylacetonate doped coke after oxidation in CO_2 for 190 minutes (525 °C), pit formation. *Calcium oxide particles observed in bottom of pits*

As seen from the micrograph given in Figure 5.6, the calcium catalyzed air gasification reaction causes other surface textural changes than the CO_2 gasification reaction. Instead of pit-formation, large parts of the coke surface have gotten a ”corroded” appearance. The oxidized areas are covered with a lot of small calcium oxide particles.

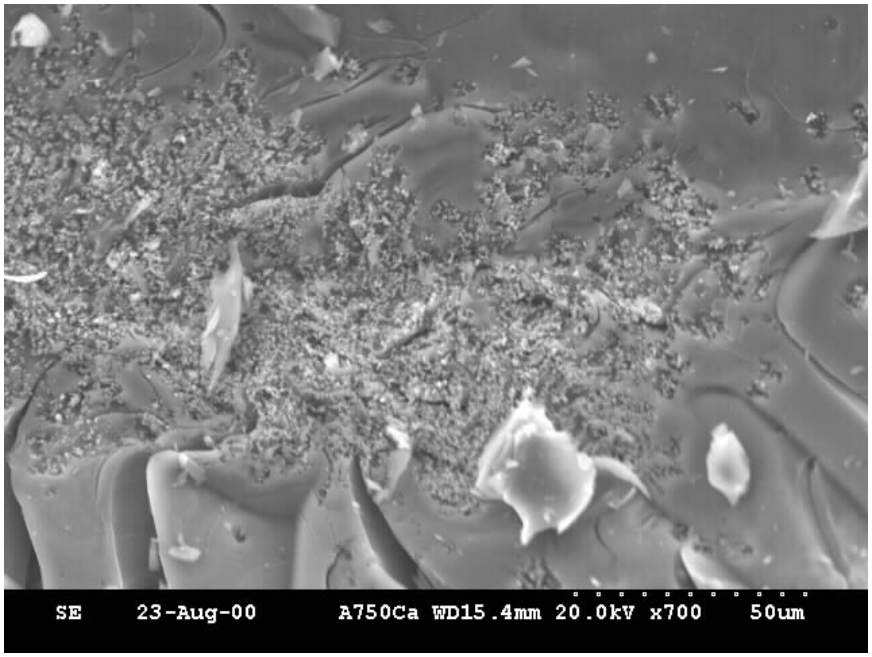

Figure 5.6 Surface of Ca-acetylacetonate-doped coke after oxidation in air for 190 minutes (525 °C). *Oxidized areas covered with CaO particles (light)*

5.1.2 Optical texture and turbostratic structure

Micrographs showing the optical texture of some of the calcium acetylacetonate doped cokes are given in Figure 5.7. The textural features are comparable to those observed for the cokes doped with sodium acetylacetonate. The texture is not disturbed by the small dopant grains, which are located both within and between the coke lamellas (black spots, see especially micrograph B).

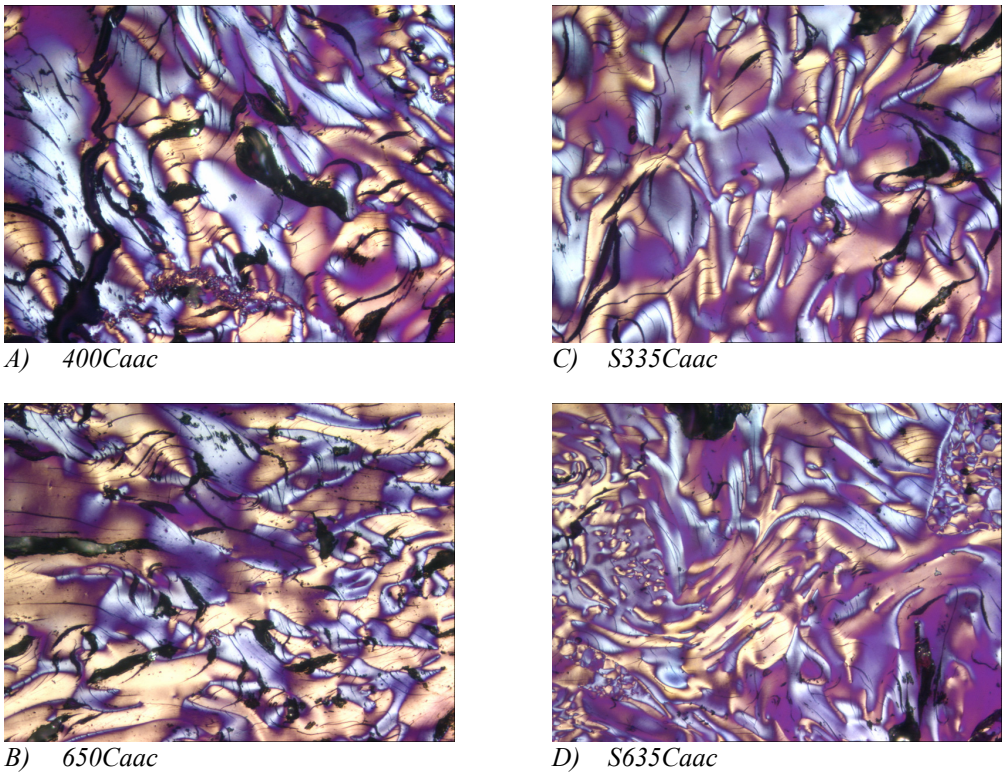

A) 400Caac *C) S335Caac*

B) 650Caac *D) S635Caac*

Figure 5.7 Texture of cokes doped with calcium acetylacetonate

Figure 5.8 and Figure 5.9 give the calculated mosaic and fiber indexes. The average mosaic index seems to increase slightly with increasing calcium concentrations, but because of the low homogeneity (high standard deviations among analyzed grains) the variation among the different samples is not statistically significant (α = 0.0005). Due to the addition of dibenzothiophene, the "high"-sulfur cokes are slightly finer and more homogeneous than the "low"-sulfur cokes.

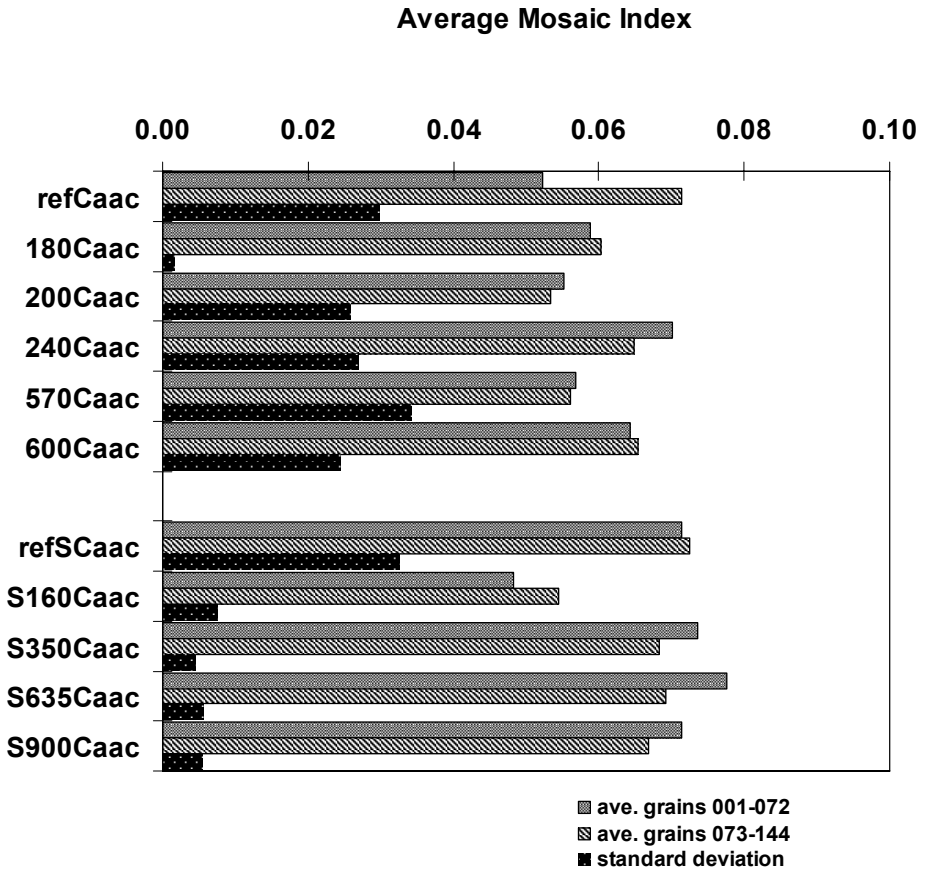

Figure 5.8 Mosaic Index, cokes doped with calcium acetylacetonate. *Average of two halves of analyzed grains with standard deviation*

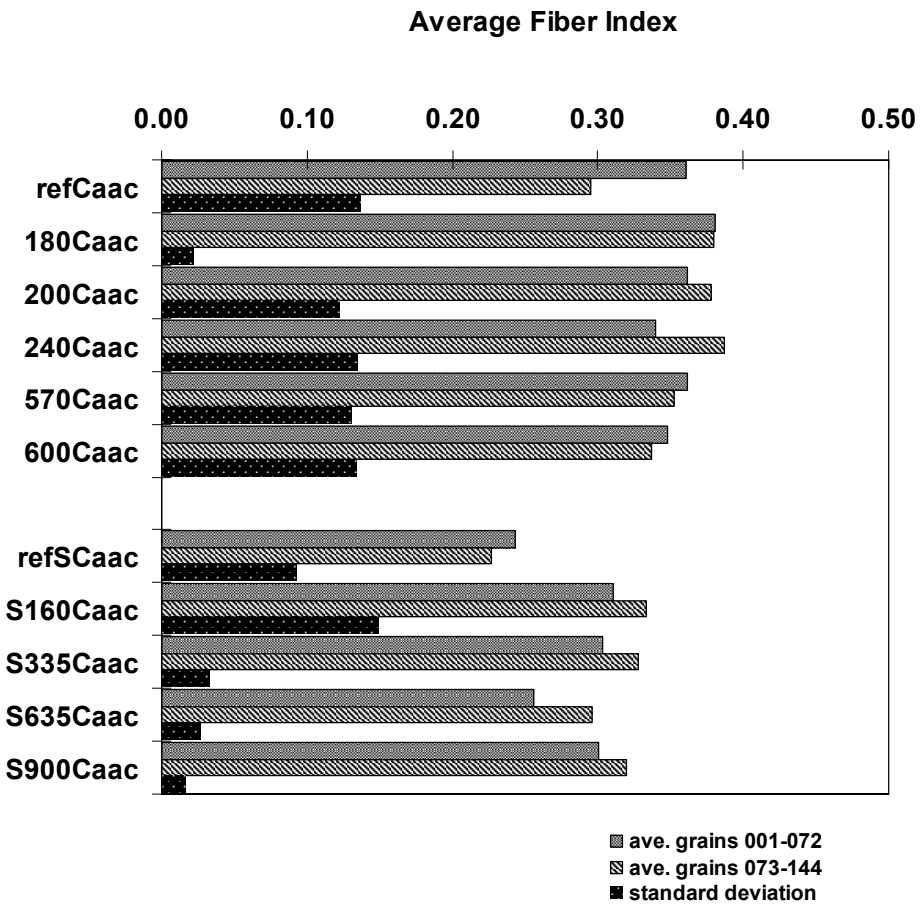

Figure 5.9 Fiber Index, cokes doped with calcium acetylacetonate. *Average of two halves of analyzed grains with standard deviation*

X-ray diffractograms showing the graphite 002 diffraction peak of the different calcium acetylacetonate doped coke samples is given in
Figure 5.10. The calculated coherent stacking heights (L_c), the distance between the graphene layers (d_{002}) and the average number of graphene layers in a coherent domain (N) are shown graphically in Figure 5.11.

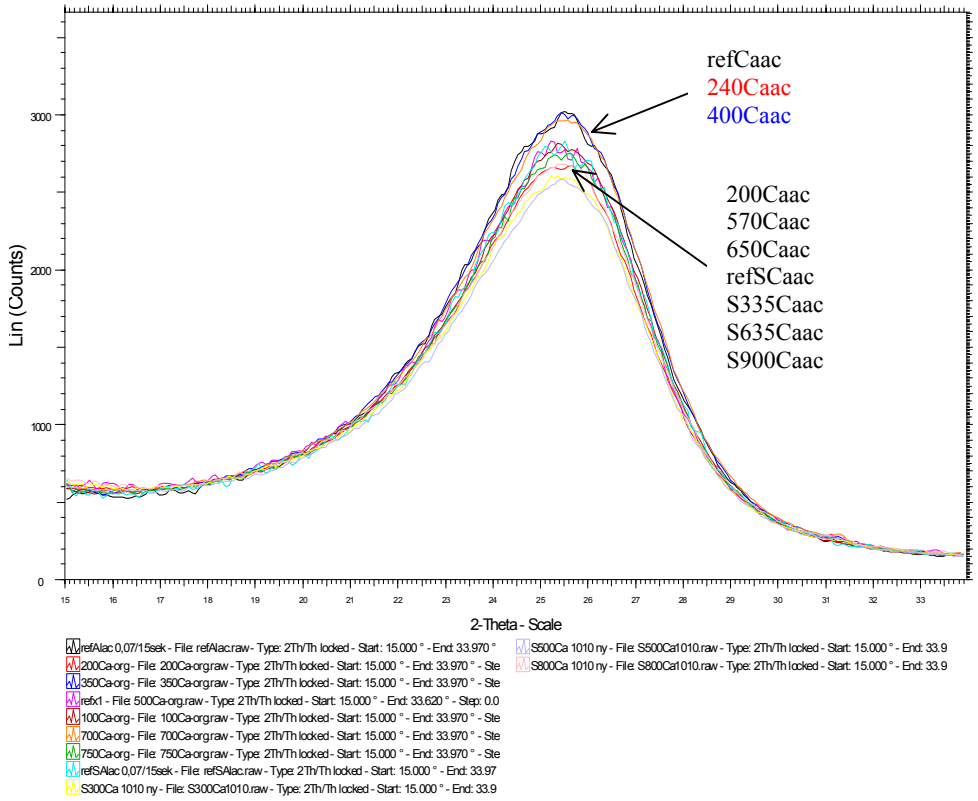

Figure 5.10 Graphite 002 diffraction peak, cokes doped with calcium acetylacetonate

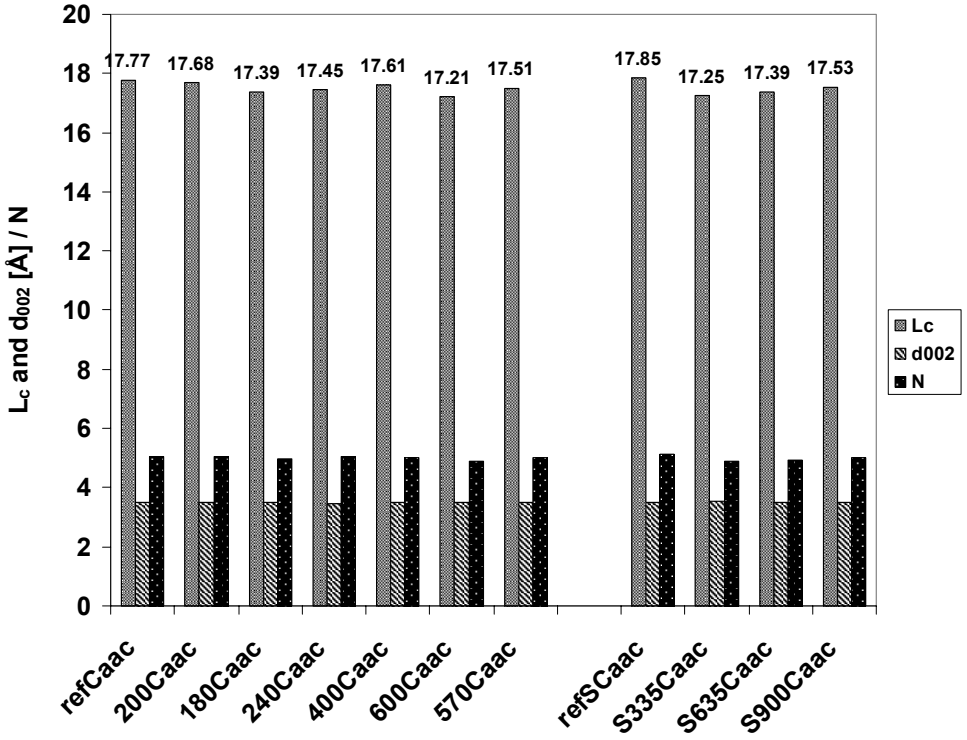

Figure 5.11 Coherent stacking height (L_c), distance between graphene layers (d_{002}) and average number of graphene layers in a coherent domain (N). *Variance between two parallel measurements: L_c: < 0.0016, d_{002}: < 0.000016*

There is no statistically significant difference between the "low"-sulfur and the "high"-sulfur cokes. The pure reference cokes (refCaac and refSCaac) seem to have slightly higher L_c-values than the doped samples. However, there is no correlation between the structure parameters and the amount of calcium acetylacetonate added.

5.2 Cokes doped with calcium fluoride

Three series of calcium fluoride doped cokes were prepared by the method described in chapter 3.1.4. To the first series (labeled "CaF2"), a pro analysis quality calcium fluoride (purity > 99 %) was added. A suprapure calcium fluoride (99.95 %) was used as an additive in the second series (labeled "2-CaF2"). "High"-sulfur cokes ("S 2-CaF2") were made by concurrent additions of suprapure CaF_2 and dibenzothiophene. An overview of some of the samples is given in Table 5-2.

Table 5-2 Cokes doped with calcium fluoride.
DBT = dibenzothiophene

Sample	Additions	Analyzed dopant content calcined cokes			
		Ca	Na	F	S
			ppm		*wt%*
500CaF2.1	0.11 wt% CaF_2 (p.a.)	780	90		
500CaF2.2		220	55	200	
500CaF2.3		380	20		
500CaF2.4		80	25	600	
750CaF2.1	0.17 wt% CaF_2 (p.a.)	940	60		
750CaF2.2		400	35	300	0.43
750CaF2.3		850	20		
750CaF2.4		1390	30	1200	0.44
2-750CaF2.1	0.18 wt% CaF_2 (suprapure)	1550	25		
2-750CaF2.2		960	15	900	0.45
2-750CaF2.3		210	10	200	0.40
2-750CaF2.4		135	10		
2-1000CaF2.1	0.25 wt% CaF_2 (suprapure)	1860	25		
2-1000CaF2.2		765	20	700	
2-1000CaF2.3		590	10	500	
2-1000CaF2.4		375	10		
S 2-1000CaF2.1	0.23 wt% CaF_2 (suprapure) + 4.5 wt% DBT	1250	25	1000	1.28
S 2-1000CaF2.2		720	10	700	0.76
S 2-1000CaF2.3		815	10	800	0.68
S 2-1000CaF2.4		775	10	800	0.72

Between 80 and 85 percent of the fluorine added (as calcium fluoride) remains in the calcined coke samples. The F/Ca mole ratio varies between 1.6 and 2 indicating a slight fluorine deficiency compared to the calcium content. X-ray diffraction analyses reveal that fluorite is the main crystalline phase within the calcined coke-matrix (see Figure 5.12). Both pure calcium fluoride and calcium fluoride particles containing 10 – 15 atomic percent oxygen were found at the surface of the calcined cokes (particles analyzed by EDX, see micrograph given in Figure 5.13). Compared to the "low"-sulfur cokes, there was no enrichment of sulfur in the particles at the surface of the "high"-sulfur cokes.

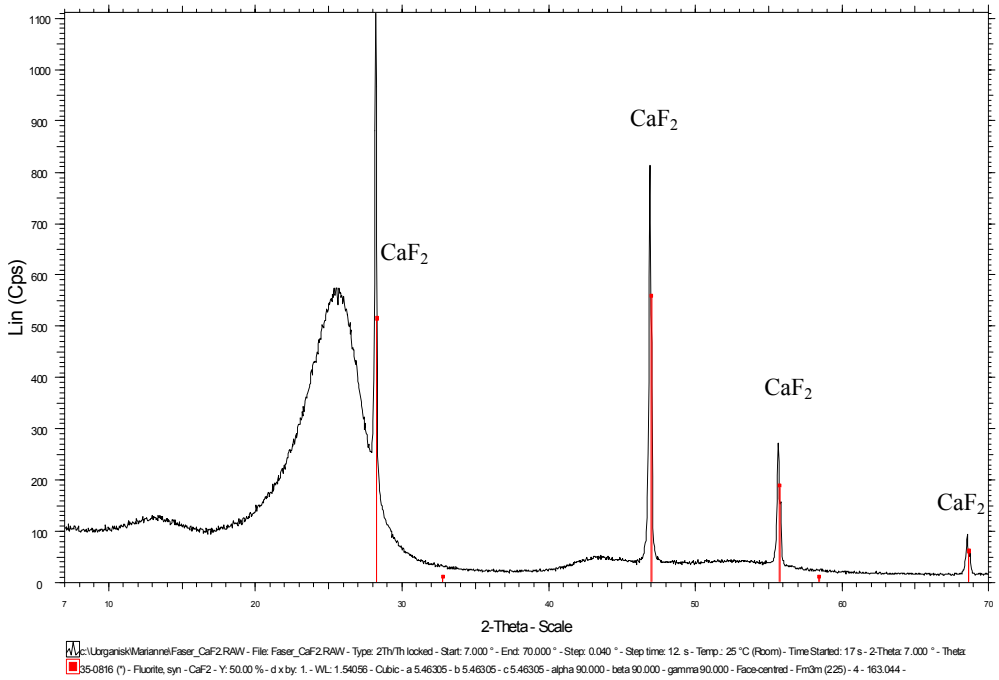

Figure 5.12 XRD-diffractogram, coke doped with calcium fluoride. *Broad peak at 2θ ~ 25° is identified as the graphite 002 diffraction peak*

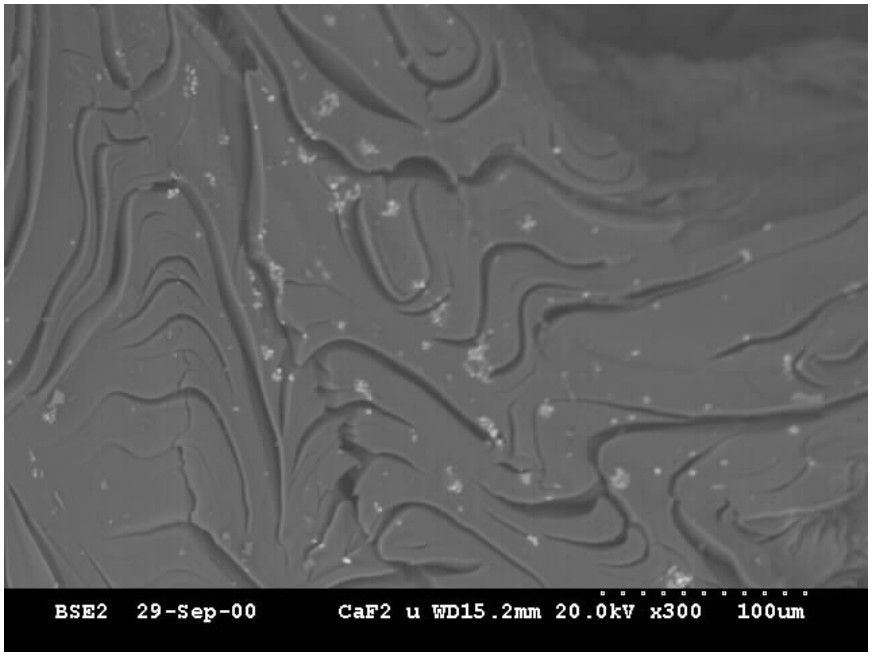

Figure 5.13 Calcium fluoride particles (light gray) on surface of coke doped with calcium fluoride. *SEM-micrograph, backscatter detector*

5.2.1 Air and CO_2 reactivity

As seen from Figure 5.14, calcium fluoride catalyzes the CO_2 gasification reaction strongly. Compared to calcium oxide, calcium fluoride retains its dispersion to higher catalyst loadings and the system does not reach saturation before at about 900 ppm Ca. There is no difference between the cokes doped with p.a. quality CaF_2 (CaF2) and those doped with suprapure CaF_2 (2-CaF2). The additions of dibenzothiophene do not affect the CO_2 reactivities of the calcium fluoride doped cokes.

As seen from the SEM-micrograph given in Figure 5.15, the topographical changes are similar to those observed for the Ca-acetylacetonate doped cokes. Calcium fluoride particles (containing 10 – 15 at% oxygen) are found in the bottom of many of the pits. There is no detectable enrichment of sulfur in the particles at the surface of the "high"-sulfur cokes.

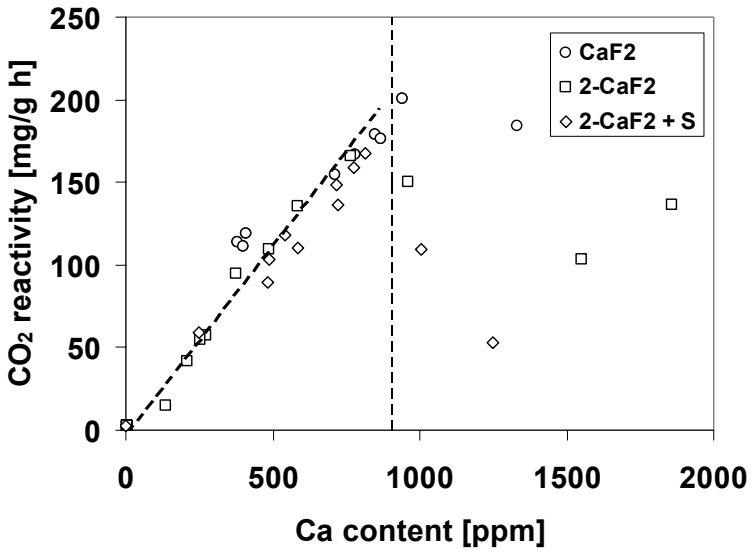

Figure 5.14 CO_2 reactivity (960 °C) of calcium fluoride doped cokes *vs.* analyzed calcium content. *Average values of two parallel measurements. Standard deviations < 1.2 mg/g·h*

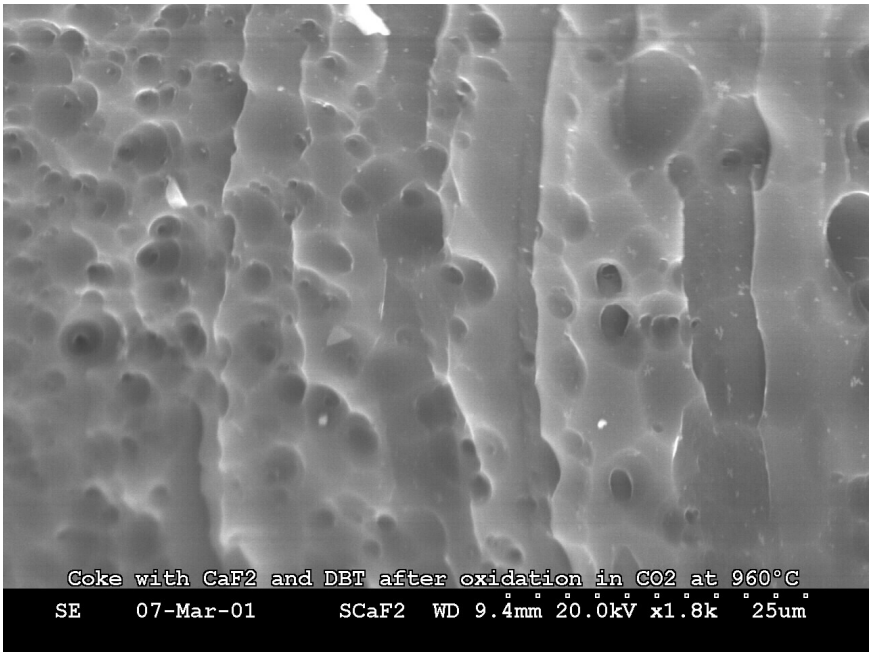

Figure 5.15 Surface of calcium fluoride doped coke after oxidation in CO_2 for 190 minutes (960 °C), pit formation. *Calcium fluoride particles found in bottom of pits*

As seen from Figure 5.16, the air reactivities of the 2-CaF2 cokes (doped with suprapure CaF_2) increase slightly with the increasing calcium concentrations. There is no significant difference between the "high"-sulfur and the "low"-sulfur cokes. For the cokes doped with the p.a. quality calcium fluoride (CaF2), there appears to be no correlation between the air reactivities and the analyzed calcium concentrations.

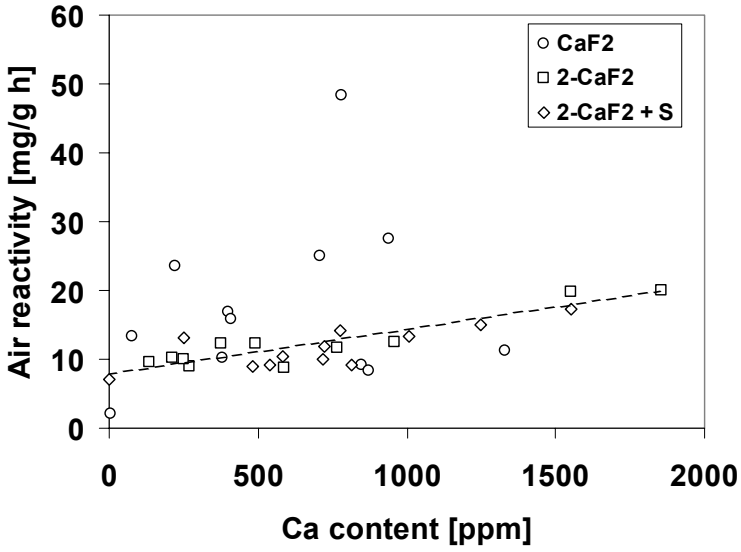

Figure 5.16 Air reactivity (525 °C) of calcium fluoride doped cokes *vs.* analyzed calcium content. *Average values of two parallel measurements. Standard deviations < 0.9 mg/g·h*

Chemical analyses reveal that the p.a. quality CaF_2 is contaminated by small amounts of sodium (~ 0.02 %), silicon (~ 0.06 %) and iron (~ 0.03 %). As a consequence the CaF2 cokes contain considerably more of these elements than the cokes doped with suprapure CaF_2 (2-CaF2) (see Table 5-3). Especially iron and sodium act as strong air gasification catalysts and it is believed that the catalytic effect of even small amounts of these elements is able to totally suppress the weak catalytic activity of calcium. As seen from Table 5-4 and Figure 5.17 there is a strong correlation between the air reactivities of the CaF2-cokes and their sodium contents.

Table 5-3 Average metal impurity level in cokes doped with calcium fluoride

	Na	Mg	Al	Si	K	V	Fe	Ni	Zn	Pb
					ppm					
CaF2	40 ± 20	12 ± 4	10 ± 3	33 ± 17	1	7 ± 1	80 ± 40	3 ± 1	1	7 ± 1
2-CaF2	20 ± 19	11 ± 5	8 ± 3	6 ± 2	1	6 ± 1	40 ± 30	2 ± 1	1	6 ± 3
S 2-CaF2	25 ± 20	10 ± 3	14 ± 8	35 ± 20	1	7 ± 3	53 ± 26	3 ± 2	3 ± 1	6 ± 3

Table 5-4 Reactivity-impurity correlation matrix, cokes doped with various amounts of p.a. quality CaF_2

	Na	Si	Ca	Fe	R(Air)	$R(CO_2)$
Na	-					
Si	0.05	-				
Ca	-0.01	0.76	-			
Fe	-0.11	0.90	0.87	-		
R(Air)	**0.97**	0.29	**0.05**	**-0.08**	-	
$R(CO_2)$	0.27	0.78	**0.88**	0.79	0.18	-

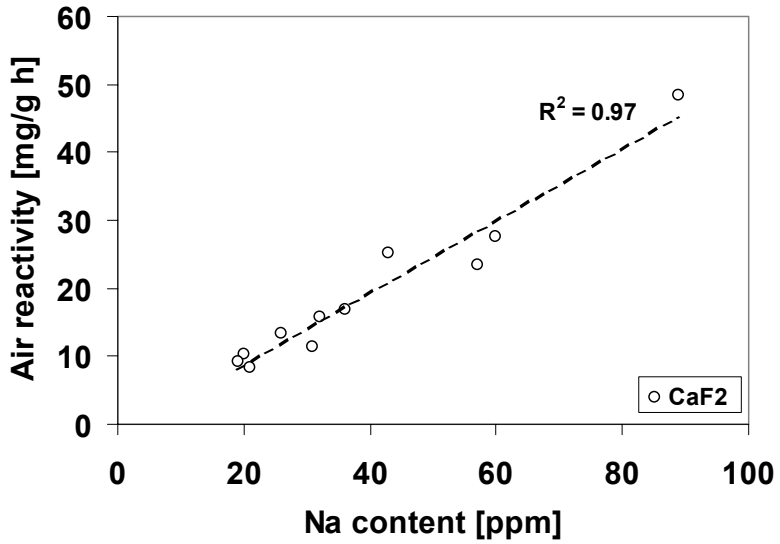

Figure 5.17 Air reactivity (525 °C) *vs.* sodium content, cokes doped with various amounts of p.a. quality CaF_2

However, from Figure 5.17 it is observed that at a given sodium concentration, the air reactivity of a CaF2-coke is about 5 times higher than the air reactivity of a similar coke doped with sodium fluoride (see Figure 4.16). As will be shown in chapter 6, there are no cocatalytic effects between calcium and sodium. The high apparent catalytic activity of sodium is therefore not caused by the concurrent presence of calcium fluoride.

An important point that should taken into consideration, is the different reaction temperature used when measuring the air reactivities of the sodium fluoride and the calcium fluoride doped cokes (475 ° *vs.* 525 °C). In order to study the effect of temperature on the sodium activity towards air gasification, some of the sodium acetylacetonate doped coke samples were oxidized at both 475 °C and 525 °C. The results are shown in Figure 5.18. At 525 °C the gasification rate appears to be controlled by mass transport limitations at sodium concentrations above approximately 200 ppm. Linear regression analysis in the chemically

controlled zones reveals that the apparent activity of sodium (graph slope) is about seven times higher at 525 °C than at 475 °C. Presumably, this temperature effect explains the high activity of sodium in the p.a. quality CaF_2-cokes.

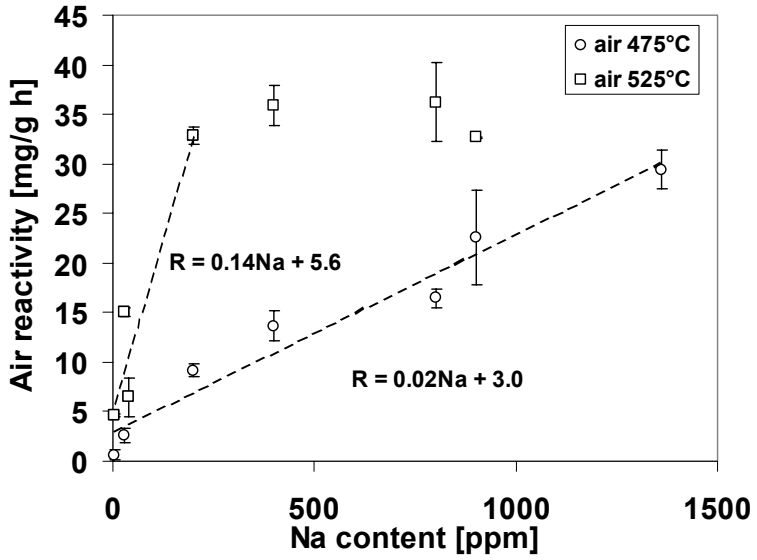

Figure 5.18 Effect of reaction temperature on air reactivity of cokes doped with sodium acetylacetonate

A SEM-micrograph showing the surface of a calcium fluoride doped coke grain after gasification in air is given in Figure 5.19. The surface is less oxidized than after gasification in CO_2. Signs of selective oxidation like pitting and channeling are scarce. Large clusters of calcium fluoride particles containing as much as 30 at% oxygen are located in the oxidized areas. Some particles have poor contact with the carbon surface, while others seem to be catalytically active.

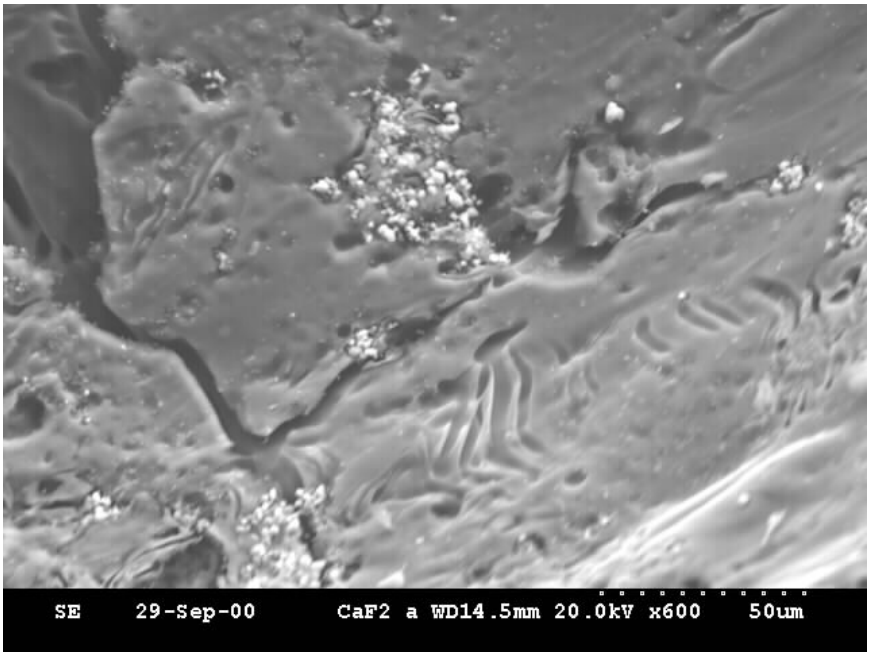

Figure 5.19 Surface of calcium fluoride doped coke after oxidation in air for 190 minutes (525 °C). *Clusters of calcium fluoride particles (light) in oxidized areas*

5.2.2 Optical texture and turbostratic structure

Figure 5.20 and Figure 5.21 show the calculated mosaic and fiber indexes of some of the calcium fluoride doped cokes. In general, the cokes are coarser and more homogeneous than the calcium acetylacetonate doped cokes. Due to a gradually enrichment of non-soluble inorganic compounds, the texture gets slightly finer when moving upwards in a coke sample (from slice 4 to slice 1, see Figure 3.5). However, the variation is small ($\Delta MI_{max.} = 0.005$) and is believed not to have any significant influence on the measured coke reactivities.

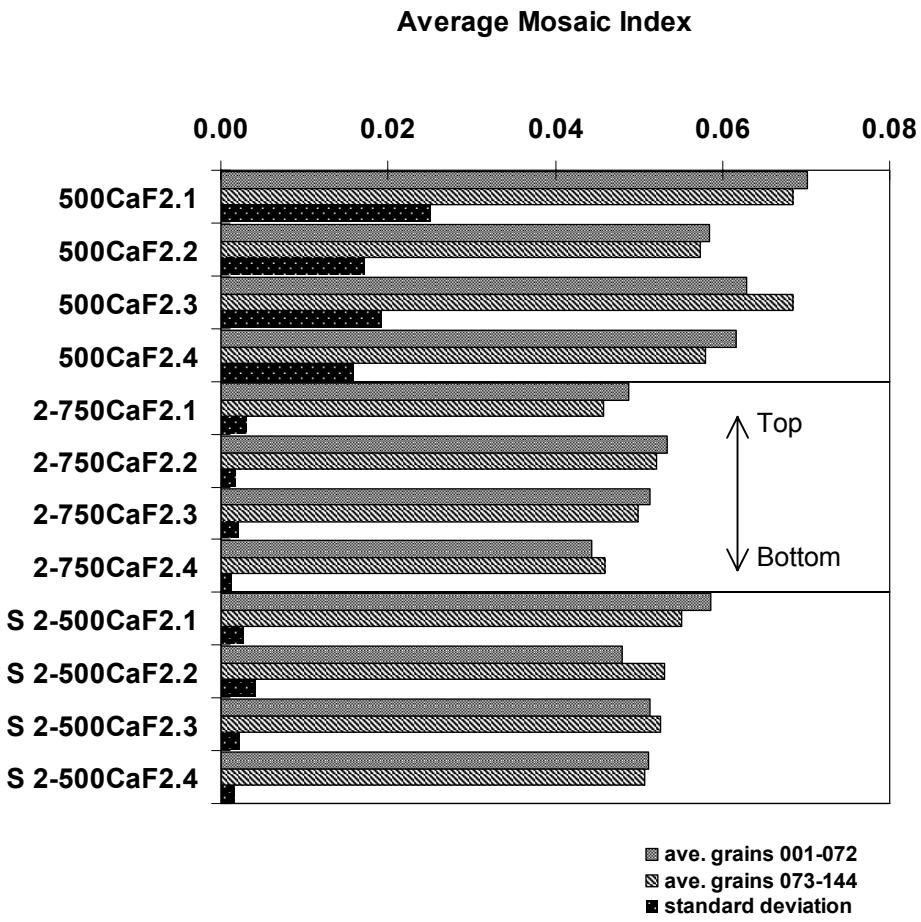

Figure 5.20 Mosaic Index, cokes doped with calcium fluoride. *Average of two halves of analyzed grains with standard deviation*

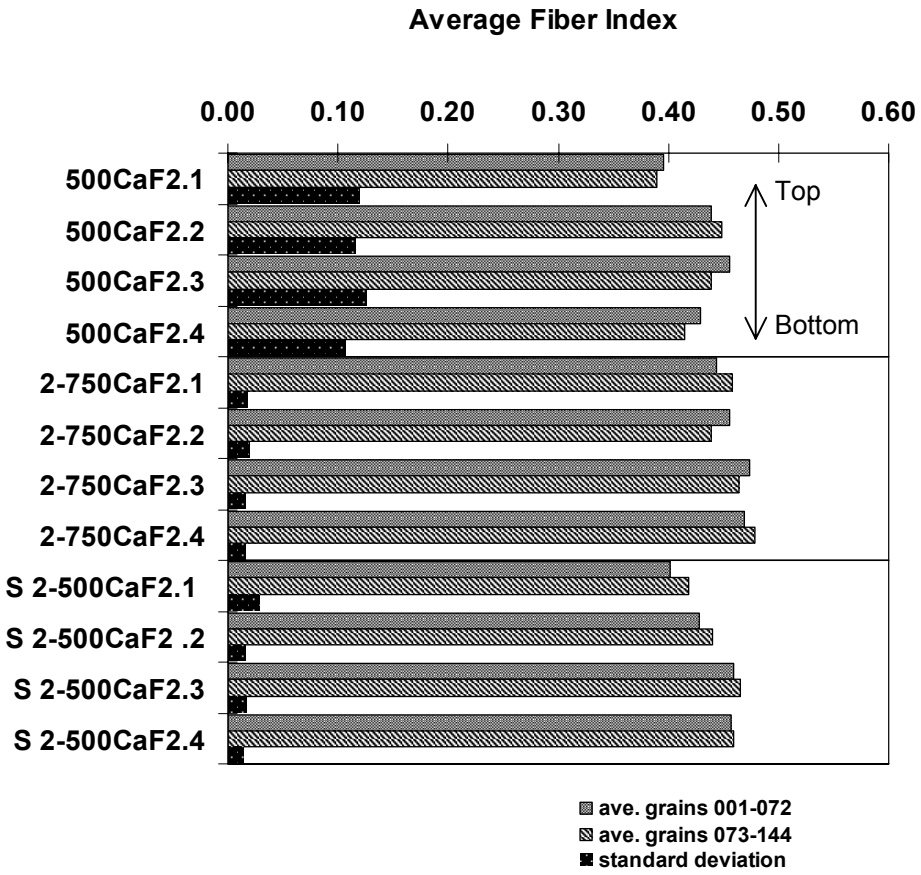

Figure 5.21 Fiber Index, cokes doped with calcium fluoride. *Average of two halves of analyzed grains with standard deviation*

The measured L_c, d_{002} and N-values are given in Figure 5.22 below. As for the calcium acetylacetonate doped cokes, the difference between the coke samples is negligible.

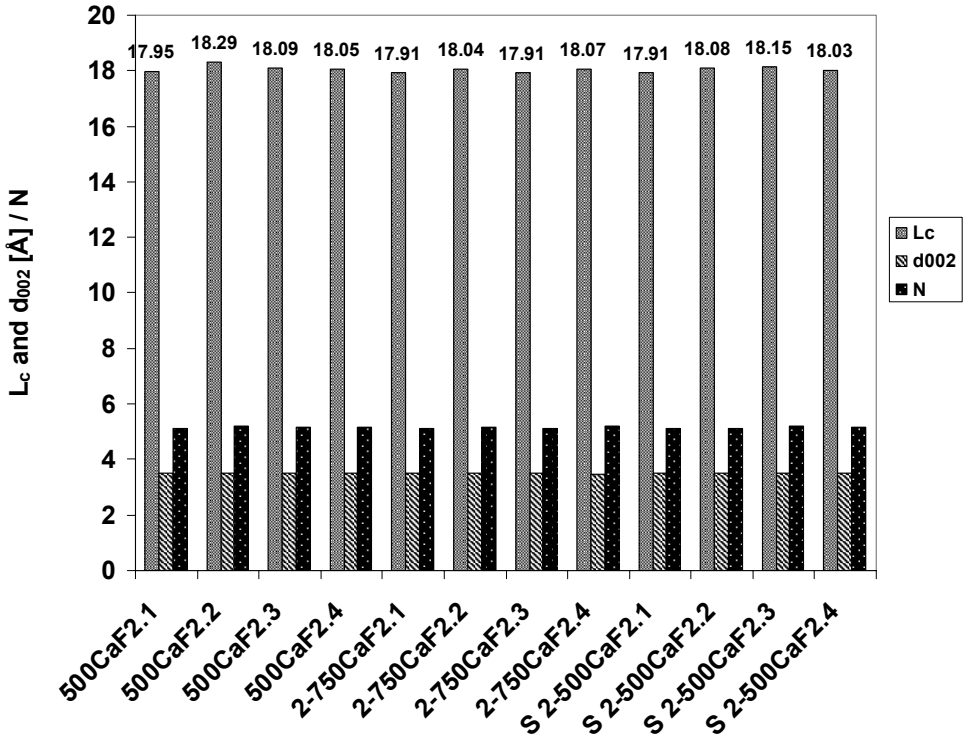

Figure 5.22 Coherent stacking height (L_c), distance between graphene layers (d_{002}) and average number of graphene layers in a coherent domain (N). *Variance between two parallel measurements: L_c: < 0.0016, d_{002}: < 0.000016*

5.3 Mechanistic considerations

5.3.1 Catalytic activity of calcium oxide

As analyzed by X-ray diffraction, calcium acetylacetonate decomposes completely to calcium carbonate and calcium oxide during preparation of the coke samples (see Figure 5.1). In the literature several mechanisms have been proposed to explain the catalysis of the carbon-CO_2 gasification reaction by alkaline earth oxides and carbonates and CaO is by many identified as the catalytically active species [41, 46, 56, 57, 59-61, 66, 80-82] (see review in chapter 2.2.2).

As seen from the free energy changes of reaction 5.1 and 5.2, $CaCO_3$ is not stable at the CO_2 gasification temperatures.

$CaCO_3 \Leftrightarrow CaO + CO_2\ (g)$ $\Delta G^0_{960°C} = -9.7$ kJ/mol **Eq. 5.1**

$CaCO_3 + C \Leftrightarrow CaO + 2\ CO\ (g)$ $\Delta G^0_{960°C} = -54.6$ kJ/mol **Eq. 5.2**

Hence, during the initial stages of gasification, it is believed that any calcium carbonate present on the coke surface will decompose to calcium oxide. Most likely the calcium oxide particles catalyze the CO_2 gasification reaction in the same way as the sodium oxide particles, *i.e.* by first providing sites for dissociative adsorption of CO_2 and thereby redistribute the adsorbed oxygen atoms to the carbon surface (see mechanism in Figure 4.28).

As seen from Figure 5.3, the air reactivity of the calcium acetylacetonate doped cokes is barely influenced by the increasing calcium concentrations. The following reasons seem plausible:

1. Lack of neighboring active sites. Dissociative adsorption of O_2 requires two neighboring active sites at the catalyst surface (see Eq. 2.35 and Figure 4.29). Adsorption of CO_2 on the other hand involves only one active site per CO_2 molecule.

2. Temperature effect. The low air gasification temperature may influence the catalytic activity in the following ways: (a) Few catalytically active calcium oxide clusters are formed at the air gasification temperature (high stability of $CaCO_3$; Eq. 5.1: $\Delta G^0_{525°C}$ = 84.8 kJ/mol, Eq. 5.2: $\Delta G^0_{525°C}$ = 53.7 kJ/mol). (b) The concentration of active sites on the CaO surface is temperature dependent. Probably, the concentration increases with increasing temperature. (c) Low mobility of adsorbed oxygen atoms on the catalyst surface. (d) Low mobility of catalyst particles on the carbon surface.

The experimental data of this work give no basis to either confirm or reject one of the above mechanisms. However, since other workers have reported a moderate catalytic activity of calcium oxide at higher temperatures (> 650 °C) [64, 66, 67], the low activity observed in this work is believed to mainly be determined the relatively low air gasification temperature.

5.3.2 Catalytic activity of calcium fluoride

Calcium fluoride is extremely stable ($\Delta G_{f\ 1000\ °C}^{0}$ = -1012.8 kJ/mol) and a bulk chemical transformation of calcium fluoride into *e.g.* calcium oxide or calcium carbonate is hence not likely. As seen from the stability diagram given in Figure 5.23, only a small calcium evaporation loss might be expected during calcination of the calcium fluoride doped coke samples to 1010 °C (activities at 1010 °C are tabulated in Table 5-5). At temperatures above 850 °C, some metallic calcium, CF_4 (g) and COF_2 (g) are formed.

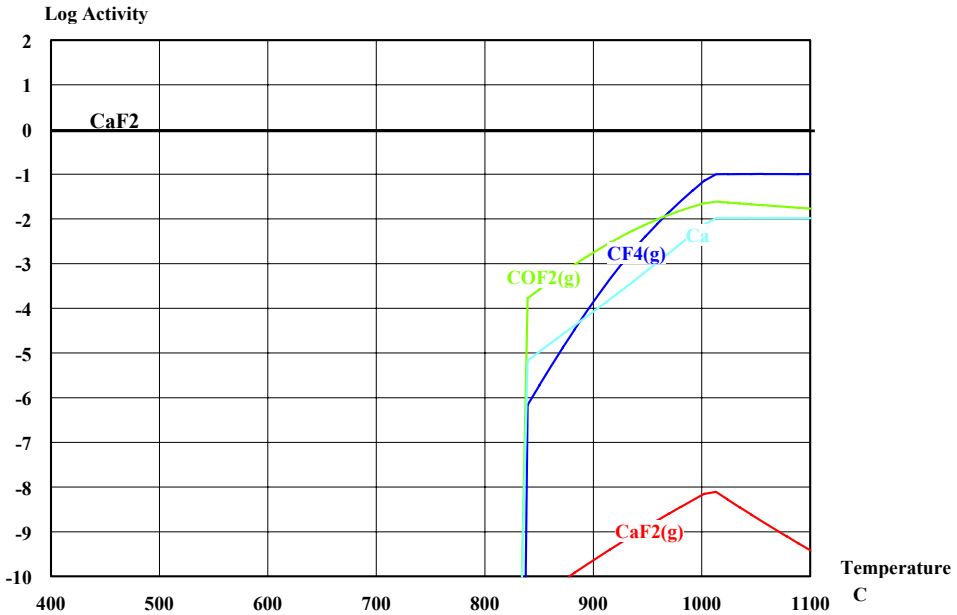

Figure 5.23 Calculated activities (logarithmic) *vs.* temperature, calcination of cokes doped with calcium fluoride. *Calculated by use of HSC Chemistry* © [79]. *Initial conditions: T = 25 °C, p_{O2} = 0.2 atm, p_{N2} = 0.8 atm, c_{CaF2} = 0.25 wt%, excess carbon. Activities of C, O_2, CO and CO_2 are not shown, CO dominates at temperatures above 700 °C*

Table 5-5 Calculated activities of most stable solid and gaseous species at maximum calcination temperature (1010 °C), cokes doped with calcium fluoride. *Calculated by use of HSC Chemistry* © [79]. *Initial conditions: T = 25 °C, p_{O2} = 0.2 atm, p_{N2} = 0.8 atm, c_{CaF2} = 0.25 wt%, excess carbon. Activities of C, O_2, CO and CO_2 are not given.*

Species	**Log Activity** *1010 °C*
CaF_2 (s)	0
Ca (s)	-2.0
CF_4 (g)	-1.0
COF_2 (g)	-1.7
CaF_2 (g)	-8.5
Sum gas phase activities	-0.9
Sum activities gaseous Ca species	-8.5
Sum activities gaseous F species with polar oxygen groups (COF_2)	-1.7

As seen from the free energy changes of Eq. 5.3 and 5.4 below, calcium fluoride is also stable at the air and CO_2 gasification conditions. In the same way as for sodium fluoride and cryolite, is it therefore believed that calcium fluoride catalyzes the gasification reactions directly and not via an intermediate oxide phase. CO_2 and O_2 adsorb dissociatively on the active sites at the surface of the calcium fluoride particles and the adsorbed oxygen atoms diffuse easily over the catalyst surface before they are redistributed to the active carbon sites. Chemical analyses reveal that about 20 % calcium is lost through evaporation during the CO_2 reactivity measurements whereas no calcium is lost during the air reactivity tests.

$$CaF_2 + \tfrac{1}{2}\,O_2\,(g) \Leftrightarrow CaO + F_2\,(g) \qquad \Delta G^0_{525°C} = 537.7\ \text{kJ/mol} \quad \textbf{Eq. 5.3}$$

$$CaF_2 + 2\,CO_2\,(g) \Leftrightarrow CaCO_3 + COF_2\,(g) \qquad \Delta G^0_{525°C} = 347.7\ \text{kJ/mol} \quad \textbf{Eq. 5.4}$$

6 Cocatalytic effects of sodium and calcium

In order to investigate whether the apparent catalytic activity of sodium is influenced by the concurrent presence of calcium and *vice versa*, cokes doped with both sodium and calcium acetylacetonate were prepared from the tar oil. The calcium concentration was varied in three steps between 0 and 635 ppm, while the sodium concentration was varied between 0 and 800 ppm. An overview of the coke samples is given in Table 6-1.

Table 6-1 Cokes doped with sodium acetylacetonate and calcium acetylacetonate.
Na-ac = Na acetylacetonate, Ca-ac = Ca acetylacetonate

Sample	Additions	Analyzed dopant content calcined cokes	
		Na	Ca
		ppm	
refcoke	-	3	2
0Naac-200Caac [1]	0 wt% Na-ac, 0.05 wt% Ca-ac	5	200
0Naac-570Caac [1]	0 wt% Na-ac, 0.34 wt% Ca-ac	4	570
200Naac-0Caac [1]	0.11 wt% Na-ac, 0 wt% Ca-ac	200	1
400Naac-0Caac [1]	0.22 wt% Na-ac, 0 wt% Ca-ac	400	2
800Naac-0Caac [1]	0.44 wt% Na-ac, 0 wt% Ca-ac	800	6
180Naac-270Caac	0.09 wt% Na-ac, 0.10 wt% Ca-ac	180	270
350Naac-270Caac	0.18 wt% Na-ac, 0.10 wt% Ca-ac	350	270
565Naac-225Caac	0.35 wt% Na-ac, 0.09 wt% Ca-ac	565	225
155Naac-580Caac	0.09 wt% Na-ac, 0.29 wt% Ca-ac	155	580
350Naac-635Caac	0.18 wt% Na-ac, 0.30 wt% Ca-ac	350	635
600Naac-635Caac	0.35 wt% Na-ac, 0.30 wt% Ca-ac	600	635

[1] Samples from work investigating the individual effect of Ca and Na-acetylacetonate.

The 3-D graphs given in Figure 6.1 and Figure 6.2 show the measured air and CO_2 reactivities plotted as a function of the analyzed sodium and calcium concentrations.

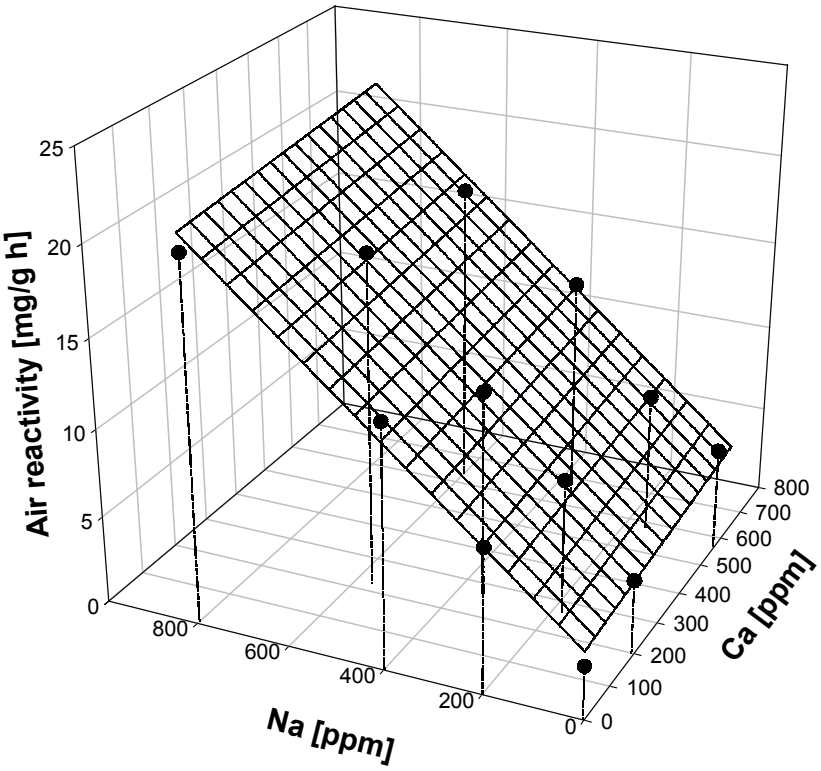

Figure 6.1 Air reactivity (475 °C) of cokes doped with sodium and calcium acetylacetonate *vs.* analyzed sodium and calcium content. *Average values of four parallel measurements. Standard deviations < 1.3 mg/g·h*

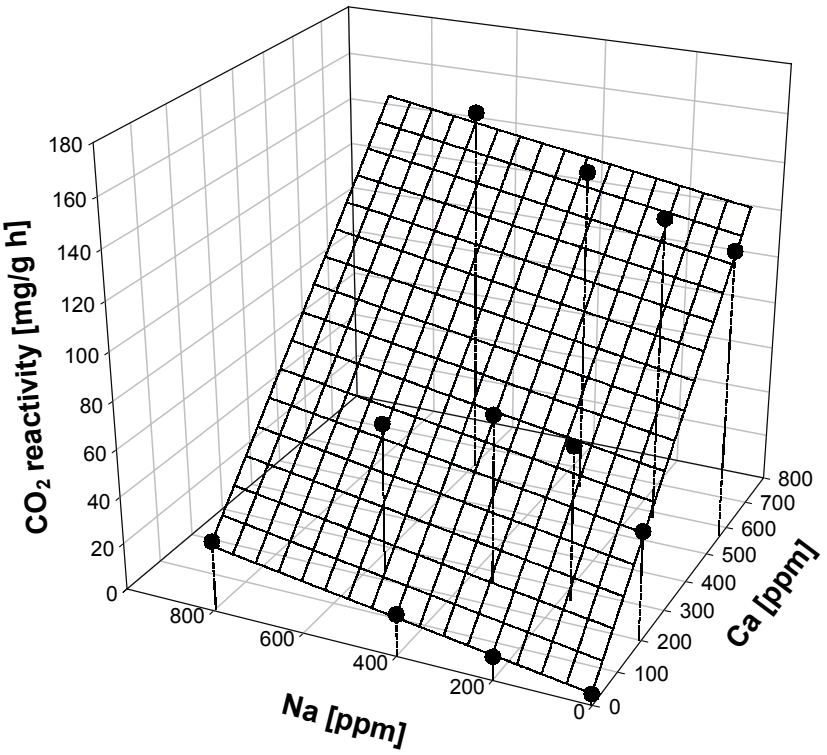

Figure 6.2 CO_2 reactivity (960 °C) of cokes doped with sodium and calcium acetylacetonate *vs.* analyzed sodium and calcium content. *Average values of four parallel measurements. Standard deviations < 1.0 mg/g·h*

The air reactivity increases strongly with the increasing sodium concentrations, but is barely affected by the increasing calcium concentrations. The CO_2 reactivity on the other hand, is dominated by the calcium content. 3D-plane regression analysis (least squares method) gives the following equations:

$$R_{air} = 0.022 \cdot x_{Na} + 0.003 \cdot x_{Ca} + 3.75 \qquad R^2 = 0.97 \qquad \text{Eq. 6.1}$$

$$R_{CO2} = 0.029 \cdot x_{Na} + 0.205 \cdot x_{Ca} + 4.45 \qquad R^2 = 0.98 \qquad \text{Eq. 6.2}$$

where x_{Na} and x_{Ca} are the analyzed sodium and calcium concentrations (ppm).

From the reactivity *vs.* dopant concentration plots presented in the preceding chapters (Figure 4.3-4.4 and Figure 5.3-5.4) the following regression equations are obtained:

Na:

$$R_{air} = 0.021 \cdot x_{Na} + 2.83 \qquad R^2 = 0.96 \qquad \text{Eq. 6.3}$$

$$R_{CO2} = 0.032 \cdot x_{Na} + 3.62 \qquad R^2 = 0.98 \qquad \text{Eq. 6.4}$$

Ca:

$$R_{air} = 0.004 \cdot x_{Ca} + 3.50 \qquad R^2 = 0.85 \qquad \text{Eq. 6.5}$$

$$R_{CO2} = 0.207 \cdot x_{Ca} + 4.32 \qquad R^2 = 0.91 \text{ (linear part only)} \qquad \text{Eq. 6.6}$$

The regression coefficients calculated from Figure 6.1 and Figure 6.2 are nearly equal to the corresponding coefficients in Eq. 6.3-6.6. It is hence concluded that there are no cocatalytic effects between sodium and calcium.

The above conclusions are in accordance with the results obtained by Hume [83]. During her Ph.D work, she characterized over 600 anode grade petroleum cokes. From statistical analyses, the following model was presented for the CO_2 reactivity:

$$R_{CO2}(\%) = 4.0 + \frac{0.0411 \cdot Na(ppm) + 0.101 \cdot Ca(ppm)}{S(\%)} \qquad \text{Eq. 6.7}$$

The air reactivity was mainly determined by the coke's sodium, vanadium and sulfur content. No cocatalytic effects were found.

7 Effect of aluminium compounds on coke reactivity

7.1 Cokes doped with aluminium acetylacetonate

In order to investigate the catalytic effect of aluminium oxide, cokes doped with various amounts of aluminium acetylacetonate were prepared by the method described in chapter 3.1.3. An overview of the coke samples is given in Table 7-1.

Table 7-1 Cokes doped with aluminium acetylacetonate.
Al-ac = aluminium acetylacetonate, DBT = dibenzothiophene

Sample	Additions	Analyzed dopant content calcined cokes	
		Al	S
		wt%	
refAlac	0 wt% Al-ac	0.0007	0.26
0.11Alac	1.2 wt% Al-ac	0.11	
0.20Alac	2.3 wt% Al-ac	0.20	0.30
0.30Alac	4.7 wt% Al-ac	0.30	0.30
0.75Alac	7.4 wt% Al-ac	0.75	0.29
0.93Alac	9.0 wt% Al-ac	0.93	
refSAlac	0 wt% Al-ac + 4.5 wt% DBT	0.0012	0.74
S0.11Alac	1.3 wt% Al-ac + 4.5 wt% DBT	0.11	0.92
S0.20Alac	2.4 wt% Al-ac + 4.5 wt% DBT	0.20	0.86
S0.46Alac	4.7 wt% Al-ac + 4.5 wt% DBT	0.46	0.90

Figure 7.1 shows the XRD pattern obtained for a coke doped with 10 weight percent aluminium acetylacetonate. As seen, only the broad graphite diffraction peaks are visible. Aluminium species are not detected and are thus believed to be well dispersed within the coke matrix. A crystallite size less than 5 nm is arbitrary assumed. This is the usually cited lower XRD detection limit for supported metal oxide catalysts [66]. However, a few particles (size 5 – 15 μm) were found at the surface of the coke samples (see SEM-micrograph given in Figure 7.2). The elemental composition of the particles corresponds to Al_2O_3 (analyzed by EDX). Thermogravimetric analysis revealed that pure aluminium acetylacetonate decomposes completely to aluminium oxide when heated to temperatures above 110 °C.

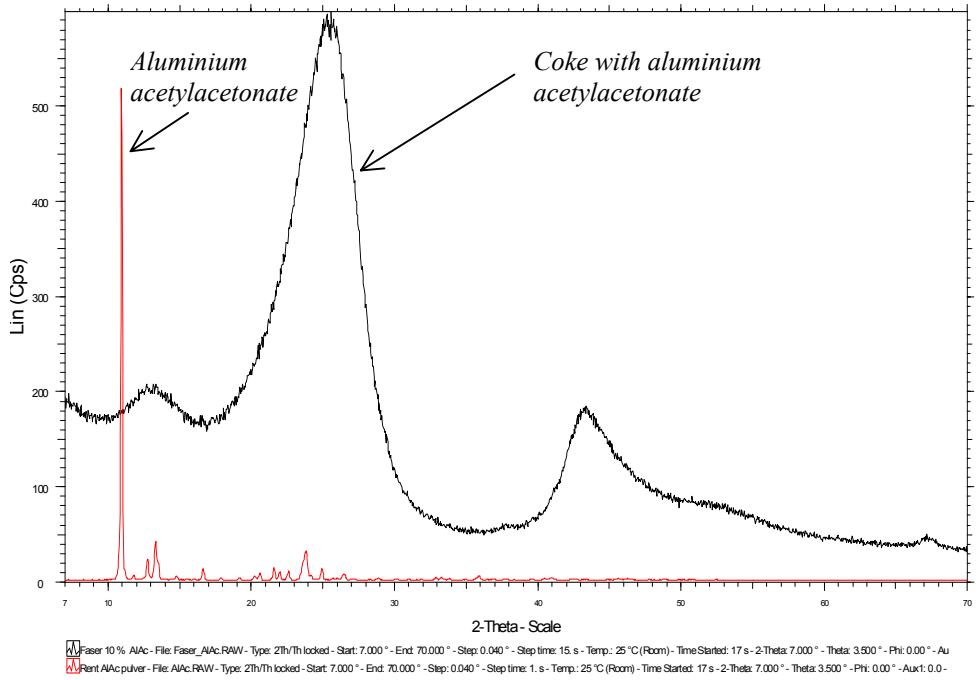

Figure 7.1 X-ray diffractogram, coke doped with aluminium acetylacetonate. *Diffractogram from analysis of aluminium acetylacetonate powder is included. Broad peaks at 2θ ~ 25 ° and 44 ° are identified as graphite 002 and 101 diffraction peaks*

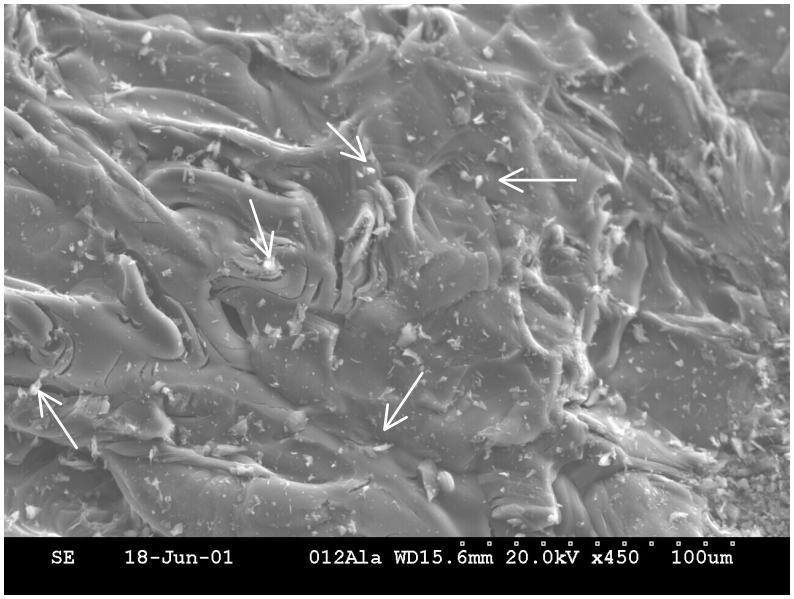

Figure 7.2 Aluminium oxide particles (light particles, see arrows) on surface of coke doped with aluminium acetylacetonate

7.1.1 Air and CO_2 reactivity

Figure 7.3 and Figure 7.4 show the air and CO_2 reactivities of the aluminium acetylacetonate doped coke samples. The reactivities are given as a function of the analyzed bulk aluminium contents.

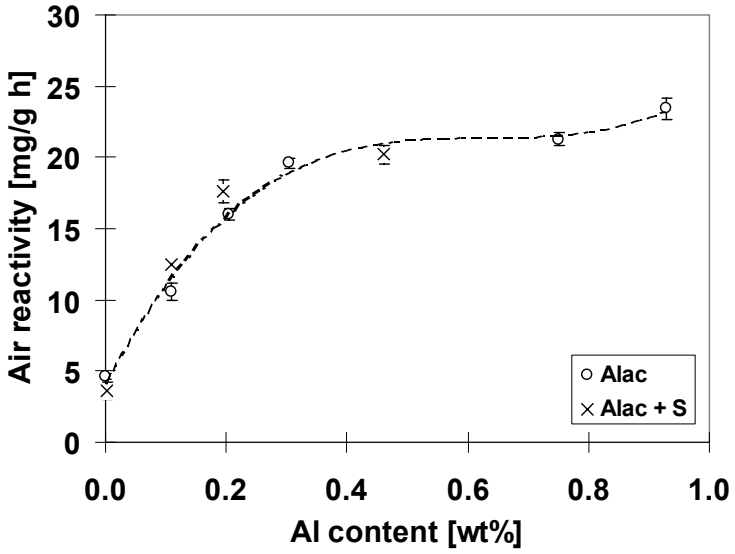

Figure 7.3 Air reactivity (525 °C) of aluminium acetylacetonate doped cokes *vs.* analyzed aluminium content. *Average values of five parallel measurements. Standard deviations represented by error bars*

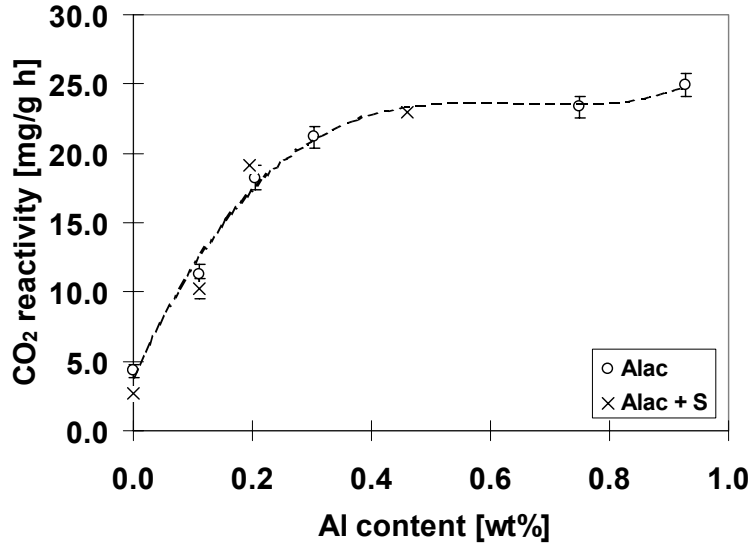

Figure 7.4 CO_2 reactivity (960 °C) of aluminium acetylacetonate doped cokes *vs.* analyzed aluminium content. *Average values of five parallel measurements. Standard deviations represented by error bars*

Aluminium oxide (from decomposition of aluminium acetylacetonate) seems to be a moderate catalyst towards the air and CO_2 gasification reactions. At low concentrations, both the air and CO_2 reactivity increase linearly with the aluminium content. However, at aluminium contents above about 0.3 weight percent, the reactivity increase diminishes. The phenomenon might be due to agglomeration of the catalyst particles or structural changes. Mass transfer limitations are believed not to be of importance since the saturation reactivities are considerably lower than the maximum reactivities measured for similar cokes doped with sodium and calcium acetylacetonate (see chapter 4.1.1 and 5.1.1). The subject will be further discussed in chapter 7.1.3.

The measured air and CO_2 reactivities are not influenced by the addition of 4.5 weight percent dibenzothiophene. Compared to the "low"-sulfur cokes, there is no enrichment of sulfur in the aluminium oxide particles at the surface of the "high"-sulfur cokes (analyzed by EDX).

A SEM-micrograph of the surface of a CO_2 oxidized coke grain is given in Figure 7.5. The carbon between the coke lamellas has been selectively gasified and the oxidized coke surface has gotten a fissured appearance. Only a few aluminium oxide particles remain at the surface of the oxidized coke grains. These are rather large (diameter ~ 20 μm) and seems to have poor contact with the carbon substrate. There are no signs of enhanced oxidation (pitting, channeling etc.) in their immediate vicinity.

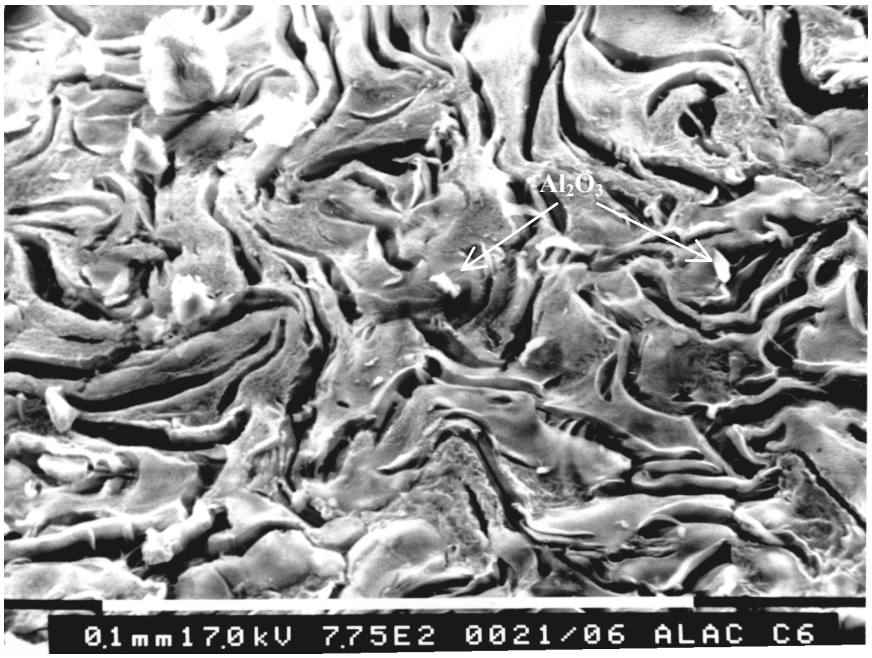

Figure 7.5 Surface of aluminium acetylacetonate doped coke grain after oxidation in CO_2 for 190 minutes (960 °C)

Previously Müftüoglu and Øye [9] have reported that the CO_2 reactivity of baked carbon anode samples is not influenced by the addition of various amounts of Al_2O_3 powder (0 – 5 wt%). The air reactivity decreased linearly with increasing Al_2O_3 content. On the other hand, Rakszawski and Parker [3] found that Al_2O_3 catalyzed the reaction between pure graphite and air/CO_2.

The disagreement between the result reported by Müftüoglu *et al.* and those obtained in this work are believed mainly to arise from different dopant dispersions within the carbon. Müftüoglu *et al.* used Al_2O_3 powder which were added during mixing of filler coke and binder pitch prior to baking. The powder grain size is not reported, but is probably between 20 and 150 μm (normal grain size of smelter alumina). This work uses aluminium acetylacetonate, which decomposes to finely dispersed aluminium oxide during the preparation of the coke samples. The aluminium oxide phase is not detectable by XRD and the grain size is hence believed to be very small (< 5 nm).

7.1.2 Optical texture and turbostratic structure

Graphs which show the calculated mosaic and fiber indexes of the aluminium acetylacetonate doped cokes are given in Figure 7.6 and Figure 7.7.

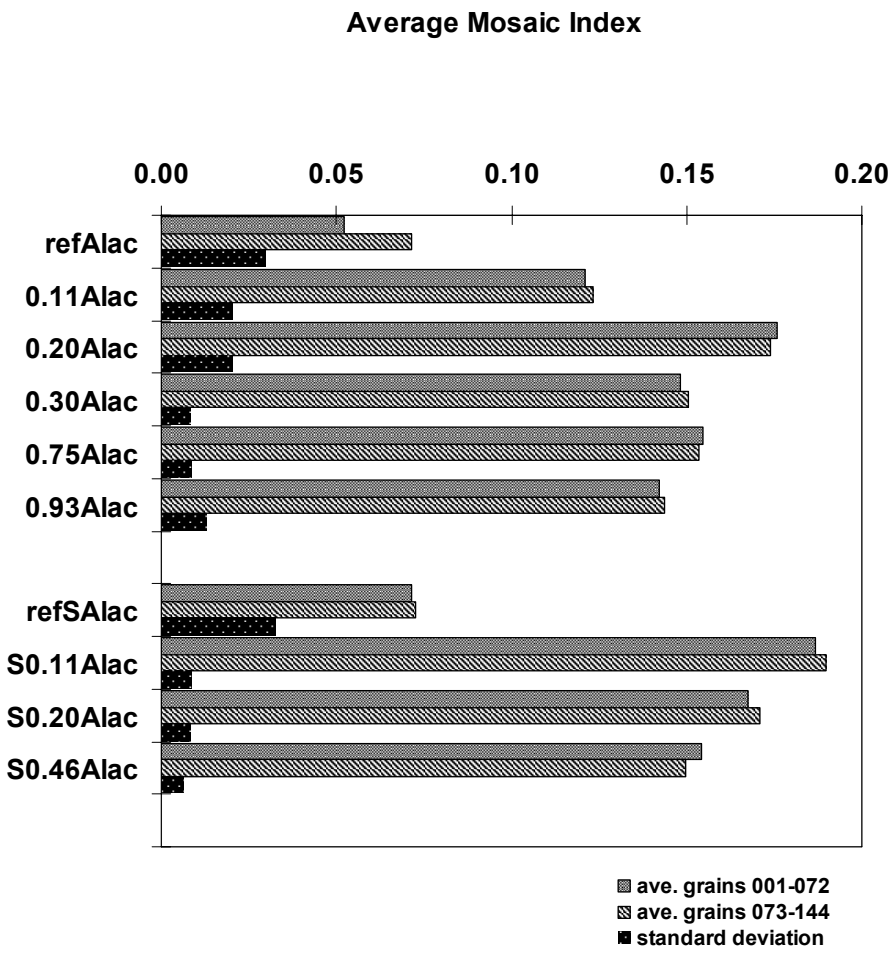

Figure 7.6 Mosaic Index, cokes doped with aluminium acetylacetonate. *Average of two halves of analyzed grains with standard deviation*

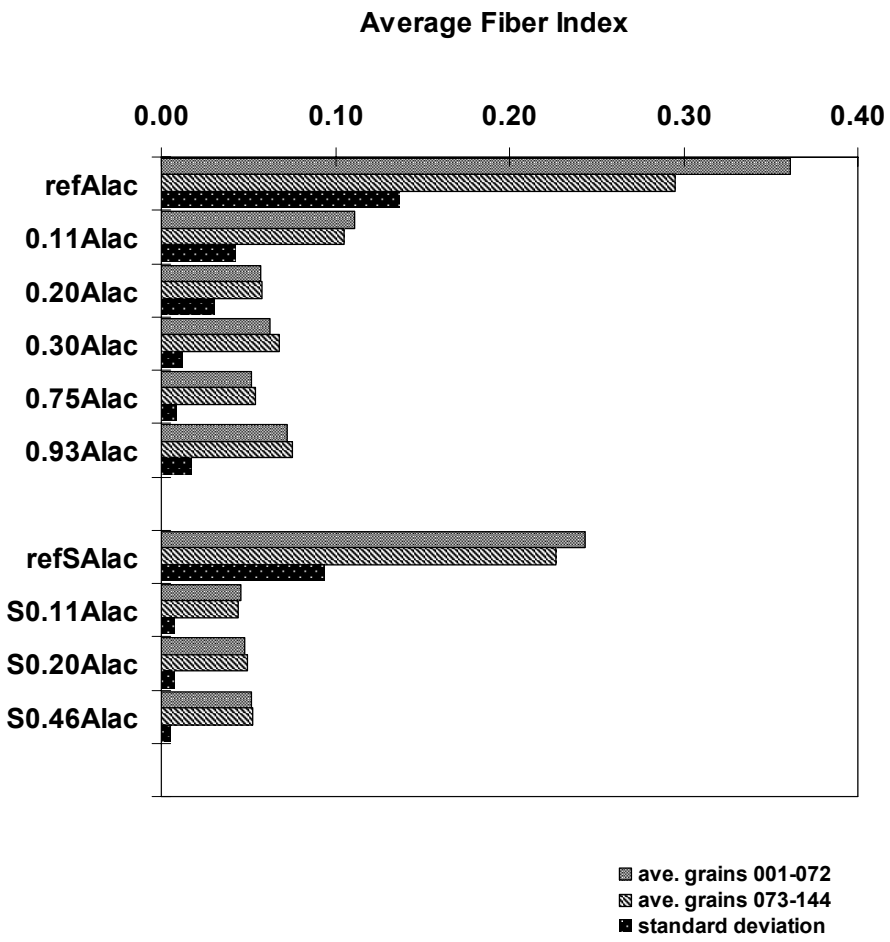

Figure 7.7 Fiber Index, cokes doped with aluminium acetylacetonate. *Average of two halves of analyzed grains with standard deviation*

In difference to the cokes doped with sodium and calcium acetylacetonate, the texture of the aluminium acetylacetonate doped cokes varies strongly with the dopant concentration. The reference coke with no additions of aluminium acetylacetonate or dibenzothiophene (refAlac) has a mosaic index of about 0.07 with a high standard deviation. Addition of 2.3 weight percent aluminium acetylacetonate to the tar oil prior to carbonization (0.20Alac) causes the mosaic index to increase to 0.18. The fiber index decreases from 0.32 to 0.06. The mosaic index decreases slightly again when more aluminium acetylacetonate is added while the fiber index remains almost constant. The same textural changes are observed for the "high"-sulfur cokes, but here the coke with 1.3 wt% aluminium acetylacetonate (S0.11Alac) has the highest mosaic index. In general, the texture of the "high"-sulfur cokes is slightly finer than the texture of the corresponding "low"-sulfur cokes.

Inspection of the micrographs given in Figure 7.8, reveals that whereas the reference cokes has developed a coarse flow-domain texture, the cokes doped with aluminium acetylacetonate mainly consist of solidified mesophase spheres. The aluminium acetylacetonate dissolves completely in the liquid tar oil and seems to affect the texture development during the carbonization heavily. Possible mechanisms are discussed in the next section.

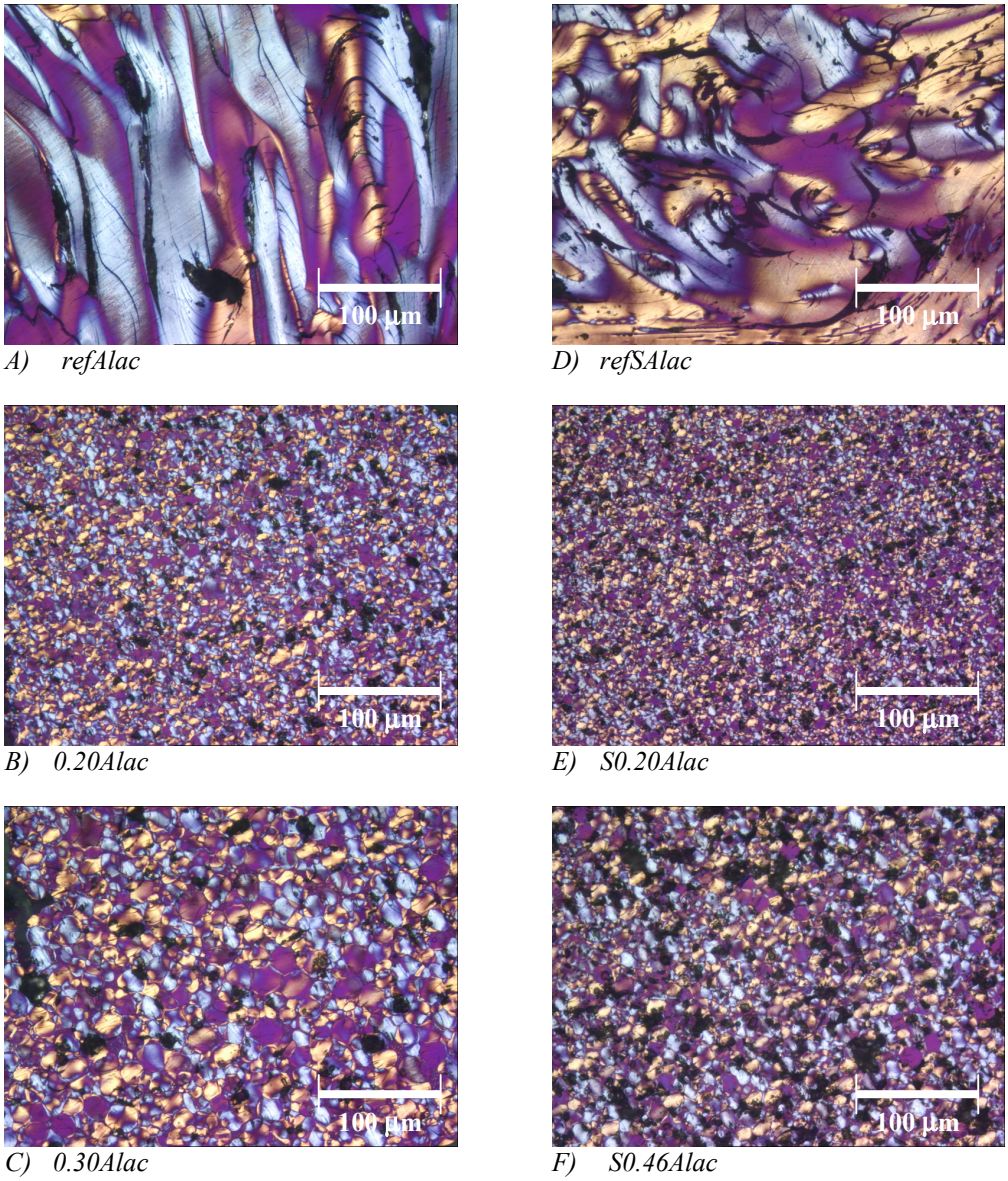

A) refAlac *D) refSAlac*

B) 0.20Alac *E) S0.20Alac*

C) 0.30Alac *F) S0.46Alac*

Figure 7.8 Optical texture of cokes doped with aluminium acetylacetonate

X-ray diffractograms showing the graphite 002 diffraction peak of the aluminium acetylacetonate doped coke samples are given in Figure 7.9. The coherent stacking heights (L_c), the distance between the graphene layers (d_{002}) and the average number of graphene layers in a coherent domain (N) are represented graphically in Figure 7.10.

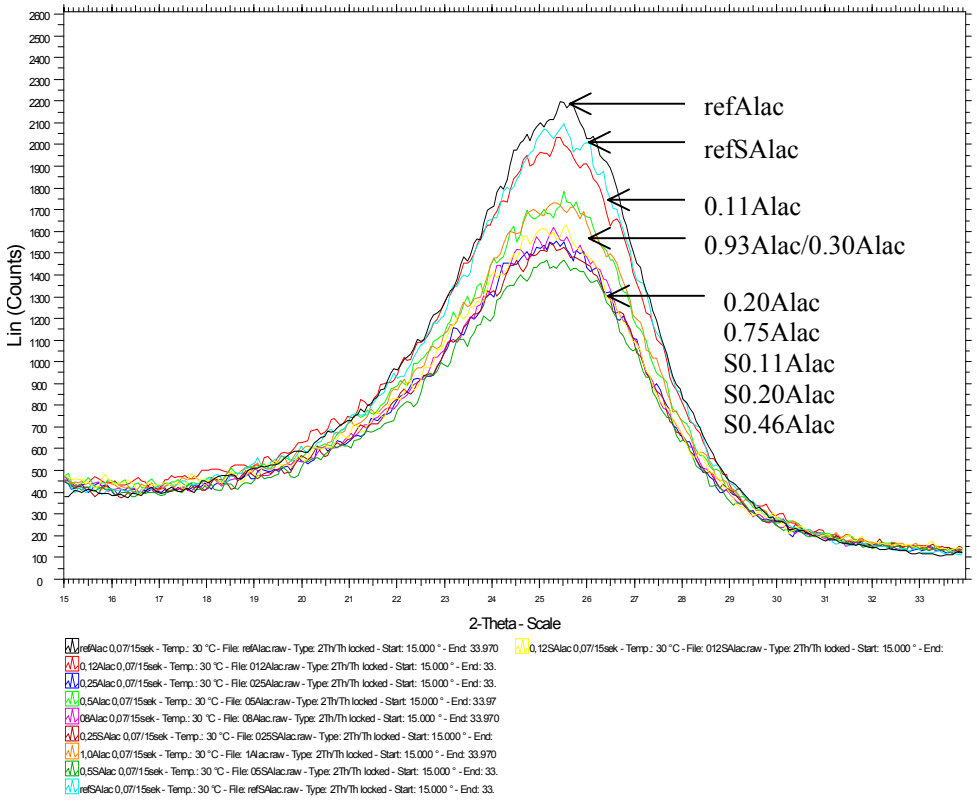

Figure 7.9 Graphite 002 diffraction peak, cokes doped with aluminium acetylacetonate

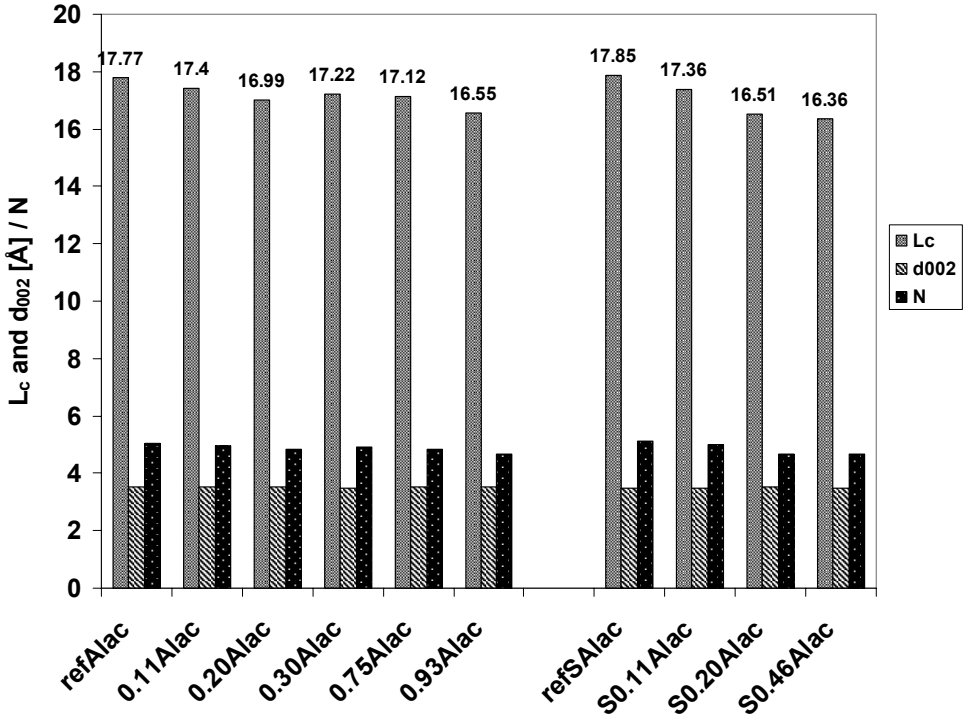

Figure 7.10 Coherent stacking height (L_c), distance between graphene layers (d_{002}) and average number of graphene layers in a coherent domain (N). *Variance between two parallel measurements: L_c: < 0.0015, d_{002}: < 0.000016*

The aluminium acetylacetonate additions seem to slightly suppress the graphitization process. However, there is no clear correlation between the structure parameters (L_c, d_{002} and N) and the amount of aluminium acetylacetonate added ($|R^2| < 0.6$). There is no statistically significant differences between the "high" and "low"-sulfur cokes ($\alpha = 0.005$).

7.1.3 Influence of aluminium acetylacetonate on carbonization

The texture of the aluminium acetylacetonate doped cokes varies strongly with the dopant concentration. Addition of 2.3 weight percent aluminium acetylacetonate to the tar oil prior to carbonization causes an abrupt increase in the calculated mosaic index. At higher additions, the mosaic index decreases slightly from the maximum value. Possible reasons might be:

1. Aluminium acetylacetonate acts as a dehydrogenation catalyst and thus increases the reactivity of the tar oil constituents. If the reactivity is accelerated disproportionally at temperatures where the fluidity of the aromatic system is too low, extensive condensation prior to orientation occurs and a resultant mosaic coke is formed.

2. Aluminium acetylacetonate increase the viscosity of the tar oil, slowing down the physical transformation of large molecules into mesophase.

3. Aluminium acetylacetonate increases the viscosity of the mesophase and thereby hinder the spheres to reorientate and coalesce on contact.

4. Small aluminium oxide particles (from decomposition of aluminium acetylacetonate) adsorb to the surface of the mesophase spheres and prevent them from coalesce on contact. At high aluminium acetylacetonate additions, the aluminium oxide particles form clusters and the coalescence process it not so effectively hindered as for lower additions.

Of these four possibilities, number 4 seems most plausible. Solid particles of size less than 1 μm may adhere to the surface of the mesophase spheres and hinder coalescence on contact [27, 86, 87]. As seen from the SEM-micrographs given in Figure 7.11, the surface of the mesophase spheres is covered with a layer of aluminium oxide (light). The aluminium oxide layer is considerably thicker for 0.30Alac (micrograph B) than for 0.20 Alac (micrograph A). At increasing dopant concentrations, the particles tend to form agglomerates. Sample 0.75Alac (micrograph C) has obtained a high degree of coalescence and agglomerates of aluminium oxide are found in the junctures between the coke lamellas.

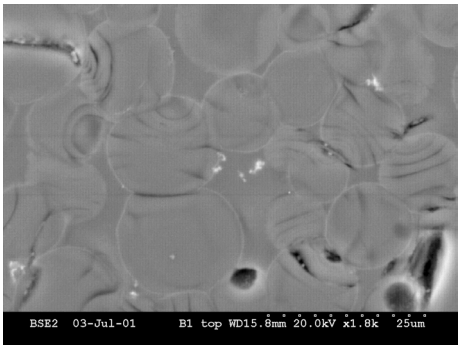

A) 0.20Alac

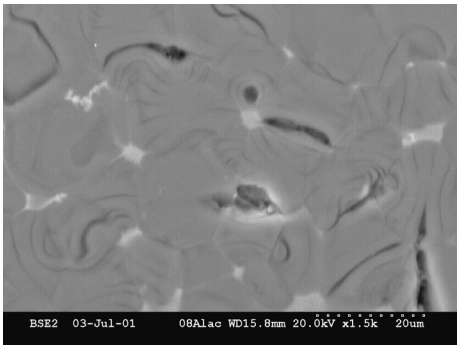

C) 0.75Alac

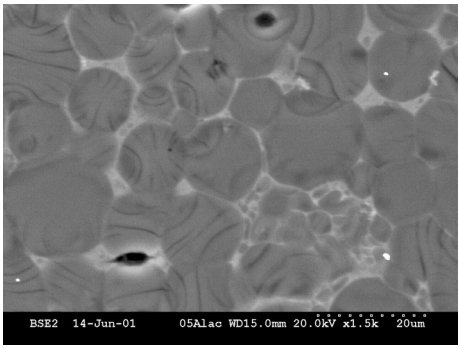

B) 0.30Alac

Figure 7.11 Layer of aluminium oxide particles (light gray areas) on surface of mesophase spheres, cokes doped with aluminium acetylacetonate

As seen from Figure 7.31 the phenomenon is not precursor dependent. Cokes made by carbonization of a petroleum pitch with 2.5 and 5 percent aluminium acetylacetonate have the same optical texture as the cokes made from the tar oil (compare with Figure 7.8).

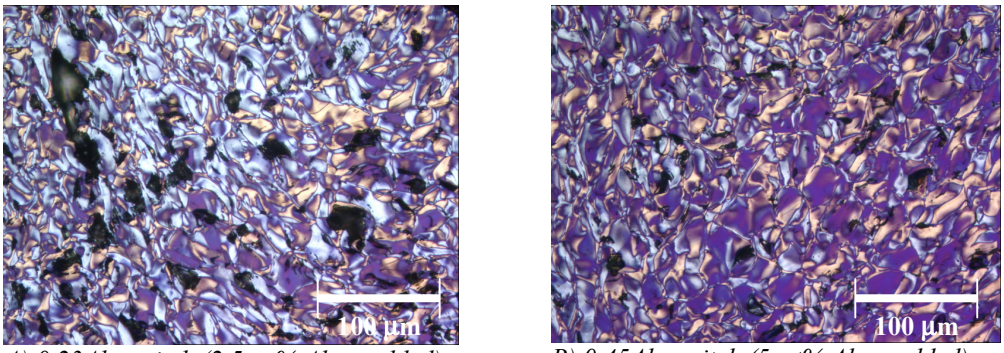

A) 0.23Alac-pitch (2.5 wt% Al-ac added) *B) 0.45Alac-pitch (5 wt% Al-ac added)*

Figure 7.12 Texture of aluminium acetylacetonate doped cokes made by carbonization of petroleum pitch

In order to investigate if the mesophase coalescence also is impeded by small amounts of aluminium oxide, cokes doped with 0.25 and 0.75 weight percent aluminium acetylacetonate were prepared from the tar oil. However, as seen from the micrographs given in Figure 7.12 the optical textures of these low-doped cokes are comparable to the texture of the pure reference coke (see Figure 7.8 A). The textures are relatively coarse (mosaic index 0.06 and 0.08, reference coke: 0.062) and there is no signs of mesophase. These findings support the assumption that the impediment of the texture development is purely physical. The critical aluminium acetylacetonate concentration seems to lie between 0.8 and 1.2 weight percent.

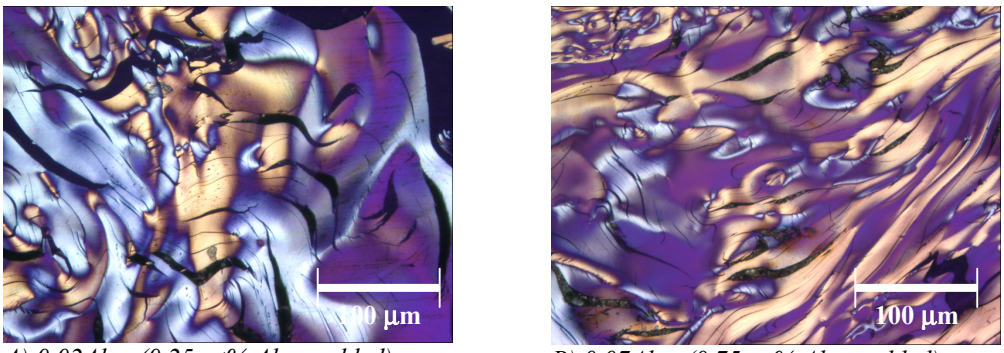

A) 0.02Alac (0.25 wt% Al-ac added) *B) 0.07Alac (0.75 wt% Al-ac added)*

Figure 7.13 Cokes doped with small amounts of aluminium acetylacetonate. *Tar oil used as coke precursor*

In general, the "high"-sulfur cokes have a slightly finer texture than the corresponding "low"-sulfur cokes. This may be ascribed to a dilution effect, since the addition of 4.5 weight percent dibenzothiophene lower the concentration of large aromatic molecules in the coke precursor.

7.1.4 Influence of texture on coke reactivity

The overall coke reactivity can be divided into a structural and a chemical part. Catalysts affect the chemical part. The structural or intrinsic part is affected by the optical coke texture, the turbostratic structure and the surface area available for reaction. A fine mosaic texture with small turbostratic structural units is believed to give a higher concentration of active sites for the gasification reactions than a coarse texture/structure. As seen from the previous section, the addition of various amounts of aluminium acetylacetonate influence the carbonization of the coke samples and the observed reactivity behavior might hence be affected by the varying coke texture as well as the aluminium concentration. Figure 7.14 and Figure 7.15 show the air and CO_2 reactivity of the aluminium acetylacetonate doped cokes plotted as a function of both the aluminium content (chemical-part) and the calculated mosaic index (structural-part).

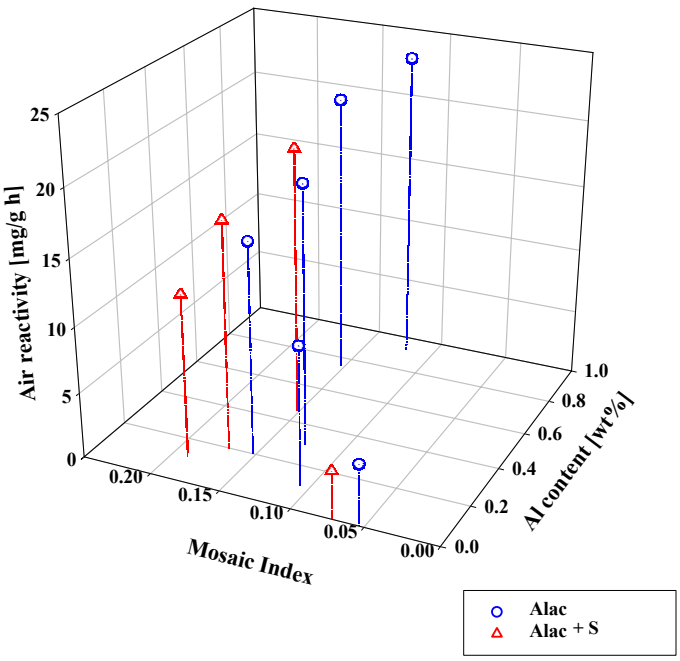

Figure 7.14 Air reactivity of aluminium acetylacetonate doped cokes *vs.* aluminium content and Mosaic Index

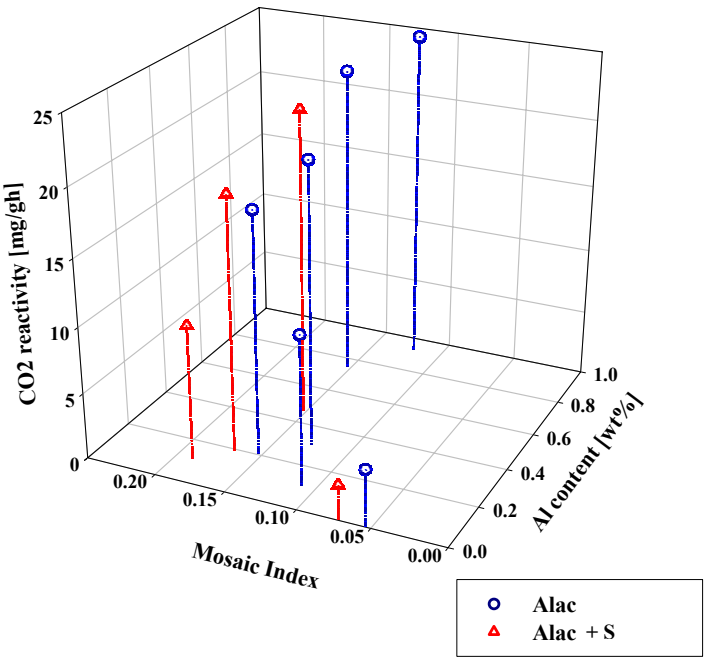

Figure 7.15 CO_2 reactivity of aluminium acetylacetonate doped cokes *vs.* aluminium content and Mosaic Index

As seen from the figures, the measured coke reactivities correlate as well with the calculated mosaic indexes as with the aluminium content. Due to a high degree of covariance between the two variables, it is not possible to separate the measured coke reactivity into a chemical and a structural term. However, because of the textural contributions, aluminium oxide (from aluminium acetylacetonate) is expected to be a weaker catalyst than it appears from Figure 7.3 and Figure 7.4.

The activity of the catalyst is directly related to the catalyst-carbon contact area [44, 88]. As seen from the micrographs given in Figure 7.11, the aluminium oxide particles tend to form aggregates at high loadings. Above the saturation limit, the reactivity will not be enhanced by further catalyst additions. Because of the high degree of covariance between the optical coke texture and the degree of aggregate formation, it is not known which variable that brings about the reactivity saturation level observed in Figure 7.3 and Figure 7.4.

7.2 Cokes doped with aluminium fluoride

Cokes doped with various amounts of aluminium fluoride were prepared from the petroleum pitch by the methods described in chapter 3.1.4. Table 7-2 gives an overview of some of the samples produced. The cokes labeled "2x" were made by the two times carbonization procedure, while the others were made by the standard single carbonization procedure. Because of the more complicated preparation route, the two-times (2x) carbonized cokes are generally more contaminated than the single carbonized cokes. Due to their extraordinary high sodium content, some of the top slices of the single carbonized cokes are not included in the reactivity study (sample name printed in *italic*).

Table 7-2 Cokes doped with aluminium fluoride.
DBT = dibenzothiophene

Sample	**Additions**	**Analyzed dopant content calcined cokes**			
		Al	F	S	Na
			wt%		*ppm*
refAlF3 2x	-	0.003			18
0.08AlF3 2x	0.4 wt% AlF_3	0.080	0.02		19
0.24AlF3 2x	0.9 wt% AlF_3	0.224	0.12	0.45	19
0.35AlF3 2x	1.7 wt% AlF_3	0.350	0.23	0.45	17
0.53AlF3 2x	2.0 wt% AlF_3	0.530	0.35	0.44	19
0.63AlF3 2x	2.2 wt% AlF_3	0.630	0.48	0.43	15
0.65AlF3 2x	2.3 wt% AlF_3	0.650	0.52		10
0.8AlF3.1	2.7 wt% AlF_3	1.010	1.09		21
0.8AlF3.2		0.970	1.20	0.44	5
0.8AlF3.3		0.400	0.62		5
0.8AlF3.4		0.064	0.09		3
1.2AlF3.1	4.5 wt% AlF_3	1.610	1.90		26
1.2AlF3.2		1.820	2.37	0.44	11
1.2AlF3.3		1.010	1.26		6
1.2AlF3.4		0.380	0.54		8
S0.5AlF3.1	1.9 wt% AlF3 + 4.6 wt% DBT	0.771	0.79	1.14	27
S0.5AlF3.2		0.654	0.82		9
S0.5AlF3.3		0.290	0.36	0.87	1
S0.5AlF3.4		0.037	0.03		2
S1.2AlF3.1	4.3 wt% AlF_3 + 4.7 wt% DBT	1.062	1.49	1.09	2
S1.2AlF3.2		1.268	2.20		1
S1.2AlF3.3		0.891	1.47		1
S1.2AlF3.4		0.340	0.56	0.89	1

About 95 percent of the aluminium added as AlF_3 prior to carbonization remains in the calcined cokes. The bulk chemical analysis reveal a slight fluorine deficiency compared to the AlF_3 composition (calculated from the analyzed aluminium concentrations). About 60 % of the fluorine added remains in the single carbonized cokes while about 50 % remains in the 2x carbonized samples.

The X-ray diffractogram given in Figure 7.16 shows that some aluminium oxide are formed during calcination of the aluminium fluoride doped coke samples. Most of the particles at the surface of the calcined coke grains consist of an Al-O-F phase containing ~ 30 at% Al, ~ 60 at% O, ~ 10 at% F (analyzed by EDX). As seen from the SEM-micrograph given in Figure 7.17, small particles (size 1 – 10 µm) are uniformly distributed over the coke surface arrows. Some large clusters (~ 100 – 200 µm) are also observed.

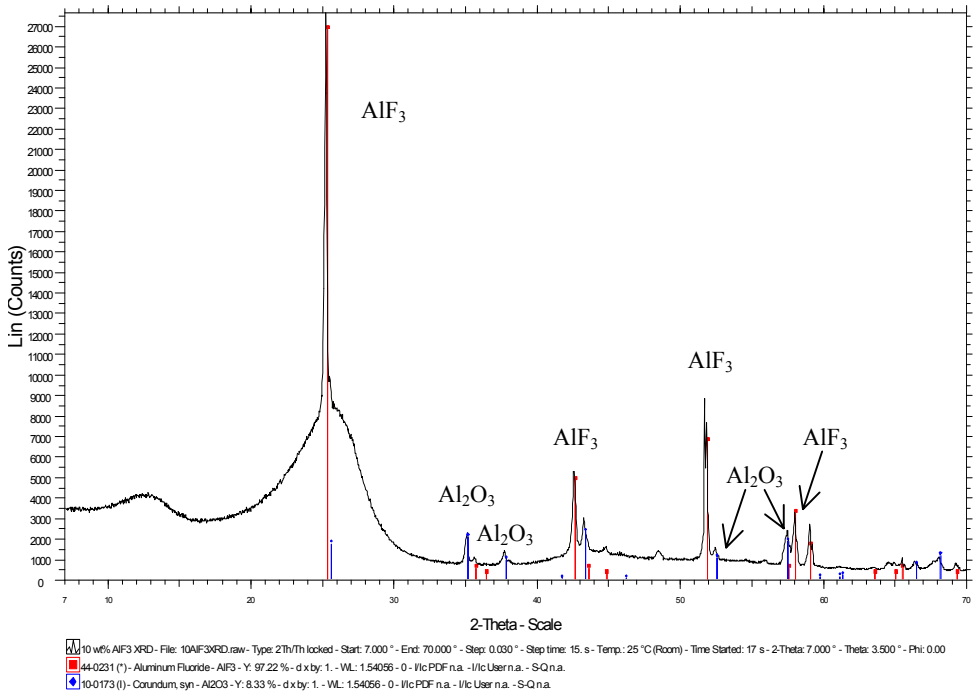

Figure 7.16 X-ray diffractogram of coke doped with aluminium fluoride. *Broad peak at $2\theta \sim 25°$ is identified as the graphite 002 diffraction peak*

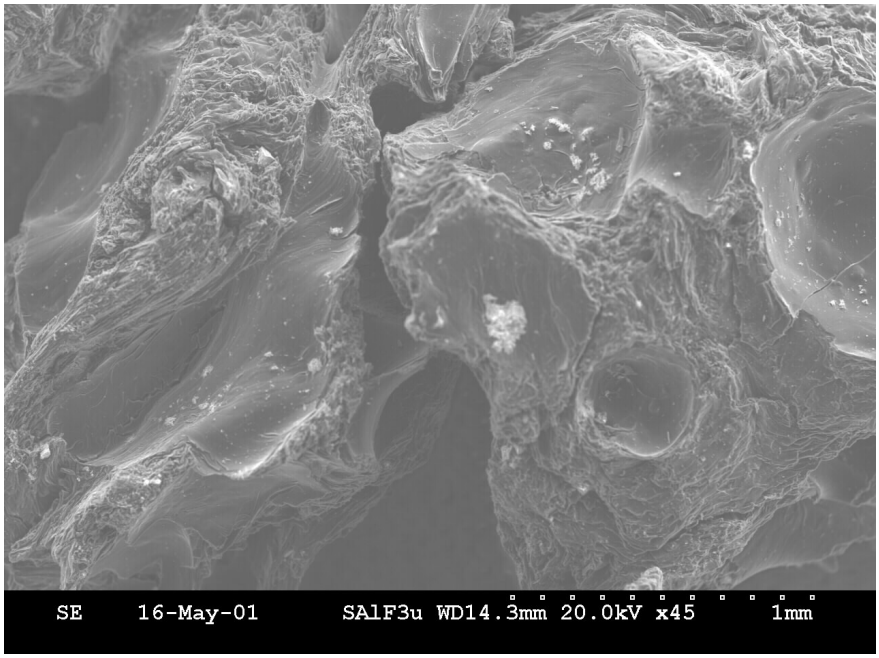

Figure 7.17 Al-O-F particles (light) on surface of coke doped with aluminium fluoride

7.2.1 Air and CO_2 reactivity

Figure 7.18 and Figure 7.19 show the air and CO_2 reactivities 2x carbonized cokes as a function of the analyzed aluminium contents.

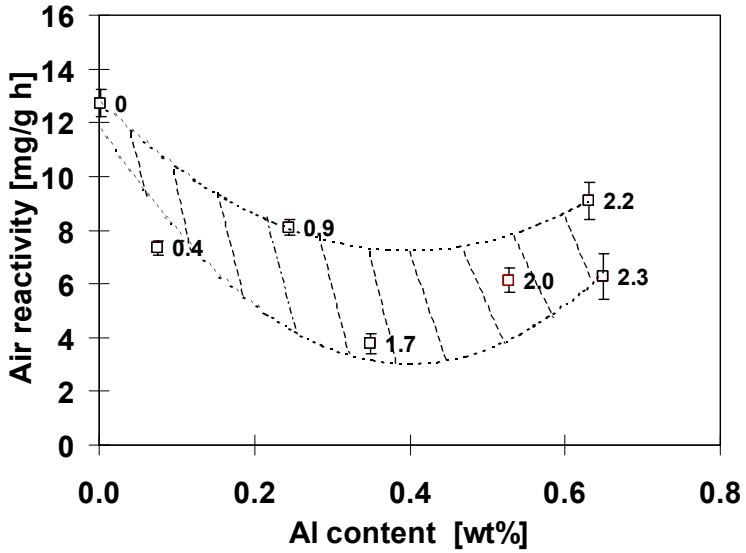

Figure 7.18 Air reactivity (525 °C) of 2x carbonized aluminium fluoride doped cokes *vs.* analyzed aluminium content. *Average values of five parallel measurements. Standard deviations represented by error bars. Amount of AlF_3 added to pitch prior to carbonization is indicated*

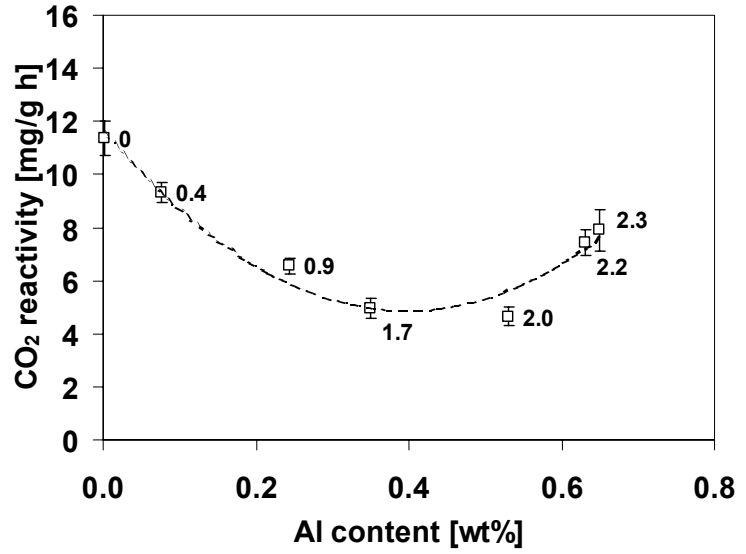

Figure 7.19 CO_2 reactivity (960 °C) of 2x carbonized aluminium fluoride doped cokes *vs.* analyzed aluminium content. *Average values of five parallel measurements. Standard deviations represented by error bars. Amount of AlF_3 added to pitch prior to carbonization is indicated*

The results correspond well with those reported by Sørlie *et al.* [12, 13]. The aluminium fluoride additions seem to lower the coke reactivity towards both the CO_2 and air gasification reactions. The reactivities go through a minimum at an aluminium concentration of about 0.5 weight percent, which corresponds to an addition of approximately 1.7 weight percent AlF_3 to the pitch (1.5 wt% to a green coke). Since the air gasification rate is far more sensitive towards small temperature variations and catalytically active impurities, the air reactivities are more scattered than the CO_2 reactivities.

The reactivities of the single carbonized cokes are given in Figure 7.20 and Figure 7.21. Due to their low reactivity, the cokes were oxidized at 550 °C and 990 °C instead of at the standard reaction temperature of 525/960 °C. Both the air and CO_2 reactivity seem to be slightly lowered by the AlF_3 additions, going through a shallow minimum at about 0.5 – 0.6 wt% Al (corresponds to an addition of approximately 1.8 wt% AlF_3 to the pitch). At higher additions, the reactivities show a minor increase. As will be discussed in chapter 7.2.3, the reactivity depression is much less than for the 2x carbonized cokes.

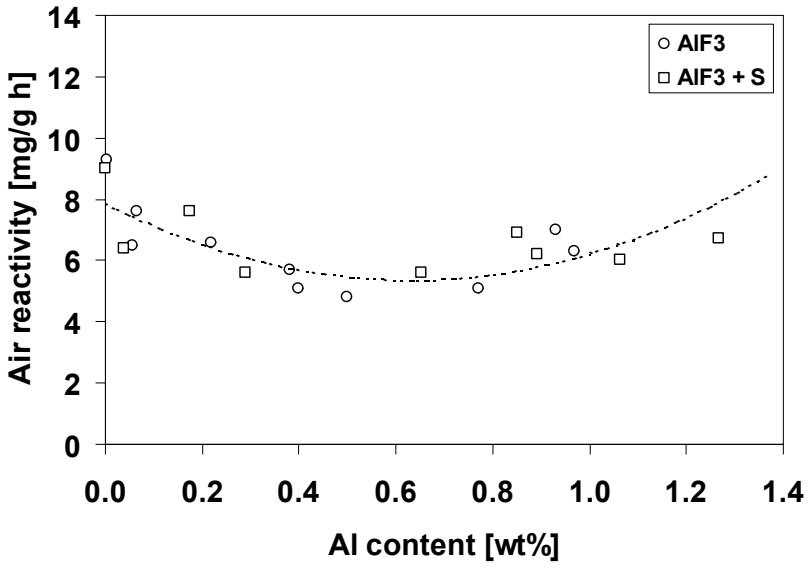

Figure 7.20 Air reactivity (550 °C) of single carbonized aluminium fluoride doped cokes *vs.* analyzed aluminium content. *Average values of two parallel measurements. Standard deviations < 1.0 mg/g·h*

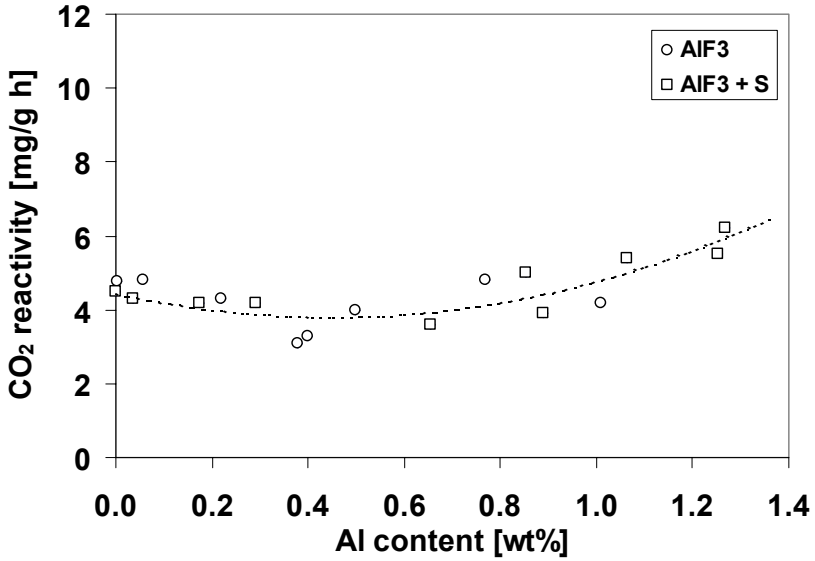

Figure 7.21 CO_2 reactivity (990 °C) of single carbonized aluminium fluoride doped cokes *vs.* analyzed aluminium content. *Average values of two parallel measurements. Standard deviations < 1.1 mg/g·h*

The addition of 4.5 weight percent dibenzothiophene has no significant influence on the reactivities of the single carbonized cokes.

The reactivity of the single carbonized aluminium fluoride doped coke samples was measured at temperatures well above the standard reaction temperatures. As mentioned in chapter 2.1.3, the true effect of a catalyst or inhibitor can only be studied in the temperature range where the reaction is chemically controlled. Only in this temperature range will the observed activation energy be identical to the true reaction activation energy. At higher temperatures pore diffusion controls the gasification rates and the observed activation energy is lower than the activation energy of the catalyzed reaction. The transition temperature is dependent on the coke particle diameter, the reaction rate coefficient and the effective diffusion coefficient within the coke grain [84]. As seen from the Arrhenius plots given in Figure 7.22 and Figure 7.23, the CO_2 gasification rate is chemically controlled in the range 940 – 1000 °C (10^3/T = 1 – 1.06). The carbon-air reaction rate appears to be chemically controlled up to temperatures around 550 °C (1/T = 1.82). At higher temperatures there is a transition to a diffusion-controlled regime.

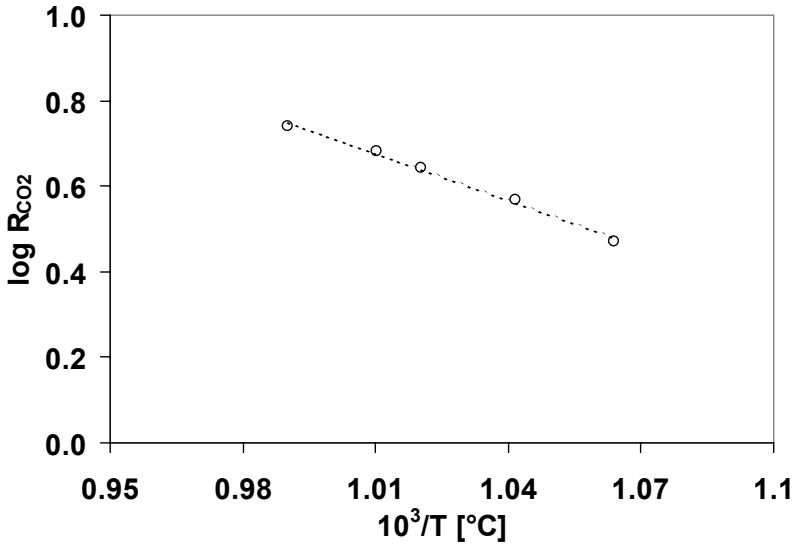

Figure 7.22 CO_2 reactivity (logarithmic) of single carbonized aluminium fluoride doped cokes *vs.* inverse reaction temperature

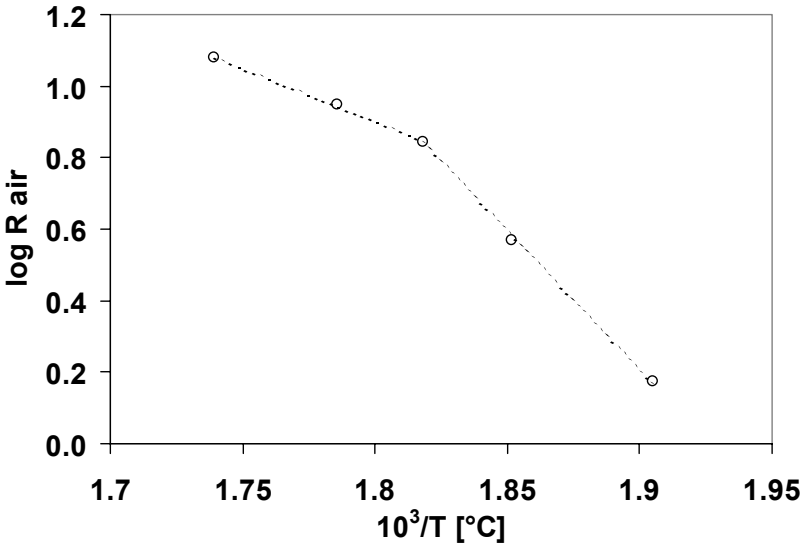

Figure 7.23 Air reactivity (logarithmic) of single carbonized aluminium fluoride doped cokes *vs.* inverse reaction temperature

The SEM micrograph given in Figure 7.24 shows the surface of an aluminium fluoride doped coke after gasification in CO_2. Only aluminium oxide containing particles are found at the coke surface. Some of the Al_2O_3 particles are small and rather "fluffy" while others have a clear hexagonal shape (diameter ~ 10 – 20 μm). As for the aluminium acetylacetonate doped cokes, there are no signs of enhanced gasification in the vicinity of the aluminium oxide particles.

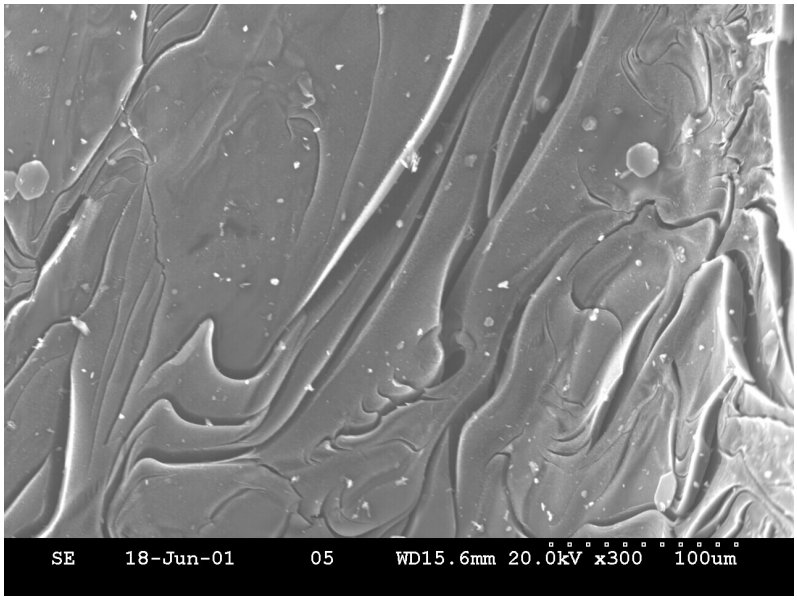

Figure 7.24 Aluminium oxide crystals at the surface of an aluminium fluoride doped coke grain after oxidation in CO_2 for 190 minutes (990 °C)

For some of the coke samples with high dopant loadings, the CO_2 gasification weight loss decreased gradually with increasing reaction time. This is probably caused by the formation of a protective aluminium oxide surface layer (see micrograph given in Figure 7.25), which reduces the surface area available for reaction.

Figure 7.25 Aluminium oxide layer on surface of CO_2-oxidized coke grain. *Backscatter detector. 2.0 wt% AlF3 added to pitch prior to carbonization*

7.2.2 Optical texture and turbostratic structure

Graphs representing the calculated mosaic and fiber indexes of some of the single carbonized aluminium fluoride doped cokes are given in Figure 7.26 and Figure 7.27.

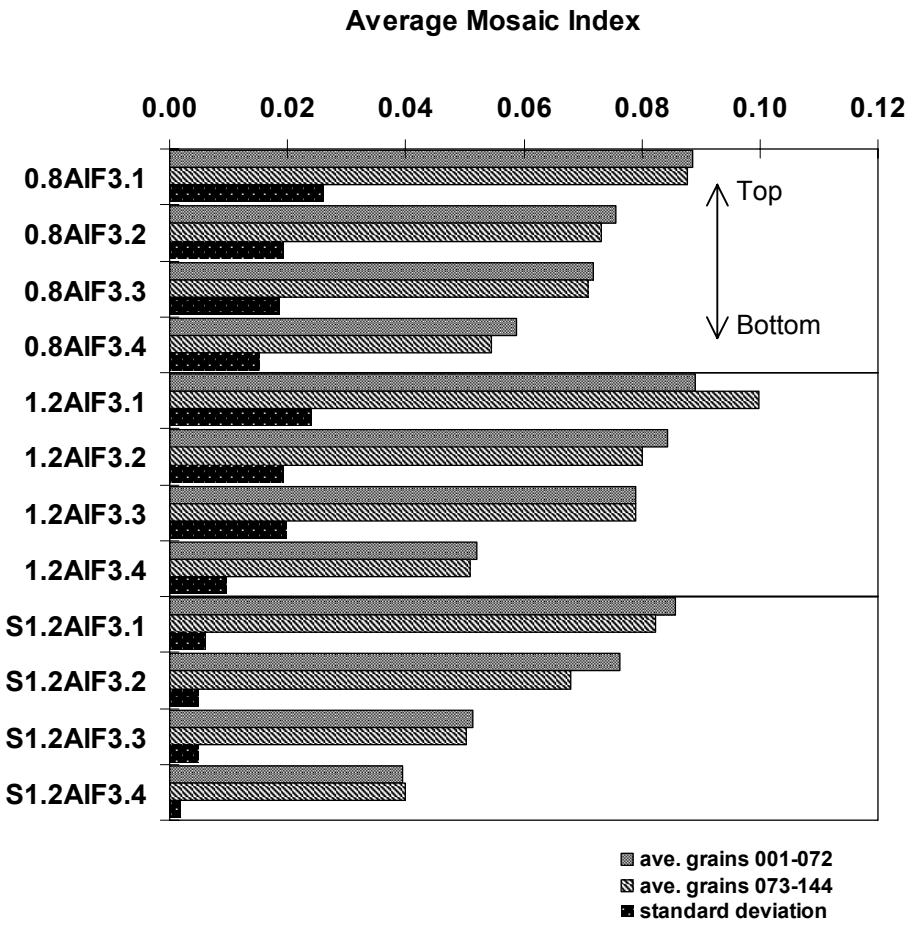

Figure 7.26 Mosaic Index, cokes doped with aluminium fluoride. *Average of two halves of analyzed grains with standard deviation*

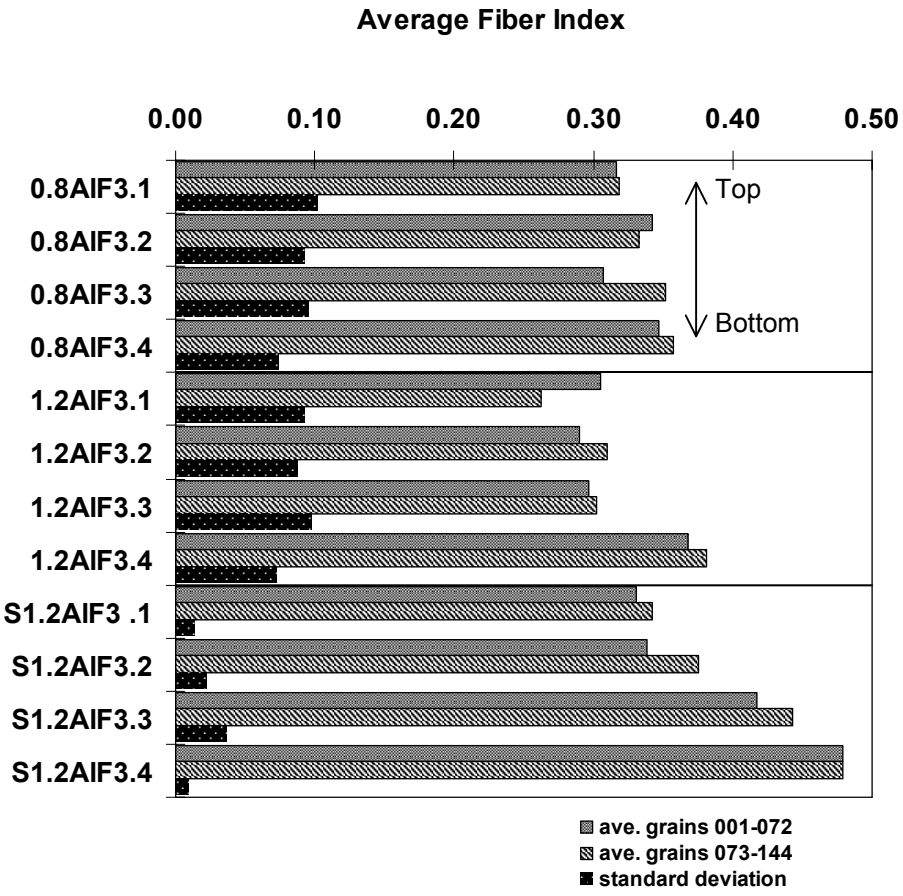

Figure 7.27 Calculated Fiber Index, cokes doped with aluminium fluoride. *Average of two halves of analyzed grains with standard deviation*

Due to enrichment of aluminium fluoride at increasing heights, the average mosaic index decreases from about 0.09 for slice 1 (top) to about 0.04 – 0.06 for slice 4. The "low"-sulfur cokes are very inhomogeneous (large standard deviations both within and among analyzed grains) and the variation observed is not statistically significant ($\alpha = 0.005$). For the "high"-sulfur cokes, the fiber index increases steadily from a value of 0.34 for slice 1 to 0.48 for slice 4. It should be noted that despite the fact that more than 10 times as much AlF_3 was added, the magnitude of the texture change from top to bottom, as well as the average values, is similar to that observed for the sodium fluoride, cryolite and calcium fluoride doped cokes.

After the first carbonization step, the two-times carbonized cokes were ground in a swinging mill to a grain size less than 63 μm. The coke powder were mixed with small amounts of molten petroleum pitch (same as coke precursor) into a non-fluid paste which was

carbonized once more in the coke reactor. This procedure ensured a homogenous distribution of AlF_3 within the finished coke samples, but the original texture elements (from the first carbonization) were broken down during the milling step. As can be seen from the micrographs given in Figure 7.28, the texture of the 2x carbonized cokes differs from the texture of the single carbonized cokes. It consists of relatively coarse-textured aggregate grains (< 63 µm) embedded in a fine-textured binder-phase. It is however, not possible to quantify the texture precisely by image analysis since the calculated mosaic and fiber indexes rather will be a measure on the number and size of the aggregate grains in the analyzed areas than true textural differences. However, on basis of qualitative observations and results from image analysis of the single carbonized cokes, it is assumed that the texture of the 2x carbonized cokes does not vary significantly from one sample to another.

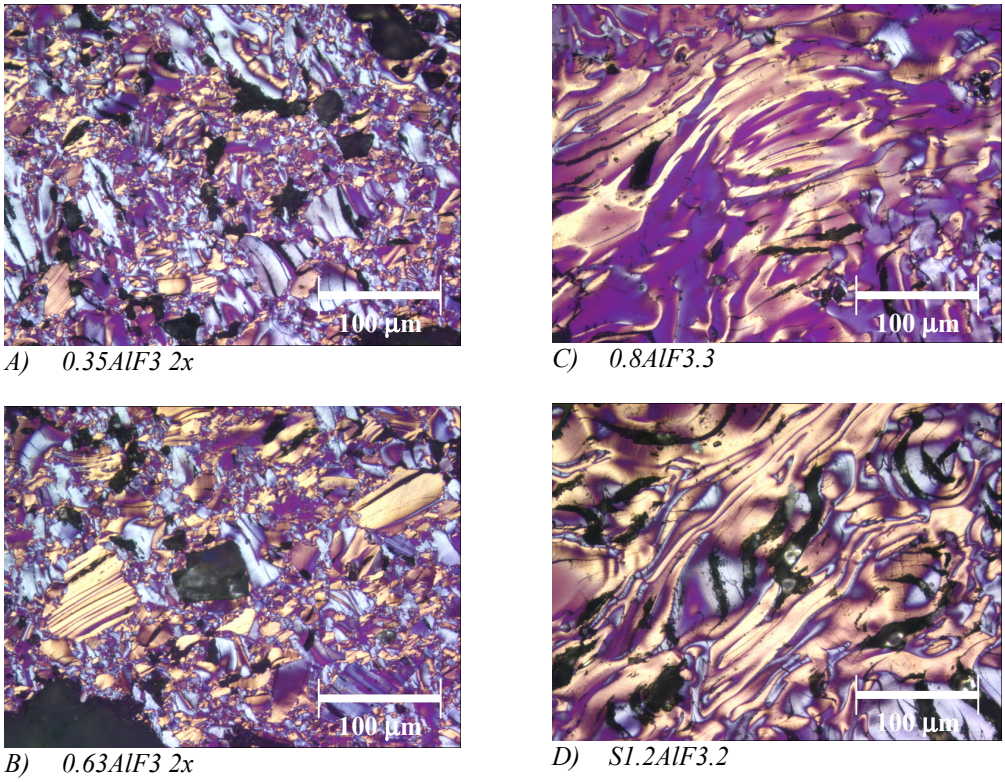

A) 0.35AlF3 2x

C) 0.8AlF3.3

B) 0.63AlF3 2x

D) S1.2AlF3.2

Figure 7.28 Texture of 2x carbonized and single carbonized aluminium fluoride doped cokes

In contrast to the aluminium acetylacetonate doped cokes, quantitative observations of the micrographs show that coke lamellas "bend" around the AlF_3 powder grains (see micrograph in Figure 7.29). This is as expected as the aluminium fluoride does not dissolve in the carbon precursor prior to coking.

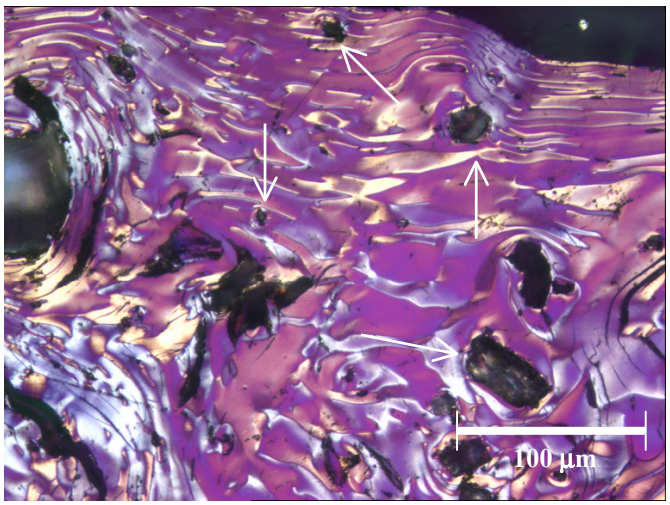

Figure 7.29 Aluminium fluoride grains (see arrows) within calcined coke matrix

The measured L_c, d_{002} and N-values are shown graphically in Figure 7.30. Due to similar calcination programs, both the single carbonized and the 2x carbonized cokes have L_c-values between 18 and 20 Å. There is no statistically significant difference between the coke series.

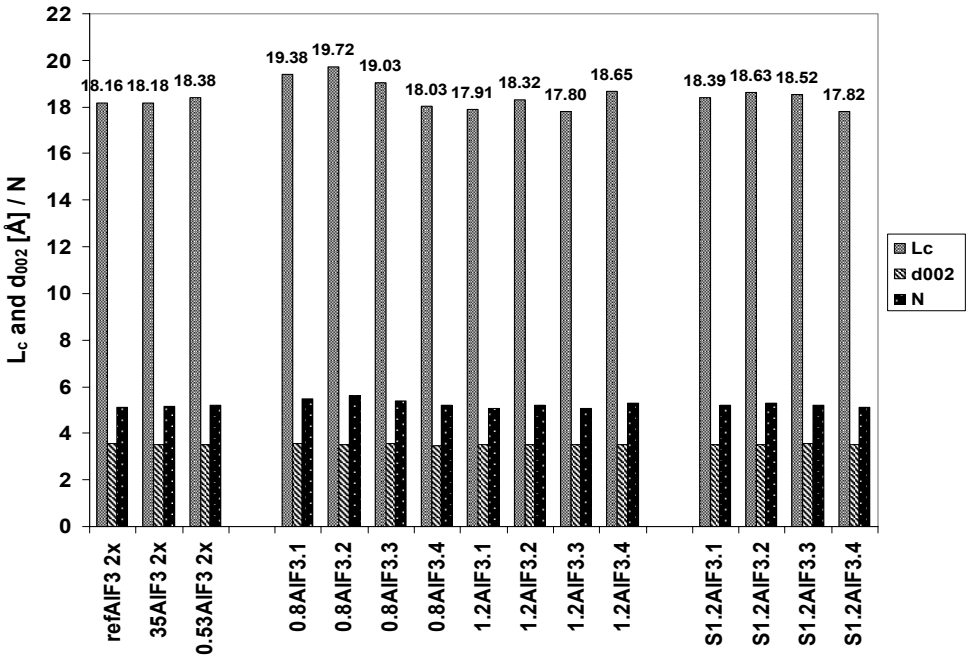

Figure 7.30 Coherent stacking height (L_c), distance between graphene layers (d_{002}) and average number of graphene layers in a coherent domain (N). *Variance between two parallel measurements: L_c: < 0.0019, d_{002}: < 0.000015*

Since the variance among the different samples is larger than the variance between two parallel measurements of the same sample, it is believed to be a true (not due to experimental errors). The variance is slightly higher than the variance between the aluminium acetylacetonate doped cokes (0.31 *vs.* 0.27), but there is no correlation between the structure parameters and the amount of AlF_3 added. Hence it is believed that the small variations observed are caused by minor temperature differences during the heat treatment rather than the varying AlF_3 content. It is unlikely that the relatively large and insoluble aluminium fluoride grains will affect the graphitization process to any significant extent.

In order to investigate how L_c and d_{002} vary with the calcination temperature, a pure reference green coke was split into four parts and heat-treated at four different temperatures (800 °C, 1010 °C, 1235 °C and 1265 °C) for 2 hours. The results are presented in Figure 7.31 and Figure 7.32 and show that the coherent stacking height, L_c, increases nonlinearly with temperature whereas the distance between the graphene layers, d_{002}, remains constant. Figure 7.33 shows how the samples air and CO_2 reactivity vary with the calcination temperature.

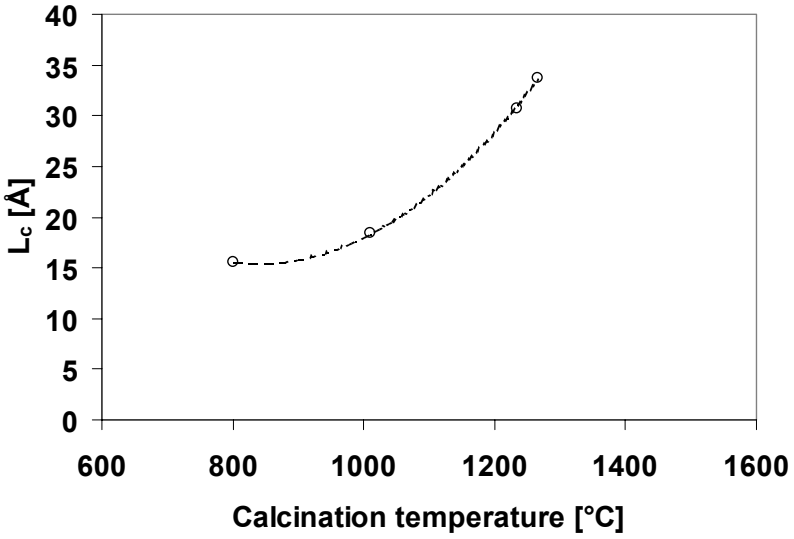

Figure 7.31 L_c *vs.* maximum heat-treatment temperature. *Maximum temperature hold for 2 hours*

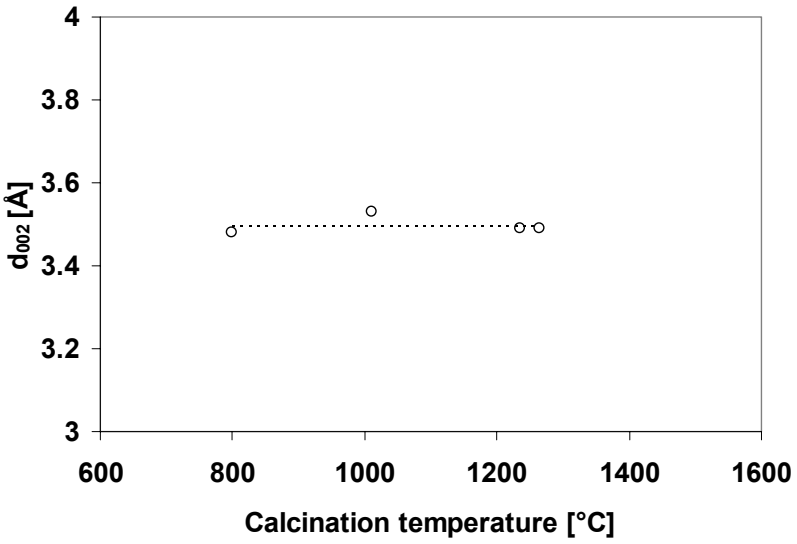

Figure 7.32 d_{002} *vs.* maximum heat-treatment temperature. *Maximum temperature hold for 2 hours*

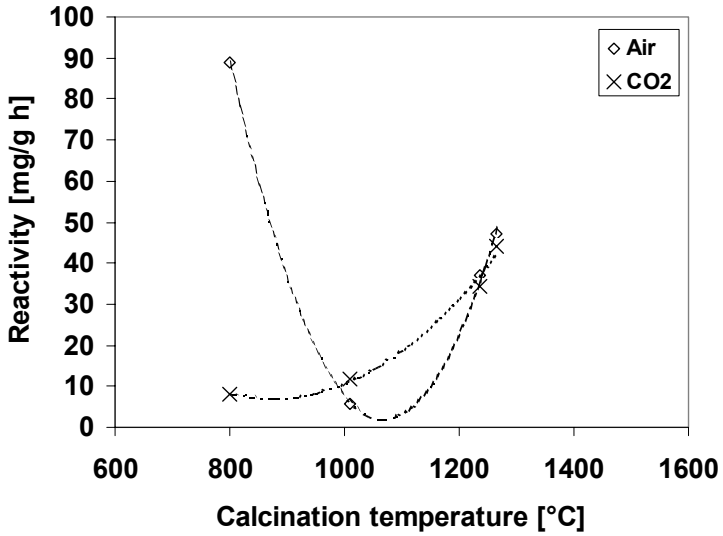

Figure 7.33 Air and CO_2 reactivity *vs.* maximum heat-treatment temperature

As seen from Figure 7.34, the coke porosity also increases with increasing calcination temperature. Due to increasing surface area available for reaction, the coke reactivity is expected to increase with increasing porosity. The influence of the porosity on the coke reactivity is thus diametrically opposed to the influence of L_c. At increasing heat treatment

temperatures and times, the intrinsic coke reactivity is determined by a competing effect between the increasing coke porosity and the increasing degree of structural ordening [85].

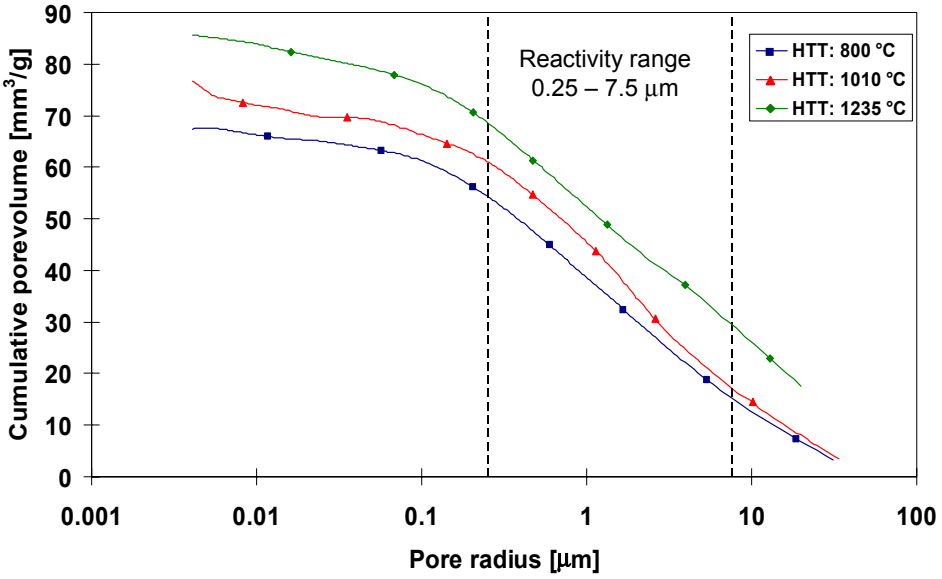

Figure 7.34 Porosity and pore size distribution of cokes calcined at 800 °C, 1010 °C and 1235 °C. *Solid markers used to separate the different lines (not measuring points)*

The air reactivity of the coke calcined at 800 °C is extremely high (90 mg/g·h). Since L_c only is 15 percent lower than for coke calcined at 1010 °C, it is believed that the high air reactivity mainly is caused by the high amounts of hydrogen remaining in the coke structure. However, as the calcination temperature increases, the coke reactivity towards air gasification drops quickly. At temperatures above about 1100 °C the porosity increase appears to become important and the air reactivity increases again. The CO_2 reactivity increases within the whole temperature range and is therefore believed to mainly be determined by the increasing porosity, not by L_c.

In Figure 7.35 the air and CO_2 reactivities of the aluminium fluoride doped cokes are plotted as a function of the measured L_c-values. It is seen that within the current variation range, there is no correlation between the two variables.

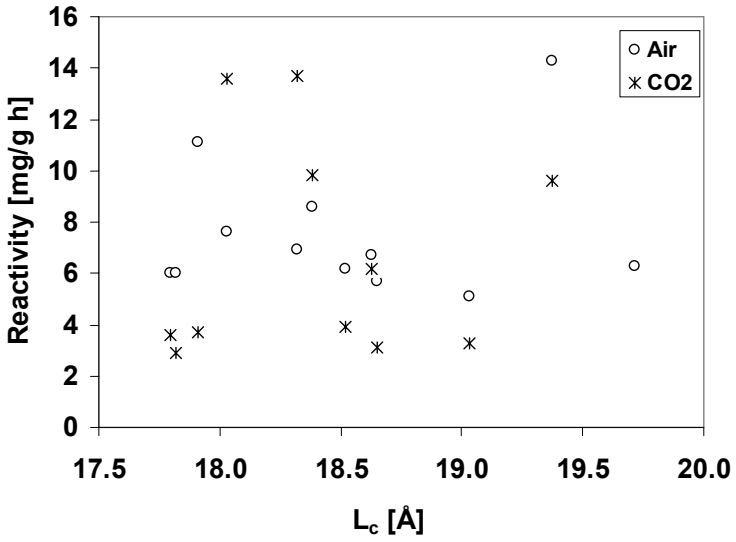

Figure 7.35 Reactivity of single carbonized aluminium fluoride doped cokes *vs.* L_c

7.2.3 Mechanistic considerations, inhibiting effect of aluminium fluoride

7.2.3.1 Formation of gaseous fluorides, thermodynamical considerations

Figure 7.36 shows how the equilibrium conditions change with temperature during calcination of the aluminium fluoride doped coke samples. The activities at the maximum calcination temperature (1010 °C) are tabulated in Table 7-3.

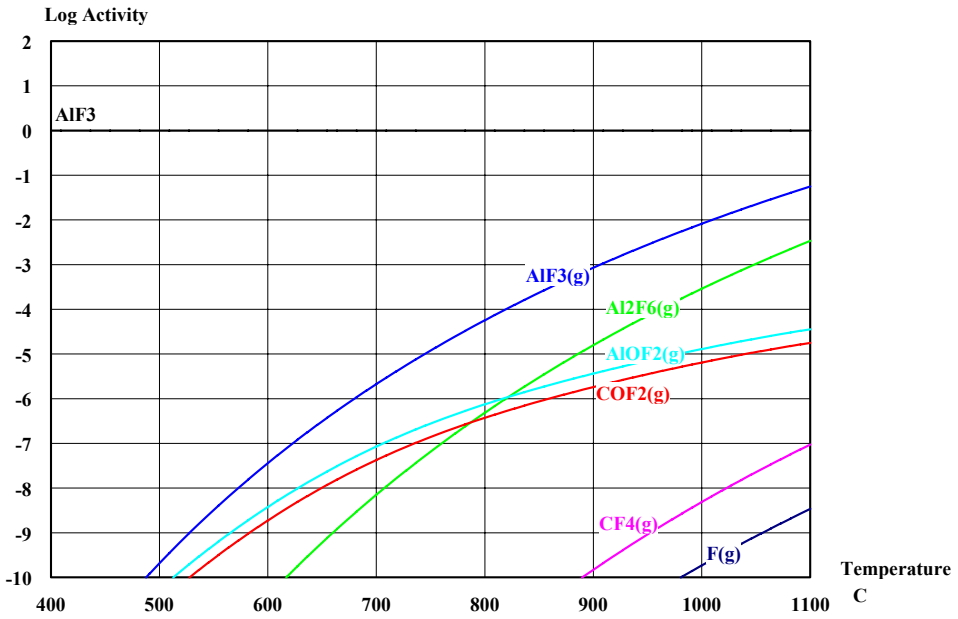

Figure 7.36 Calculated activities (logarithmic) of gases and solid phases *vs.* temperature, calcination of cokes doped with aluminium fluoride. *Calculated by use of HSC Chemistry* © [79]. *Initial conditions: T = 25 °C, p_{O2} = 0.2 atm, p_{N2} = 0.8 atm, c_{AlF3} = 1.8 wt%, excess carbon. Activities of C, O_2, CO and CO_2 are not shown, CO dominates at temperatures above 700 °C*

Table 7-3 Calculated activities of most stable condensed and gaseous species at maximum calcination temperature (1010 °C), cokes doped with aluminium fluoride. *Calculated by use of HSC Chemistry* © [79]. *Initial conditions: T = 25 °C, p_{O2} = 0.2 atm, p_{N2} = 0.8 atm, c_{AlF3} = 1.8 wt%, excess carbon. Activities of C, O_2, CO and CO_2 are not shown, CO dominates at temperatures above 700 °C*

Species	**Log Activity** *1010 °C*
AlF_3 (s)	0
AlF_3 (g)	-1.8
Al_2F_6 (g)	-3.2
$AlOF_2$ (g)	-4.8
COF_2 (g)	-5.1
CF_4 (g)	-7.9
F (g)	-9.7
Sum gas phase activities	-1.8
Sum activities gaseous Al species	-1.8
Sum activities gaseous F species with polar oxygen groups ($AlOF_2$, COF_2)	-4.6

Aluminium fluoride, which is the only solid phase (except from carbon), appears to be stable to temperatures well above the maximum calcination temperature (sublimes at 1291 °C [89]). The activities of AlF_3 (g) and Al_2F_6 (g) (dimer) increase steadily with increasing temperatures and reach values of 10^{-2} (AlF_3) and $10^{-3.4}$ (Al_2F_6) at 1010 °C. Minor amounts of $AlOF_2$ (g) and COF_2 (g) are formed by reaction between the gaseous aluminium fluoride species and CO/CO_2. The experimentally observed aluminium oxide (see Figure 7.16 and Figure 7.25) is probably formed by condensation of $AlOF_2$ (g) during the subsequent cooling to room temperature:

$$6\ AlOF_2\ (g) \quad \Rightarrow \quad 4\ AlF_3\ (s) + Al_2O_3\ (s) + 3/2\ O_2\ (g) \qquad \textbf{Eq. 7.1}$$

$\Delta G^0_{1000°C} = 304.8$ kJ/mol
$\Delta G^0_{700°C} = 1.07$ kJ/mol
$\Delta G^0_{300°C} = -421.9$ kJ/mol

Table 7-4 gives the equilibrium activities of the C-AlF_3 system at the air and CO_2 gasification conditions. In the same way as for the sodium fluoride and cryolite doped cokes, the equilibrium calculations do only give qualitative information of the stability of the aluminium fluoride particles at the gasification conditions (lack of detailed knowledge of local environment precludes quantitative calculations).

Table 7-4 Equilibrium composition in vicinity of aluminium fluoride particles on coke surface during air and CO_2 gasification. *Activities calculated at actual gasification temperature in excess of carbon and O_2/CO_2, c_{AlF3} = 1.8 wt% (HSC Chemistry © [79]). Activities of C, O_2, CO and CO_2 are not given.*

Species	Log Activity			
	CO_2 gasification		**Air gasification**	
	960 °C	*990 °C*	*525 °C*	*550 °C*
AlF_3 (s)	0	0	0	0
AlF_3 (g)	-2.5	-2.2	-9.1	-8.5
$AlOF_2$ (g)	-3.6	-3.4	-5.4	-5.1
COF_2 (g)	-3.9	-3.7	-5.7	-5.4
Al_2F_6 (g)	-4.0	-3.6		
CF_4 (g)	-7.8	-7.3	(-10.4)	-9.8
F (g)	-9.2	-8.7	(-11.5)	(-10.9)
Sum gas phase activities	-2.4	-2.1	-5.2	-4.9
Sum activities gaseous Al species	-2.5	-2.2	-5.4	-5.1
Sum activities gaseous F species with polar oxygen groups ($AlOF_2$, COF_2)	-3.4	-3.2	-5.2	-4.9

AlF_3 shows about the same volatility at the CO_2 gasification conditions as at the maximum calcination temperature. However, due to the excess amounts of oxidizing gas present, the gas phase composition is shifted slightly more towards COF_2 and $AlOF_2$.

7.2.3.2 Proposed mechanism

The coke reactivity reduction, which is observed when small amounts of aluminium fluoride are added, is believed to be caused by adsorption of polar fluorine gases, *i.e.* $AlOF_2$ and COF_2 at the active carbon sites. As illutrated in Figure 7.37, the number of "free" active carbon sites is expected to decrease when increasing amounts of aluminium fluoride are added. At the same time, the concentration of catalytically active aluminium species (Al_2O_3, AlF_3) increases. The observed reactivities are believed to be a result of the competing effect between fluorine deactivation of the active carbon sites and the weak catalytic effect of the condensed aluminium compounds.

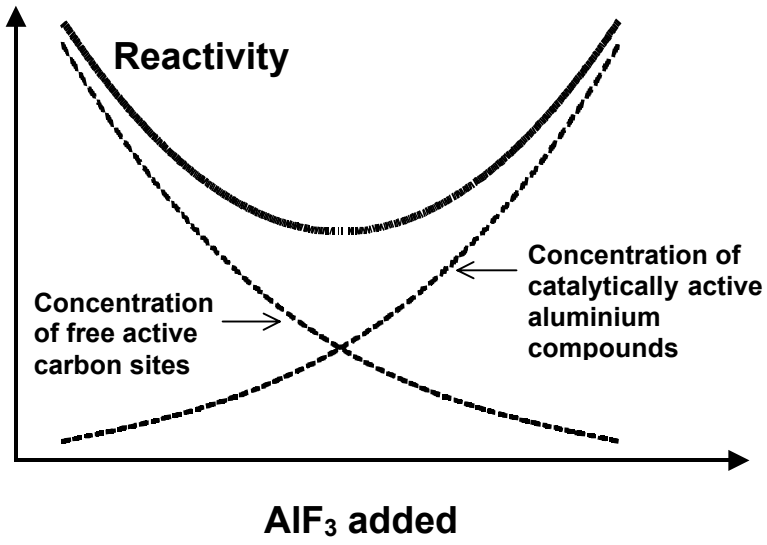

Figure 7.37 Proposed mechanism, reactivity of cokes doped with aluminium fluoride

The 2x carbonized cokes show a far more pronounced reactivity reduction than the single carbonized cokes. As was shown in chapter 7.2.2, the turbostratic structures of the two coke series are comparable, but the optical textures differ greatly. The 2x carbonized cokes have a very fine mosaic texture (coarse aggregate grains and fine-textured binder phase) while the texture of the single carbonized cokes is coarse and flow-type like. It is hence expected that the 2x carbonized cokes have a higher concentration of active sites than the single carbonized samples. If aluminium fluoride inhibits the gasification reactions by deactivating the active carbon sites, it is reasonable to believe that the effect is largest when the concentration of active sites is high. When the concentration is low, the structure might quickly be saturated. Findings made by other workers support a saturation effect. For example, Pallmer [76] investigated the reduction in oxidation rate caused by additions of small amounts of freon (CCl_2F_2) to an air stream passing over graphite at 700 °C. The poisoning effect was found to be most marked at very low concentrations of the halogen compound and freon concentrations above a few percent result in little further diminution in oxidation rate.

Figure 7.38 and Figure 7.39 compare the reactivities of the 2x carbonized aluminium fluoride doped cokes with the reactivities of similar cokes doped with aluminium oxide (Al_2O_3 powder added to pitch prior to carbonization). As seen, while the gasification reactions are inhibited by the aluminium fluoride additions, the reactivities increase slightly when increasing amounts of aluminium oxide powder are added. It is hence confirmed that the presence of gaseous fluorine compounds plays an essential role. The low catalytic activity of aluminium oxide might probably be ascribed to high stability of Al_2O_3 towards oxidation/reduction.

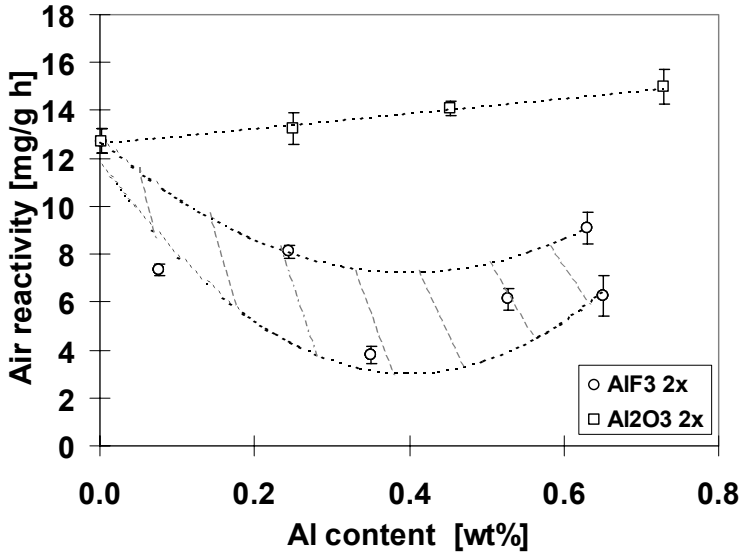

Figure 7.38 Air reactivity (525 °C) of 2x carbonized cokes doped with aluminium fluoride or aluminium oxide *vs.* analyzed aluminium content

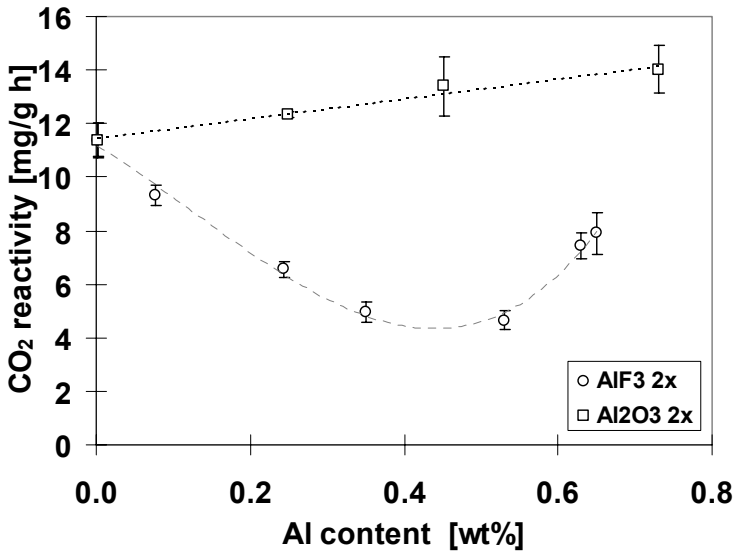

Figure 7.39 CO_2 reactivity (960 °C) of 2x carbonized cokes doped with aluminium fluoride or aluminium oxide *vs.* analyzed aluminium content cokes

The protection afforded by adsorbed halogen species is limited to temperatures below the the upper stablility limit of the carbon-halogen adsorption complexes. At higher temperatures, desorption from the active sites occures and the gasification rates return to normal [90]. In this work the CO_2 reactivities of the single carbonized cokes were measured at 990 °C instead of at the standard reaction temperature of 960 °C. However, as seen from Figure 7.40 below, the fluorine adsorption products appear to be stable also at this temperature. For the 2x carbonized cokes, the reactivity reduction is even more pronounced at 990 °C than at 960 °C.

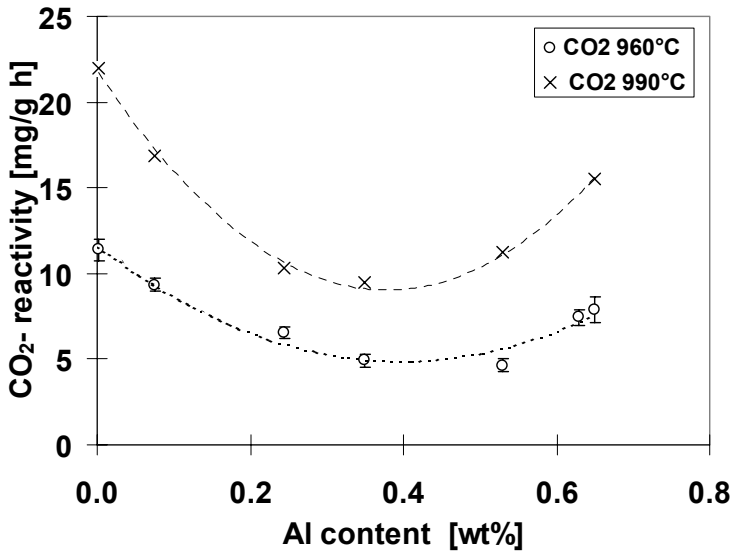

Figure 7.40 Effect of reaction temperature on CO_2 reactivity of 2x carbonized aluminium fluoride doped cokes

At atmospheric pressures, AlF_3 sublimes at about 1290 °C. In industrial aluminium electrolysis cells, the excess anode consumption is strongly dependent on the gas permeability of the anode. Condensation of aluminium fluoride within the open pore network may reduce the permeability and thus give an additional beneficial effect. This effect is expected to be especially pronounced in prebaked anodes, which are baked at temperatures of about 1200 °C. Qualitative examinations (optical microscope) revealed that sublimation and subsequent condensation of aluminium fluoride in the pore network does not occur in any significant extent during calcination of the laboratory made cokes to 1010 °C. The majority of the dopant grains are located within the coke matrix (between coke lamellas). No signs of pore plugging are observed.

8 Comparative discussion of catalytic activity

8.1 Cokes doped with acetylacetonates

8.1.1 Relative catalytic strengths

Figure 8.1 and Figure 8.2 compare the reactivities of the sodium, calcium and aluminium acetylacetonate doped "low"-sulfur cokes with the reactivities of similar cokes doped with vanadium (III) acetylacetonate (Vac) and iron (III) acetylacetonate (Feac) (data taken from Eidet [70]). Only the linear parts of the reactivity plots are shown. Vanadium, which is a common impurity in petroleum cokes, is regarded as a very strong gasification catalyst, especially towards airburn. Iron is reported to act as a moderate catalyst. The apparent catalytic activitities (slope of reactivity *vs.* dopant concentration (ppm) graphs) of the different dopant species are tabulated in Table 8-1 (both "low"-sulfur and "high"-sulfur cokes are given).

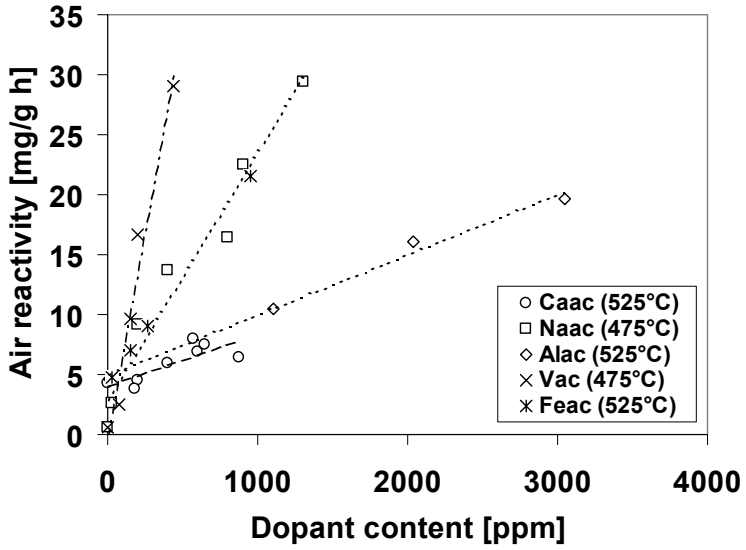

Figure 8.1 Air reactivity *vs.* analyzed dopant concentration, cokes doped with metal acetylacetonates, "low"-sulfur cokes. *Data for vanadium and iron contaminated cokes are taken from Eidet* [70]

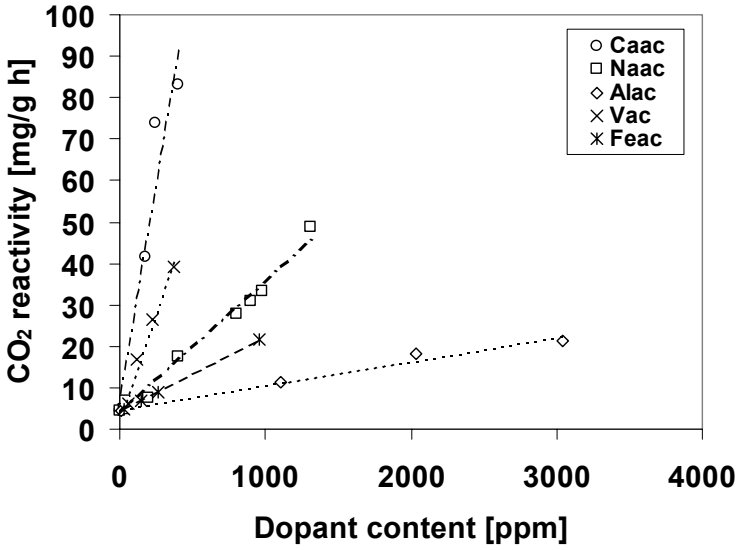

Figure 8.2 CO_2 reactivity (960 °C) *vs.* analyzed dopant concentration, cokes doped with metal acetylacetonates, "low"-sulfur cokes. *Data for vanadium and iron contaminated cokes are taken from Eidet* [70]

Table 8-1 Catalytic activities towards air and CO_2 gasification reactions, cokes doped with metal acetylacetonates

Catalyst [1]	Catalytic activity			
	Air gasification *525 °C*		CO_2 gasification *960 °C*	
	"low"-sulfur cokes	"high"-sulfur cokes	"low"-sulfur cokes	"high"-sulfur cokes
CaO	0.004	0.004	0.207	0.104
Al_2O_3	0.005 [4]	0.005 [4]	0.006 [4]	0.006 [4]
Na_2O	0.021 [2]	0.019 [3]	0.032	0.032
FeO	0.018	0.012	0.018	0.018
V_2O_3	0.069 [2]	0.060 [1]	0.099	0.033

[1] Exact oxidation state of active catalyst unknown, [2] reactivity measured at 475 °C, [3] activity decreases with increasing reactivity, [4] observed catalytic activity higher than actual activity because of textural variations

Sodium oxide appears to be a considerably weaker catalyst than vanadium oxide. Calcium oxide on the other hand, which barely affects the air gasification rate (even though gasified at 525 °C), acts as a very strong catalyst towards the carbon-CO_2 gasification reaction. The air reactivities of the sodium acetylacetonate doped cokes are comparable with the reactivities of the iron-contaminated samples. However, it should be noted that the sodium acetylacetonate doped cokes are oxidized at 475 °C while the iron acetylacetonate doped cokes are oxidized

at 525 °C. As was shown in chapter 5.2, the catalytic activity of sodium is strongly temperature dependent and increases significantly when the temperature is increased from 475 to 525 °C. Sodium oxide also acts as a stronger catalyst than iron oxide towards the CO_2 gasification reaction. The difference between calcium oxide and sodium oxide may arise from the different stability of the carbonate phases at the reaction temperature (ref. chapter 4.3.1 and 5.3.1). The transformation of calcium carbonate into calcium oxide is thermodynamically favored while the decomposition of sodium carbonate is not:

$CaCO_3$	$\Leftrightarrow$	$CaO + CO_2$	$\Delta G^0_{960°C}$ = -9.7 kJ/mol	**Eq. 8.1**
$CaCO_3 + C$	$\Leftrightarrow$	$CaO + 2\ CO$	$\Delta G^0_{960°C}$ = -54.6 kJ/mol	**Eq. 8.2**
Na_2CO_3	$\Leftrightarrow$	$Na_2O + CO_2$	$\Delta G^0_{960°C}$ = 150.2 kJ/mol	**Eq. 8.3**
$Na_2CO_3 + C$	$\Leftrightarrow$	$Na_2O + 2\ CO$	$\Delta G^0_{960°C}$ = 105.3 kJ/mol	**Eq. 8.4**

(Thermodynamical data are taken from Barin [38]).

However, although the observed reactivity differences may be understood from thermodynamics, it can not be excluded that calcium oxide simply is a stronger CO_2 gasification catalyst than sodium oxide by *e.g.* having a higher capacity for providing adsorbed oxygen atoms to the active carbon sites or facilitating the desorption of CO. For instance, it has been proposed that the covalent character of the O-M bond in the carbon phenolate group determines the catalytic activity of an alkali or alkaline earth salt [37]. A high covalent character increases the chance that CO can be eliminated from the metal-oxygen-carbon group during gasification. This has been confirmed by experimental findings, which have revealed that cesium is a stronger gasification catalyst than for example sodium or lithium [39, 55].

Even though Al^{3+} shows a high charge density and the measured reactivities of the aluminium acetylacetonate doped cokes are influenced by textural and structural variations (see chapter 7.1.3), the apparent catalytic activity of aluminium oxide is low. The low catalytic activity is believed to arise from the high stability of Al_2O_3 towards oxidation and reduction.

The catalytic activity of aluminium oxide is not affected by the concurrent addition of 4.5 wt% dibenzothiophene to the coke precursor prior to carbonization. The dibenzothiophene additions lower the catalytic activity of calcium oxide towards the carbon-CO_2 reaction, but the activity towards the air gasification reaction is unchanged. Sodium and iron oxide show the opposite behavior, *i.e.* the activities towards the carbon-air reaction is reduced while the CO_2 gasification activities are unaffected. The influence of the dibenzothiophene additions on the catalytic activities is further discussed in chapter 8.3.

Figure 8.3 shows the amount of CO_2 evolved when some of the acetylacetonate doped coke samples are heated in flowing oxygen (UHP, 750 cm^3/min) at a rate of 19.5 °C/min. The ignition temperatures (temperature at the inflection point) are given in Table 8-2. The curves were taken up by using a multiphase carbon/hydrogen/moisture analyzer from LECO (method described in chapter 3.2.3).

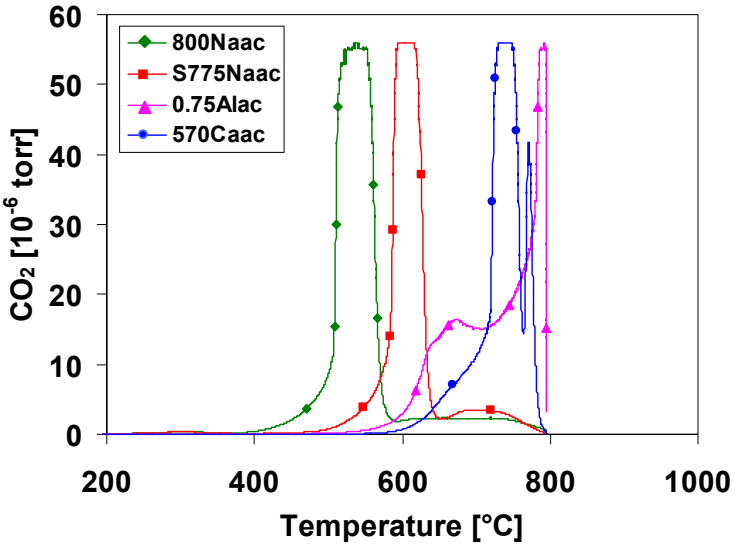

Figure 8.3 CO_2 evolution *vs.* temperature, acetylacetonate doped cokes. *Solid markers used to separate the different lines (not measuring points)*

Table 8-2 Ignition temperatures

	Dopant/Conc.	**$T_{ignition}$ °C**
800Naac	800 ppm Na	460
S775Naac	775 ppm Na + 4.5 wt% DBT	540
0.75Alac	0.75 wt% Al	580
570Caac	570 ppm Ca	650

The results coincide with the previous findings. Sodium oxide is a considerably stronger catalyst than calcium oxide towards the carbon-O_2 gasification reaction. The catalytic activity of sodium is markedly reduced when 4.5 weight percent dibenzothiophene is added. Compared to the others, aluminium oxide is a very weak O_2 gasification catalyst. Although the dopant concentration is about 13 times higher, the ignition temperature of the aluminium acetylacetonate doped coke is only 70 degrees lower than that of the calcium acetylacetonate doped coke.

8.1.2 Surface area development during oxidation

Figure 8.4 and Figure 8.5 show the measured surface area (measured by N_2 adsorption at 77 K) of the acetylacetonate doped coke aggregates (grain size: – 2 + 1 mm) as a function of the percent burnoff achieved during 190 minutes of gasification in the reactivity apparatus. The surface area of the unoxidized coke grains was 0.5 ± 0.1 m^2/g.

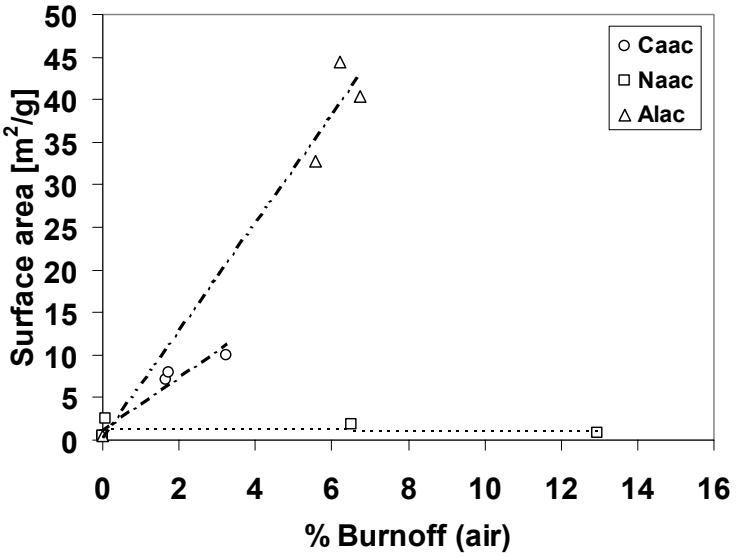

Figure 8.4 Surface area of acetylacetonate doped coke aggregate (- 2 + 1 mm) *vs.* percent burnoff after 190 minutes of air oxidation, "low"-sulfur cokes. *Average value of 2 parallel measurements, standard deviation < 0.5 m^2/g*

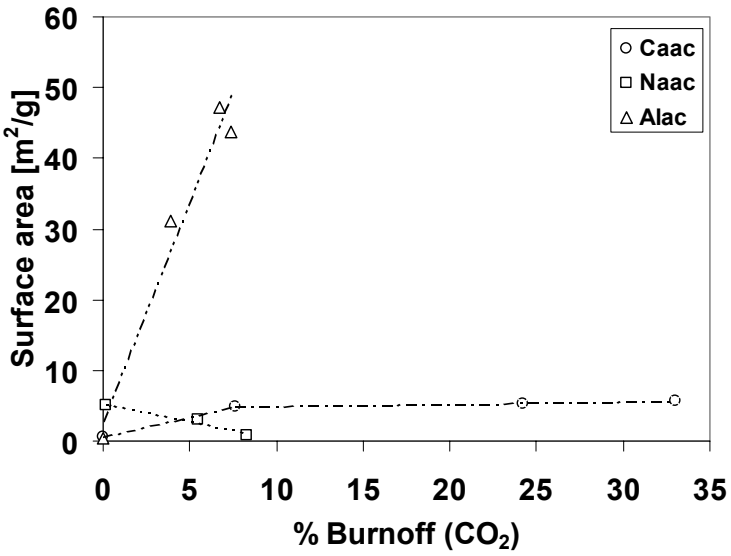

Figure 8.5 Surface area of acetylacetonate doped coke aggregate (- 2 + 1 mm) *vs.* percent burnoff after 190 minutes of CO_2 oxidation, "low"-sulfur cokes. *Average value of 2 parallel measurements, standard deviation < 0.4 m^2/g*

The surface area measurements reveal that the catalysts behave quite differently during gasification. Aluminium oxide is a weak gasification catalyst and the total burnoff achieved is therefore low. However, the surface area increases strongly at increasing burnoff. At 6.5 percent the surface area is as high as 45 m^2/g (both in air and CO_2). The large surface area increase might be ascribed to the formation of a lot of new micropores (small fissures, see Figure 7.5), probably formed by enhanced gasification in the immediate vicinity of the well-dispersed aluminium oxide particles.

Sodium oxide acts as a strong gasification catalyst. Because of the increased gasification rate in the vicinity of the sodium oxide particles, the surface area increases sharply at low burnoffs (CO_2: 0.15 % burnoff: $\rightarrow$ 5.2 m^2/g, air: 0.10 % burnoff: $\rightarrow$ 2.5 m^2/g). However, at higher burnoffs, pore enlargement and coalescence of existing pits and channels appear to be dominating. As a result, the surface area decreases rapidly from its maximum value.

The catalytic behavior of calcium oxide seems to differ from that of sodium oxide. Although calcium oxide acts as a stronger CO_2 gasification catalyst, the surface area remains more or less constant when the total burnoff increases. Hence the formation of new micropores appears to be balanced with the enlargement of the existing ones.

8.2 Cokes doped with fluorides

8.2.1 Relative catalytic strengths

Figure 8.6 and Figure 8.7 compare the reactivities of the fluoride doped "low"-sulfur cokes. Due to high dopant levels and low reactivities, the aluminium fluoride doped samples are not included. The catalytic activities of both the "low"-sulfur and "high"-sulfur cokes are tabulated in Table 8-3. In both coke series, calcium fluoride is a considerable stronger CO_2 gasification catalyst than sodium fluoride and cryolite. The sodium fluoride doped cokes are more reactive than the corresponding cokes doped with cryolite. The activities may be ordered as follows: CaF_2 >> NaF > Na_3AlF_6 (both "low"-sulfur and "high"-sulfur cokes). The activity orders towards airburn are: NaF >> Na_3AlF_6 >> CaF_2 ("low"-sulfur cokes) and CaF_2 > NaF > Na_3AlF_6 ("high"-sulfur cokes). In the same manner as for the acetylacetonate doped cokes, the catalytic activities of sodium fluoride and cryolite towards the air gasification reaction are reduced when 4.5 wt% dibenzothiophene is added to the coke precursor. The activities towards the CO_2 gasification reaction remain nearly unchanged. The catalytic activity of calcium fluoride is not affected by the dibenzothiophene additions.

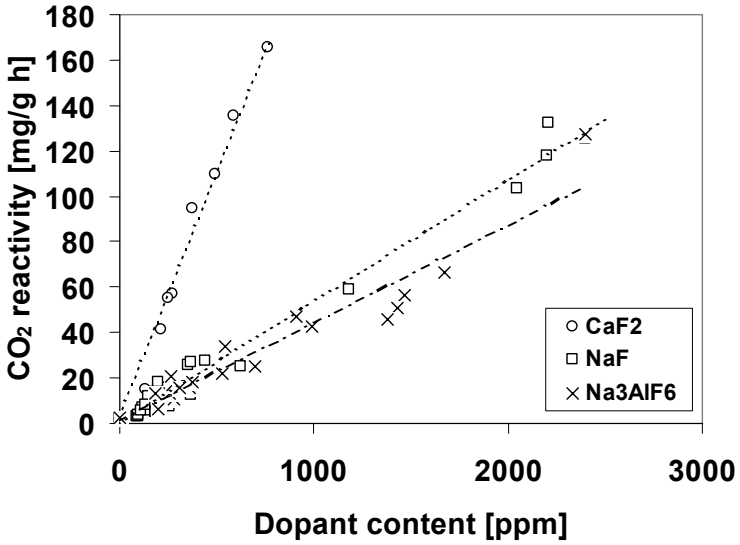

Figure 8.6 CO_2 reactivity (960 °C) *vs.* analyzed dopant concentration, cokes doped with fluorides ("low"-sulfur)

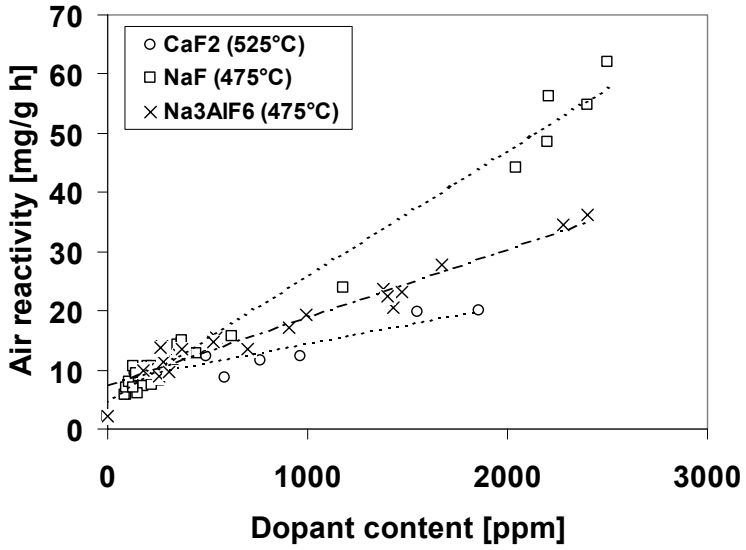

Figure 8.7 Air reactivity *vs.* analyzed dopant concentration, cokes doped with fluorides ("low"-sulfur)

Table 8-3 Catalytic activities towards air and CO_2 gasification, cokes doped with fluorides

Catalyst	Catalytic activity			
	Air gasification *525 °C*		CO_2 gasification *960 °C*	
	"low"-sulfur cokes	"high"-sulfur cokes	"low"-sulfur cokes	"high"-sulfur cokes
CaF_2	0.006	0.006	0.208	0.208
Na_3AlF_6	0.012 [1]	0.004 [1]	0.043	0.043
NaF	0.021 [1]	0.005 [1]	0.054	0.052

[1] Reactivity measured at 475 °C

Aluminium fluoride acts as a gasification inhibitor rather than a catalyst.

As discussed in chapter 4.3, the difference between the sodium fluoride and cryolite doped cokes does probably mainly arise from the formation of different amounts of inhibiting fluorine gases.

8.2.2 Surface area development during oxidation

Figure 8.8 and Figure 8.9 show the measured surface area of the fluoride doped coke samples (aggregate grain size: – 2 + 1 mm) as a function of the percent burnoff achieved during 190 minutes of gasification in the reactivity apparatus.

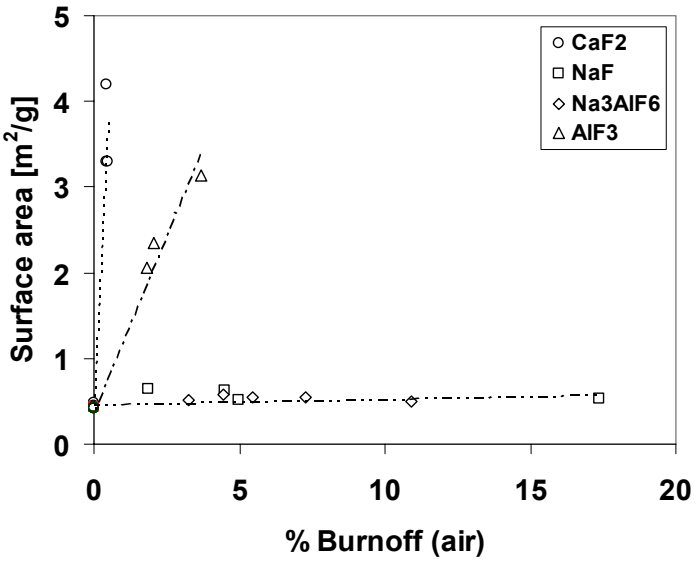

Figure 8.8 Surface area of fluoride doped coke aggregate (- 2 + 1 mm) *vs.* percent burnoff after 190 minutes of air oxidation, "low"-sulfur cokes. *Average value of 2 parallel measurements, standard deviation < 0.3 m^2/g*

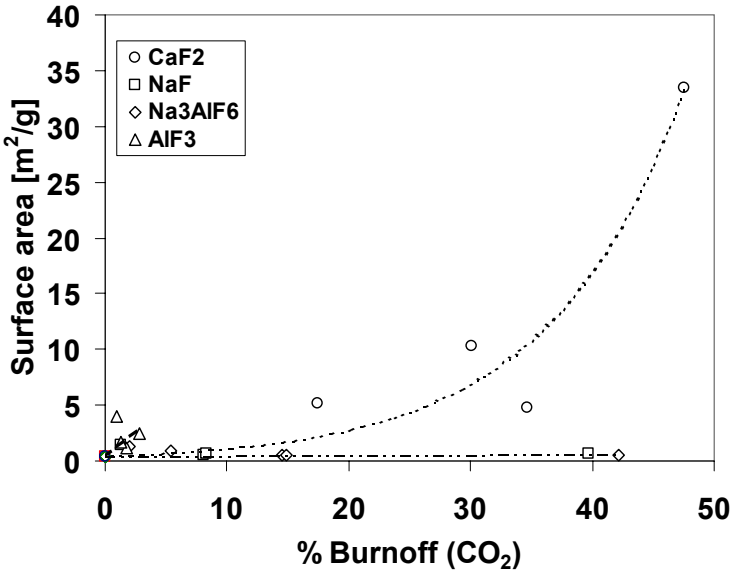

Figure 8.9 Surface area of fluoride doped coke aggregate (- 2 + 1 mm) *vs.* percent burnoff after 190 minutes of CO_2 oxidation, "low"-sulfur cokes. *Average value of 2 parallel measurements, standard deviation < 0.3 m^2/g*

The surface area of the unoxidized coke grains was 0.4 ± 0.2 m^2/g. During air oxidation, the fluorides appear to behave in the same manner as the corresponding oxides (see Figure 8.4). The surface area of the calcium fluoride and aluminium fluoride doped cokes increases strongly with increasing burnoff, while the surface area of the sodium fluoride and cryolite doped cokes is nearly unaffected. There is no difference between the sodium fluoride and cryolite doped cokes. During gasification in CO_2, the aluminium fluoride and sodium fluoride/cryolite doped samples show the same surface area development trends as the cokes doped with aluminium and sodium acetylacetonate (Figure 8.5). For the calcium fluoride doped cokes, formation of new micropores appears to dominate over enlargement and coalescence of existing ones. Calcium fluoride maintains its dispersion to higher catalyst loadings than calcium oxide, and because of this, the surface area of the calcium fluoride doped cokes increases in the entire burnoff interval.

8.3 Influence of sulfur on catalytic activities

Previously, pyrolysis studies have shown that dibenzothiophene is stable to temperatures well above 950 °C [91-93]. Thus it is expected that only minor amounts of elemental sulfur are released by thermal decomposition of the sulfur-containing aromatic molecules during carbonization and calcination of the "high"-sulfur cokes. However, as the carbon matrix is gasified, the aromatically bound sulfur is expected to be liberated as sulfur compounds in low oxidation states. In catalyzed carbon gasification, these sulfur compounds may cause considerable catalytic activity losses, the reason being the formation of extremely stable sulfur compounds or sulfur surface complexes [94].

According to Hume *et al.* [95], sulfur reduces the catalytic activity of sodium by forming a stable non-mobile Na-S-O complex that prevents sodium from migrating to and catalyzing the gasification reaction at the active sites:

$$Na_xO_y + S_z \quad \Rightarrow \quad Na_xS_zO_y \qquad \textbf{Eq. 8.5}$$

Müftüoglu and Øye [9] reported that additions of ZnS reduced the CO_2 reactivity of carbon anodes impregnated with Na_2CO_3. ZnS was added in stoichiometric amounts relative to Na_2CO_3. The authors adopted the mechanism initially proposed by Fox and White [40] (see Eq. 4.1-4.3) and the observed sodium activity reduction was ascribed to the formation of Na_2S which reduces the free sodium vapor pressure:

$$ZnS\ (s) + 2\ Na\ (g) \quad \Leftrightarrow \quad Na_2S\ (s) + Zn\ (g) \qquad \textbf{Eq. 8.6}$$

$$\Delta G^0_{960°C} = -128.3\ kJ/mol$$

In the present work, the air reactivities of the sodium contaminated cokes are significantly reduced when 4.5 weight percent dibenzothiophene is added to the liquid coke precursors. The CO_2 reactivities on the other hand, are not affected by the sulfur additions. EDX-analyses revealed that the sulfur content of the sodium oxide particles at the surface of the unoxidized "high"-sulfur cokes only was a little higher than the sulfur content of the particles at the surface of the corresponding "low"-sulfur cokes (6 – 8 at% *vs.* 4 – 5 at%). After the air reactivity tests, the sulfur content of the particles at the "high"-sulfur cokes was slightly enhanced while it, after the CO_2 reactivity tests, was reduced to the same level as for the "low"-sulfur cokes (~ 5 at%). However, even after the air reactivity tests, the particles' sulfur content is too low to accomplish a bulk chemical transformation of the active sodium species into stoichiometric Na_2S. Instead it is believed that the sulfur, which is released from the gasifying coke matrix, adsorbs to the surface of the sodium catalyst. The sulfur adsorption complexes may block the active sites at the surface of the catalyst particles and lower their catalytic activity. The higher the coke reactivity is, the more sulfur becomes available for catalyst poisoning.

The sodium-sulfur adsorption complexes appear to be thermally unstable at the CO_2 gasification temperature.

Otto *et al.* [81] studied the effect of H_2S and SO_2 on the alkaline earth (Ca, Sr, Ba) catalyzed steam gasification of graphite. During the measurements, two distinguishable effects of sulfur-deactivation were observed. The first one was an elimination of the active carbon sites presumably by adsorption of H_2S or sulfur complexes. This deactivation mode was quickly established and it was completely reversible. The second effect was a chemical change of the catalytically active species, which was accompanied by a consistent increase in the apparent activation energy for the reaction. This sulfur poisoning was found to be far more important in counteracting catalysis by alkaline earths than competitive deactivation by adsorption of H_2S or SO_2.

The CO_2 reactivity of the calcium acetylacetonate doped cokes is markedly reduced when 4.5 weight percent dibenzothiophene is added to the tar oil prior to carbonization. The results from the EDX-analyses support sulfur poisoning of the catalytically active calcium oxide particles. The sulfur content of the calcium particles is too low to account for a complete transformation of the catalytically active phase into *e.g.* CaS. Hence, the CaO particles are

most likely deactivated by the formation of Ca-S adsorption complexes. In difference to the Na-S adsorption product, the Ca-S complex appears to be thermally stable at the CO_2 gasification temperature. Calcium oxide shows a low catalytic activity towards the air gasification reaction, and because of this, the amount of sulfur released from the coke matrix is too low to provide a measurable air reactivity reduction.

The catalytic activities of calcium fluoride and aluminium oxide are not affected by the dibenzothiophene additions. As analyzed by EDX, there was no enrichment of sulfur in neither the CaF_2 particles nor the Al_2O_3 particles after the reactivity measurements. A plausible reason is the high positive free energy changes for the sulfide formations:

$$CaF_2 + S_{8/8} \quad \Leftrightarrow \quad CaS + F_2\,(g) \qquad \textbf{Eq. 8.7}$$

$\Delta G^0_{525°C} = 634.3$ kJ/mol
$\Delta G^0_{960°C} = 581.9$ kJ/mol

$$Al_2O_3 + 3\,S_{8/8} \quad \Leftrightarrow \quad Al_2S_3 + 3/2\,O_2\,(g) \qquad \textbf{Eq. 8.8}$$

$\Delta G^0_{525°C} = 743.5$ kJ/mol
$\Delta G^0_{960°C} = 649.8$ kJ/mol

As for the calcium acetylacetonate doped cokes, the air reactivity of the calcium fluoride doped cokes and the air and CO_2 reactivity of the aluminium acetylacetonate and aluminium fluoride doped cokes are very low. Thus only minor amounts of sulfur are expected to be liberated during the reactivity measurements.

8.4 Relative catalytic strength, fluorides versus oxides

As mentioned in chapter 8.1.1, it has been proposed that the covalent character of the O-M bond in the phenolate group determines the catalytic activity of an alkali or alkaline earth salt [37]. However, the covalent character is not only affected by the cation, but also by the associated anion [55]. For example, anions with high charge densities will be more effective in altering the electron distribution and polarizability of the metal-oxygen bond than anions with low charge densities. It has also been suggested that some anions could compete with the carbon material for the alkali and alkaline earth cations and thus inhibit the formation of metal-carbon complexes [55]. In general it has been found that the alkali salts of weak acids are good gasification catalysts, while those of strong acids are poor (see Figure 2.13).

The fluoride ion has a high charge density while the charge density of the cryolite anion (AlF_6^{3-}) is low. The charge density of the oxygen anion is less than that of the fluoride anion. Thus, according to the above theory, the fluorides (NaF and CaF_2) should be expected to be less catalytic active than the corresponding oxides. Cryolite on the other hand, should be a strong gasification catalyst. However, as seen from Figure 8.10 the findings of the present work do not follow this theory entirely. The cokes doped with cryolite are less reactive than those doped with sodium fluoride (see discussion in chapter 4.3). Although the intrinsic coke reactivity is lower, the apparent catalytic activity of sodium oxide towards airburn is equal to the activity of sodium fluoride. Towards the CO_2 gasification reaction the activity of sodium oxide is a bit lower than the activity of cryolite. Calcium fluoride appears to be a slightly

stronger catalyst towards airburn than calcium oxide. The two calcium phases show an equal activity towards the CO_2 gasification reaction.

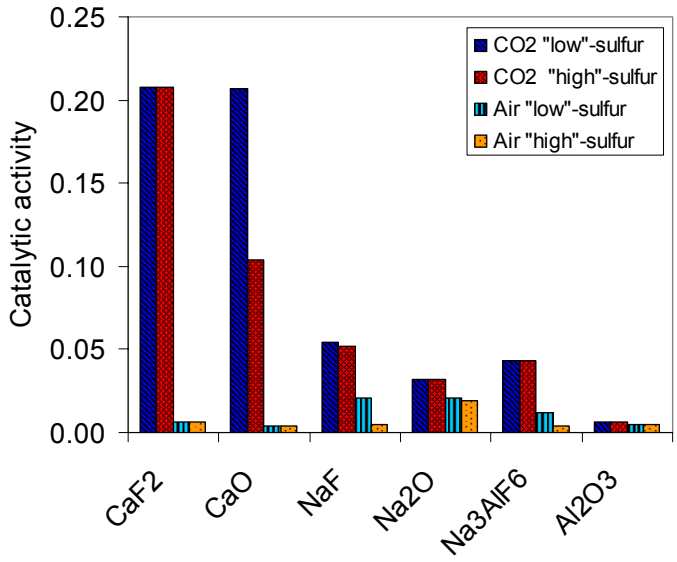

Figure 8.10 Comparison of catalytic activities

For the "low"-sulfur cokes, the activity orders may be summarized as:

CO_2 gasification: $CaF_2 = CaO >> NaF > Na_3AlF_6 > Na_2O >> Al_2O_3$

Air gasification: $NaF = Na_2O >> Na_3AlF_6 >> CaF_2 > Al_2O_3 > CaO$

It should be noted that the air reactivities of the sodium doped cokes are measured at 475 °C instead of at the standard reaction temperature of 525 °C. The ranking is however not expected to be affected this.

Due to a varying degree of sulfur poisoning, the "high"-sulfur cokes follow a slightly different order with respect to air reactivity. The activities may be arranged as:

CO_2 gasification: $CaF_2 >> CaO >> NaF > Na_3AlF_6 > Na_2O >> Al_2O_3$

Air gasification: $Na_2O >> CaF_2 = Al_2O_3 > NaF > Na_3AlF_6 = CaO$

However, since different coke and catalyst precursors are used, it might be dangerous to compare the reactivities only on the basis of the bulk metal concentrations. For example, the acetylacetonates are homogeneously soluble in the aromatic oil and it is thus expected that the catalyst particles are much more finely dispersed in these cokes than in the cokes doped with the inorganic salts. Hence, in order to perform real quantitative comparisons, variables such as catalyst dispersion and number of active sites should also be taken into consideration (turnover frequency).

9 Gas reactivity of industrial anodes

9.1 Impurities in recycled anode butts

Prebaked anodes consist of about 50 – 65 % petroleum coke, 14 – 17 % coal tar pitch and 15 – 30 % recycled anode butts. The anodes are contaminated by a number of inorganic impurities. Some follow the anode raw materials while others are introduced through the anode manufacturing process. In the production of prebaked anodes, ball mills are the most important iron contamination source. Vanadium and nickel are common impurities in petroleum cokes, while coal tar pitches may contain considerable amounts of zinc and lead. In addition, some pitch distillers introduce sodium to neutralize the small amounts of HCl formed in the still.

The crushed anode butts are regarded as one of the most important contamination sources. When the prebaked anode butts are removed from the cells, the surfaces are covered with frozen electrolyte. Hence, if the butts are not properly cleaned before crushing and recycling, considerable amounts of bath contaminations may be transferred to the new anodes. The butts addition particularly contaminates the filter dust and the ball mill fines if the coke and butts grains are not processed separately in the paste plant [96]. Due to different procedures, the contamination level and particle sizes may vary from anode plant to anode plant.

Sørlie [97] compared analysis data for return-butts from two Norwegian smelters (A and B). The average content of sodium, aluminium, calcium and fluorine during a period of 27 months are given in Table 9-1 below. Smelter A has good routines for anode butts cleaning and is regarded as “Best in Class”.

Table 9-1 Impurities in butts (particles > 50 mm). *Data taken from Sørlie* [97]

	Smelter A	**Smelter B**
Na	628 ppm	1351 ppm
Al	470 ppm	1113 ppm
Ca	95 ppm	167 ppm
F	2272 ppm	3717 ppm

Over a period of 10 months, Fischer and Perruchoud [10] sampled and tested about 2000 anode butts taken from 4 different smelters. Table 9-2 compares the average impurity profile of the initial anode population and the 500 (25 %) “hardest” and “softest” of the tested butt samples. The selection was based on measurements of the compressive strength of the samples.

Table 9-2 Average impurity level of 2000 butt samples compared with the level in the initial anodes. *Data taken from Fischer and Perruchoud* [10]

	200 Anodes	500 (25%) "Hardest" butts	500 (25%) "Softest" butts
V	110 ppm	110 ppm	115 ppm
Fe	220 ppm	230 ppm	270 ppm
Na	300 ppm	600 ppm	500 ppm
Ca	50 ppm	80 ppm	70 ppm
F	100 ppm	900 ppm	750 ppm

Table 9-3 shows the estimated sodium and calcium content of 10 fictitious prebaked anodes (labeled A-Bx 15% and A-Bx 30%) containing 15 or 30 percent butts with varying contamination profiles (B1–B5, numbers based on findings from Sørlie [97] and Fischer *et al.* [10]). Since acidic baths normally are used, all sodium is believed to be present as Na_3AlF_6. Any excessive aluminium (not bound as Na_3AlF_6) is expected to be found as AlF_3 or Al_2O_3. Calcium exists mainly as CaF_2. Some sodium and calcium are also introduced as impurities in the petroleum coke and the binder pitch. Petroleum cokes normally contain about 20 – 100 ppm Na and 10 – 50 ppm Ca [11], while coal-tar pitches may contain as much as 150 – 200 ppm Na and 50 – 150 ppm Ca [98]. However, since the aim of this work is to investigate the effect of butt contaminations on the anode reactivity, these contamination sources are not included.

Table 9-3 Contamination profile of 10 fictitious prebaked anodes (A-Bx 15% and A-Bx 30%) containing 15 or 30% butts with varying contamination profiles (B1 – B5).
All Na and Ca exist as Na_3AlF_6 and CaF_2. Excess Al bound as AlF_3 or Al_2O_3

	Na_3AlF_6		AlF_3/Al_2O_3	CaF_2
Sample	**Na**	**Al (total)**	**Al (excess)**	**Ca**
	ppm			
B1	300	300	183	50
B2	600	600	365	80
B3	900	900	548	110
B4	1200	1200	731	140
B5	1500	1500	913	170
A-B1 15%	45	45	27	8
A-B2 15%	90	90	55	12
A-B3 15%	135	135	82	17
A-B4 15%	180	180	110	21
A-B5 15%	225	225	137	26
A-B1 30%	90	90	55	15
A-B2 30%	180	180	110	24
A-B3 30%	270	270	164	33
A-B4 30%	360	360	219	42
A-B5 30%	450	450	274	51

Assuming no cocatalytic effects between cryolite, aluminium fluoride and calcium fluoride (see chapter 6), the anode reactivity might be expressed as:

$$R_{est.} = a_{Na3AlF6} \cdot x_{Na} + a_{AlF3} \cdot x_{Al\,(AlF3)} + a_{Al2O3} \cdot x_{Al\,(Al2O3)} + a_{CaF2} \cdot x_{Ca} + R_0 \qquad \textbf{Eq. 9.1}$$

where $a_{Na3AlF6}$, a_{AlF3}, a_{Al2O3} and a_{CaF2} are the catalytic activities of Na_3AlF_6, AlF_3, Al_2O_3 and CaF_2, R_0 the reactivity of a pure reference coke and x_{Na}, x_{Ca}, $x_{Al(AlF3)}$ and $x_{Al(Al2O3)}$ the concentration (ppm) of sodium, calcium and aluminium bound as Na_3AlF_6, CaF_2, AlF_3 and Al_2O_3 respectively.

The catalytic activities may be taken from the graphs showing the reactivities of the laboratory made coke samples as a function of the analyzed dopant concentrations (see chapter 4, 5 and 7). Equation 9.2 and Figure 9.1 show how the estimated anode CO_2 reactivity, $R_{CO2,est.}$, varies as a function of the anode sodium and calcium content. Since there is no reactivity data for the single carbonized AlF_3 and Al_2O_3 doped cokes at 960 °C, these terms are not included (due to different optical coke textures the data for the 2x carbonized cokes are not applicable). However, the excess aluminium concentrations are low (< 300 ppm) and the influence of AlF_3 and Al_2O_3 is thus expected to be negligible (see Figure 7.18, 7.20 and 7.38).

$$R_{CO2,est.} = 0.043 \cdot x_{Na} + 0.208 \cdot x_{Ca} + 4.6 \qquad \textbf{Eq. 9.2}$$

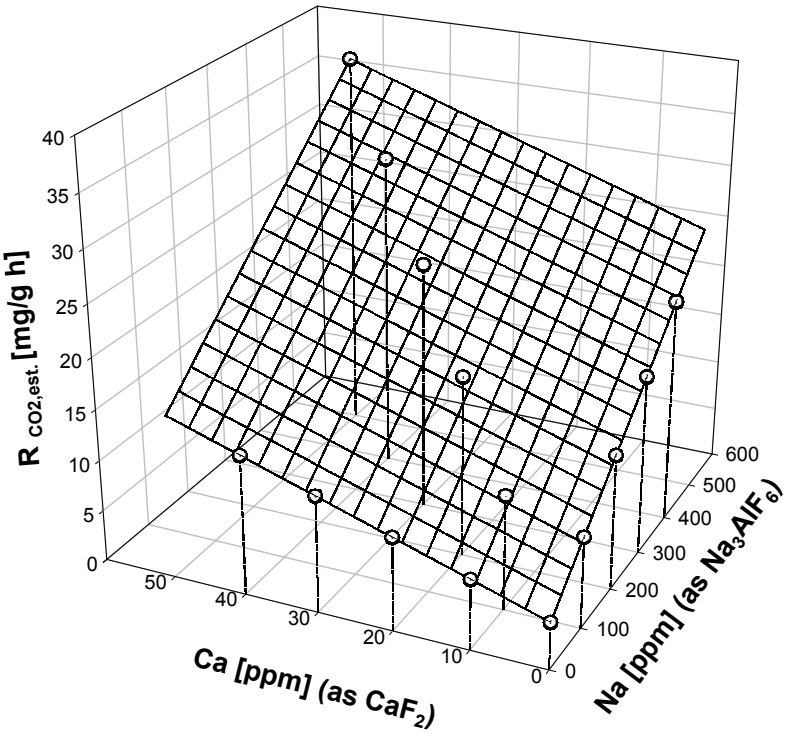

Figure 9.1 Estimated CO_2 reactivity of prebaked anode as a function of anode sodium and calcium content. *Assumes all sodium present as Na_3AlF_6. All calcium bound as CaF_2*

Since the air reactivities of the laboratory made cokes were measured at three different temperatures (Na_3AlF_6: 475 °C, CaF_2: 525 °C, AlF_3 and Al_2O_3: 550 °C), it is not possible to make a similar expression for the anode air reactivity.

Table 9-3 and Figure 9.1 emphasize the importance of proper butt cleaning. If the butts sodium and calcium content are increased from 300 and 50 ppm to 1500 and 170 ppm respectively, the anodes CO_2 reactivity will increase with almost 200 percent from 12 mg/g·h to 35 mg/g·h (assumes addition of 30 % butts). It should however also be pointed out that since the catalytic activity is strongly related to the carbon-catalyst contact, the anode gas reactivity is also dependent on the distribution of the bath particles in the anode dry aggregate. When studying the effect of increasing fines bath content on the CO_2 reactivity and air ignition temperature of the binder matrix, Smith *et al.* [96] found that the overall anode reactivity was reduced by more than 50 percent when the average diameter of the bath powder was increased from 50 to 200 μm.

9.2 Internal gasification

In order to investigate to what extent carbon gasification occurs inside industrial anodes, prebaked anode butts and core samples from Søderberg anodes (drilled out from center of cold anodes) are characterized in terms of air permeabilities, contamination profiles and reactivities towards air and CO_2 gasification. The properties are related to findings from electron microscopy examinations. The Søderberg anode samples used in this study are received from four different smelters (A, B, L and M), all operating vertical stud Søderberg cells (dry anode paste). The prebaked anode butts are all taken from a single smelter (M).

9.2.1 Prebaked anodes

Figure 9.2 visualizes the different reaction and temperature zones of an operating prebaked anode. The consumption mechanisms associated with each zone are given in Table 9.4.

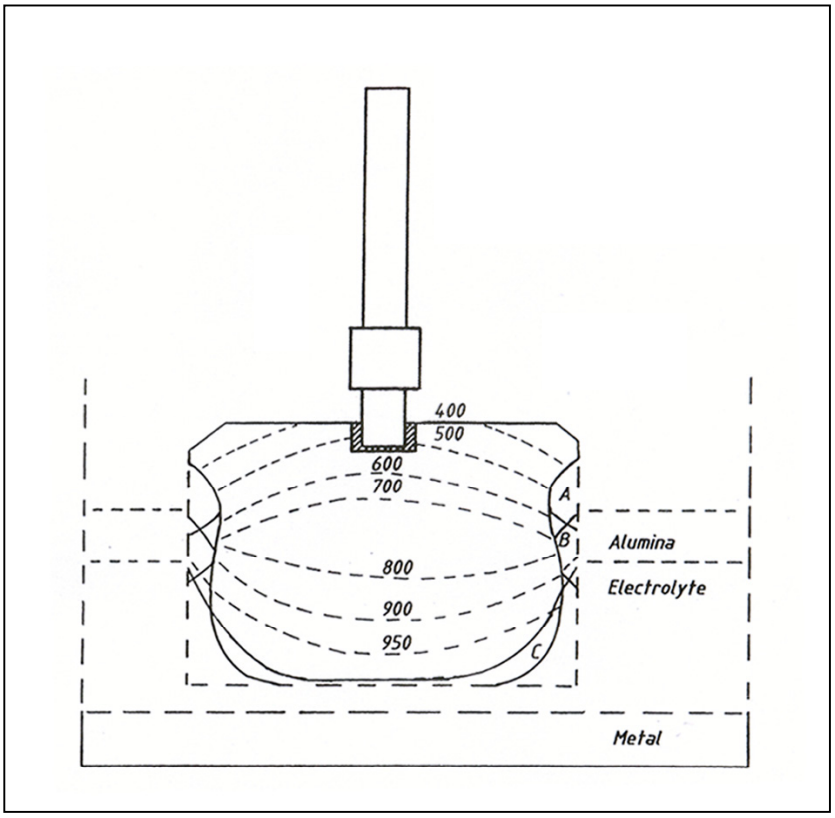

Figure 9.2 Isotherms and reaction zones of operating prebaked anode (newly set). *Taken from Foosnæs and Naterstad* [99]

Table 9-4 Anode consumption mechanisms. *Zones A, B and C refers to Figure 9.2*

Zone	Reactant gas	Typical temperature range °C	Consumption mechanism
A	Air	300-350	Air gasification, reaction controlled
A	Air	450-530	Dusting
A	Air	530-700	Mass transfer/internal diffusion controlled, Self ignition by 530-570 °C
B	CO_2	750-950	CO_2 gasification, Reaction/internal diffusion controlled
C	CO_2	920-960	Viscous flow/internal diffusion controlled
Working surface	CO_2	950-970	Electrolytic consumption Abrasion by electrolyte/aluminium oxide

By visual inspection, the working surface of all the collected anode butts appeared hard and smooth. No carbon could be removed by rubbing a finger across it. However, examinations at high magnifications in the electron microscope revealed the existence of considerable micro roughness.

Figure 9.3 shows a SEM-micrograph of the working surface of one of the anode butts (PB 1). The anode surface has undergone massive oxidation and a lot of depressions and pore channels (Ø ~ 50 – 300 μm) are formed. The carbon-CO_2 reaction does not occur on a polarized anode surface (see chapter 2.1.2), and the topographical changes are therefore assumed to mainly arise from electrolytic oxidation (CO_2 formation) on the active sites However, since the working surface is continuously consumed, some of the observed features may arise from foregoing internal CO_2 gasification. Some gasification may also have occurred when the after the hot anode butts are removed from the cell. Because of the high current density at the working surface (0.80 A/cm^2), the electrolysis is mass transfer controlled and the binder and aggregate phases are consumed at a nearly equal rate. Hence few aggregate grain protrusions (rough spots) are formed. However, due to pore diffusion and the hydrostatic pressure generated by the electrolyte, some CO_2 produced by the anode reaction, will enter the interior of the anode. The gas percolates the open pore network and reacts with accessible carbon within the anode body.

Figure 9.4 shows a SEM-micrograph of the binder coke about 0.5 cm above the working surface. Although distinct signs of CO_2 gasification is observed (pitting and edge-recession), the binder phase is mostly structurally intact.

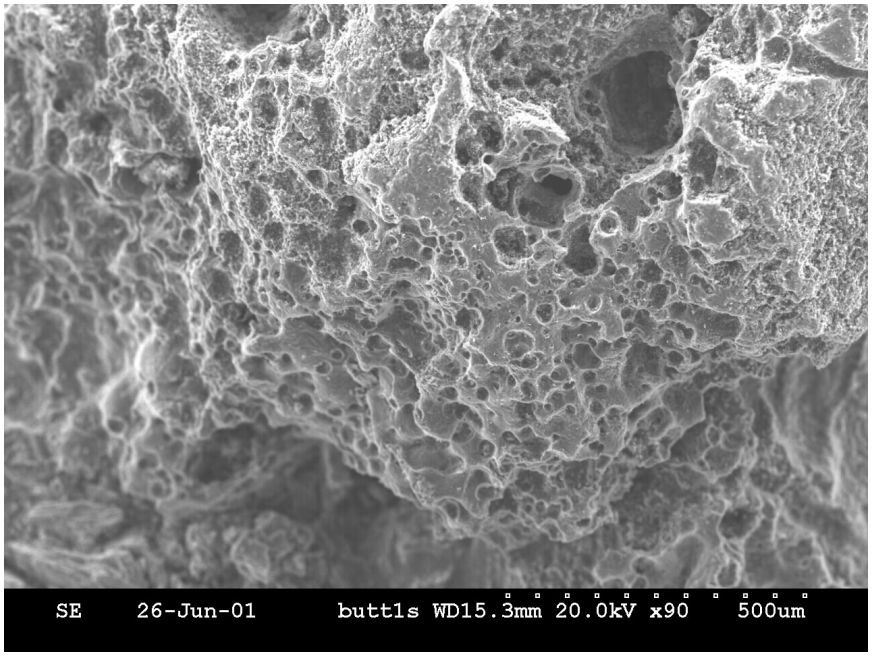

Figure 9.3 Working surface of prebaked anode. *PB 1*

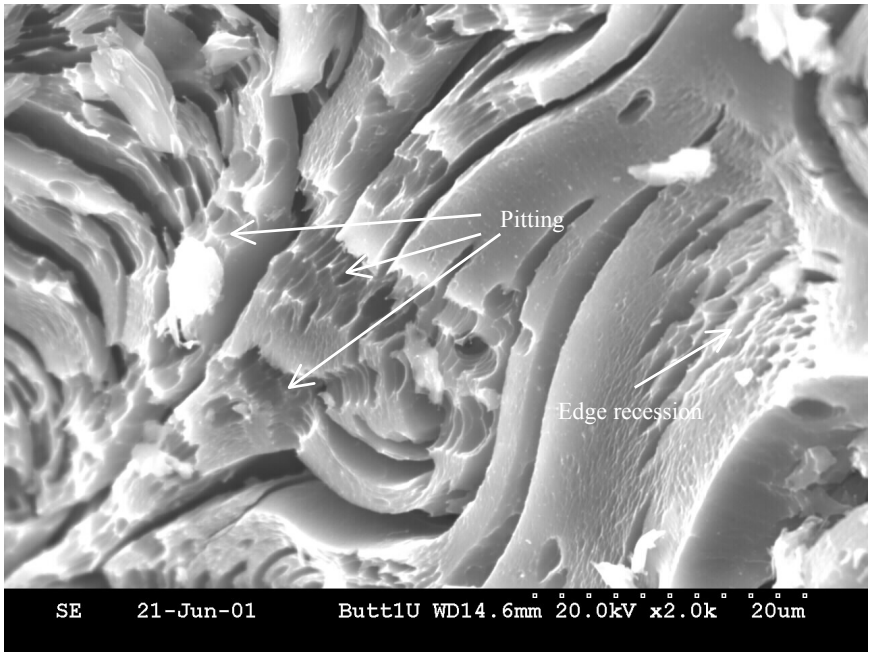

Figure 9.4 Textural changes caused by CO_2 gasification inside prebaked anode. *Binder coke, about 0.5 cm above working anode surface, PB 1*

In order to investigate how far into the anodes gasification occurs, a number of core samples (Ø 50 mm, height = local butt height) were drilled out from 3 different anode butts. The butts' dimensions and the location of the core samples are shown in Figure 9.5.

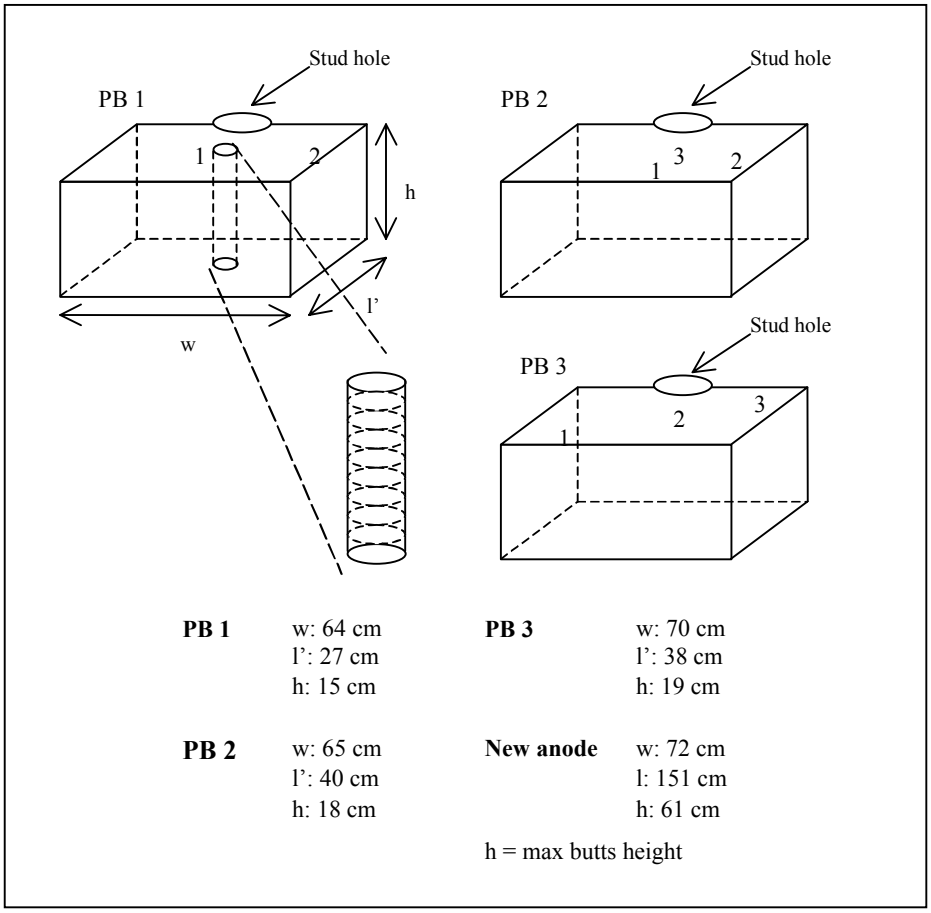

Figure 9.5 Dimensions of prebaked anode butts. *Only 1/3 of original anode butts are shown; length (l') ≈ 1/3 total butts length. Location of core samples indicated by numbers. Core height = local height of butts*

After drilling, the core samples were dried and cut into slices of 20 mm height. The air permeability of the different slices was determined by use of an AP-50 permeability apparatus from R&D Carbon, Switzerland. The measured permeabilities are tabulated in Table 9-5. A graphical presentation is given in Figure 9.6.

Table 9-5 Air permeability of anode butts. *Slices from core samples: Ø 50 mm, h 20 mm. Height = distance from slice center to working surface*

Slice	Height *cm*	PB 1		PB 2			PB 3		
		Core 1	Core 2	Core 1	Core 2	Core 3	Core 1	Core 2	Core 3
1	1.5	0.82	0.74	1.12	0.83	0.54	0.95	0.78	0.78
2	3.5	0.52	0.44	0.60	0.47	0.45	0.64	0.63	0.62
3	5.5	0.61	0.45	0.74	0.99	0.54	0.42	0.58	0.75
4	7.5	0.62	0.54	0.96	0.90	0.96	0.46	0.62	0.62
5	9.5	0.88	0.63	0.81	1.91	1.11	0.44	0.70	0.76
6	11.5	1.06	0.69	0.49	1.90	1.50	0.41	0.92	
7	13.5							2.23	
8	15.5							3.22	
Average		**0.75**	**0.58**	**0.79**	**1.17**	**0.85**	**0.55**	**1.21**	**0.71**
STD		**0.20**	**0.13**	**0.23**	**0.60**	**0.41**	**0.21**	**0.98**	**0.08**

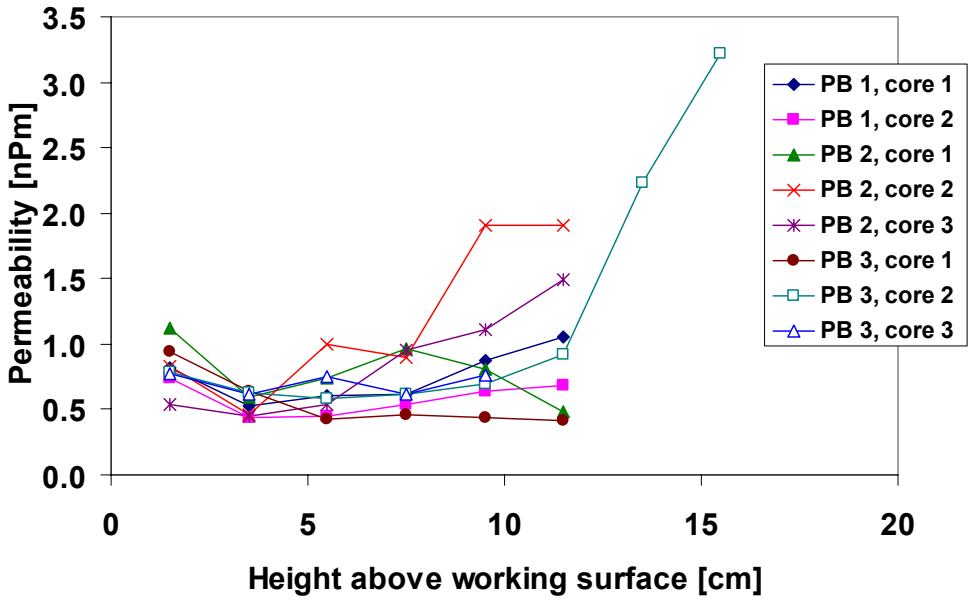

Figure 9.6 Air permeability *vs.* height above working surface, prebaked anode butts

The average air permeabilities vary between 0.55 and 1.21 nPm. Due to internal CO_2 gasification, the permeability of the lowest 0 – 3 centimeters of the anode butts (slice 1) is slightly higher than the permeability of the next 3 – 7 centimeters (slice 2, 3 (and 4)). Previously, similar observations have been made by Cutshall and Bullough [100, 101] who investigated the influence of baking temperature, current density and anode effects on anode gasification during electrolysis. Their investigations showed that due to the mould forming procedure, the permeability of the lower 5 cm of a non-electrolyzed anode block was considerably lower than the permeability of the rest of the block (~ 3.5 nPm *vs.* ~ 5 nPm). After 2 days of electrolysis, the permeability of the lower 5 cm was increased to about 6 nPm whereas the permeability of the rest of anode remained unchanged [101].

In an exhaustive study of internal CO_2 gasification, Sadler and Algie [102] found that in the zone immediately above the working surface (0 – 1 cm) the anode porosity was a factor of 1.4 greater than in the bulk anode. Based on porosity measurements, they found that sub-surface gasification occurred to a height of around 4 cm above the anode working surface.

SEM-examinations of fracture surfaces (core slices cleaved in two) show the porous nature of the lower parts of the anode butts (see micrograph given in Figure 9.7). The pores are relatively large (Ø 50 – 300 µm) and topographical changes characteristic to the carbon-CO_2 reaction (pitting, edge recession and crack opening), are observed on the surface of some of the protruding aggregate grains (see Figure 9.8 and Figure 9.9). The surface textural changes are similar to those observed at the surface of the CO_2-oxidized laboratory made cokes. Most gasification signs are found in the lowest 3 cm of the anode butts. They are only occasionally observed at heights above approximately 4 cm (slice 3).

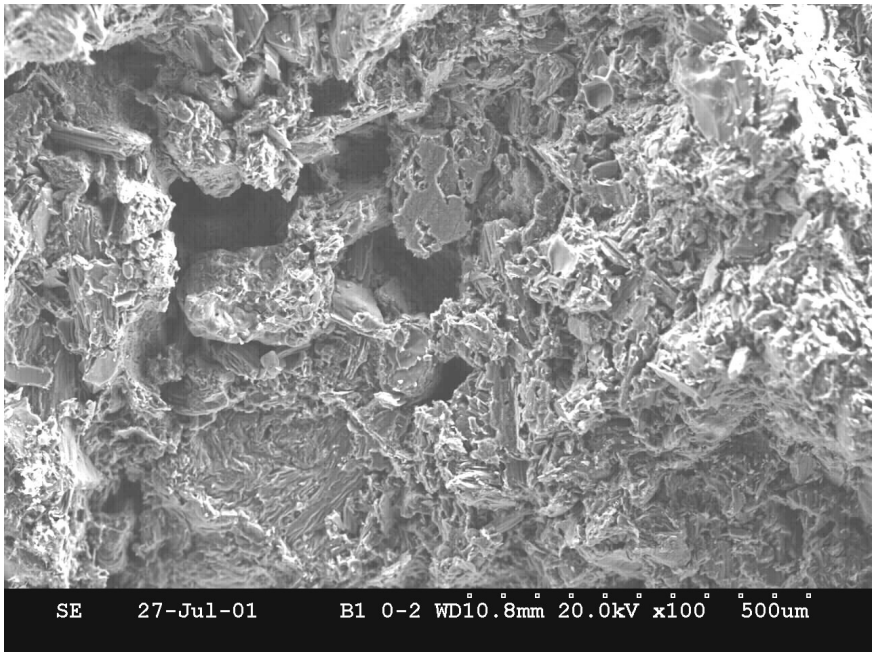

Figure 9.7 CO_2 gasification near anode working surface. *Reactive binder phase selectively oxidized. Fracture surface ~ 1 cm above working surface, PB 1 core 1*

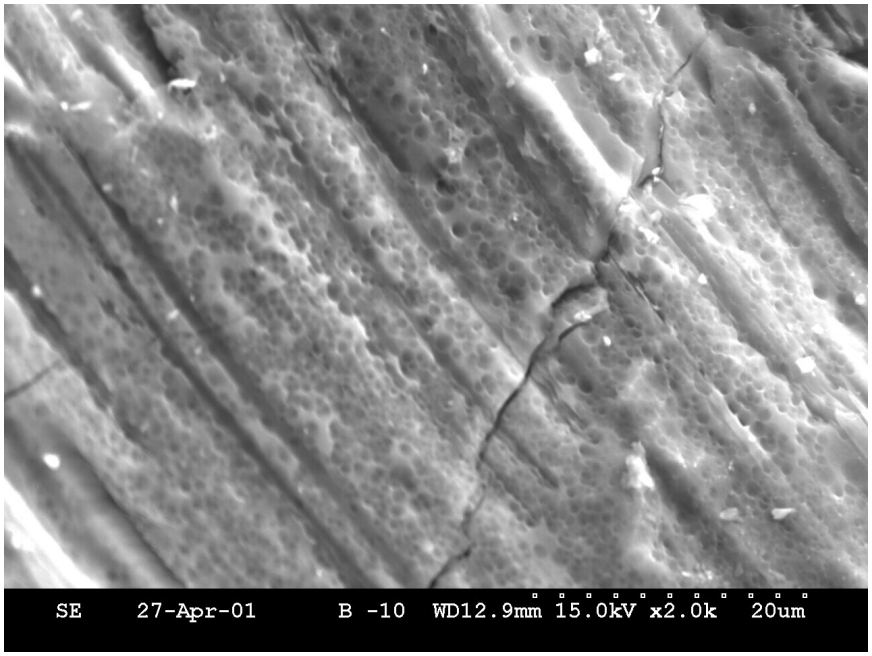

Figure 9.8 Pit formation on aggregate coke grain near anode working surface. *Fracture surface ~ 1 cm above working surface, PB 1 core 1*

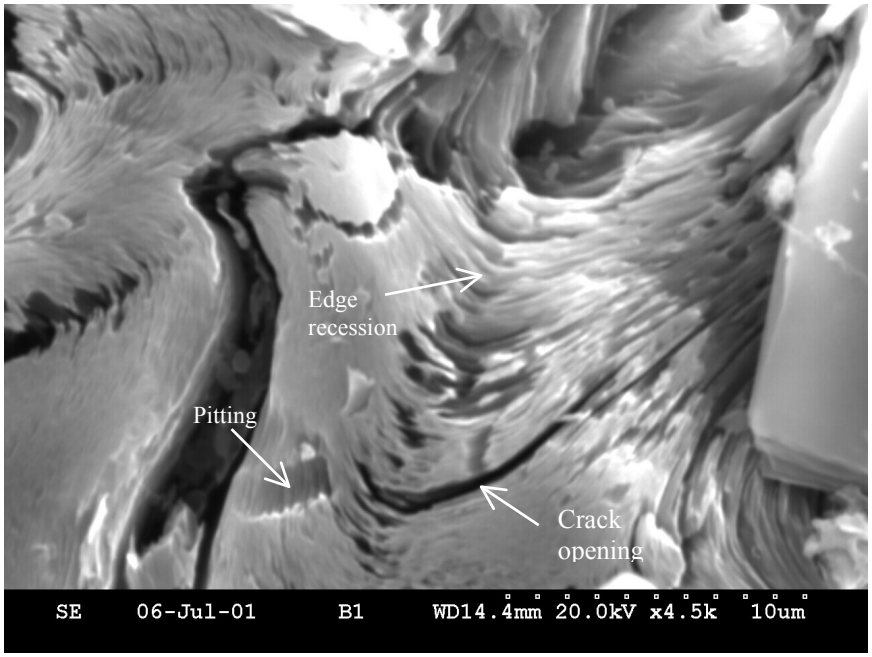

Figure 9.9 Edge recession, pitting and crack formation, aggregate coke grain near anode working surface. *Fracture surface ~ 1 cm above working surface, PB 1 core 1*

As seen from Figure 9.2 and Table 9.4, the internal anode CO_2 gasification is mainly mass transport controlled. In addition to being influenced by the operational temperature and hydrostatic pressure, the rate of diffusion between the anode surface and the reactive sites inside the pores is related to anode bulk properties such as pore size and pore volume. Studies have confirmed the significance of both bulk and Knudsen diffusion (pore size dependent mass transfer, pore size < 0.1 μm) of O_2, CO and CO_2 in carbon anodes [102]. However, in ordinary anodes with major pore size above 5 μm, the main internal transport mechanism of the immersed parts are governed by viscous flow and is hence related to the anode pore distribution and gas permeability. Large feeder pores that can provide CO_2 at relatively high mass transport rates are connected directly to microcracks and smaller pores that provide active surface area for the reaction [102]. Normally, the immersed parts of the anode faces an overpressure of 85 to 95 % CO_2 up to 4 kPa at the wear surface [99]. Increased overpressure by increased anode immersion depth increases the surface area accessible for gasification.

The prebaked anodes studied in this work had an anode immersion depth of 15 – 16 cm. Based on the permeability and SEM results it appears as internal CO_2 gasification is important to a height of about 3 – 5 cm above the working surface. However, since the gas permeability only are influenced by pores larger than 50 μm [85], smaller-scale gasification might have occurred even higher up in the anodes (gasification rate controlled by pore diffusion). Possible gasification signs such as pitting and edge recession are however not observed when studying the fracture surfaces in the electron microscope.

The vertical anode sides experience a much lower current density (normally ~ 0.1 A/cm^2) and are thus more vulnerable to selective oxidation than the working surface. At low current densities, the electrochemical reaction is chemically controlled and the more reactive binder phase is therefore consumed more rapidly than the aggregate phase. Additionally, the vertical anode surfaces may be oxidized by the CO_2 that is transported up along the anode sides. However, CO, which is the predominant electrolytically generated gas at low current densities [103], acts as an inhibitor towards the carbon-CO_2 gasification reaction.

Surface textural changes characteristic to gasification was observed when examining samples taken from the vertical anode sides in the electron microscope (see micrographs given in Figure 9.10). Since the anodes are continuously consumed at the working face, it is uncertain if the observed changes arise from oxidation in air, CO_2 or both.

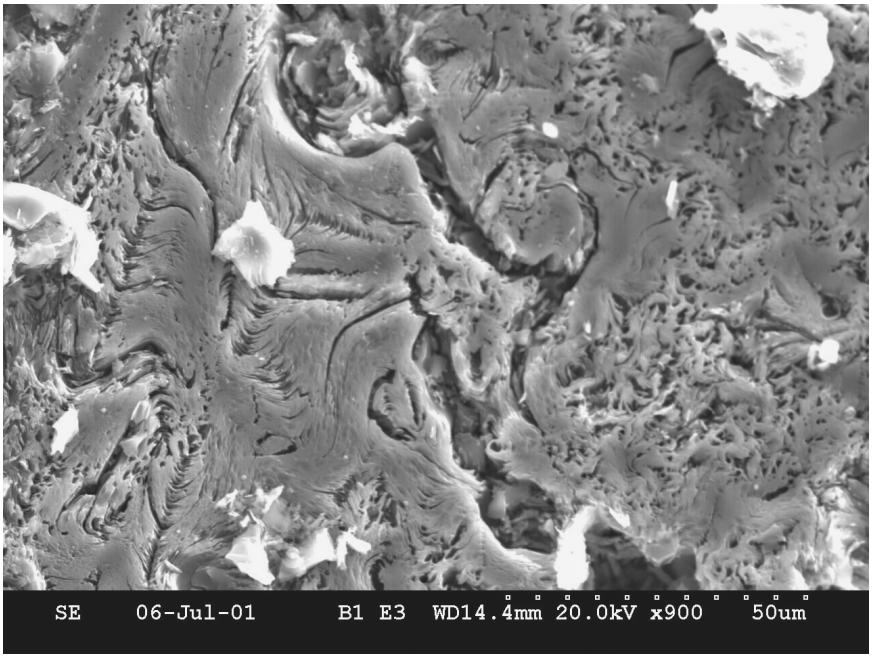

A) About 3 cm above working surface

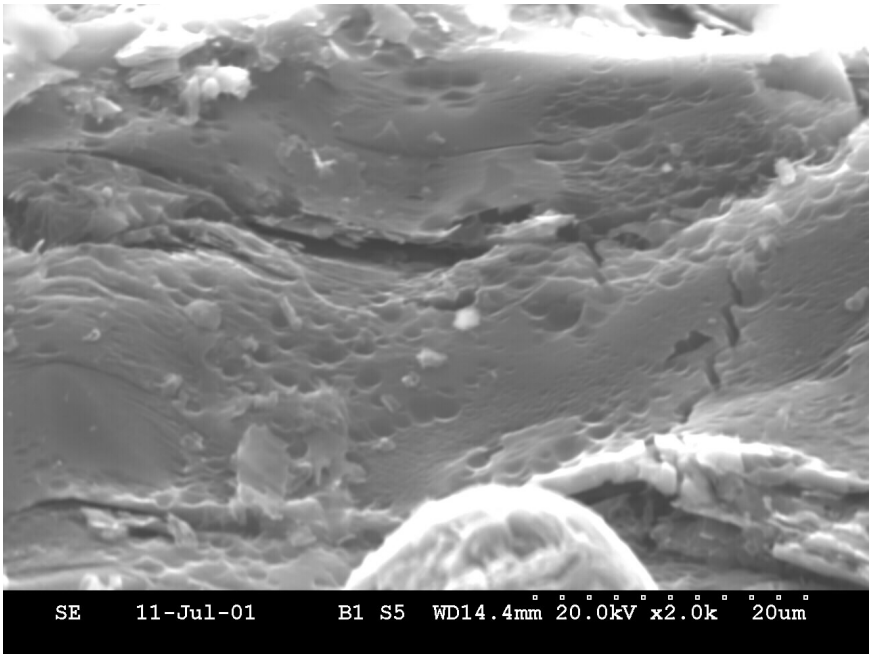

B) About 5 cm above working surface

Figure 9.10 Oxidation of vertical anode sides. *PB 1*

The air permeabilities increase significantly as the anode top is approached (see especially PB 3 core 2, which is taken from a position close to the edge of the anode butts). Air has access to the vertical sides of the prebaked anodes (directly above bath level) only if it leaks in through the top crust cover. If not properly covered by crushed bath and/or alumina, the hot anode tops are exposed to air at atmospheric pressures. Considerably air oxidation might then occur. The SEM-micrograph given in Figure 9.11 shows the high porosity of the upper parts of the anodes. As in the lower parts, the binder phase has been selectively oxidized.

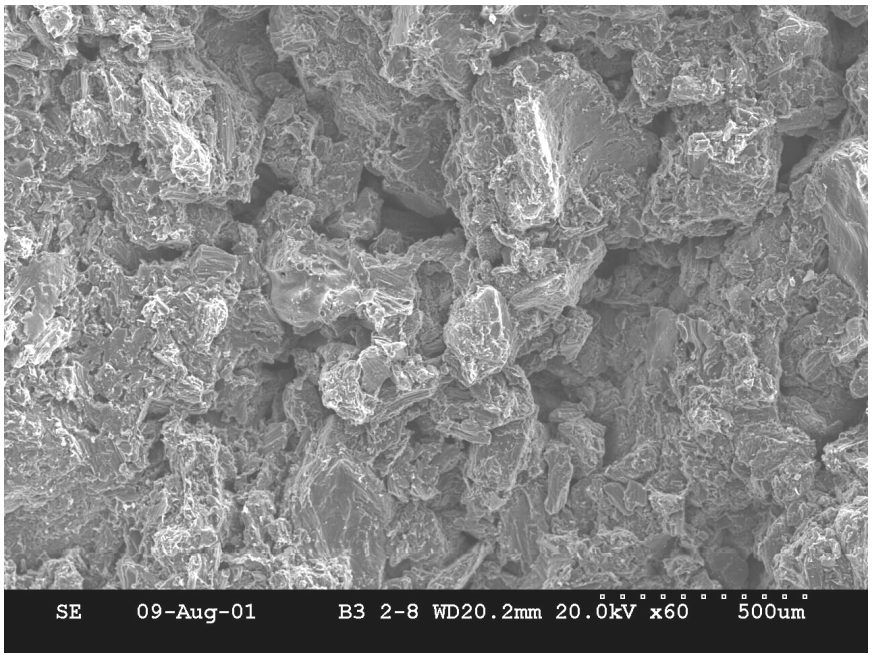

Figure 9.11 Air gasification near anode top. *Reactive binder phase selectively oxidized. Fracture surface ~ 1 cm below anode top surface, PB 3 core 2*

The micrograph given in Figure 9.12 shows an example of pitting caused by the catalytic activity of a cryolite contamination particle. Figure 9.13 shows a typical example of edge recession.

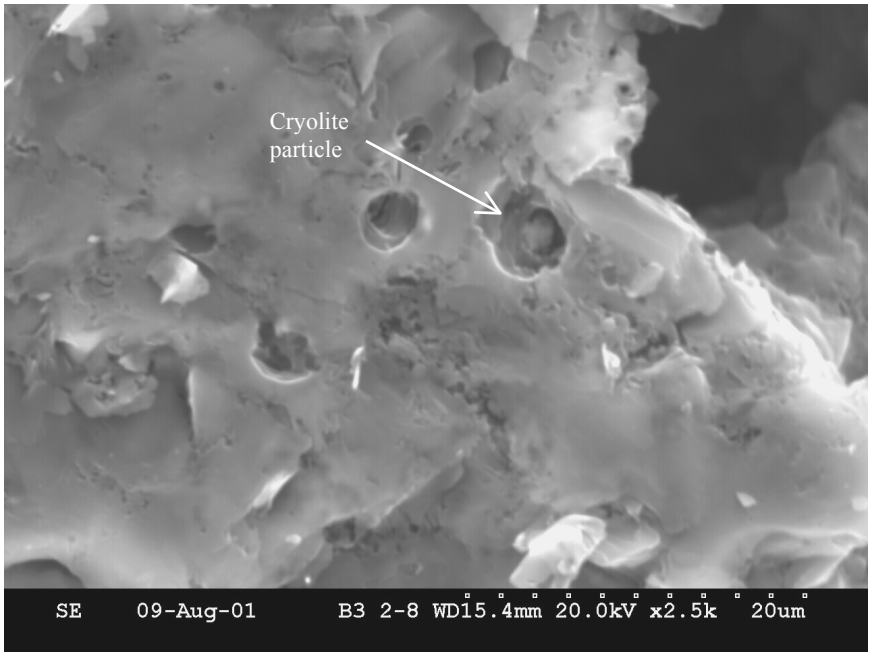

Figure 9.12 Air gasification of binder phase, cryolite induced pit-formation. *Cryolite particle observed in bottom of pit (gray shadow). Fracture surface ~ 1 cm below anode top surface, PB 3 core 2*

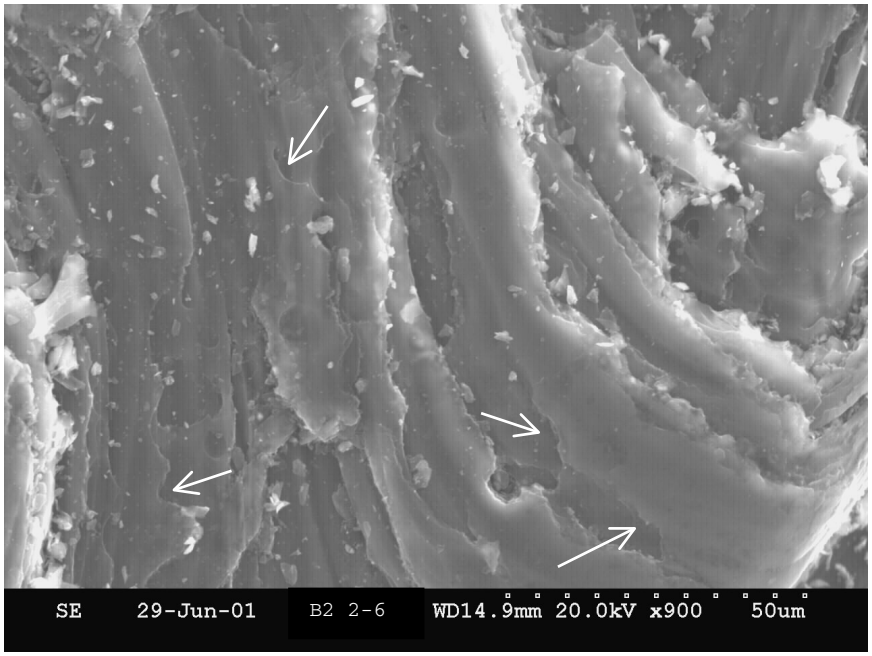

Figure 9.13 Air gasification of binder phase near anode top, edge recession (see arrows). *Fracture surface ~ 2 cm below anode top surface, PB 3 core 2*

The temperature of the anode top depends on the anode height and thermal conductivity. The surface temperature of newly set prebaked anodes (height ~ 60 cm) is normally within the temperature range where the air gasification rate is chemically controlled (300 – 400 °C). However, for anodes of height 15 – 19 cm, the temperature of the upper parts is well within a diffusion controlled regime (~ 800 – 900 °C). A concentration gradient is set up and the air concentration reaches zero at some point within the anode. From the air permeability data in Table 9-5, air gasification seems significant to a distance of 2 – 4 cm below the anode top surface. The momentary air gasification depth is however dependent on the actual top surface temperature and does therefore vary with the anode height. If the top surface temperature is low (new anodes) air gasification may proceed deep into the anodes (chemically controlled). At high surface temperatures (small anodes) only the very topmost parts are gasified. The anodes studied in this work has gone through all regimes from chemically controlled gasification shortly after resetting to diffusion controlled gasification as they are worn down.

As discussed in the previous chapter, prebaked anodes are contaminated by bath particles introduced via the addition of butts. Examinations of the fracture surfaces using the SEM's backscatter detector (element contrast) reveal the presence of considerable amounts of contamination particles. The particles are of varying size (~ 0.5 – 50 μm) and their elemental composition is equivalent to that of Na_3AlF_6, CaF_2 or AlF_3/Al_2O_3. In some cases, signs of enhanced oxidation are observed in immediate vicinity of the smallest contamination particles indicating that they are catalytically active (Figure 9.12). As also observed for the laboratory-made cokes, the larger particles seem inactive and appear to have poor contact with the carbon substrate.

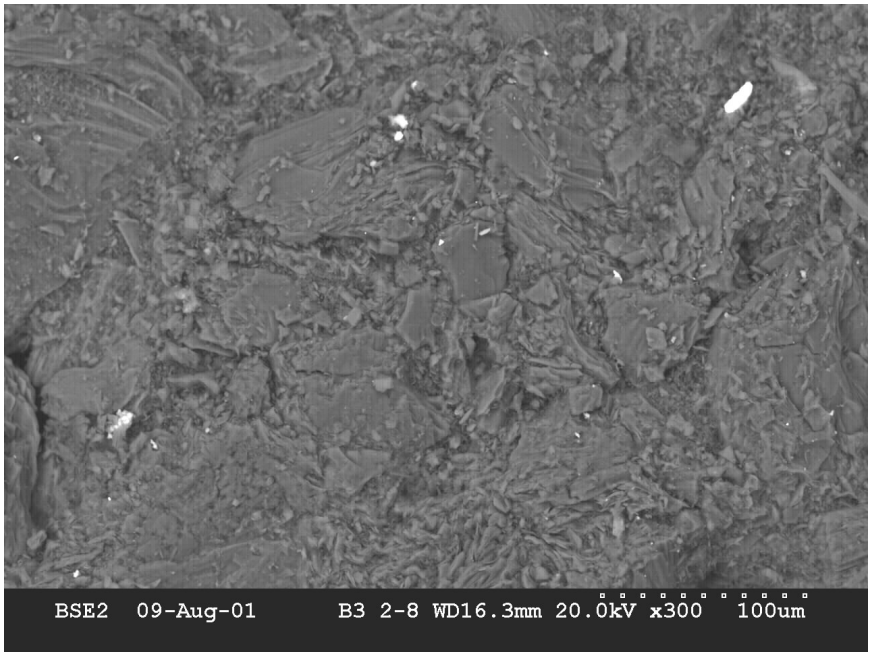

Figure 9.14 Bath particles (light) in prebaked anode. *Fracture surface ~ 10 cm above working surface, PB 3 core 2*

After the air permeability measurements and SEM examinations were completed, the anode slices were crushed. The – 1 + 0.5 mm size fraction were sieved out for bulk metal impurity analyses. Table 9-6 shows the analyzed contamination profiles (Na, Ca, Al) of three of the core samples. The contamination profile of PB 2 core 2 is graphically presented in Figure 9.15.

Table 9-6 Contamination profiles, PB 1 core 1, PB 2 core 2 and PB 3 core 1. *Analyzed by atomic absorption spectroscopy of ash from – 1 + 0.5 mm fraction dissolved in HNO_3*

slice	h	PB 1 core 1				PB 2 core 2				PB 3 core 1			
		Ash	Na	Ca	Al	Ash	Na	Ca	Al	Ash	Na	Ca	Al
	cm	*wt%*		*ppm*		*wt%*		*ppm*		*wt%*		*ppm*	
1	1.5	0.116	115	50	25	0.812	260	50	200	1.130[1]	2240[1]	105[1]	325[1]
2	3.5	0.109	65	40	20	0.123	75	50	75	0.136	125	125	50
3	5.5	0.088	50	40	25	0.123	75	50	50	0.154	140	140	45
4	7.5	0.091	50	40	25	0.118	85	45	40	0.176	165	195	55
5	9.5	0.095	65	45	35	0.161	90	45	100	0.172	145	185	40
6	11.5	0.298	105	50	125	0.161	200	40	200	0.173	180	245	45
Ave.		0.133	75	44	43	0.250	131	47	111	0.324	499	166	93
STD		0.082	28	5	41	0.276	79	4	72	0.395	853	52	114

[1] High values due to solidified bath in pores.

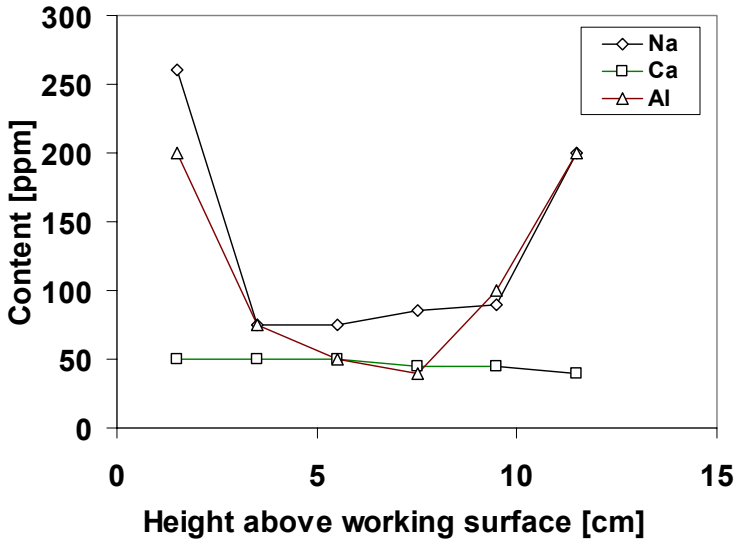

Figure 9.15 Sodium, calcium and aluminium content *vs.* height above anode working surface. *PB 2 core 2*

The impurities in the middle parts of the anode butts (height ~ 4 – 9 cm above working surface) are believed to mainly arise from the butts (background contamination level). The amounts vary significantly from one anode to another. Due to some penetration and subsequent condensation of gaseous bath species, the concentration of sodium and aluminium is especially high in the lowest 3 – 4 cm of the anodes. At 1000 °C, the vapor pressure over a molten mixture of cryolite and aluminium oxide (2.5 wt% Al_2O_3) is reported to be 0.40 kPa [104]. For melts with NaF/AlF_3 molar ratios (cryolite ratio) higher than 1.0, $NaAlF_4$ (g) and NaF (g) are regarded as the most important gaseous species [103]. The total vapor pressure increases exponentially with decreasing cryolite ratio, while increasing contents of aluminium oxide and calcium fluoride lower the melts vapor pressure [103].

At condensation, both $NaAlF_4$ (s) and $Na_5Al_3F_{14}$ (s) are formed [103]. $NaAlF_4$ is however metastable in the solid phase and decompose readily at 680 °C [105]:

$$5\ NaAlF_4\ (s) \quad \Leftrightarrow \quad Na_5Al_3F_{14}\ (s) + 2\ AlF_3\ (s) \qquad \textbf{Eq. 9.3}$$

Due to the low volatility of calcium fluoride, calcium is not introduced via bath vapor penetration. The recycled anode butts are thus regarded as the main Ca contamination source and the calcium concentrations are therefore nearly constant.

The high impurity level of the upper 2 cm of the anodes arises probably from penetration of liquid bath. Just before they are replaced, the anodes may be almost completely immersed in the electrolyte. Although the butts surfaces were cleaned by wire brushing and air blasting before the core samples were taken out for analyses, some solidified bath may still be present in the pores.

Table 9-7 shows the air and CO_2 reactivities of the different slices of PB 2 core 2 and PB 3 core 1. The reactivities were measured as described in chapter 3.2.1 (grain size: - 2 + 1 mm, T_{air}: 525 °C, T_{CO2}: 960 °C). The estimated CO_2 reactivities ($R_{CO2,est}$) are calculated from equation 9.2 using the impurity concentrations in Table 9-6.

Table 9-7 Air and CO_2 reactivities, PB 2 core 2 and PB 3 core 1. *Air reactivity measured at 525 °C, CO_2 reactivity measured at 960 °C. Aggregate grain size: - 2 + 1 mm. Average values of 3 parallel measurements. Standard deviations given in parenthesis*

		PB 2 core 2			PB 3 core 1		
Slice	Height	R_{Air}	R_{CO2}	$R_{CO2,est.}$	R_{Air}	R_{CO2}	$R_{CO2,est}$
	cm		*mg/g·h*			*mg/g·h*	
1	1.5	103.2 *(0.2)*	92.8 *(0.6)*	57.4	195.1 *(2.6)*	188.5 *(2.1)*	168.1
2	3.5	31.8 *(1.8)*	28.3 *(1.2)*	23.0	41.6 *(1.9)*	28.3 *(1.6)*	20.3
3	5.5	31.9 *(1.7)*	26.7 *(1.5)*	18.2	49.0 *(0.6)*	29.1 *(0.4)*	20.0
4	7.5	32.3 *(0.9)*	30.5 *(0.4)*	16.7	48.4 *(1.2)*	32.3 *(1.3)*	23.1
5	9.5	39.6 *(0.5)*	36.2 *(0.3)*	29.4	37.6 *(0.8)*	29.1 *(1.7)*	19.2
6	11.5	47.3 *(1.3)*	56.0 *(1.1)*	54.8	35.9 *(1.4)*	29.4 *(1.3)*	21.6

As was shown in the previous chapters, the bath compounds, especially calcium fluoride, but also sodium fluoride and cryolite catalyze the carbon-CO_2 gasification reaction strongly. Sodium fluoride and cryolite also act as strong air gasification catalysts. AlF_3 on the other hand may act as a gasification inhibitor.

As seen from the correlation matrix given in Table 9-8, there are good correlations between the measured CO_2 reactivities and the analyzed sodium and calcium contents. The air reactivities on the other hand, appear to be mainly influenced by the sodium contents. The apparently good correlations between the air and CO_2 reactivities and the aluminium concentrations are caused by the high covariation between aluminium and sodium (sodium mainly present as Na_3AlF_6). The measured CO_2 reactivities correlate well with the CO_2 reactivities calculated from Eq. 9.2 (R^2 = 0.99). The small absolute value differences probably arise from differences in calcination temperature, porosity and background contamination level between the industrial prebaked anodes and the laboratory made coke samples.

Table 9-8 Correlation matrix, impurity concentrations and reactivities.
PB 2 core 2 and PB 3 core 1

	Na	Al	Ca	R_{Air}	R_{CO2}	$R_{CO2,est.}$
Na	-					
Al	0.97	-				
Ca	0.80	0.66	-			
R_{Air}	0.94	0.87	0.88	-		
R_{CO2}	0.94	0.85	0.93	0.99	-	
$R_{CO2,est.}$	0.96	0.89	0.93	0.96	0.99	-

9.2.2 Søderberg anodes

The Søderberg anode core samples (Ø 50 mm) were cut in cylinders of 60 mm height and analyzed in terms of air permeability, impurity content and reactivity towards CO_2 gasification.

Figure 9.16 and Table 9-9 show the measured air permeabilities. Due to visible bath penetration, the lower 13 – 14 cm of the anodes (cyl. no. 1 – 2) is not analyzed.

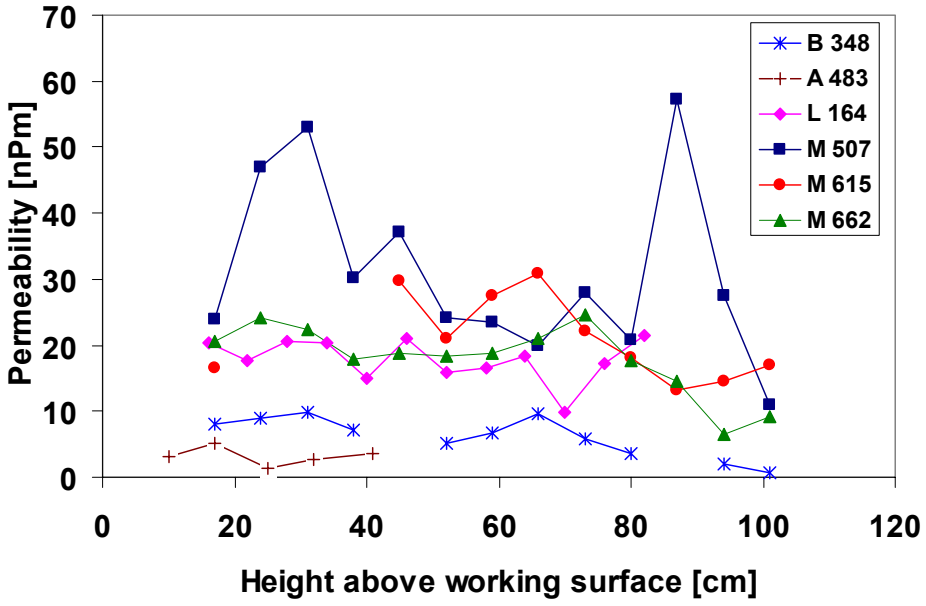

Figure 9.16 Air permeability *vs.* average height above working surface, Søderberg anodes. *Average height defined as distance from cylinder center to working surface*

Table 9-9 Air permeability of Søderberg anodes. *Cylinders (Ø 50 mm, h 60 mm) from cores drilled from cold anodes after cell shut-down. h = distance from cylinder center to working surface. Samples below lines are from the anode baking zone (noncalcined binder phase)*

Cyl.	B 348		A 483		L 164		M 507		M 615		M 662	
	h *cm*	Perm. *nPm*	h [1] *cm*	Perm. *nPm*	h *cm*	Perm. *nPm*	h *cm*	Perm. *nPm*	h *cm*	Perm. *nPm*	h *cm*	Perm. *nPm*
1	5		4		4		5		5		5	
2	11		10	3.14	10		11		11		11	
3	17	7.95	17	5.21	16	20.26	17	23.83	17	16.64	17	20.52
4	24	8.93	25	1.37	22	17.76	24	46.99	24	crack	24	24.13
5	31	9.92	32	2.79	28	20.49	31	52.91	31	crack	31	22.27
6	38	7.11	41	3.63	34	20.45	38	30.21	38	crack	38	17.81
7	45	crack	48	crack	40	15.06	45	37.07	45	29.70	45	18.82
8	52	5.23			46	20.99	52	24.14	52	21.01	52	18.28
9	59	6.79			52	15.90	59	23.43	59	27.41	59	18.69
10	66	9.69			58	16.64	66	19.86	66	30.87	66	20.93
11	73	5.71			64	18.45	73	27.97	73	22.23	73	24.60
12	80	3.69			70	9.84	80	20.73	80	18.20	80	17.59
13	87	crack			76	17.12	87	57.29	87	13.10	87	14.46
14	94	1.91			82	21.42	94	27.41	94	14.44	94	6.38
15	101	0.78					101	10.97	101	17.10	101	9.09
Average all		**6.16**		**3.23**		**17.77**		**30.99**		**21.07**		**17.97**
STD all		**3.05**		**1.39**		**3.18**		**13.76**		**6.35**		**5.34**
Average ca. 20 – 60 cm		**7.60**		**2.60**		**18.18**		**35.79**		**26.04**		**20.00**
STD ca. 20 – 60 cm		**1.85**		**1.14**		**2.44**		**12.16**		**4.50**		**2.57**

[1] Sections between cylinder no. 2 – 3 (2 cm) and no. 4 – 5 (2 cm) discarded due to cracks

Due to less optimal forming and baking conditions, Søderberg anodes are normally more porous and show higher permeabilities than prebaked anodes. While the prebaked anodes studied in this work had a fairly constant permeability of 0.5 – 1.2 nPm, the permeability of Søderberg anodes varies significantly (average values from 3.23 to 30.99 nPm). The permeability of anode M 507 is high and shows large variations (30.99 ± 13.76 nPm). Due to a more optimal anode recipe, the permeabilities of A 483 and B 348 are almost as low as the permeability of a "poor" prebaked anode.

The CO_2 gasification rate is only significant at temperatures above 750 – 800 °C. For most anode qualities the reaction rate roughly doubles per 40 degrees temperature increase above 800 °C [99]. The temperature of the immersed parts of the Søderberg anodes is equal to the bath temperature (940 – 970 °C). However, the anode temperature decreases with increasing distance from the working surface. According to measurements and computer simulations performed by Tørklep *et al.* [106], the 900 °C isotherm is normally located at a distance of about 30 – 35 cm above the working surface (center of anode, anode immersion depth: 12 cm). At 60 – 65 cm the temperature is about 750 °C.

The high-permeability anodes (L 164, M 615 and M 662) show a relatively constant permeability up to the baking zone, indicating that CO_2 gasification occurs as long as the temperature is sufficiently high. The permeability peaks of M 507 are probably caused by the presence of vertical hail-line cracks, which severely influence the air permeability values. The low-permeability anodes, especially A 483 show an abrupt permeability drop at heights above approximately 20 cm. Apparently, CO_2 gasification occurs in the lower parts of the anodes, but because of mass transfer limitations, the gasification zone does not proceed as high up as in the high-permeability anodes. In addition to CO_2 gasification losses, the increased permeabilities in the lower high temperature parts of the anodes are probably mostly due to increased contraction and cracking of the binder coke.

In the same way as for the prebaked anode butts, Søderberg anode samples (fracture surfaces) taken from different heights above the working surface were examined in the electron microscope. It was especially searched for surface textural changes indicative of gasification. The micrographs given in Figure 9.17 show the porous structure of high-permeability M 507 anode. As seen, the porosity is mainly located in the low-calcined binder phase (see also micrograph given in Figure 9.18). The fracture surfaces are extremely loose and aggregate grains may easily be removed by rubbing a finger across them. Since much of the binder phase is consumed, substantial dusting is expected from the working surface of these anodes. Topographical changes like pitting, edge recession and channeling are only observed in less destroyed areas and further from the working surface where the gasification has been less severe (see Figure 9.19).

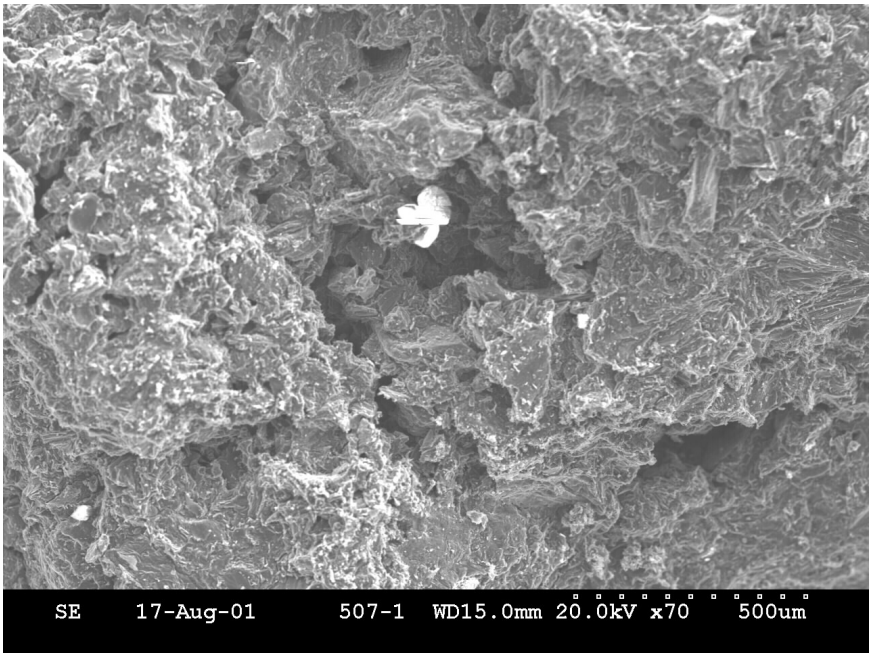

A) Fracture surface ~ 15 cm above working surface

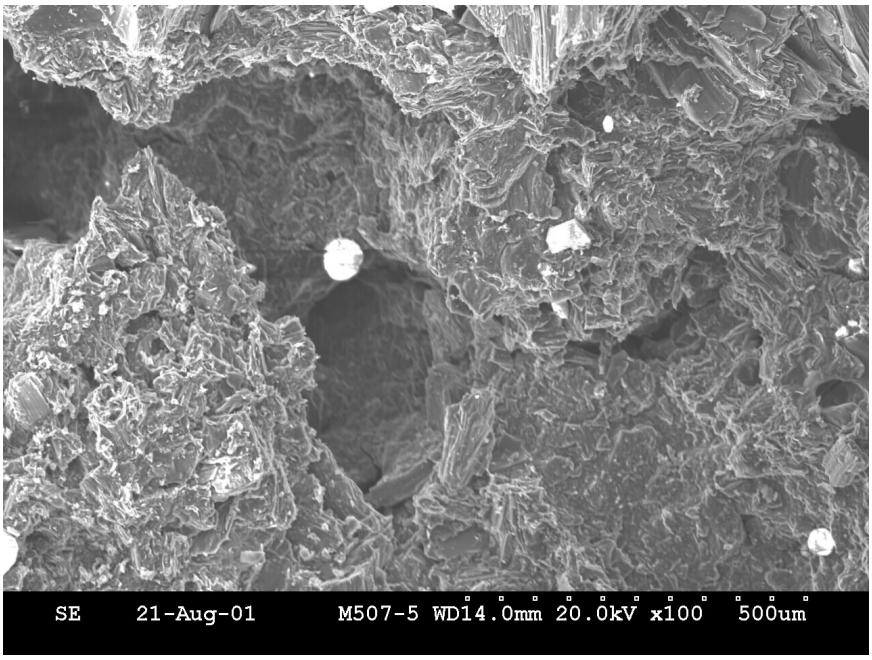

B) Fracture surface ~ 50 cm above working surface

Figure 9.17 Porosity in lower parts of a high-permeability Søderberg anode. *M 507*

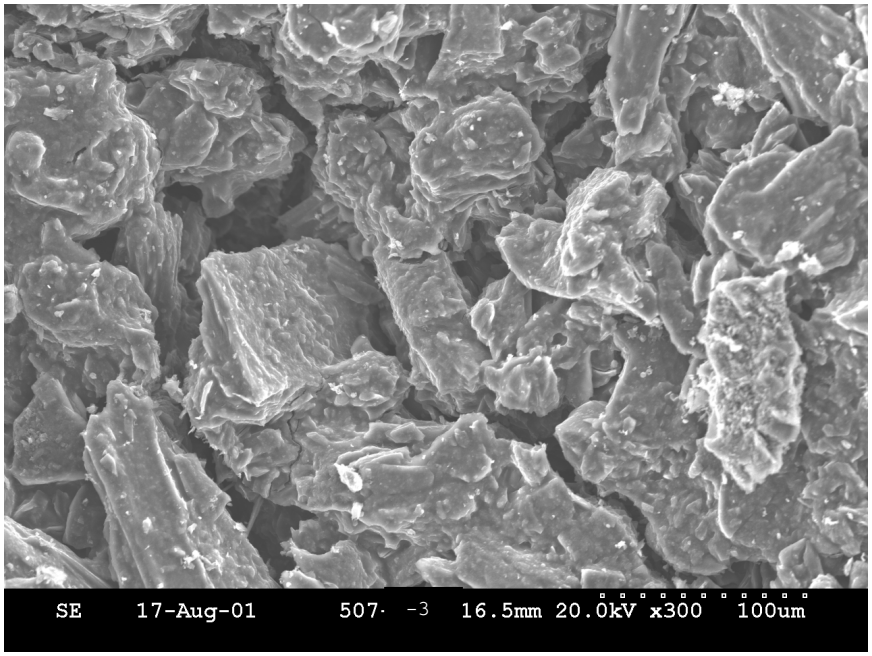

Figure 9.18 Selective gasification of low-calcined binder coke in lower part of Søderberg anode. *Fracture surface ~ 15 cm above working surface, M 507*

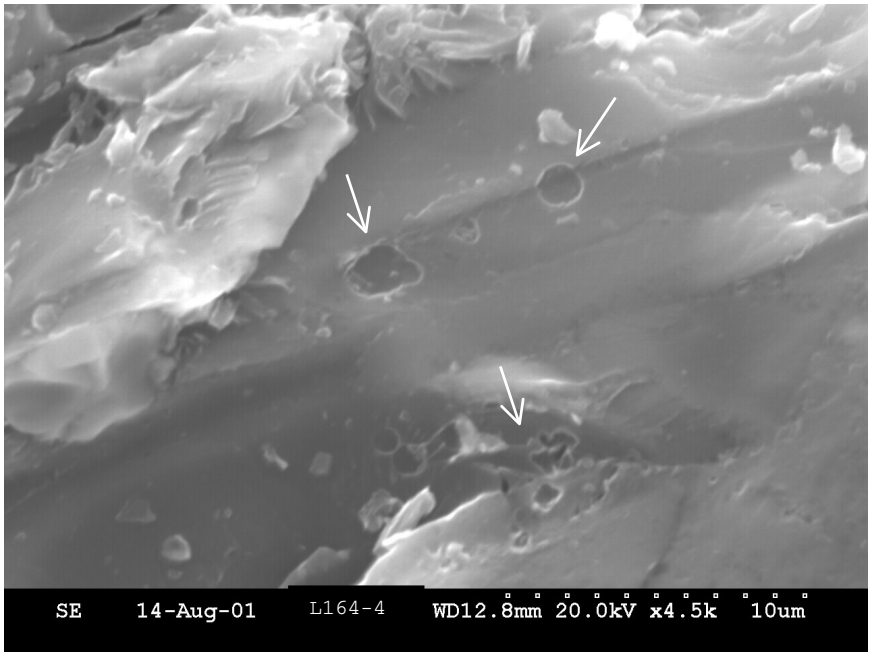

Figure 9.19 CO_2 gasification, incipient pitting (see arrows). *Fracture surface ~ 22 cm above working surface, L 164*

Figure 9.20 shows a SEM-micrograph of the lower part of the far denser A 483 anode. As seen, the binder phase gasification is much less severe in this anode than in the high-permeability M 507 anode (Figure 9.17). In general, the fracture surfaces of A 483 and B 384 were far firmer than the fracture surfaces of the high-permeability anodes (L 164, M 507, M 615 and M 662).

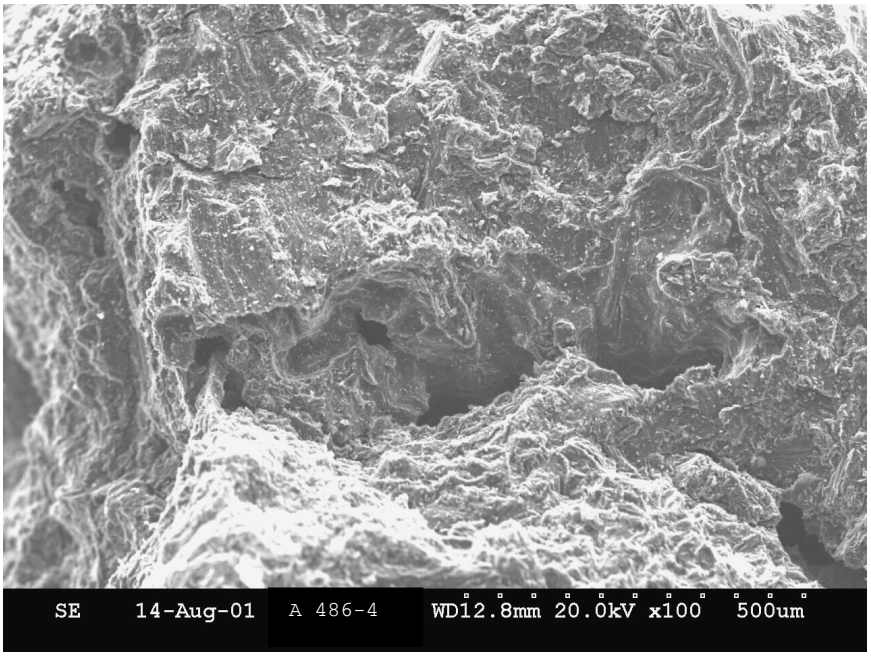

Figure 9.20 Porosity in lower parts of a low-permeability Søderberg anode. *Fracture surface ~ 15 cm above working surface, A 483*

Due to the often high porosity and permeability of Søderberg anodes, signs of gasification (pitting, edge-recession etc.) are found at far greater distances from the working surfaces than for the prebaked anodes. The micrograph given in Figure 9.21 show an example of selective CO_2 gasification occurring as far as 65 cm above the working surface (high-permeability anodes). In the low-permeability anodes (B 348 and A 483) the gasification signs are scarce at heights above 15 – 20 cm.

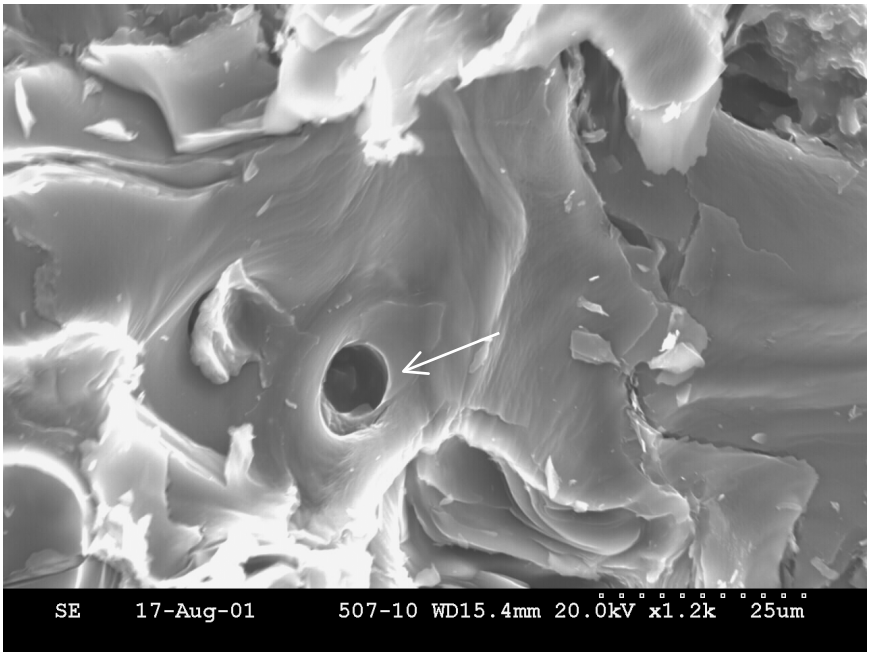

Figure 9.21 Pit formed from catalyzed CO_2-gasification. *Sodium-rich particle observed in bottom of pit (gray shadow). Fracture surface ~ 65 cm above working surface, M 507*

From his work about the influence of anode baking temperature and current density upon dusting, Cutshall [100] concluded that the majority of the carbon dust comes from the vertical anode sides, below bath level and not from the anode working surface. However, it should be noticed that instead of using real Søderberg anodes, Cutshall used prebaked anodes that were baked to Søderberg baking temperatures (942 – 956 °C). The obtained anode permeabilities were lower than the usual Søderberg anode permeabilities (~ 4 – 6 nPm *vs.* ~ 10 – 30 nPm) and the extent of internal gasification was therefore far less severe than in real Søderberg anodes.

In a Søderberg anode the magnitude of air exposure to the anode side depends on air leaks through the top crust and gas manifolds and the magnitude of negative pressure in the gas channels. The temperature of the anode side directly above the bath level is, however, well within the diffusion controlled regime, *i.e.* the reaction rate depends on how fast O_2 can be transported to the reaction zone. Air has also free access to the Søderberg anode top, but the temperature there is too low for gasification.

Table 9-10 shows the analyzed impurity contents of L 164, M 507, M 662 and A 483 (samples with molten bath infiltration have been excluded). The contamination profile of L 164 is graphically presented in Figure 9.22. In spite of that no butts are used, the Søderberg anodes are far more contaminated than prebaked anodes. The high concentration of sodium and aluminium in the lower parts of L 164, M 507 and M 662 arises from penetration and subsequent condensation of bath vapors ($NaAlF_4$ and NaF vapor, see chapter 9.2.1). The temperature in the lower 10 cm of the anodes appears to be too high to allow effective condensation of the bath gases, which is first reached at a height of approximately 10 – 15 cm above the working surface (cyl. 3). From here, the contamination levels decrease with increasing distances from the working surface until they reach a more or less constant

background contamination level at heights above approximately 50 cm (from cyl. 9). The high calcium content of the lowest 10 cm of A 483 reveals that this anode mainly is contaminated by liquid bath penetration (because of low volatility of CaF_2, Ca is not introduced by bath vapor condensation). During controlled shut-down, the Søderberg cell is normally short-circuited by lowering the anode into the metal pool. Metal and electrolyte may then penetrate into the open pore structure of the lower parts of the anodes. Microscopy studies done by Sørlie [107] reveal that the pores in the lower 10 cm of the anodes may be completely filled after a normal shut-down procedure.

The anodes are also contaminated from pot-room atmospheric dust. The dust (mainly aluminium oxide and cryolite) settles on the anode tops and is incorporated in the carbon matrix as the anode paste moves down through the baking zone. The dust level and hence also the background impurity level varies from pot-room to pot-room. The SEM-micrograph given in Figure 9.23, reveals the presence of large hexagonal aluminium oxide crystals (Ø 50 – 100 μm) and smaller and more irregular shaped cryolite particles inside the anode matrix.

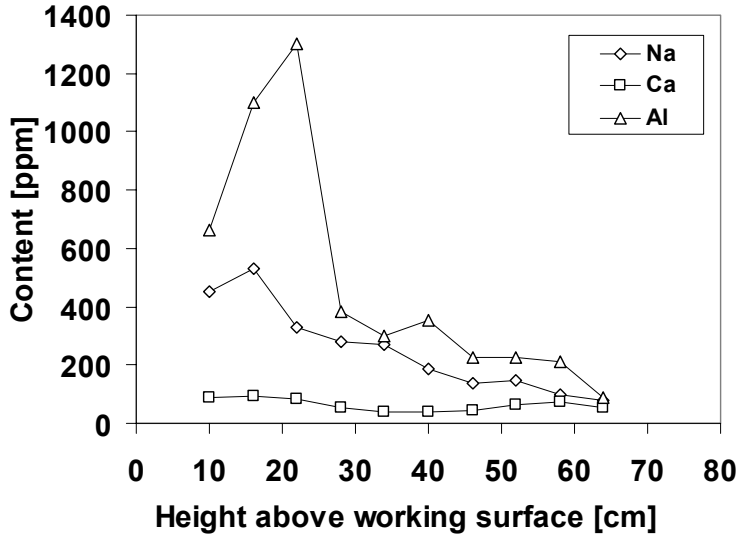

Figure 9.22 Sodium, calcium and aluminium content *vs.* height above anode working surface. *L 164.*

Table 9-10 Contamination profiles of L 164, M 507, M 662 and A483. *Analyzed by atomic absorption spectroscopy of ash from – 1 + 0.5 mm fraction dissolved in HNO_3. Background cont. level = average ~ 50 – 80 cm (cyl. 9 – 12)*

	L 164					M 507					M 662					A 483				
Cyl.	h	Ash	Na	Ca	Al	h	Ash	Na	Ca	Al	h	Ash	Na	Ca	Al	h	Ash	Na	Ca	Al
	cm	*wt%*		*ppm*		*cm*	*Wt%*		*ppm*		*cm*	*wt%*		*ppm*		*cm*	*wt%*		*ppm*	
1						5	0.392	440	40	750	5	0.295	330	30	540	4	1.122	625	150	3580
2	10	0.411	450	85	665	11	0.506	555	45	1225	11	0.383	365	35	885	10	0.458	170	100	1395
3	16	0.665	525	95	1100	17	0.515	605	45	1165	17	0.569	390	45	1520	17	0.723	135	95	430
4	22	0.500	335	85	1300	24	0.438	420	60	950	24	0.391	285	35	930	25	0.262	110	90	440
5	28	0.263	275	55	385	31	0.347	295	30	825	31	0.415	205	40	1135	32	0.305	100	80	685
6	34	0.227	270	40	300	38	0.273	235	30	545	38	0.448	135	35	1495	41	0.479	120	95	1270
7	40	0.214	190	40	355	45	0.315	285	50	840	45	0.292	80	35	860					
8	46	0.187	135	45	230	52	0.444	310	50	1375	52	0.253	55	30	645					
9	52	0.211	145	65	225	59	0.231	205	40	515	59	0.278	65	35	770					
10	58	0.175	95	75	210	66	0.392	165	50	1170	66	0.326	65	35	1030					
11	64	0.150	80	50	90	73	0.367	130	55	1070	73	0.243	55	30	645					
12						80	0.168	95	35	298										
Average all cyl.		**0.288**	**230**	**60**	**465**		**0.365**	**310**	**45**	**890**		**0.354**	**185**	**35**	**950**		**0.558**	**210**	**102**	**1300**
STD		**0.175**	**140**	**20**	**430**		**0.106**	**165**	**10**	**330**		**0.099**	**15**	**5**	**325**		**0.320**	**205**	**25**	**1190**
Backgr.cont. level (ave. cyl 9 – 12)		**0.181**	**115**	**60**	**190**		**0.290**	**150**	**45**	**760**		**0.282**	**60**	**30**	**815**					
STD		**0.025**	**30**	**15**	**65**		**0.107**	**50**	**10**	**525**		**0.042**	**10**	**1**	**195**					

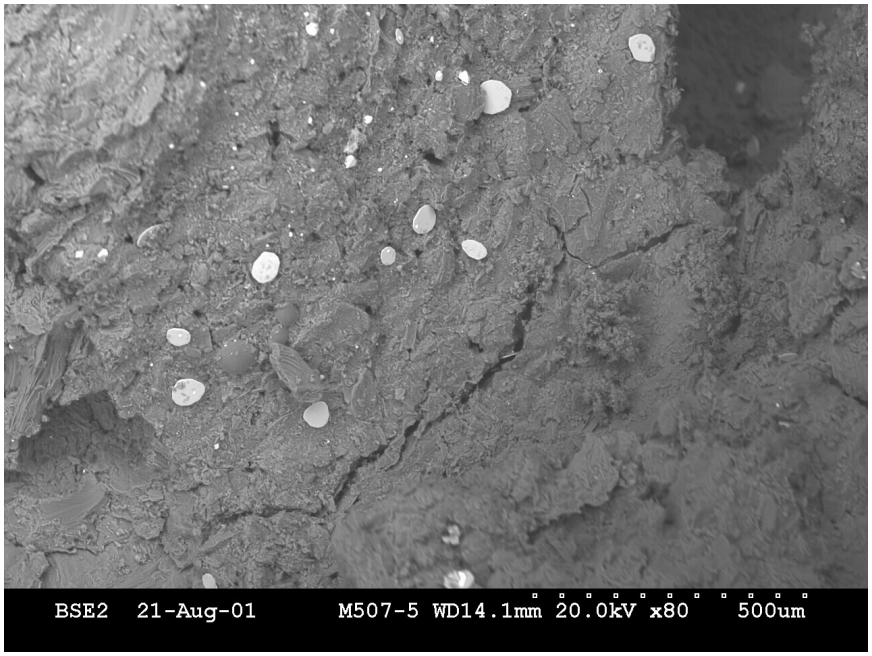

Figure 9.23 Aluminium oxide (large hexagonal crystals) and cryolite (small particles) contaminations inside Søderberg anode matrix. *Fracture surface ~ 30 cm above working surface M 507*

Table 9-11 gives the CO_2 reactivities of L 164, M 507, M 662 and A 483. The estimated reactivities $R_{CO2,est}$, calculated from Eq. 9.2, are also shown. Because of higher porosities, lower calcination temperatures and higher impurity levels, the Søderberg anode aggregates are considerably more reactive towards gasification than the prebaked anode aggregates. Especially calcium, but also sodium is known to catalyze the CO_2 gasification reaction strongly. As found by correlation analysis (see Table 9-12), the measured CO_2 reactivities correlate fairly well with the analyzed sodium concentrations ($R^2 = 0.91$), but because of the low and relatively constant calcium contents, the correlation between the CO_2 reactivities and the calcium concentrations is poor. Although the absolute values differ considerably, the measured reactivities correlate fairly well with the reactivities calculated from Eq. 9.2 ($R^2 = 0.80$).

Table 9-11 CO_2 reactivities of L 164, M 507, M 662 and A483. *Reactivities measured at 960 °C. Aggregate grain size: -2 + 1 mm. Average of 3 parallel measurements. Standard deviations given in parenthesis.*

	L 164			M 507			M 662			A 483		
Cyl.	h	R_{CO2}	$R_{CO2,est}$	h	R_{CO2}	$R_{CO2,est}$	h	R_{CO2}	$R_{CO2,est}$	h	R_{CO2}	$R_{CO2,est}$
	cm	*mg/g·h*		*cm*	*mg/g·h*		*cm*	*mg/g·h*		*cm*	*mg/g·h*	
1				5	138.0 *(10.9)*	32.0	5	111.4 *(13.0)*	25.0	4	151.8 *(8.6)*	62.1
2	10	153.7 *(14.5)*	42.0	11	154.0 *(15.5)*	37.6	11	104.6 *(10.2)*	27.4	10	81.3 *(6.8)*	32.1
3	16	106.2 *(18.6)*	46.9	17	148.0 *(4.5)*	40.2	17	115.4 *(14.9)*	30.5	17	67.3 *(4.2)*	30.2
4	22	141.9 *(9.1)*	36.5	24	138.1 *(12.5)*	34.7	24	93.1 *(14.0)*	24.6	25	68.3 *(3.7)*	27.8
5	28	109.9 *(15.6)*	27.7	31	101.2 *(13.8)*	23.5	31	69.3 *(9.4)*	21.7	32	65.4 *(7.6)*	25.7
6	34	95.5 *(11.9)*	24.4	38	103.2 *(6.3)*	21.2	38	53.2 *(6.1)*	17.3	41	75.0 *(3.4)*	29.4
7	40	80.5 *(5.4)*	20.8	45	75.9 *(4.0)*	26.8	45	52.2 *(7.0)*	15.4			
8	46	68.4 *(4.5)*	20.2	52	81.2 *(9.3)*	28.5	52	55.9 *(5.7)*	13.2			
9	52	74.3 *(6.7)*	24.4	59	58.5 *(3.7)*	22.2	59	54.5 *(5.1)*	14.2			
10	58	75.5 *(5.7)*	24.6	66	61.3 *(2.7)*	21.7	66	49.4 *(3.8)*	14.3			
11	64	66.9 *(2.6)*	19.0	73	53.8 *(4.7)*	21.8	73	49.1 *(3.1)*	13.3			
12				80	45.6 *(3.2)*	15.8	80	49.0 *(3.2)*				

Table 9-12 Correlation matrix, impurity concentrations and CO_2 reactivities.
L 164, M 507, M 662 and A 483

	Na	Al	Ca	R_{CO2}	$R_{CO2,est.}$
Na	-				
Al	0.51	-			
Ca	0.26	0.47	-		
R_{CO2}	**0.91**	0.37	0.29	-	
$R_{CO2,est.}$	0.84	0.61	0.74	**0.80**	-

In addition to be influenced by the presence of catalyzing bath compounds, the measured gas reactivities are also affected by variations in porosity and calcination level (temperature and time). Both variables are highest close to the working surface, but they affect the coke reactivity in opposite directions, *i.e.* the reactivity increases with increasing porosity and decreases with increasing calcination level.

Concluding remarks

This work shows the importance of keeping the sodium and calcium contamination content of the anodes at a minimum level. Aluminium fluoride on the other hand, may have a beneficial effect on the anode gas reactivity.

Future research in the influence of bath contaminations on the gas reactivity of carbon anodes should aim at understanding the inhibiting effect of fluorine gases. If properly utilized, this effect may reduce the gas reactivity of the carbon materials significantly. In the Hall-Héroult process some aluminium fluoride has to be added to the electrolyte in order to keep the cryolite ratio constant during cell operation. As proposed by Sørlie *et al.* [12], introduction through the anodes may thus be convenient. Impregnating the anodes by organo fluorine compounds may also be beneficial. However, since most fluorine gases are both poisonous and environmentally hazardous, special care should be taken when selecting impregnating species and procedure.

Since the anode gasification loss is strongly dependent on the anodes gas permeability and the surface area accessible for reaction, it may also be advantageous to add species that sublime at temperatures below the maximum anode baking temperature and condense within the open pore network during cooling (prebaked anodes).

References

1. K. Grjotheim and H. Kvande, "*Introduction to Aluminum Electrolysis*", 2 ed. Aluminium-Verlag, Düsseldorf (1993) pp. 260
2. G.J. Houston and H.A. Øye, Aluminium **61** (1985) 250
3. J.F. Rakszawski and W.E. Parker, Carbon **2** (1964) 53
4. G.F. Vedernikov and M.M. Yetykukov, Sov J Non-Ferrous Metals **1** (1967) 80
5. P. Rhedey, Light Metals (1971) 385
6. E.A. Yanko, V.D. Lazarev, M.G. Voronkov and E.N. Deryagina, Sov J Non-Ferrous Metals **10** (1975) 45
7. V.D. Lazarev, E.A. Yanko and V.V. Zakharov, Sov J Non-Ferrous Metals **19** (1978) 38
8. P.J. Rhedey, Light Metals (1982) 713
9. T. Müftüoglu and H.A. Øye, Light Metals (1987) 471
10. W.K. Fischer and R. Perruchoud, Light Metals (1991) 721
11. S.H. Hume, W.K. Fischer, R.C. Perruchoud and B.J. Welch, Light Metals (1993) 525
12. M. Sørlie, Z. Kuang and J. Thonstad, in "*Extended Abstracts and Program, 21st. Biennial Conference on Carbon*", Buffalo NY (1993) 677
13. Z. Kuang, J. Thonstad and M. Sørlie, Carbon **33** (1995) 1479
14. M. Aanvik, M. Sørlie and H.A. Øye, in "*Abstracts and Programme, 1st. World Conference on Carbon*", Berlin (2000) 347
15. M. Aanvik, M. Sørlie and H.A. Øye, Light Metals (2000) 555
16. M.Aa. Engvoll, H.A. Øye and M. Sørlie, Light Metals (2001) 661
17. M.Aa. Engvoll, H.A. Øye and M. Sørlie, in "*Extended Abstracts, Carbon '01*", Lexington KY (2001)
18. M.Aa. Engvoll, H.A. Øye and M. Sørlie, in "*Conference proc. Eleventh International Aluminium Symposium*", Trondheim-Bergen-Trondheim, Norway (2001)
19. M.Aa. Engvoll, H.A. Øye and M. Sørlie, Light Metals (2002) *In Press*
20. M. Zander, in "*Science of Carbon Materials*", ed. by H. Marsh and F. Rodríguez-Reinoso, University of Alicante, Alicante (2000) 205
21. M. Zander, in "*Introduction to Carbon Technologies*", ed. by H. Marsh, E.A. Heintz and F. Rodríguez-Reinoso, University of Alicante, Alicante (1997) 425
22. J.D. Brooks and G.H. Taylor, in "*Chemistry and Physics of Carbon*", vol 4, ed. by P.L. Walker jr, Marcel Dekker, New York (1968) 243
23. R. Menéndez, M. Granda, J. Bermejo and H. Marsh, in "*Introduction to Carbon Technologies*", ed. by H. Marsh, E.A. Heintz and F. Rodríguez-Reinoso, University of Alicante, Alicante (1997) 461
24. M.B. Redmount and E.A. Heintz, in "*Introduction to Carbon Technologies*", ed. by H. Marsh, E.A. Heinz and F. Rodríguez-Reinoso, University of Alicante, Alicante (1997) 519
25. J. Biscoe and B.E. Warren, J Appl Phys **13** (1942) 364
26. X. Bourrat, in "*Science of Carbon Materials*", ed. by H. Marsh and F. Rodríguez-Reinoso, University of Alicante, Alicante (2000) 3
27. H. Marsh, "*Introduction to Carbon Science*", Butterworths, London (1989) pp. 321
28. J. Gadsby, F.L. Long, P. Sleightholm and K.W. Sykes, Proc Roy Soc Lond **A 193** (1948) 357
29. S. Ergun, Jounal of Physical Chemistry **60** (1956) 480
30. P.L. Walker, F. Rusinko and L.G. Austin, in *"Advances in Catalysis"*, vol 11 (1959) 133
31. J. Thonstad, Journal of the Electrochemical Society **111** (1964) 959

32. J.A. Moulijn and F. Kapteijn, in "*Science of Carbon Materials*", ed. by H. Marsh and F. Rodríguez-Reinoso, University of Alicante, Alicante (2000) 379
33. J.M. Thomas, in "*Chemistry and Physics of Carbon*", vol 1, ed. by P.L. Walker jr, Marcel Dekker, New York (1965) 122
34. P.L. Walker, M. Shelef and R.A. Anderson, in "*Chemistry and Physics of Carbon*", vol 4, ed. by P.L. Walker, Marcel Dekker, New York (1968) 287
35. S.G. Chen and R.T. Yang, Journal of Catalysis **138** (1992) 12
36. S.G. Chen and R.T. Yang, Journal of Catalysis **141** (1993) 102
37. B.J. Wood and K.M. Sancier, in "*Catalysis reviews: science and engineering*", vol 26, Marcel Dekker, New York (1984) 233
38. I. Barin, "*Thermochemical Properties of Pure Substances*", VCH, Weinheim (1995)
39. D.W. McKee and D. Chatterji, Carbon **13** (1975) 381
40. D.A. Fox and A.H. White, Ind Eng Chem **23** (1931) 259
41. D.W. McKee, in "*Chemistry and Physics of Carbon*", vol 16, ed. by P.L. Walker and P.A. Thrower, Marcel Dekker, New York (1981) 2
42. D.W. McKee and D. Chatterji, Carbon **16** (1978) 53
43. F. Kapteijn, G. Abbel and J.A. Moulijn, Fuel **63** (1984) 1036
44. F. Kapteijn, O. Peer and J.A. Moulijn, Fuel **65** (1986) 1371
45. R. Meijer, M. Weeda, F. Kapteijn and J.A. Moulijn, Carbon **29** (1991) 929
46. F. Kapteijn, H. Porre and J.A. Moulijn, AIChE J **32** (1986) 691
47. C.A. Mims and J.K. Pabst, Prepr ACS div Fuel Chem **25** (1980) 258
48. I.L.C. Freriks, H.M.H. van Wechem, J.C.M. Stuiver and R. Bouwman, Fuel **60** (1981) 463
49. C.A. Mims, K.D. Rose and M.T. Melchior, Journal of American Chemical Society **104** (1982) 6886
50. P.J.J. Tromp and E.H.P. Cordfunke, Thermochimica Acta **81** (1984) 113
51. C.A. Mims and J.K. Pabst, Ibid **62** (1983) 176
52. W.L. Holstein and M. Boudart, Fuel **62** (1983) 162
53. F. Kapteijn and J.A. Moulijn, Fuel **62** (1983) 221
54. K.J. Hüttinger and R. Minges, Fuel **65** (1986) 1122
55. R.J. Lang, Fuel **65** (1986) 1324
56. D.W. McKee, Carbon **17** (1979) 419
57. J.-S. Chang, J.P. Adcock, L.L. Lauderback and J.L. Falconer, Carbon **27** (1989) 593
58. A. Pérez-Florindo, D. Cazorla-Amarós and A. Linares-Solano, Carbon **31** (1993) 493
59. D. Cazorla-Amorós, A. Linares-Solano, A.F. Marcilla Gomis and C. Salinas-Martínez de Lecea, Energy & Fuels **5** (1991) 796
60. D. Cazorla-Amorós, A. Linares-Solano, C. Salinas-Martínez de Lecea and J.P. Joly, Carbon **29** (1991) 361
61. D. Cazorla-Amarós, A. Linares-Solano, C. Salinas-Martínez de Lecea and F. Kapteijn, Carbon **32** (1994) 423
62. A. Linares-Solano, C. Salinas-Martínez de Lecea, D. Cazorla-Amorós, J.P. Joly and H. Charcosset, Energy & Fuels **4** (1990)
63. D. Cazorla-Amorós, A. Linares-Solano, C. Salinas-Martínez de Lecea, T. Kyotani, H. Yamashita and A. Tomita, Carbon **7** (1992) 995
64. S.S. Jones and R.D. Hildebrandt, Light Metals (1974) 901
65. S.S. Jones, R.D. Hildebrandt and M.C. Hedlund, Light Metals (1979) 553
66. L.R. Radovic, P.L. Walker Jr and R.G. Jenkins, Journal of Catalysis **82** (1983) 382
67. T. Ganga Devi and M.P. Kannan, Fuel **77** (1998) 1825
68. L.R. Radovic, "*Importance of Catalysis and Carbon Active Sites in Lignite Char Gasification, Ph.D. thesis*", Penn State University, University Park PA (1982)

69. V.A. Braunswarth, J.A. Brown, E.A. Hollingshead and P.J. Rhedey, Light Metals (1975) 325
70. T. Eidet, "*Reactions on carbon anodes in aluminium electrolysis, Dr.Ing thesis*", Norwegian university of science and technology, Trondheim (1997)
71. S. Rørvik, M. Aanvik, M. Sørlie and H.A. Øye, Light Metals (2000) 549
72. E.S. Pearson and H.O. Hartley, "*Biometrika Tables for Statisticans*", 3 ed. Cambridge University Press, (1966)
73. S. Yokoyama, K. Tanaka, I. Toyoshima, K. Mihyahara, K. Yoshida and J. Tashiro, Chemistry Letters (1980) 599
74. K.J. Hüttinger and R. Minges, Fuel **65** (1986) 1112
75. R.J. Day, P.L. Walker and C.C. Wright, in "*Industrial Carbon & Graphite*", Soc. Chem. Ind., London (1958) 348
76. P.G. Pallmer, Carbon **4** (1966) 145
77. P. Hawtin and J.A. Gibson, in "*Proceedings Conference on Industrial Carbon and Graphite*", London (1970) 309
78. D.W. McKee and C.L. Spiro, Carbon **23** (1985) 237
79. "*HSC Chemistry ver. 3.02*", Outokumpu Research OY, Finland (1997)
80. D.W. McKee, Fuel **59** (1980) 308
81. K. Otto, L. Bartosiewicz and M. Shelef, Carbon **17** (1979) 351
82. J.T. Sears, H.S. Muralidhara and C.Y. Wen, Ind Eng Chem Des Dev **19** (1980) 358
83. S.M. Hume, "*Influence of Raw Material Properties on the Reactivity of Carbon Anodes, Ph.D thesis*", School of Engineering, University of Auckland, Auckland (1994)
84. A. Holmen, "*Heterogen Katalyse*", Institutt for kjemisk prosessteknologi, NTNU, Trondheim (1999) pp. 185
85. W.K. Fischer and R.C. Perruchoud, Light Metals (1985) 811
86. G.R. Romovacek, J.P. McCullough and A.J. Perrotta, Fuel **62** (1983) 1236
87. G.H. Taylor, G.M. Pennock, J.D. Fitz Gerald and L.F. Brunckhorst, Carbon **31** (1993) 341
88. H. Freund, Fuel **64** (1985) 657
89. "*Handbook of Chemistry and Physics*" vol 71, CRC Press, Boston (1990)
90. D.W. McKee, in "*Science of Carbon Materials*", ed. by H. Marsh and F. Rodríguez-Reinoso, University of Alicante, Alicante (2000) 403
91. J. Aiken, T. Heeps and W. Steedman, Fuel **47** (1968) 353
92. R.A. Greinke and I.C. Lewis, Carbon **17** (1979) 471
93. W.H. Calkins, Energy and Fuels **1** (1987) 59
94. J. Adler, K.J. Hüttinger and R. Minges, Fuel **64** (1985) 1215
95. S.M. Hume, W.K. Fischer, R.C. Perruchoud, J.B. Metson and R.T. Baker, Light Metals (1993) 535
96. M.A. Smith, R.C. Perruchoud, W.K. Fischer and B. Welch, Light Metals (1991) 593
97. M. Sørlie, "*Internal report F 50/99*", Elkem Research, Kristiansand (1999)
98. M. Sørlie and T. Eidet, in "*Conference Proceedings of the 23rd Biennial Conference on Carbon*", Penn State University, University Park PA (1997)
99. T. Foosnæs and T. Naterstad, in "*Introduction to Aluminum Electrolysis*", ed. by K. Grjotheim and H. Kvande, Aluminium-Verlag, Düsseldorf (1993) 87
100. E.R. Cutshall, Light Metals (1986) 629
101. E.R. Cutshall and V.L. Bullough, Light Metals (1985) 1039
102. B.A. Sadler and S.H. Algie, Light Metals (1991) 687
103. K. Grjotheim, C. Krohn, M. Malinovský, K. Matiasovský and J. Thonstad, "*Aluminium Electrolysis, Fundamentals of the Hall-Héroult Process*", 2 ed. Aluminium-Verlag, Düsseldorf (1982) pp. 443

104. H. Kvande, "*Thermodynamics of the system NaF-AlF_3-Al. Studied by vapour pressure measurements, Dr. Techn. thesis*", University of Trondheim, NTH, Trondheim (1979)
105. H. Ginsberg and K. Wefers, Erzmetall **20** (1967) 4
106. K.E. Tørklep, S.A. Halvorsen and T.P. Pedersen, Light Metals (1983) 843
107. M. Sørlie, "*Internal report F 89/83*", Elkem Reseach, Kristiansand (1983)